Dissertation

submitted to the
Combined Faculties of Natural Sciences and Mathematics
of the Ruperto-Carola-University of Heidelberg, Germany,
for the degree of
Doctor of Natural Sciences

Put forward by
Christos Vourellis
born in Mytilini, Greece

Oral examination: January 21st, 2020

GRMHD Launching of Outflows from Resistive and Dynamo Active Disks

Referees:

apl. Prof. Dr. Christian Fendt
Prof. Dr. Cornellis P. Dullemond

Σὰ βγεῖς στὸν πηγαιμὸ γιὰ τὴν Ἰθάκη,
νὰ εὔχεσαι νᾅναι μακρὺς ὁ δρόμος,
γεμάτος περιπέτειες, γεμάτος γνώσεις.
Τοὺς Λαιστρυγόνας καὶ τοὺς Κύκλωπας,
τὸν θυμωμένο Ποσειδῶνα μὴ φοβᾶσαι,
τέτοια στὸν δρόμο σου ποτέ σου δὲν θὰ βρεῖς,
ἂν μέν᾽ ἡ σκέψις σου ὑψηλή, ἂν ἐκλεκτὴ
συγκίνησις τὸ πνεῦμα καὶ τὸ σῶμα σου ἀγγίζει.
Τοὺς Λαιστρυγόνας καὶ τοὺς Κύκλωπας,
τὸν ἄγριο Ποσειδώνα δὲν θὰ συναντήσεις,
ἂν δὲν τοὺς κουβανεῖς μὲς στὴν ψυχή σου,
ἂν ἡ ψυχή σου δὲν τοὺς στήνει ἐμπρός σου.

Νὰ εὔχεσαι νά ᾽ναι μακρὺς ὁ δρόμος.
Πολλὰ τὰ καλοκαιρινὰ πρωϊὰ νὰ εἶναι
ποὺ μὲ τί εὐχαρίστηση, μὲ τί χαρὰ
θὰ μπαίνεις σὲ λιμένας πρωτοειδωμένους·
νὰ σταματήσεις σ᾽ ἐμπορεῖα Φοινικικά,
καὶ τὲς καλὲς πραγμάτειες ν᾽ ἀποκτήσεις,
σεντέφια καὶ κοράλλια, κεχριμπάρια κ᾽ ἔβενους,
καὶ ἡδονικὰ μυρωδικὰ κάθε λογῆς,
ὅσο μπορεῖς πιὸ ἄφθονα ἡδονικὰ μυρωδικά.
Σὲ πόλεις Αἰγυπτιακὲς πολλὲς νὰ πᾷς,
νὰ μάθεις καὶ νὰ μάθεις ἀπ᾽ τοὺς σπουδασμένους.

Πάντα στὸ νοῦ σου νᾅχῃς τὴν Ἰθάκη.
Τὸ φθάσιμον ἐκεῖ εἶν᾽ ὁ προορισμός σου.
Ἀλλὰ μὴ βιάζῃς τὸ ταξείδι διόλου.
Καλλίτερα χρόνια πολλὰ νὰ διαρκέσει.
Καὶ γέρος πιὰ ν᾽ ἀράξῃς στὸ νησί,
πλούσιος μὲ ὅσα κέρδισες στὸν δρόμο,
μὴ προσδοκώντας πλούτη νὰ σὲ δώσῃ ἡ Ἰθάκη.

. . .

As you set out for Ithaca
hope your road is a long one,
full of adventure, full of discovery.
Laistrygonians, Cyclops,
angry Poseidon—don't be afraid of them:
you'll never find things like that on your way
as long as you keep your thoughts raised high,
as long as rare excitement stirs your spirit and your body.
Laistrygonians, Cyclops,
wild Poseidon—you won't encounter them
unless you bring them along inside your soul,
unless your soul sets them up in front of you.

Hope your road is a long one.
May there be many summer mornings when,
with what pleasure, what joy,
you enter harbors you're seeing for the first time;
may you stop at Phoenician trading stations
to buy fine things,
mother of pearl and coral, amber and ebony,
sensual perfume of every kind—
as many sensual perfumes as you can;
and may you visit many Egyptian cities
to learn and go on learning from their scholars.

Keep Ithaca always in your mind.
Arriving there is what you're destined for.
But don't hurry the journey at all.
Better if it lasts for years,
so you're old by the time you reach the island,
wealthy with all you've gained on the way,
not expecting Ithaca to make you rich.

. . .

Abstract

Astrophysical jets appear as linear collimated objects of high speed that are typically found in young stellar objects, X-Ray binaries, gamma-ray bursts, or active galactic nuclei. The physical procedures that lead to the development of these jets have been studied extensively in the past years. We believe that the launching of highly relativistic jets requires the existence of an accretion disk threaded by a strong magnetic field that rotates around a black hole. We perform general relativistic magnetohydrodynamic simulations of outflow launching from thin accretion disks. As in the nonrelativistic case, resistivity is essential for the mass loading of the disk wind. We implemented resistivity in the ideal GRMHD code `HARM3D`, which allows us to run simulations with larger physical grids, higher spatial resolution, and longer simulation time. We present the numerical details of the code and we show numerical test in the resistive regime that prove the robustness of the code. As a reference simulation, we consider an initially thin, resistive disk orbiting the black hole, threaded by a large-scale magnetic flux. As the system evolves, outflows are launched from the black hole magnetosphere and the disk surface. We mainly focus on disk outflows, investigating their MHD structure and energy output in comparison with the Poynting-dominated black hole jet. The disk wind encloses two components – a fast component dominated by the toroidal magnetic field and a slower component dominated by the poloidal field. The disk wind transitions from sub- to super-Alfvénic speed, reaching velocities $\sim 0.1c$. We provide parameter studies varying spin parameter and resistivity level and measure the respective mass and energy fluxes. A higher spin strengthens the B_ϕ-dominated disk wind along the inner jet. We disentangle a critical resistivity level that leads to a maximum matter and energy output for both, resulting from the interplay between reconnection and diffusion, which in combination govern the magnetic flux and the mass loading. For counterrotating black holes the outflow structure shows a magnetic field reversal. We also show the structure and direction of the electric field and its connection with the velocity and magnetic field vectors. Finally, we present the first fully dynamical simulation of dynamo generated poloidal magnetic field in a GRMHD environment. We simulate cases of both accretion tori and disks and we find induced magnetic field with both dipolar and quadrupolar structure. We follow the evolution of the field structure and strength and we show the launching of outflows from the torus/disk surface and the black hole magnetosphere.

Zusammenfassung

Kosmische Jets sind kollimierte Materieströme mit hohen Geschwindigkeiten, die typischerweise in jungen stellaren Objekten, X-Ray binaries, Gamma-ray bursts oder Aktiven Galaktischen Kernen vorkommen. Die physikalischen Prozesse, die zu der Entstehung dieser Jets führen, sind Gegenstand extensiver Forschung der letzten Jahre. Wir vermuten, dass die Entstehung relativistischer Jets die Präsenz einer Akkretionsscheibe erfordert, die von einem starken Magnetfeld durchdrungen wird und um ein zentrales schwarzes Loch rotiert. Wir führen allgemein-relativistische magnetohydrodynamische (GRMHD) Simulationen von "Ausflüsse" (outflows) durch, die von dünnen Akkretionsscheiben ausgehen. Wie im nichtrelativistischen Fall ist Resistivität notwendig, um ein Massengewinn des Scheibenwinds zu ermöglichen. Wir implementieren eine Resistivität in den `HARM3D` Code der idealen GRMHD, welcher uns erlaubt, Simulationen mit größeren physikalischen Rastern, höherer räumlicher Auflösung und längerer Simulationszeit durchzuführen. Wir präsentieren numerische Details des Codes und zeigen numerische Tests im Fall der Resistivität, welche die Robustheit des Codes bestätigen. Als Referenzsimulation betrachten wir eine anfangs dünne, resistive Scheibe um ein schwarzes Loch, die von einem großskaligen magnetischen Fluss durchdrungen wird. Während deren Entwicklung entstehen Ausflüsse, die von der Magnetosphäre des schwarzen Lochs und der Scheibenoberfläche ausgehen. Wir betrachten im Genaueren Ausflüsse der Scheibe und untersuchen deren magnetohydrodynamische Strukturen sowie Energieoutputs im Vergleich zu Poynting-dominierten Jets schwarzer Löcher. Der Scheibenwind besteht aus zwei Komponenten – eine schnelle Komponente, die durch das toroidale Magnetfeld beherrscht wird, und eine langsame Komponente, welche durch das poloide Magnetfeld dominiert wird. Der Scheibenwind zeigt einen Übergang von sub-Alfvén- zu super-Alfvén-Geschwindigkeiten und erreicht absolute Geschwindigkeiten von bis zu $\sim 0.1c$. Wir präsentieren des Weiteren Parameterstudien, bei welchen wir den Spinparameter und die Resistivität variieren, und messen die entsprechenden Massen und Energieflüsse. Ein höherer Spin verstärkt den B_ϕ-dominierten Scheibenwind entlang des inneren Jets. Wir leiten daraus eine kritischen Resistivitätlevel ab, welcher zu einem Maximum des Masse- und Energieoutputs aufgrund des Zusammenspiels zwischen Rekonnektion und Diffusion führt. Dieses Zusamenspiel bestimmt den magnetischen Fluss sowie den Massengewinn. Im Falle gegenläufig rotierender schwarzer Löcher zeigt die Ausflüsse Struktur eine Umkehrung des Magnetfelds. Wir zeigen zudem die Struktur und Richtung des elektrischen Feldes in Verbindung mit Geschwindigkeits- und Magnetfeldvektoren. Zuletzt präsentieren wir die erste volldynamische Simulation eines dynamo-generierten poloiden Magnetfelds in einer GRMHD Umgebung. Wir simulieren sowohl Akkretionstori als auch -scheiben und finden induzierte Magnetfelder mit dipolarer als auch quadrupolarer Struktur. Wir verfolgen die Entwicklung der Feldstruktur und -stärke und zeigen Ausflüsse, die von der Torus-/Scheibenoberfläche sowie der Magnetosphäre des schwarzen Lochs ausgehen.

Περίληψη

Αυτή εδώ η διδακτορική διατριβή είναι αφιερωμένη στην περιγραφή και μελέτη δίσκων προσαύξησης γύρω από μαύρες τρύπες και στην εκτόξευξη εκροών και πιδάκων. Η μελέτη έγινε με τη χρήση υπολογιστικών προγραμάτων ειδικών στην επίλυση των αντίστοιχων εξισώσεων μαγνητοϋδροδυναμικής σε περιβάλλον της Γενικής Σχετικότητας.

Τώρα θα μου πείτε ότι δε καταλαβάτε τίποτα απ΄ όλα αυτά που έγραψα, και θα έχετε δίκιο. Θα προσπαθήσω να τα πω λίγο πιο απλά. Η βασική δομική μονάδα του σύμπαντος, σε μακροσκοπικό επίπεδο είναι οι γαλαξίες. Γνωρίζουμε πως η Γη περιφέρεται γύρω από τον Ήλιο ο οποίος με τη σειρά του περιφέρεται σε σχεδόν κυκλική τροχιά γύρω από το κέντρο του Γαλαξία μας. Τι βρίσκεται λοιπόν στο κέντρο του Γαλαξία μας· Πέρα από μια υψηλή συγκέντρωση αστέρων και αστρικής σκόνης στο κέντρο βρίσκεται και μια μαύρη τρύπα. Προς αποφυγή παρεξηγήσεων θα εξηγήσω με απλά λόγια τι είναι η μάυρη τρύπα. Μαύρη τρύπα είναι το τελευταίο στάδιο της εξέλιξης των άστρων. Όταν ένας αστέρας πεθαίνει, τρία είναι τα πιθανά καταλικτικά σενάρια. Αστέρες μικρής μάζας αποβάλουν σταδιακά τα ανώτερα στρώματα τους μέσω ισχυρών αστρικών ανέμων αφήνοντας στο τέλος εναν πυκνό, ζεστό πυρήνα που ονομάζουμε λευκό νάνο. Σε μεσαίας και υψηλής μάζας αστέρες η βαρύτητα είναι πολύ ισχυρή για να αφήσει το υλικό του αστέρα να φύγει με αποτέλεσμα ο αστέρας να καταρρεύσει σε μια έκρηξη υπερκαινοφανούς αστέρα (supernova). Το τελικό αποτέλεσμα της έκρηξης είναι είτε ένας αστέρας νετρονίων ή για τα αστέρια πολύ μεγάλης μάζας, μια μαύρη τρύπα. Ένα αστρικό αντικείμενο του οποίο η πυκνότητα είναι τόσο μεγάλη ώστε καμιά άλλη δύναμη της φύσης δε μπορεί να σταματήσει τη βαρυτική έλξη. Το βαρυτικό πεδίο της μαυρης τρύπας είναι τόσο ισχυρό που σε κοντινές αποστάσεις από αυτή ούτε το φώς, που τρέχει με $1\,000\,000\,000\ km/h$, μπορεί να δραπετεύσει δημιουργώντας μια περιοχή σαν σφαιρική τρύπα στον χώρο, εξ ού και το όνομα. Για να φανταστείτε, ο Ήλιος με τη μάζα που έχει σήμερα για να γίνει μαύρη τρύπα θα έπρεπε να συμπυκνωθεί σε μια μπάλα ακτίνας 3 χιλιομέτρων και για τη Γη η αντίστοιχη σφαίρα έχει τις διαστάσεις μιας μπάλας του πινγκ-πόνγκ.

Τέτοια αντικείμενα βρίσκονται και στο κέντρο των γαλαξιών, μόνο που η μαζα τους είναι εκατομμύρια ή και δισεκατομμύρια φορές μεγαλύτερη από τη μάζα του Ήλιου. Σαν αναφορά, η μάζα του Ήλιου είναι περίπου $2\,000\,000\,000\,000\,000\,000\,000\,000\,000\ kg$ (δύο εννιάκισεκατομμύρια κιλά). Γύρω από αυτές τις μαύρες τρύπες συνήθως βρίσκουμε δίσκους προσαύξησης, δηλαδή αέριο υλικό το οποίο περιφέρεται γύρω από την τρύπα σε κυκλικές τροχιές, όπως οι πλανήτες γύρω από τον Ήλιο, δημιουργώντας έναν δίσκο. Μόνο που το αέριο έχει ιδιότητες ρευστού με αποτέλεσμα μέσω της τριβής και άλλων φαινομένων το ρευστό να πλησιαζει συνεχώς την τρύπα μέχρι να απορροφηθεί από αυτή μεγαλώνοντας τη μάζα της. Λόγω της ηλεκτρικής φόρτισης του ρευστού, μαγνητικά πεδία δημιουργούνται τα οποία διατρέχουν τον δίσκο και μέσω φυσικών μηχανισμών δημιουργούν πίδακες ρευστού οι οποίοι εκτοξεύονται από τον δίσκο και την περιοχή κοντά στη μαύρη τρύπα. Τέτοιοι πίδακες είχαν παρατηρηθεί από τις αρχές του 1900 με τηλεσκόπια αλλά η διαδικάσια δημιουργίας τους ήταν παντελώς άγνωστη. Ακόμα και σήμερα, που γνωρίζουμε πολλά περισσότερα, οι ακριβείς διαδικασίες δημιουργίας των πιδάκων έχει κενά. Η δική μου δουλειά ήταν να μελετήσω τον τρόπο δημιουργίας των πιδάκων χρησιμοποιώντας συγκεκριμένους νόμους της φυσικής. Οι εξισώσεις που περιγράφουν τη φυσική των δίσκων και των πιδάκων είναι πολύπλοκοι για να λυθούν με χαρτί και μολύβι οπότε χρησιμοποιούμε υπολογιστές που μπορούν πολύ πιο γρήγορα να βγάλουν την λύση και να μας δώσουν την χρονική εξέλιξη των φυσικών φαινομένων. Στις σελίδες που ακολουθούν μπορείτε να δείτε παραδείγματα του προφίλ των δίσκων και των πιδάκων

Στους γονείς μου...

To my parents...

Contents

List of Figures

List of Tables

List of Abbreviations

BZ	**B**landford-**Z**najek
CT	**C**onstrained **T**ransport
EHTC	**E**vent **H**orizon **T**elescope **C**ollobaration
GR(MHD)	**G**eneral **R**elativistic (**M**agneto**H**ydro**D**ynamics)
GRRMHD	**G**eneral **R**elativistic **R**adiative **M**agneto**H**ydro**D**ynamics
HST	**H**ubble **S**pace **T**elescope
ISCO	**I**nnermost **S**table **C**ircular **O**rbit
MAD	**M**agnetically **A**rrested **D**isk
MPI	**M**essage **P**assing **I**nterface
MRI	**M**agneto**R**otational **I**nstability
SMBH	**S**uper**M**assive **B**lack **H**ole
VLBI	**V**ery **L**ong **B**aseline **A**rray
WENO	**W**eighted **E**ssentially **N**on-**O**scillatory

Chapter 1

Introduction

In this chapter we will highlight the rich bibliography around astrophysical jets with a focus on jets from Active Galactic Nuclei. We refer to observation of jets including a reference in the structure of the jets and the different types of sources that are considered as hosts. We continue with simulations of jets in general relativistic environment.

1.1 Introduction to Astrophysical Jets

Astrophysical jets appear as linearly collimated structures of high speed that are typically found in young stellar objects (YSOs), X-Ray binaries, gamma-ray bursts, or active galactic nuclei (AGN). The physical mechanisms that produce these jets (jet launching) have been studied extensively, leading to a consensus that the launching of relativistic jets requires the existence of an accretion disk around a central, gravitationally dominating object and a strong magnetic field. In the following sections, we briefly describe the three environments that show astrophysical jets: jets from young stellar objects, gamma-ray bursts and extra-galactic jets.

1.1.1 Jets from Young Stellar Objects

In the case of YSOs, the role of the central object is played by a star in the first stages of its life with a mass in the range of tens of solar masses. The first astrophysical jet from a YSO was (accidentally) observed by Burnham (1890) who described it as an elongated star in the middle of a nebula with a varying magnitude. He was referring to the original *T Tauri* star discovered by John Russell Hind in 1852 (Hind, 1852). Today we know, that the variations is the nebula Burnham was observing were the result of the wind, launched by the newly formed star, interacting with the surrounding nebula.

In the 1940's George Herbig and Guillermo Haro were interested in the early stages of star formation. Working independently, they performed observations on a variety of T Tauri stars, including Burnham's varying nebula-star. Some of the strange characteristics of these stars were strong emission lines of hydrogen, oxygen and sulfur along with low visibility in the infrared spectrum (Herbig, 1951; Haro, 1952). Nowadays, these stars (which carry the name of Herbig and Haro, HH stars) are a special phase in the process of star formation characterized by an accretion disk rotating around the star and strong outflows in the form of a jet (see Figure 1.1). Their jets/outflows can reach distances that vary between 100 and 10^6AU while their velocities can go up to 500 km/s. The first jet that was observed from a

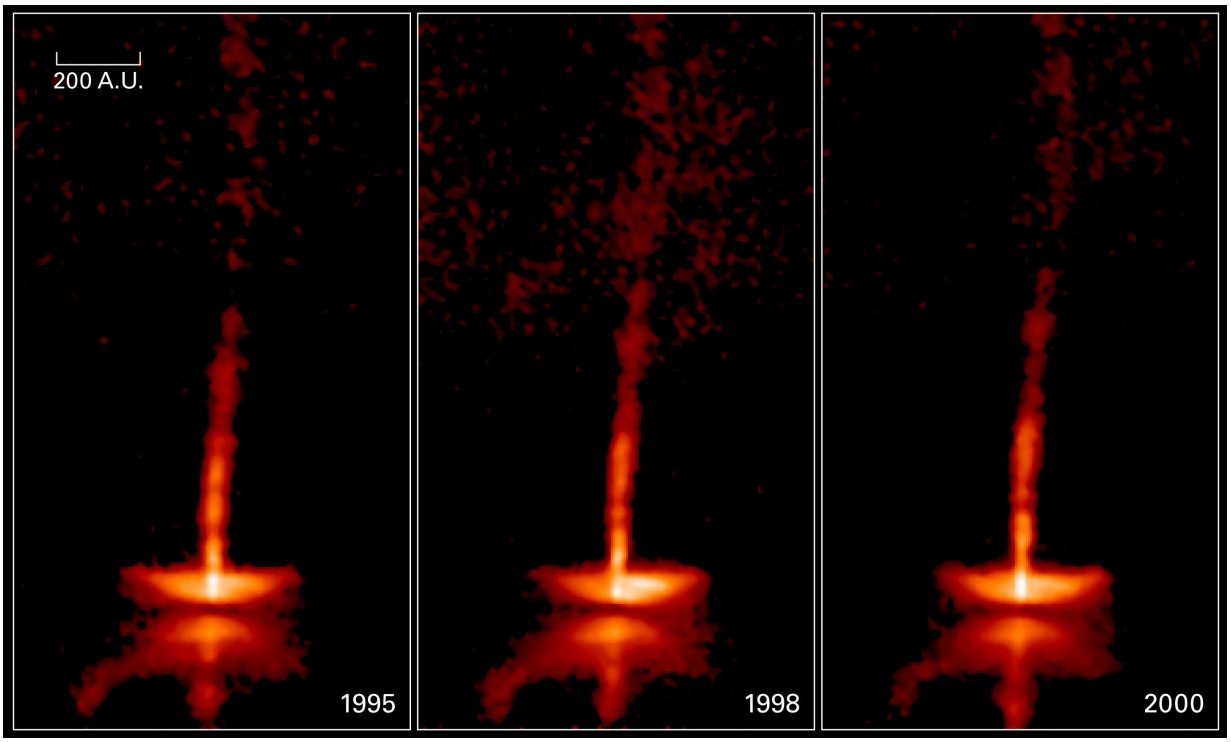

FIGURE 1.1: The dynamic HH 30 disk and jet complex. Images of the HH30 disk and jets in a period of five years. The newly born star is surrounded by an edge-on disk of dust whose top and bottom surfaces are illuminated by the star. The jet is launched from the inner region of the disk and possibly from the star itself. We notice the changes in the jet structure and orientation that are mainly caused by the knotty shape of the ejection. Guilloteau et al. (2008) showed that the host star is in fact a binary complex in short eccentricity.
(Image credit: Hubble Space Telescope, NASA/ESA)

YSO was in the HH 46/47 complex observed by Dopita, Schwartz, and Evans (1982) using high resolution spectra in the region of $[OI]$ and $H\alpha$.

1.1.2 Jets in Gamma-Ray Bursts

Another category closely related to jets on small scales are Gamma-Ray Bursts (GRB). GRBs release an energy of up to 10^{54}ergs/s in a narrow jet funnel, in a time period that ranges from less than a second to several hours. They are among the brightest electromagnetic events the Universe and they are observed in distant galaxies. GRBs were first detected accidentally by spying satellites in 1967 (at the peak of the Cold War) as published in Klebesadel, Strong, and Olson (1973). In the following years many models were proposed that tried to explain the physical processes that lead to GRBs.

The large variety in the light curves of GRB events makes them difficult to classify. The duration of the events is being used to distinguish between them. GRBs with duration of less than 2 seconds are classified as short GRBs. The initial idea that short GRBs are the result of the collision and merging of binary neutron stars and black holes was confirmed when Laser Interferometer Gravitational-wave Observatory (LIGO) detected a gravitational wave event on 17 August 2017. 1.7 seconds later, the *Fermi* Gamma-ray Burst Monitor detected

a short GRB from the same location (Goldstein et al., 2017). The analysis showed that the gravitational wave event was the result of a binary neutron star inspiral that merged and exploded, resulting in the gravitational and electromagnetic events (Abbott et al., 2017b) (see Figure 1.2). Long GRBs constitute the majority of the GRBs and are easier to observer due to the long afterglows they have. The majority of them has been connected with galaxies with high star formation rates and even with core-collapse supernova events (Woosley and Bloom, 2006).

1.1.3 Jets from Active Galactic Nuclei

The first observation of a jet being launched from a galaxy was by Curtis (1918). He observed the galaxy M87 and noticed, apart from the absence of spiral structure, the existence of a "curious straight ray that lies in the gap of the nebulosity connected with the nucleus by a thin line of matter. The ray also is brightest at its inner end." Nine years before that, Fath (1909) had showed the first photo of an AGN. Also, radio astronomy which started with Jansky (1933) would provide in the future an enormous amount of information for AGN jets and their sources.

Based on their observations of the broad emission lines originating from high velocity gas, Seyfert (1943) proposed that there must exist a gravitational potential well should exist in the center of AGN. Jennison and Das Gupta (1953) managed to resolve the two different lobes in the radio source Cygnus A, while Shklovskii (1955) showed that the synchrotron mechanism was responsible for the radio emission which required large amounts of energy. In 1963, Hazard, Mackey, and Shimmins (1963) and Schmidt (1963) discovered the first quasar, 3C273. It shows very large luminosity with a compact, flat radio spectrum core. In contrast with the spectrum of Cygnus A which is characterized by its narrow emission lines , 3C273 displays broad compact lines, a distinguishing feature between radio-loud quasars and radio galaxies. 3C273 also shows variations in the optical and radio luminosity that go up to days or even years (Smith and Hoffleit, 1963; Dent, 1965).

Many observations of extra-galactic jets and their host galaxies followed up. They were mostly detected in galaxies with unusual spectra, an indication that the source of the light was not coming just from stars. Observation of blazars (AGN with its jet directed towards the Earth) in different parts of the spectrum showed that variations in the luminosity can be as short as minutes (Schmidt, 1963; Hughes, 1965; Bignami et al., 1981; Schreier, Gorenstein, and Feigelson, 1982; Punch et al., 1992). Moreover, radio-quiet quasars were found to be 10 times more numerous than the radio-loud ones (Sandage, 1965). Our own Milky Way galaxy was confirmed as the host of a nucleus (SgrA*), with a luminosity of $L \sim 10^{26} J$ (Balick and Brown, 1974), even though not active enough to be branded as an AGN (Keel, 1983).

Soon the term AGN was used to describe these sources. It became an umbrella term including other categories of astrophysical objects such as the quasars and the Seyfert galaxies. In 1964 Salpeter and Zel'dovich independently proposed that the source of energy output of quasars was the accretion of gas into a supermassive black hole (SMBH) (Salpeter, 1964; Zel'dovich, 1964) and five years later Lynden-Bell (1969) and Bardeen (1970) introduced the idea that black holes exist in the center of most of galaxies as a result of collapsed quasars surrounded by accretion disks. Rees (1971) showed that double-lobe radio sources can be powered by a jet launched from the center of the galaxy, with their rapid variability to be attributed to relativistic motion (Rees, 1966).

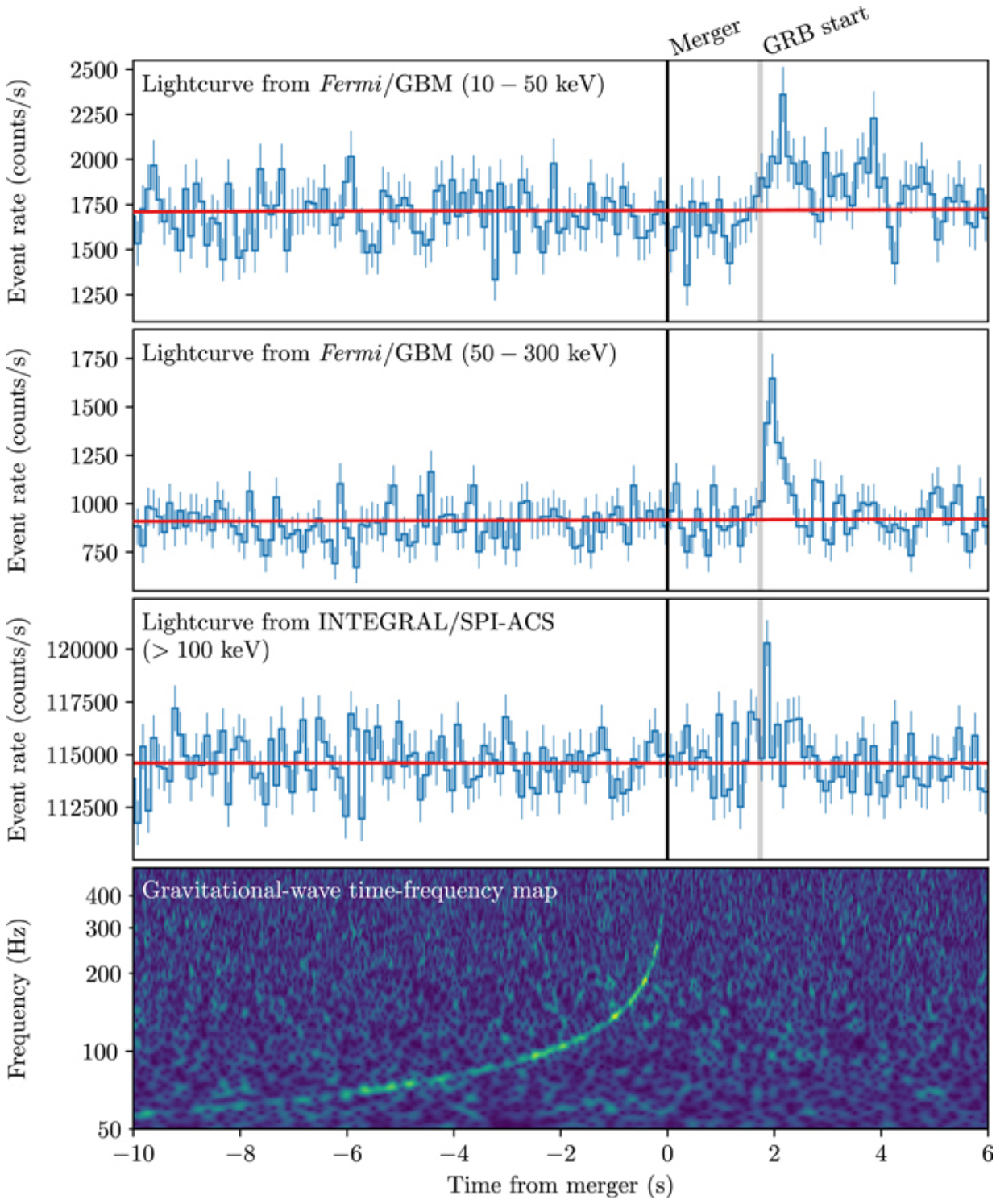

FIGURE 1.2: The detection of the neutron star merger and the subsequent GRB. The top three panels show the lightcurves before and after the merging of the neutron stars in three different frequencies as they were detected by *Fermi* and *INTEGRAL*. The GRB is detected in all three frequencies at approximately the same time, even though the higher energies "arrive" earlier. The last panel shows the frequency map for the gravitational wave emission from the neutron star inspiral. The GRB starts 1.7 seconds after the merging is completed.
(Image credit: Abbott et al. (2017a)

Over the years, many theories were developed regarding the formation of astrophysical jets. A consensus has now been reached that the interaction between a massive central object and a magnetized accretion disk are the fundamental requirements for the jet launching. In the case of the AGN jets, this central object is a SMBH. In 1977, Roger Blandford and Roman Znajek proposed the idea that a strong magnetic field threading the black hole magnetosphere would be able to extract some of its rotational energy and thereby power ejecta similar to what we observe in the cores of AGN jets (BZ mechanism) (Blandford and Znajek, 1977). Five years later, Blandford and Payne (1982) established another mechanism of jet launching, this time from the surface of an accretion disk rotating around the central object. The magnetic field lines can work as pathways for material that is centrifugally accelerated along them by the rotating disk. Also, Lynden-Bell (1996) described another mechanism that creates (or enhances) disk launched jets, in which the toroidal magnetic field generated by the rotation of the disk results in an increased magnetic pressure which launches and collimates material above the disk. In following chapters we will refer to these mechanisms extensively and we will also provide a more detailed description of their effects.

A hundred and one years after Curtis' original observation, the Event Horizon Telescope Collaboration (EHTC), using Very Long Baseline Interferometry (VLBI) with a cooperating network of telescopes from all around the world, was able to penetrate the layers of M87, look straight into its nucleus and present the first picture of the shadow of a super-massive black hole (SMBH) (Event Horizon Telescope Collaboration et al., 2019) (see Figure 1.3). Observing M87's SMBH is not only important because it confirms the existence of this astrophysical object, but also because it confirms the ideas of Salpeter Zel'dovich and Lynden-Bell for the nuclei of galaxies. The light we see in the right panel of Figure 1.3 is the first light emitted from the black hole's photon surface and after it's orbit was disturbed by the strong gravitational field and the black hole's rotation. Unfortunately resolution was not high enough to establish the angular momentum of the black hole. Dokuchaev and Nazarova (2019) compared simulations of thin accretion disk with the actual image and claimed that the Kerr parameter of the black hole is $a = 0.75 \pm 0.15$.

1.2 Observations of AGN Jets

AGN jets are being observed in different scales, ranging from less than 1AU to Mpc. One of the most popular observational methods is the use of VLBI where arrays of many radio telescopes are used in order to increase the resolution. As a result, more than 12000 AGN have been observed until nowadays with VLBI. According to Blandford, Meier, and Readhead (2019) AGN jets may be separated in three categories:
i) The galaxy jets, where the dynamics are governed by the gravitation field of the combined stellar and dark matter with the interstellar medium (ISM),
ii) the black hole jets, where the gravitational potential of the central SMBH far exceeds the one from the galaxy and the jet is a result of the material the accretes towards the black hole forming an accretion disk, and the outflows from the disk's surface, and
iii) the lobe jets are further extensions of the galaxy jets and the environment is controlled mainly by the material at the end of the jet and the surrounding intergalactic medium.

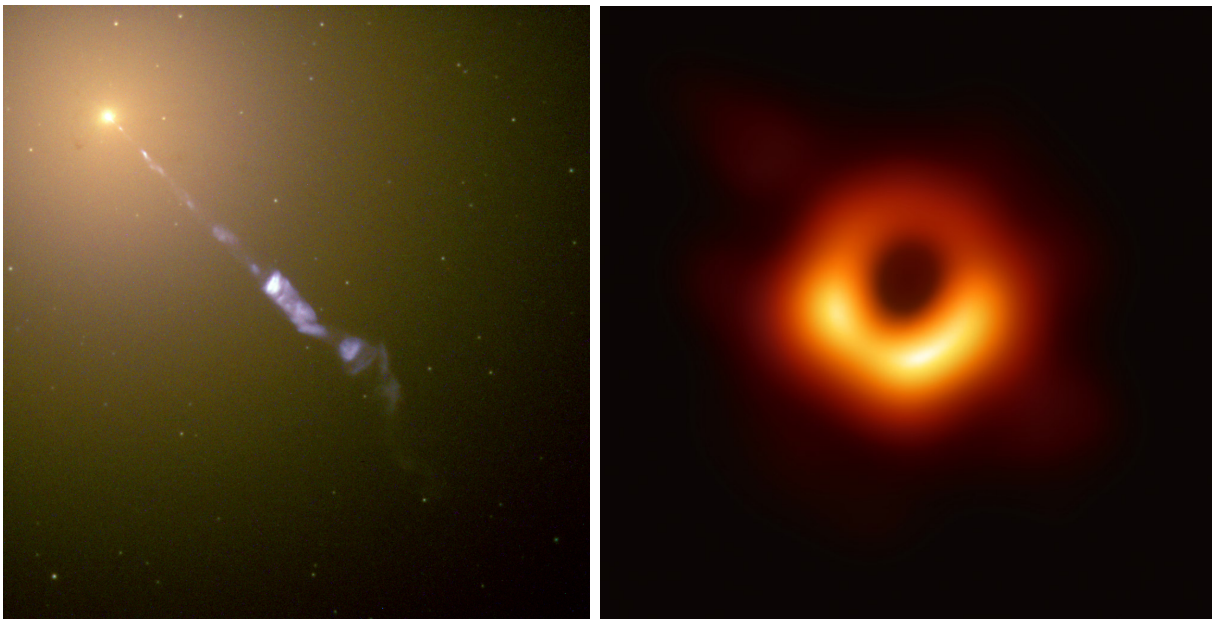

FIGURE 1.3: *Left*: M87 galaxy and its prominent jet. The jet has length of 1.5 kiloparsecs with the material in it reaching apparent velocities up to six times the speed of light. The energy of the electrons that produce the synchrotron radiation is estimated at 10^{56}ergs. *Right*: The SMBH in the centre of M87. The high luminosity area around the black hole shows the brightness temperature which is of the order of 10^{9}K.
(Image credit: Hubble Space Telescope, NASA/ESA; European Southern Observatory.)

1.2.1 Details of the Jet Structure

Since the development of Very Large Array (VLA) and VLBI in the 1980s a large number of extragalactic radio sources have been observed. Over the years there was an attempt to qualitatively classify these objects, based mainly on their structural features. However, it is well known that each one of them is a result of unique set of conditions and circumstances, and as a result of that, any classification attempt would risk loss of information in order to fit an object in a specific category. In this section we give a small general description of the different parts of the extragalactic jet, using the Cygnus A jet as an example and keeping in mind that it can only be used as a rough guide to the description of the jets.

For each extra-galactic jet we can identify the following set of structural features based on radio observations.

- Cores, the stationary part of the jet and the source of the outflow. Recent 3 mm VLBI observations has shown that it is possible to zoom into the central core, where then base of the jet exists and where the outflow is being launched, either from the disk in the form of disk wind and/or from the black hole magnetosphere.
- Jets, the linear structure connecting the core with the outer part.
- Lobes, the regions at the end of the jet which show high radio emission.
- Hotspots, the very bright components at the outer part of the lobes. They are believed to be the area where the the beam of the jet meats the ambient medium. As a result,

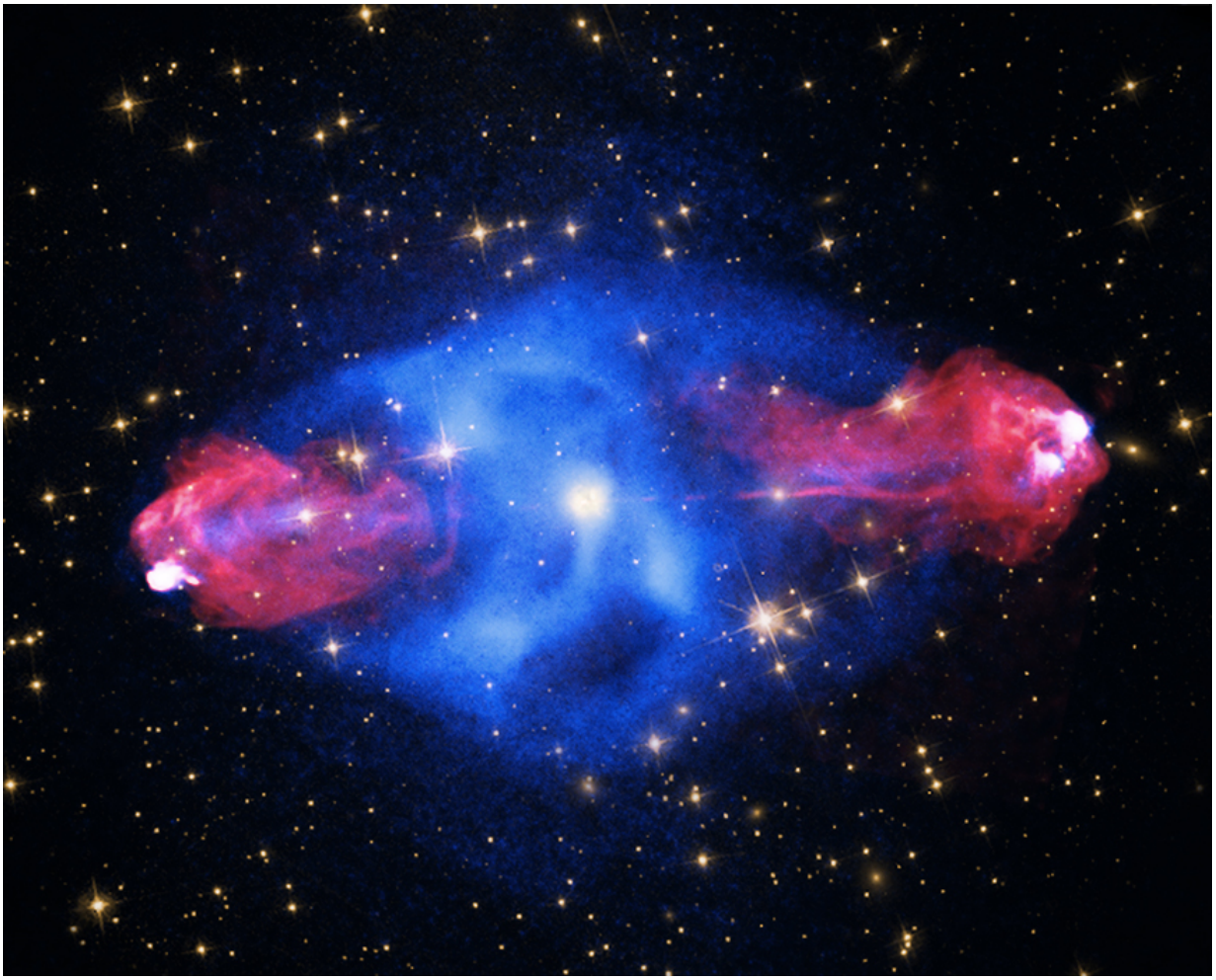

FIGURE 1.4: Cygnus A radio galaxy and its jet in three different wavelengths. X-rays (blue) are tracing the old, cold cocoon around the galaxy, while the radio emission (red) probes the newly ejected jet and its lobes. Optical data from the Hubble Space Telescope (HST) show the galaxy in the core of the jet. All the four major components of jets can be seen here. In the center lies the core galaxy. The two radio bright lines form the jet and the counter jet that extend out to two radio bright lobes, which also features radio and X-ray bright hotspots.
Image credit: X-ray,NASA/CXC/SAO; Optical,NASA/STScI; Radio,NSF/NRAO/AUI/VLA

a shock surface is developed which helps accelerating medium's particles to relativistic velocities.

We highlight these four structures using the example of Cygnus A in Figure 1.4.

1.2.2 Galactic Scale Jets

On galactic scale, the dynamics of the jet are dictated by the gravitational potential of the host galaxy and the interstellar medium. When the VLBI started being used to observe jets some basic structural characteristics became apparent. Wilkinson et al. (1977) found that the majority of the jet are one-sided, while Readhead et al. (1978) found the compact flat-spectrum core. Furthermore, parts of the jet are expanding or moving along the jet in superluminal speeds[1] (Gubbay et al., 1969).

The Monitoring Of Jets in Active galactic nuclei with Very Long Baseline Array (VLBA) Experiments (MOJAVE) group, which studied blazars using the VLBI for more than 20 years, found that almost all of them have the same one-sided core-jet structure and show relativistic motions with apparent velocities ranging from $0.03c$ to $40c$ (Lister et al., 2016; Lister, 2016). This kind of superluminal motion is very common in flat-Spectrum Radio Quasars, BL Lac Objects and Seyfert I galaxies. Mertens et al. (2016) performed 43-GHz VLBI observations of the jet in M87 and found that the jet has two different components when it comes to velocity: a mildly relativistic component along the sheath ($v \sim 0.5c$) and a faster component along the spine ($v \sim 0.92c$). Kim et al. (2018) was able to penetrate the M87 down to approximately $7R_{\rm g}$ and found further evidence of a spine-sheath structure, which is also an indication that the jet is being launched by the inner part of an accretion disk.

Pushkarev et al. (2017) used 484 sources from the MOJAVE program to study the linear polarization of synchrotron radiation. They found that the fractional polarization increases with distance from the radio core as well as towards the edges. Also, BL Lacs show a higher degree of polarization and exhibit more stable and better aligned electric vector position angles (EVPAs) with the local jet direction, compared to quasars. Homan et al. (2018) showed multi-epoch results for 278 objects from 2002 to 2009. They found that the circular polarization reaches its maximum value in the core component with the majority of the sources, including 3C279, showing a preferred sign. Zavala and Taylor (2004) studied the Faraday rotation measures and found that in the case of BL Lac objects and quasars the rotation measures are very similar in both the jets and the cores. In the case of radio galaxies, the cores do not show significant polarization while the jets show rotation measures that range up to 10^4 rad/mrad/m^2.

1.2.3 Jets from the Black Hole Magnetosphere

On the black hole scale, the gravitational potential of the black hole and its magnetosphere as well as the accreted material from the disk are defining the environment of the jet. The jet in the M87 galaxy is the most well studied case of an AGN jet. Walker et al. (2018) used

[1]Superluminal motion is the apparent motion of material with velocity that surpasses the light speed. It is common in extragalactic radio sources that usually host a black hole capable of accelerating particles in high Lorentz factors.

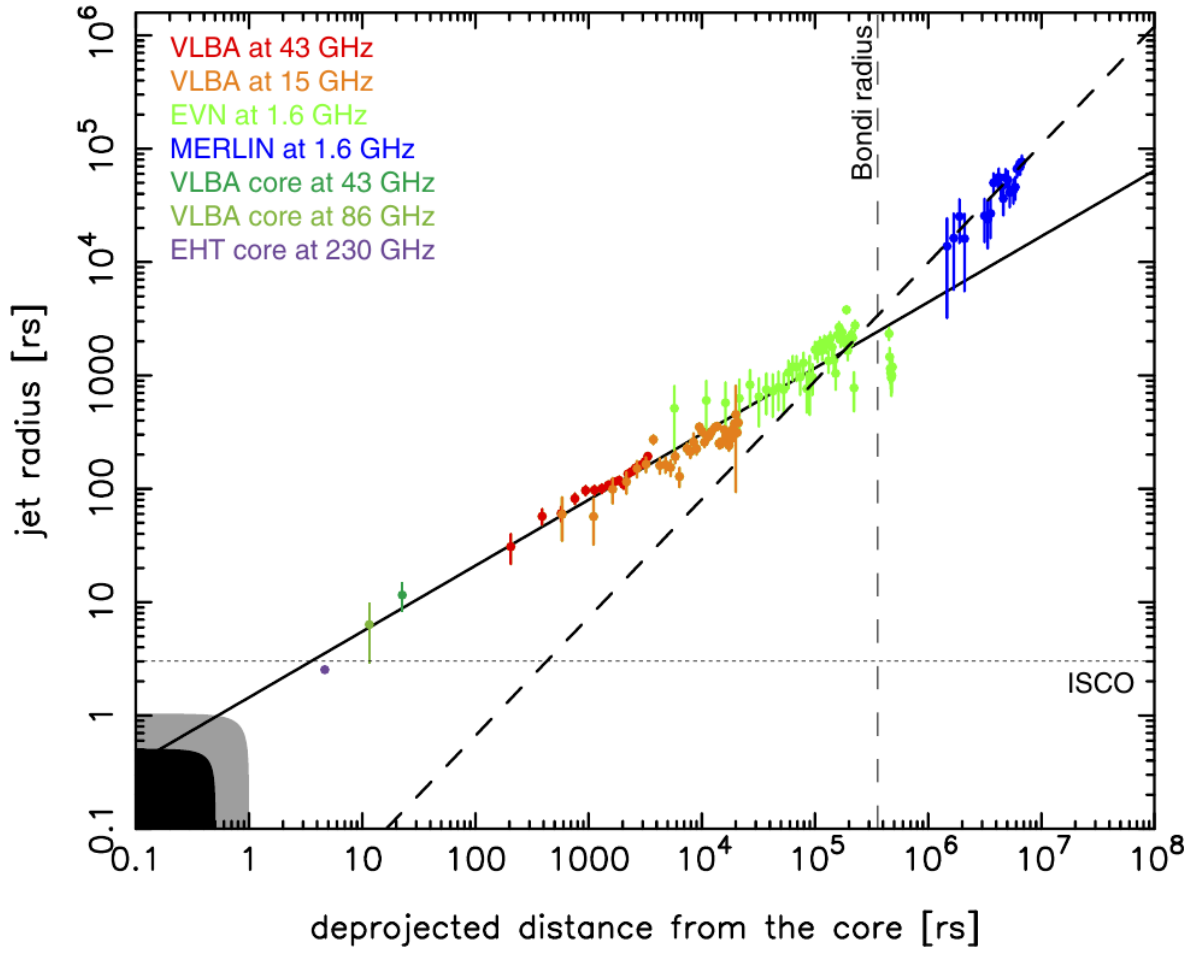

FIGURE 1.5: Distribution of the radius of the jet with respect to the deprojected distance from the core. The data include the original from Asada and Nakamura (2012) with the addition of the core data from VLBA and EHT. HST-1 is located around $5 \times 10^5 r_S$ where the apparent velocity of the jet of $\sim 6c$. The solid lined indicates the parabolic streamline, while the dashed line indicates the conical streamline. The vertical dashed line is the Bondi accretion radius. The horizontal thin dotted line is the ISCO of a Schwarzschild black hole. The gray area is the Schwarzschild radius while the black area is the horizon of a maximally rotating black hole.
Image credit: Nakamura and Asada (2013)

intense monitoring observations in combination with annual observation of M87 of the last 17 years made with VLBI at 43 GHz. Their work revealed many details in the structure of the jet including an asymmetric jet and counter-jet, both showing edge brightening. The geometry of each jet started with a rapid expansion and widening followed by a contraction and second widening. Around the second widening the counter-jet becomes invisible while the jet starts showing signs of collimation. Nakamura and Asada (2013) showed that the jet starts with an initial acceleration in a parabolic shape over a deprojected radius of $\sim 300\ pc$, at which point, a quasi-stationary shock, HST-1, forms and becomes a source of superluminal ejections (Cheung, Harris, and Stawarz, 2007; Nakamura, Garofalo, and Meier, 2010) with apparent velocities up to $6c$ (Biretta, Sparks, and Macchetto, 1999; Giroletti et al., 2012). Beyond HST-1, Asada and Nakamura (2012) found evidence for a helical magnetic field structure and Nakamura and Asada (2013) studied the transition from parabolic to conical structure (see Figure 1.5).

The recent imaging of the shadow of the SMBH in the center of M87 (Event Horizon Telescope Collaboration et al., 2019) revealed a ring of diameter $\sim 12R_{\mathrm{g}}$ for a black hole of mass $6.5 \times 10^9 M_{\odot}$. The ring has prominent asymmetric brightness due to relativistic beaming from the rotating plasma with velocities close to the speed of light. This image confirms the hypothesis that (at least part of) the M87 jet in formed in close proximity to the black hole.

Nakamura and Asada (2013) found that the M87 jet keeps a fixed conical shape downstream from the HST-1 shock which confirms the theoretical work of Blandford and Königl (1979), whereas upstream the HST-1 keeps a semi-parabolical shape down to $r \sim 6\ R_{\mathrm{g}}$ (Doeleman et al., 2012). Asada et al. (2014) found that the material in the jet moves with an almost constant acceleration from an apparent velocity of $v \sim 0.01c$ at $r \sim 400\ R_{\mathrm{g}}$ to $v \sim 6c$ at the HST-1. After HST-1, it starts decelerating down to $v \sim 0.4c$ at $r \sim 2 \times 10^7\ R_{\mathrm{g}}$.

1.2.4 Observing the Jet Lobes

On their largest scale, astrophysical jets provide information about the latest stages of their development and the conditions under which they expire into the intergalactic medium. A general characteristic shared among the majority of lobe jets is the hot spots in their lobes and the compact cores in their nuclei. Hargrave and Ryle (1974) showed that the energy flows from the cores of the jet into the lobes.

Fanaroff and Riley (1974) proposed the classification of radio galaxies we use extensively today that uses "the ratio of the distance between the regions of highest surface brightness on opposite sides of the central galaxy or quasar, to the total extent of the source up to the lowest brightness contour in the map." This practically means that the FR-I objects become fainter as we approach the outer part of the lobes, while FR-II objects show high-luminosity hotspots in the outer part of their lobes. FR-II objects are also usually hosted by a brighter central galaxy in absolute magnitude but relative to the hotspots in the lobes they are much fainter than the FR-I objects.

Laing and Bridle (2014) showed that FR-I objects undergo a faster-than-linear expansion in the first 30 *kpc* of their jet after which they switch to linear acceleration. Along with the change in the expansion, the magnetic field also switches from axial to toroidal. In contrast, FR-II objects show asymmetry in the lobes with the brighter lobe approaching us, resulting in low traces of Faraday rotation (Garrington et al., 1988). A special subcategory of very young

FR-II objects are the Compact Symmetric Objects (CSOs) (Wilkinson et al., 1994; Readhead et al., 1996), which have ages between 20 and 2000 years (Gugliucci et al., 2005). Tremblay et al. (2016) studied a large uniform sample of CSOs and concluded that even though they show elements that belong in both the FR-I and FR-II categories, their morphology depends on their luminosity.

1.3 GRMHD Simulations of AGN

The history of numerical simulations of AGN started almost 50 years ago. The first simulations involving a black hole were performed by Wilson (1972), who solved the hydrodynamic equations in a Kerr spacetime in the simple case of gas falling towards the black hole. The evolution of the technological equipment and the development of new computational methods would gradually lead to a number of codes being developed that also include more physical mechanisms such as Newtonian or general relativistic gravity, magnetic fields, dissipative processes (fluid viscosity, magnetic resistivity), radiative transfer. We will focus mostly on the case where the physical scenario that is simulated involves some kind of accretion disk around a central object, mostly a black hole, with the addition of some form of magnetic field.

Hawley, Smarr, and Wilson (1984a) and Hawley, Smarr, and Wilson (1984b) created a 2D axisymmetric, general relativistic hydrodynamic code in order to study the accretion flow in the gravitational field of Kerr spacetime. They present a thorough derivation of the equations, a discussion of the numerical techniques and a number of test including radial accretion flow (Bondi accretion), spiral infall and the formation and evolution of a pressure supported torus.

1.3.1 Studying Accretion

It was not until 15 years after the work of Hawley, Smarr, and Wilson (1984b) when the next code would be developed. Koide, Shibata, and Kudoh (1999) and Koide et al. (2000) were one of the first to develop a code that solved the equations of general relativistic magnetohydrodynamics (GRMHD). They simulated an accretion disk initially threaded by a uniform poloidal magnetic field. The differential rotation of the disk twists the magnetic field resulting in the development of a relativistic jet. At the same time, the pressure of the fluid launches a hydrodynamic jet which accompanies the magnetic one. They also investigated the case of a counterrotating black hole-disk system reporting the development of an even stronger magnetically driven jet.

De Villiers and Hawley (2003a) extended the code of Hawley, Smarr, and Wilson (1984a) using a new constrained transport method (CT) for the evolution of the magnetic fields. They presented a series of test simulations including a two-dimensional magnetized torus subject to the magnetorotational instability (MRI). (De Villiers and Hawley, 2003b) investigated the difference in the accretion mechanisms in the case of a prograde, retrograde, and nonrotating black hole. The evolution is driven by the MRI and the accretion rate is determined by the rate at which the disk feeds the black hole innermost stable circular orbit (ISCO). The model with the counterrotating black hole (and the largest ISCO) shows the least variability in accretion rate.

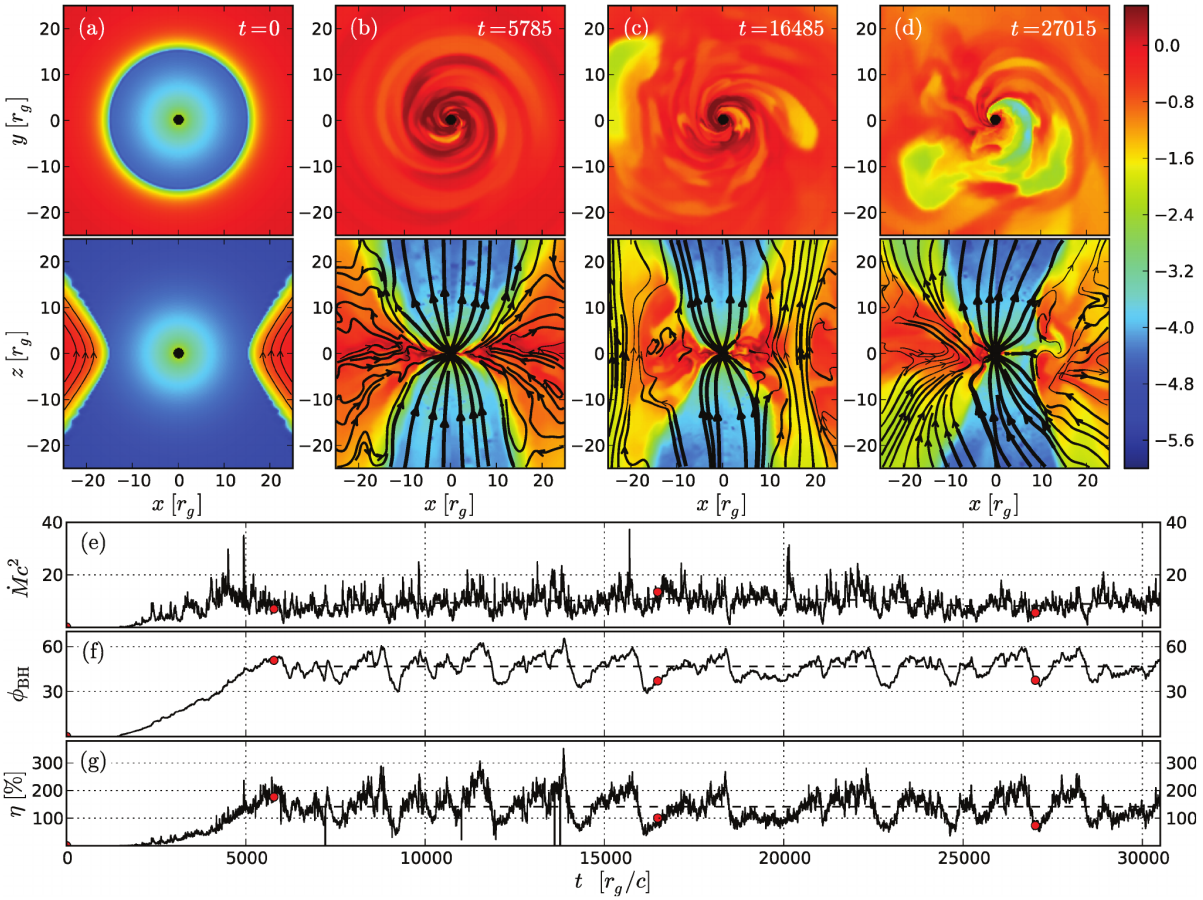

FIGURE 1.6: Simulation of an accretion disk around a rapidly spinning black hole ($a = 0.99$). The top and bottom rows show the logarithm of the rest mass density in the fluid frame in the equatorial and meridional planes. The black lines are the magnetic field lines and the black area is the black hole horizon. The top time series plot shows the evolution of the rest mass accretion rate. The middle time series plot shows the evolution of the magnetic flux that threads the black hole horizon. The bottom times series plot shows the energy outflow efficiency which on average is greater than 100% (dashed line).
Image credit: Tchekhovskoy, Narayan, and McKinney (2011)

Next, De Villiers, Hawley, and Krolik (2003) considered the cases of different black hole rotation. In a series of simulations with a Kerr parameter up to $a = 0.998$, they identified different parts of the global structure of the simulation and a reduction in the accretion rate with increased black hole spin. Finally, Krolik, Hawley, and Hirose (2005) focus on the dynamics of the inner part of the torus. They find that the decrease in the accretion rate with increasing Kerr parameter detected by De Villiers, Hawley, and Krolik (2003) is due to electromagnetic flux that propagates outwards from the black hole, while angular momentum transfer is also depressed. At the same time, the black hole loses energy due to the Poynting flux that is fed in the axial funnel.

Gammie, McKinney, and Tóth (2003) published their code named `HARM` in 2003. It featured a second order accurate conservative scheme for solving the equation of GRMHD where a set of primitive variables is used to calculate the fluxes and then an inversion scheme to go back to the primitive variables. `HARM` ended up being one of the most used GRMHD codes. The code was updated by Noble et al. (2006) with a new set of solvers for the inverse scheme of the code.

Gammie, Shapiro, and McKinney (2004) used their newly developed code in studying the change in the black hole spin by different mechanisms including disk accretion. They found that for $a \sim 0.9$ an spin equilibrium is reached which is much less than expected $a = 0.998$ from the purely hydrodynamical derivation of Thorne (1974). This might imply maximum rotation is not possible for black hole that grow from accretion. McKinney and Gammie (2004) investigated the energetics of the black hole magnetosphere in the presence of an accretion disk. Depending on the initial condition used, they found an outward Poynting flux in the black hole horizon accompanied by an outward angular momentum flux. McKinney (2006a) included into the `HARM` code the limit of force-free GRMHD which then tested in Minkowski and rotating black hole spacetimes.

Tchekhovskoy, McKinney, and Narayan (2007) introduced their version of GRMHD code `WHAM` based on the weighted essentially non-oscillatory (WENO) method which was effectively incorporated in the previous version of the `HARM` code. Shafee et al. (2008) simulated thin accretion disk around a Schwarzschild black hole and studied the magnetic coupling in the area of the ISCO finding it relatively unimportant. Penna et al. (2010) carried out a study of the Novikov and Thorne (1973) this disk model by simulating the disks with varying thickness in the environment of GRMHD. They concluded that the Novikov and Thorne (1973) model is a good description especially in the cases of accretion rate well below the Eddington limit and in the case of very thin disks.

1.3.2 Studying Jet Launching

GRMHD codes do not apply in the case of a vacuum, there must always exist a set of artificial low level fluid density and pressure values, called floor values, below which the respective quantities cannot drop. Depending on the code and the way in which the magnetic field is implemented, these floor values, may affect the jet launching especially in the jet funnel we see ejected from the black hole magnetosphere in many simulations. In the case of high floor density the acceleration introduced by the jet is hindered because of the high inertia the floor density possess. Lower floor density values can enable faster jets but impede the convergence of the implemented numerical scheme.

Hirose et al. (2004) continued with the analysis of the effect of the black hole spin on the magnetic field. They found an increase in the magnetic field with the Kerr parameters in small radii and they detected a dominant toroidal field in the main disk body and inner torus, whereas in the axial jet the field resembles more of a split monopole. Also, they measure high current in the inner torus and the plunging region, which might be an indication of some magnetic energy dissipation. De Villiers et al. (2005) focus on the outflows of the simulations. The axial funnel is dominated by a poloidal magnetic field with a hot and fast outflow and a colder and slower one along the funnel wall. The strength of the outflow increases with the black hole spin resulting in a Poynting flux-dominated outflow, while for low values of the Kerr parameter the outflow is dominated by the kinetic energy.

McKinney (2006b) evolved the `HARM` code even further simulating the evolution of the funnel jet up to 10 000 $R_{\rm g}$ and for longer times. With these addition McKinney (2006b) was able to detect current-driven instabilities in the jet beyond the Alfvén surface, which reduce the effect of acceleration and collimation. The jet is Poynting dominated and carries a magnetic pressure high enough to balance the ambient hydrodynamic pressure of the environment. At larger distances, the jet has a Gaussian angular structure in an angle of $\sim 5^\circ$ for the main component that increases to $\sim 27^\circ$ for the extended component.

McKinney and Narayan (2007a) investigate the conditions which lead to the creation of a Poynting dominated jet by showing the existence of an angular-integrated toroidal current density distribution. They find that the main collimating factor for the jet is the surrounding corona. They also investigate the case of force-free GRMHD (McKinney and Narayan, 2007b), by replacing the accretion disk with an infinitely thin rotating equatorial current sheet. They find that rotation contributes as a small decollimating factor in the jet. Afterwards, they embed the force-free field in an accretion disk which is then evolved in full GRMHD. The magnetic field in large radii in the corona is continuously pushed outward leaving behind only the disordered field. In the equatorial plane the turbulent field is advected and subsequently accreted toward the black hole. McKinney and Blandford (2009) studied the stability of relativistic jets produced by 3D GRMHD simulations using both dipolar and quadrupolar magnetic fields, concluding that a relativistic jet needs the dipolar structure to remain stable and achieve high Lorentz factors ($\Gamma \sim 10$). Broderick and McKinney (2010) calculated the Faraday rotation measures from a GRMHD simulation. They found that the AGN jets are dominated by electromagnetic energy with only 2% of being being due to energy from non-thermal particles.

Tchekhovskoy, Narayan, and McKinney (2011) showed that it is possible to have a jet which transfers more energy out of the black hole magnetosphere than the energy that is transferred via accretion. Advected magnetic flux is trapped in the black hole magnetosphere by a magnetically arrested disk (MAD) (Igumenshchev, Narayan, and Abramowicz, 2003) and it is transferred to the jet via the Penrose or BZ mechanism (Penrose, 1969; Blandford and Znajek, 1977). This was one of the first simulations that demonstrated such a high efficiency by the accretion system in generating outflowing energy in the jet and partially confirmed the aforementrioned jet production mechanisms. They measured the efficiency of the jet outflow and they found that for the case of a highly rotating black hole with $a = 0.99$ it was at 140% (see Figure 1.6). Following that, Tchekhovskoy and McKinney (2012) simulated cases of prograde and retrograde accretion disks around black holes and compared the efficiency of the launched jets. They found out that the prograde ones have higher efficiency, which increases with the disk thickness. McKinney, Tchekhovskoy, and

Blandford (2012) undertook a large parameter study for magnetically chocked accretion flows (MCAF) where the magnetic flux acts as a barrier that hinders, but does not completely halt accretion, and enhances the magnetization in the horizon. In the case of an initial toroidal field, they observe the development of patches of poloidal field that thread the black hole and initiate jet launching. For the initial condition of the poloidal field, the MCAF disk is formed which provides the conditions for BZ jet launching. McKinney, Tchekhovskoy, and Blandford (2013) showed the existence of a "magneto-spin alignment" mechanism which is responsible for the alignment of the accretion disks and their jets with the rotation of the black hole. Recently, Nakamura et al. (2018) compared the jet funnel seen in GRMHD and force-free electrodynamic simulations with VLBI data of M87, finding good agreement concerning a parabolic jet shape.

1.3.3 Using Radiative Transfer

Taking into account radiative transfer is of major importance in astrophysical hydrodynamical simulations. Since the thin disk model of Novikov and Thorne (1973) the measured luminosity has been linked to the accretion rate of the disk, especially in the case of black hole accretion where a high radiative efficiency is expected (McClintock et al., 2006), with strong coupling between radiation and the fluid (Collin et al., 2002). Recent works, have been using a cooling function to artificially cool down the accretion disk and keep it geometrically thin. As a first approximation, this method have led to important breakthroughs when it comes to understanding the evolution of the disk.

Noble, Krolik, and Hawley (2009) introduced a new 3-dimensional version of the `HARM` code, `HARM3D`. It was used to study the connection between the accretion and radiation with the inclusion of a cooling function to calculate the radiative cooling that is associated with the accreting process. They find that the standard Novikov and Thorne (1973) model underpredicts the dissipation of energy inside the ISCO. The accretion of electromagnetic stress for Schwarzschild black holes was studied by Noble, Krolik, and Hawley (2010). They found that it is independent of the disk thickness and the topology of the poloidal magnetic field. The magnetic stress also shows significant values in the plunging region. Because of that, Noble et al. (2011) focused on geometrically thin disk and found that the radiative efficiency is 6% higher than the one predicted by the Novikov and Thorne (1973) model. However, the spectrum resembles the prediction for a black hole with Kerr parameter $a \sim 0.2 - 0.3$. A convergence study was performed by Shiokawa et al. (2012) comparing quantities such as the plasma-β, which decrease steadily with the resolution but remains in convergence and synthetic spectra using the GR Monte Carlo ray tracing code Dolence et al. (2009), which are almost completely unaffected by the resolution. Fluid properties such as density, internal energy and temperature also decrease with resolution.

Anninos, Fragile, and Salmonson (2005) and Fragile et al. (2009) developed the `Cosmos++` GRMHD code which supported adaptive mesh refinement techniques and utilized a dual energy/flux-conserving formulation. A study in misaligned accretion disks with respect to the rotation axis of the black hole was performed by Fragile et al. (2007). The find that the disk fluid is accreted mainly from a plunging region that is in higher latitude and from larger radii than in the non-tilted cases. The simulation lasts for approximately 10 orbital periods during which the disk keeps its initial titled form, however the torque from the misaligned gravitation field imposes a precession of the body of the disk (see Figure 1.7).

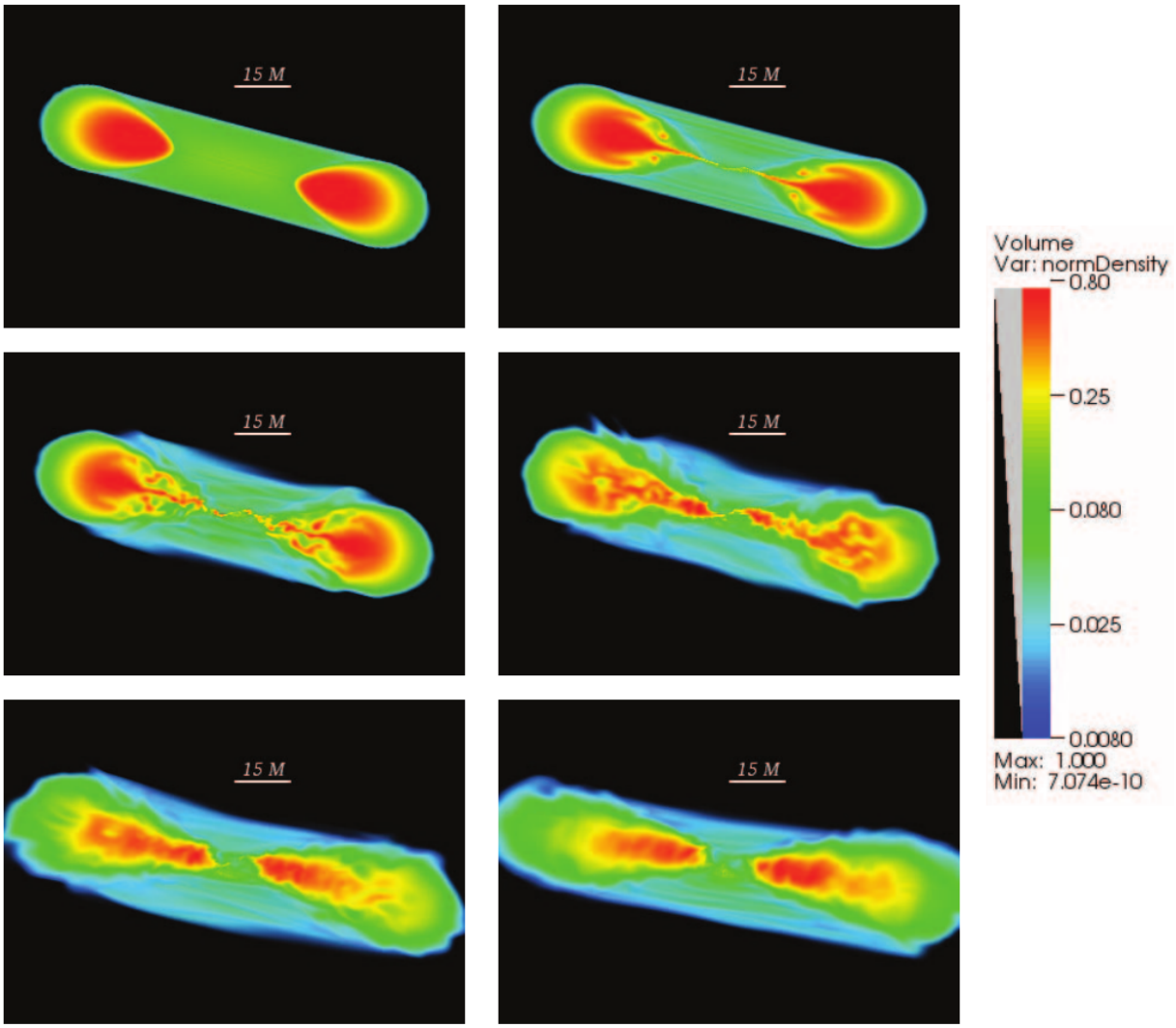

FIGURE 1.7: Simulation of a tilted accretion torus around a rotating black hole. The colored contours show the logarithm of the density at $t = 0, 1, 2, 4, 7, 10$ orbital periods. The rotation axis of the black hole is oriented vertically in each frame, with the initial condition being tilted by 15° clockwise.
Image credit: Fragile et al. (2007)

The exact treatment of the radiation is important for the black holes whose accretion rate approaches the Eddington limit (Remillard and McClintock, 2006) showed that this happens when they reach the peak of their outburst. Also, the inclusion of radiation allows the direct measurement of the luminosity and its efficiency connected with the accreting disk and the variability it shows.

McKinney et al. (2014) modified `HARM` into `HARMRAD` to also include radiation closure. Among the tests they run, they simulate the evolution of an equilibrium torus (Abramowicz, Jaroszynski, and Sikora, 1978) where they find a similar polar radiation jet in parallel with the electromagnetic one. Additionally, the radiation efficiency remain relatively low at $\sim 1\%$ while the spin-down rate of the black hole is comparable with older non-radiative simulation and can be used to explain the mass growth of the black hole in the timescale of the age of the universe. McKinney, Dai, and Avara (2015) continued studying the radiative and electromagnetic efficiency of MADs finding that the radiation reduces the efficiency of the BZ jet which drop by $\sim 35\%$ from the black hole magnetosphere to a distance of $400R_{\rm g}$. Avara, McKinney, and Reynolds (2016) used thin accretion disks and they found radiative efficiency at $\sim 15\%$ which shows higher deviation from the standard Novikov and Thorne (1973) than previous works.

Sądowski et al. (2014) presented their new ideal GRMHD code, `KORAL` that also include radiative transfer (GRRMHD). The simulations they show are dynamically similar to the ones in previous works, however, they exhibit large differences–compared with previous studies–in their radiative efficiency where the only reach values of 0.1%. Moreover, they find that large amount of the radiative luminosity comes from the jet funnel where the radiative flux is well above the Eddington limit. Sądowski et al. (2017) included electrons and ions as sub-components of the gas in their GRRMHD code `KORAL`, resulting in different thermodynamical evolutions. The effects of Coulomb interactions, synchrotron radiation , Bremsstrahlung and Compton scattering are also included. From the simulated models, the ones with low accretion rate seems unaffected by the radiation, while with larger accretion rate the accretion is much cooler and geometrically thinner. Marshall, Avara, and McKinney (2018) studied the effect of the Rayleigh-Taylor instability on the MADs where they encountered the creation of a magnetic Rayleigh-Taylor bubble around the black hole. The magnetic flux is pushed out from the black hole into the disk, halting accretion for some time. A similar effect is described in our simulations as well in Chapter 4.

Fragile et al. (2018) also implement the M1 radiative transfer closure in their `Cosmos++` code and performed GRRMHD simulation of thin accretion disks in Schwarzschild spacetime. They found evidence of thermal instabilities in radiation-pressure-dominated disks, with radiative efficiency of $\sim 6\%$.

1.3.4 Simulation in a Resistive Environment

The implementation of magnetic fields in simulations has shown that magnetic fields play a major role in the launching, acceleration and collimation of astrophysical jets. Many theoretical models try to explain how the jets are created, with two having been studied extensively. The Blandford-Znajek and Blandford-Payne (BP mechanism) mechanisms proposed two different methods for jet launching, one from the magnetosphere of the black hole and the other from the disk surface itself (see Section 2.4).

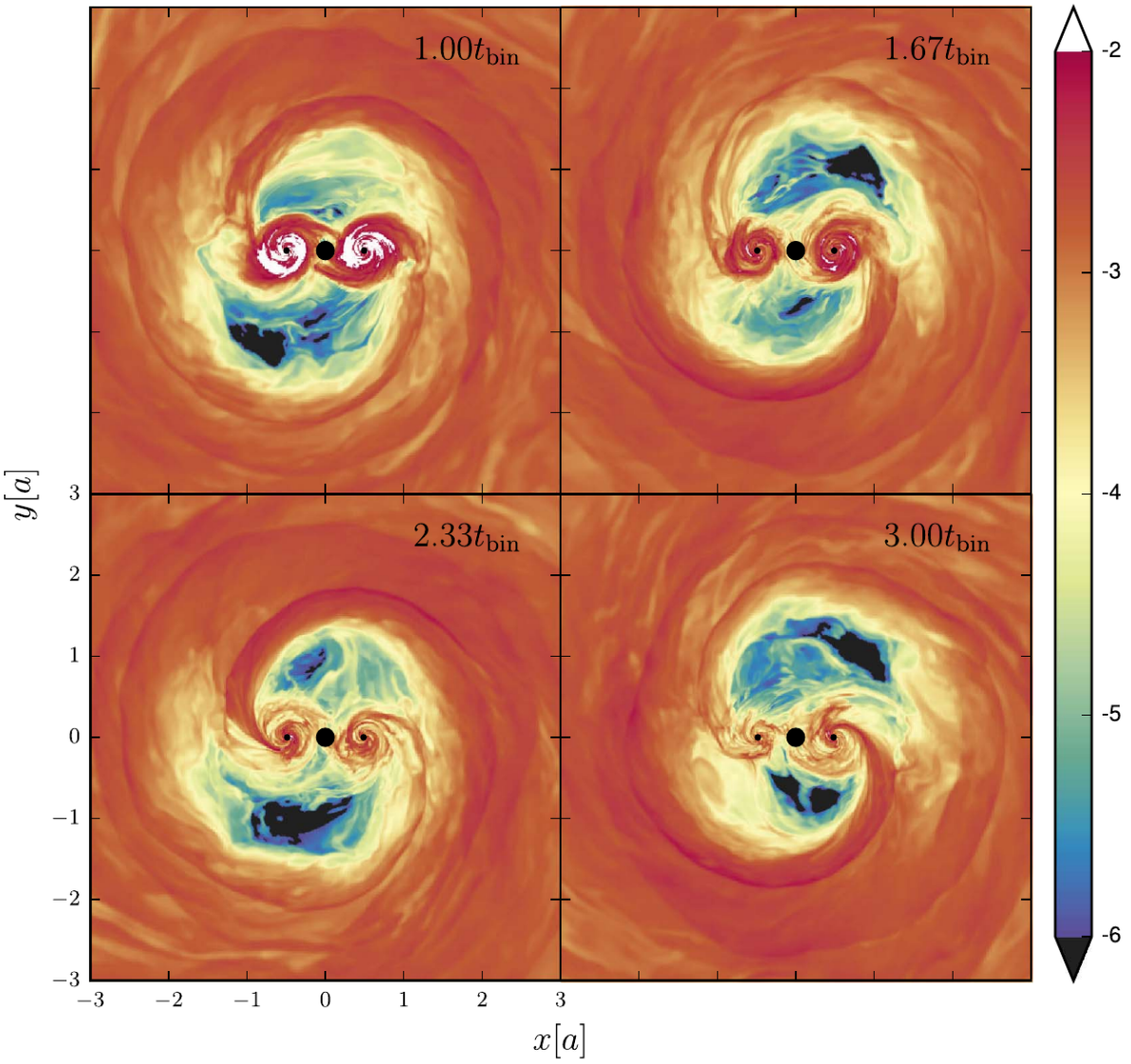

FIGURE 1.8: Time evolution of the binary black hole system with its circumbinary disk and the individual mini disk around each of the black holes in a frame corotating with the binary. The colored contours show the logarithm of the density. Spatial units are of the order of binary separation. Time is in units of the orbital period of the binary system. The two small black circles denote the binary black hole while the central black region is the boundary of the simulation in the center of mass of the system. The overdensity lump in the circumbinary can be seen in as a large spiral arm spanning over 180° in azimuth.
Image credit: Bowen et al. (2018)

The BZ mechanism has been observed in many ideal GRMHD simulation including McKinney, Tchekhovskoy, and Blandford (2012) (see reference in Section 1.3.2, however, the BP mechanism has only been observed in simulation that use (pseudo)-Newtonian gravity (Ouyed and Pudritz, 1997; Porth and Fendt, 2010; Porth et al., 2011; Porth, 2013). Magnetic resistivity in the accretion disk has also been used in Newtonian simulations (Casse and Keppens, 2002; Zanni et al., 2007; Sheikhnezami et al., 2012; Stepanovs and Fendt, 2014; Stepanovs and Fendt, 2016). In ideal MHD, when the disk wind is launched by a strong poloidal magnetic field that threads the accretion disk, it takes with it a large portion of the material that resides in the surface of the disk. The freezing of the magnetic field lines that accompanies the ideal MHD assumption does not allow for for replenishment of mass via the outer part of the disk since the fluid cannot cross the magnetic field lines. The introduction of magnetic resistivity will allow for more material to flow through the magnetic field lines resulting in an increase in the mass loading of the outflow that is generated by the BP mechanism. However, there is a lack of such works in the field of GRMHD.

The existence of magnetic resistivity also induces effects such as magnetic dissipation and reconnection which also need to be investigated in order to identify how much they enhance or hinder jet launching. In ideal (GR)MHD simulations, magnetic reconnection is observed, but it is associated with the existence of numerical diffusion due to the discrete nature of the simulation grid. The implementation of a physical model for resistivity would allow control over magnetic reconnection and its study. Komissarov (2007) and Palenzuela et al. (2009) developed the first schemes that solved the equations of resistive GRMHD and they were used as a jumping point by future works. In Qian, Fendt, and Vourellis (2018) we used our resistive code simulating thin accretion disks in a resistive environment and showed that the launching of disk outflows is definitely possible, however without identifying a clear involvement of the BP process.

Giacomazzo and Rezzolla (2007) upgraded the hydrodynamics GR code `WHISKY` (Baiotti et al., 2005) into including MHD and focused in the simulation of neutron stars and their mergers. The code was updated into its resistive GRMHD version by Dionysopoulou et al. (2013) and was applied in simulations of merging neutron stars by Dionysopoulou, Alic, and Rezzolla (2015). They detect a less efficient magnetic braking mechanism which they attribute to the reduction of outwards angular momentum transport due to the diffusive coupling of matter and magnetic field. They also simulated the system of the black hole and accretion disk that gets formed after the merging which shows significant outflows.

Del Zanna et al. (2007) presented their new GRMHD code (`ECHO`) as an extension of their old classical MHD one. They used a finite-difference conservative scheme with high-order reconstruction methods and constraint transport. Bucciantini and Del Zanna (2011) updated the code to include the option for dynamical spacetimes, while Bucciantini and Del Zanna (2013) provided the first fully covariant dynamo closure scheme in general relativistic environment and implemented it into their code. Bugli, Del Zanna, and Bucciantini (2014) applied it in the study of the toroidal field in accretion tori generated by a kinematic dynamo.

Porth et al. (2017) created the Black Hole Accretion Code (`BHAC`), a GRMHD module for the MPI-AMRVAC framework, which includes arbitrary spacetimes and adaptive mesh refinement. Ripperda et al. (2019) extended `BHAC` into the resistive MHD regime.

Qian et al. (2017) and Qian, Fendt, and Vourellis (2018) used the scheme developed by Bucciantini and Del Zanna (2013) to extend the `HARM` code into the resistive GRMHD regime. Their work was continued by Vourellis et al. (2019) by using the same extension in

the HARM3D code. More about their work can be found in the next chapters.

1.3.5 Simulating Accretion in Black Hole Binaries

Noble et al. (2012) adapts the HARM3D code to simulate the evolution of an accretion disk around a binary system of black holes. They studied the simple case of two equally massive, non-spinning, black holes that are inspiraling due to gravitational radiation. The structure of the circumbinary disk forms a gap of approximately two binary separation radii and accumulates in the outer edge of it. As the binary inspirals, the inner edge of the disk follows the black holes in a slower rate. The torque from the binary decelerates the accretion rate, however, when the separation of the binary is $\sim 10 - 20R_{\rm g}$ the radiation from the disk is large enough to make the system very luminous. Bowen et al. (2017) studied the mini disks that are formed around an system of two comparable-mass and non-spinning black holes using 2D GRMHD simulations. They found a constant exchange of material between the two disks that increases with time as the binary separation decreases and the mini disks themselves move toward the L1 point. Bowen et al. (2018) and Bowen et al. (2019) continued the work including a circumbinary disk that feeds the two mini disks. They detect a pair of accretion streams that transferred material from the circumbinary disk to the individual mini disks. They also find the existence of a overdense "lump" in the circumbinary disk that feeds with higher accretion the closest disk before it alternates to the other one as the circumbinary disk rotates. As a result, they find large fluctuations in the mass of the mini disks as they are constantly in disequilibrium because of the approaching black holes. The dynamics of the binary system break the symmetry of the circumbinary disk, resulting in the modulation of the mass and accretion rates of the mini disks and subsequently in possible fluctuations in the electromagnetic emission (see Figure 1.8).

1.3.6 More on GRMHD Codes

The field of GRMHD simulations was greatly developed in the last 15 years with many scientific groups from all over the world developing their own code and targeting specific physical phenomena that they wanted to study. Most of them were mentioned extensively previously, so here we will briefly mention some of them. Duez et al. (2005) developed a GRMHD code that also can work with dynamical spacetimes. Mizuno et al. (2006) created the RAISHIN GRMHD code that used a variety of reconstruction and slope-limiter methods. Etienne et al. (2015) released an open-source version of their GRMHD code, IllinoisGRMHD, in order to make more accessible to the scientific community. Meliani et al. (2016) created the GR-AMRVAC hydrodynamics code in order to treat strong gravity problems in the area of exotic cases such as the boson stars. For that they implemented the use of numerical spacetimes. White, Stone, and Gammie (2016) incorporated GRMHD in their already existing Athena++ framework resulting with the options for general relativistic, special relativistic and Newtonian MHD in one code.

Liska et al. (2018) used the original HARM code as a jumping point for their designing of the H-AMR code a GRMHD code with GPU paralellization featuring adaptive mesh refinement. Shiokawa et al. (2015) used the HARM3D code to simulate an interesting phenomenon, the evolution of the debris of a tidal disruption event of star by a SMBH using relativistic hydrodynamics. Stellar material get bound to the black hole eventually forming an accretion

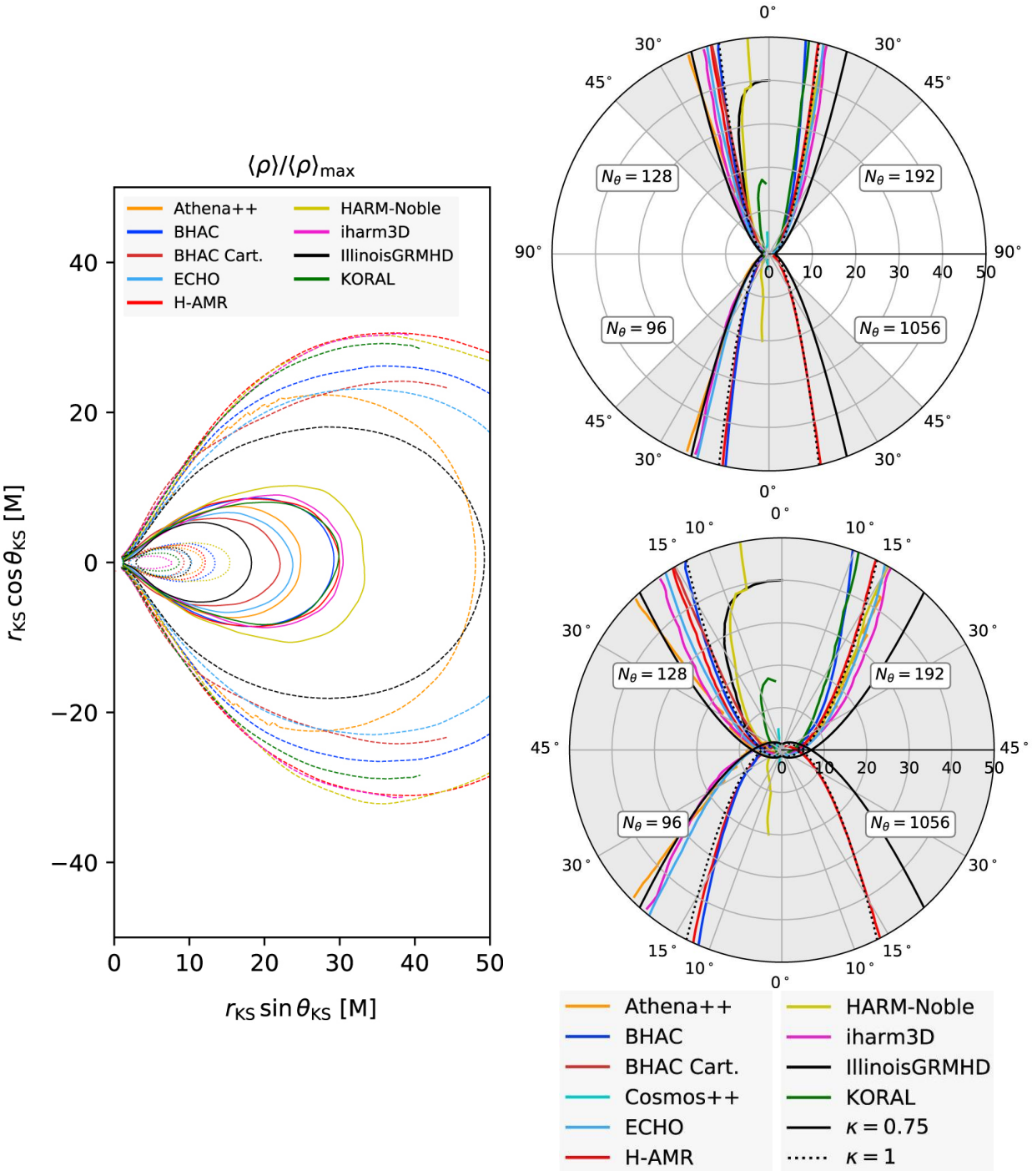

FIGURE 1.9: Comparison of the accretion disk and jet area from different GRMHD codes. The disk contours (left) are plotted for values of the normalized density $\rho/\rho_{\max} = (0.0078125, 0.125, 0.5)$ (dashed, solid, dotted). The jet surfaces are plotted for four increasing polar angular resolutions $N_\theta = (96, 128, 192, 1056)$ (right top). A zoomed version with $\theta \in [0°, 45°]$ is shown (right bottom). The black and dotted-black lines show the flux surfaces of the approximate force-free solutions for $z \propto R^2$ (thin solid black line) and $z \propto R^{1.6}$ (thin dotted black line). The codes seem to agree in the high-resolution case.
Image credit: Porth et al. (2019)

disk. The mass accumulation is slow with the accretion rate showing a jump during the disruption an then decaying approximately as a power law with its maximum being 10 times lower than expected from theory. One of the reason for that is the shocks that develop and keep material from falling towards the black hole. They studied titled accreted disks and found jets being launched along the rotational axis of the disk.

As part of the EHTC, Porth et al. (2019) made an extensive study of some of the aforementioned GRMHD codes in order to compare their ability to simulate the observations of the shadow of the SMBH that were recently released. The codes reached very good agreement in the accretion rate of the saturated turbulent state when the reach high enough resolution (see Figure 1.9).

1.4 Introduction to Dynamo Theory

The investigation of astrophysical processes involving magnetic fields has always been plagued by one fundamental question. Where does the magnetic field come from? Astrophysicists tried to answer this question for years. In 1919 Sir Joseph Larmor, motivated by observations showing the sunspots as areas of strong magnetic field, proposed that the magnetic field in the Sun is created by a combination of Faraday's and Ampere's laws. We can assume that small magnetic fields exist between the particles of a conductive plasma. The variation of the field as the conductive plasma moves creates electric currents while at the same time the motion of the material through the magnetic field also results in electric current generation. These electric current also produce magnetic field which, if their direction is favorable, can in their turn amplify the existing seed magnetic field. The mechanism is then repeated resulting in an exponential magnetic field amplification. (Deguen and Lasbleis, 2019; Larmor, 1919).

However, this whole idea, as simple as it sounds, was not easy to implement. In the following years a set of *anti-dynamo* theorems emerged which were restricting the working range of the dynamo theory. In 1933 Thomas Cowling in his seminal work *The magnetic field of sunspots* (Cowling, 1933) developed reasoning that deemed Larmor's idea completely invalid. Cowling's anti-dynamo theorem states that an axisymmetric magnetic field cannot be maintained by a dynamo.

There are ways to get around the anti-dynamo theorems. Ponomarenko (1973) developed a simple solution of a magnetic field being amplified in the limit of large magnetic Reynolds number. The most prominent of these dynamo theories is the mean-field dynamo. Started by Parker (1955) and further developed by Steenbeck and Krause (1966), Steenbeck and Krause (1969a), Steenbeck and Krause (1969b), and Krause and Raedler (1980), it is based on the idea that the magnetic and velocity fields can be expressed as variations around mean values (see, 2.1.3).

On cosmological scales, dynamo theory has been used to investigate how the magnetic field was originated and developed during inflation (Marklund and Clarkson, 2005). The most plausible and generally accepted scenario for the creation of initial primordial magnetic fields is based on the idea of a *cosmic battery* and was proposed by Ludwig Biermann in 1950 (Biermann, 1950). Xu et al. (2008) included Biermann's battery in simulations of Population II star formation where low strength magnetic fields were generated. In Kulsrud and Zweibel (2008) the authors debated the different proposed theories for the development

of the primordial magnetic field to the scale observed today in galaxies and galactic clusters. Pudritz and Silk (1989) proposed the idea that the magnetic field could be generated during the formation of a galaxy.

In accretion disk and jet theory, the dynamo has been used as the main theory for generating magnetic fields the lead to jet launching. Pudritz (1981b) and Pudritz (1981a) applied the dynamo theory in the case of thin accretion disks and showed the development of a magnetic field due to the differential rotation of the disk ($\alpha\Omega$ dynamo). Brandenburg et al. (1995) simulated magnetized shear flows and showed that a dynamo generated magnetic field can result in amplification of turbulence in the flow, which in turn is amplifying the magnetic field via the dynamo mechanism. Pariev, Colgate, and Finn (2007) showed a possible origin of the dynamo mechanism in the case of AGN accretion flows, where a passing star can heat and perturb the magnetic field inside the Keplerian accretion disk resulting in the rotation of toroidal flux into poloidal flux. Stepanovs and Fendt (2016) simulated a Keplerian accretion disk and explored the structure of the magnetic field as it was being generated by the dynamo. Their work was continued by Fendt and Gaßmann (2018) who experimented with the dynamo by switching it on and off periodically. They found that for strong dynamo values oscillating dynamo modes may occur resulting in pulsating ejection in the jet. Sądowski et al. (2015) simulated the effect of a mean field dynamo in the ideal GRMHD regime and studied the evolution of thick disks in different accretion rates. The first fully covariant implementation of dynamo closure in a general relativistic environment was done by Bucciantini and Del Zanna (2013) following the 3+1 formalism. They applied it in the `ECHO` code (Del Zanna et al., 2007; Bucciantini and Del Zanna, 2011) where Bugli, Del Zanna, and Bucciantini (2014) used it to simulate kinematic dynamo and investigate the growth of toroidal field.

1.5 Outline of the Thesis

In this thesis, we investigate the launching of jets from accretion disks in a resistive GRMHD environment as well as the generation of magnetic fields from mean-field dynamo.

Chapter 2

is a review of the rich theoretical background necessary for understanding the work presented in this thesis. We review the theory of MHD with the introduction of mean-field resistivity and dynamo, the basics of the theory of General Relativity and its application on the environment of the black holes. Combining the two theories we show the basic equation of GRMHD and we conclude with the most important theories for jet launching.

Chapter 3

is dedicated into the numerical aspects of the work and the implementation of the various physical quantities in the code. We describe the transition from the ideal to the resistive version of the code, the numerical grid that we use, the boundary and initial conditions, the diffusivity and floor value models and concludes with a set of test simulations for the resistive version of the code. Large part of this chapter is based on the published work of Vourellis et al. (2019).

Chapter 4

shows the reference simulation we performed with our code. It describes the evolution of the disk, the development of the jet, the measurement of the mass and Poynting flux and the different types of disk wind identified. This chapter is based on the published work of Vourellis et al. (2019).

Chapter 5

performs a comparison study between simulation with different levels of black hole spin and magnetic diffusivity. It also includes an interesting finding for the case of counterrotating black hole-accretion disk system and an analysis of the direction of the electric field. Large part of this chapter is based on the published work of Vourellis et al. (2019).

Chapter 6

is dedicated in the development of magnetic field by mean-field dynamo. It tests the cases of accreting tori and disks for different values of the dynamo parameter and different types of initial seed field.

Chapter 7

presents a discussion and a summary the main results of this thesis and the plans for future work.

Chapter 2

Theoretical Background

This chapter is a continuation of the introduction to simulations of jets that focuses on the theoretical background that encompasses the GRMHD simulations. We start with an introduction to the classical and the mean-field MHD theory and we continue with the theory of general relativity and its application to the black holes. Combining these theories we refer to the basic equations of GRMHD. Finally, we introduce some of the physical processes that result in the generation of jets including a physical description of the accretion disk model.

2.1 Introduction to Magnetohydrodynamics

Maxwell's theory of electromagnetism (Maxwell, 1865) was established in the middle of 19^{th} century. It provided a theoretical framework for the explanation and prediction of most magnetic and electric effects. In this chapter we will describe the basic principles of the theory of magnetohydrodynamics (MHD).

MHD began as a theory when Hannes Alfvén (Alfvén, 1942a) published a small article in *Nature* where he introduced the existence of magnetic waves (what we today call Alfvén waves) using Maxwell's equations. Alfvén's idea about magnetic waves was eventually combined with hydrodynamics in order to explain the macroscopic behavior of highly conductive fluids. The Sun's magnetic field was one of the first astrophysical applications of the newly formed theory.

However, like any other physical theory, MHD is premised on certain assumptions.

- The "fluid approximation", where the macroscopic variations of the fluid's thermodynamical properties are considered slow in comparison with the microscopic processes.
- There is a relation between the electric field in the fluid and the electric current density (*Ohm's law*).
- The fluid is considered electrically neutral.

All three together can be combined in the "MHD approximation".

Within the limits of the "MHD approximation" we can combine the equations of hydrodynamics with Maxwell's equations into a new set of equations that will describe the evolution of magnetized fluids.

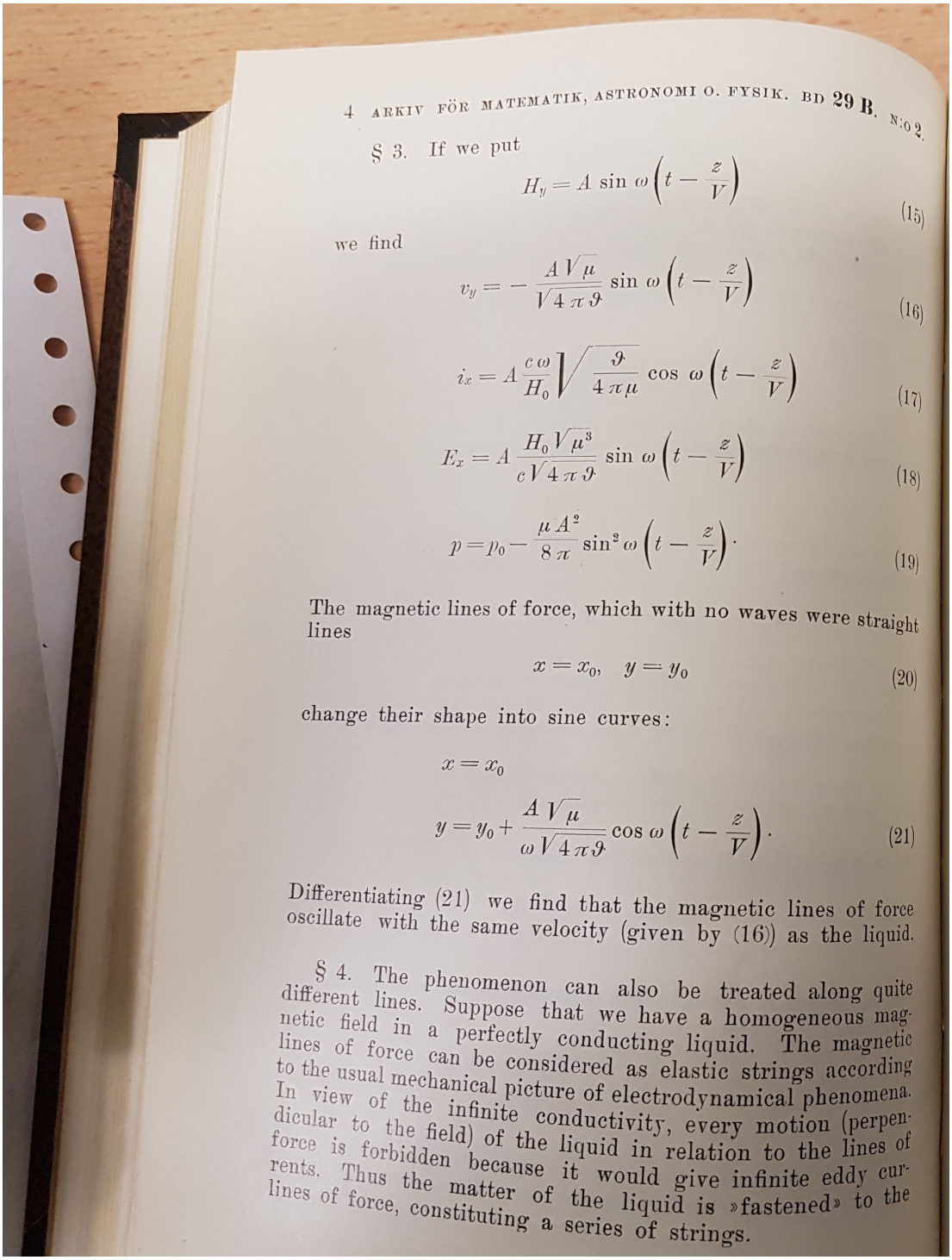

4 ARKIV FÖR MATEMATIK, ASTRONOMI O. FYSIK. BD 29 B. N:O 2.

§ 3. If we put

$$H_y = A \sin \omega \left(t - \frac{z}{V} \right) \tag{15}$$

we find

$$v_y = - \frac{A \sqrt{\mu}}{\sqrt{4 \pi \vartheta}} \sin \omega \left(t - \frac{z}{V} \right) \tag{16}$$

$$i_x = A \frac{c \omega}{H_0} \sqrt{\frac{\vartheta}{4 \pi \mu}} \cos \omega \left(t - \frac{z}{V} \right) \tag{17}$$

$$E_x = A \frac{H_0 \sqrt{\mu^3}}{c \sqrt{4 \pi \vartheta}} \sin \omega \left(t - \frac{z}{V} \right) \tag{18}$$

$$p = p_0 - \frac{\mu A^2}{8 \pi} \sin^2 \omega \left(t - \frac{z}{V} \right). \tag{19}$$

The magnetic lines of force, which with no waves were straight lines

$$x = x_0, \quad y = y_0 \tag{20}$$

change their shape into sine curves:

$$x = x_0$$

$$y = y_0 + \frac{A \sqrt{\mu}}{\omega \sqrt{4 \pi \vartheta}} \cos \omega \left(t - \frac{z}{V} \right). \tag{21}$$

Differentiating (21) we find that the magnetic lines of force oscillate with the same velocity (given by (16)) as the liquid.

§ 4. The phenomenon can also be treated along quite different lines. Suppose that we have a homogeneous magnetic field in a perfectly conducting liquid. The magnetic lines of force can be considered as elastic strings according to the usual mechanical picture of electrodynamical phenomena. In view of the infinite conductivity, every motion (perpendicular to the field) of the liquid in relation to the lines of force is forbidden because it would give infinite eddy currents. Thus the matter of the liquid is »fastened» to the lines of force, constituting a series of strings.

FIGURE 2.1: Photo of page 4 of the 1942 edition of the Swedish journal *Arkiv för Matematik, Astronomi och Fysik, 29B, N:o 2*, where the original version of Alfvén's flux freezing theorem appears. For reasons unknown, the journal (which stopped its publication in 1949 and the split into 4 different journals) is under some form of copyright prohibiting the existence of digital versions.

Maxwell's equation can be written in cgs units in the form

$$\nabla \cdot \mathbf{E} = 4\pi q \tag{2.1a}$$
$$\nabla \cdot \mathbf{B} = 0 \tag{2.1b}$$
$$\nabla \times \mathbf{E} = -\frac{1}{c}\frac{\partial \mathbf{B}}{\partial t} \tag{2.1c}$$
$$\nabla \times \mathbf{B} = \frac{4\pi}{c}\mathbf{j} + \frac{1}{c}\frac{\partial \mathbf{E}}{\partial t}, \tag{2.1d}$$

where $\mathbf{E}$ and $\mathbf{B}$ are the electric field and the magnetic induction (hereafter referred to as magnetic field), q and $\mathbf{j}$ are the charge and current densities, and c is the speed of light.

At the same time Ohm's Law dictates a relation between the electric field and the current density

$$\mathbf{E} = \sigma \mathbf{j}, \tag{2.2}$$

where σ is the electric conductivity. The motion of the fluid with velocity $\mathbf{v}$ generates another component of the electric field which enters Ohm's Law as

$$\sigma \left(\mathbf{E} + \frac{\mathbf{v} \times \mathbf{B}}{c} \right) = \mathbf{j}. \tag{2.3}$$

Combining Equations (2.1) and (2.3) we get the *induction equation*

$$\frac{\partial \mathbf{B}}{\partial t} = \nabla \times (\mathbf{v} \times \mathbf{B}) - \eta \nabla^2 \mathbf{B}, \tag{2.4}$$

which determines the evolution of the magnetic field, and where we used

$$\eta = \frac{c^2}{4\pi\sigma}, \tag{2.5}$$

as the *magnetic resistivity*. The last term $\nabla \times \frac{\partial \mathbf{E}}{\partial t}$ in the the induction equation is intentionally omitted under the assumption that we are in a non-relativistic, slow velocity environment with $v << c$. The same applies for the displacement current in Ampere's law (Equation (2.1d)). However, it is used in the case of Special and General Relativity. In the case where the plasma is not moving ($\mathbf{v} = \mathbf{0}$) the induction equation reduces to

$$\frac{\partial \mathbf{B}}{\partial t} = \eta \nabla^2 \mathbf{B}. \tag{2.6}$$

If we take the characteristic time and length scales we get $B/t \sim \eta B/l^2$, which means that η is responsible for the decay of the magnetic field on a time scale of $t \sim l^2/\eta$, justifying the name *magnetic diffusivity*.

The hydrodynamical part of MHD enters with the continuity equation for the conservation of mass

$$\frac{\partial \rho}{\partial t} + \nabla \cdot (\rho \mathbf{v}) = 0, \tag{2.7}$$

and Euler's equation of motion

$$\rho\frac{\partial \mathbf{v}}{\partial t} + \rho\left(\mathbf{v}\cdot\nabla\right)\mathbf{v} = -\nabla P + F_{\rm EM} + F_{\rm grav}, \tag{2.8}$$

where ρ is the fluid density, P is the gas pressure and $F_{\rm EM}$, $F_{\rm grav}$ are electromagnetic and gravitational forces (if they exist), and where we have made the assumption that the fluid is non-viscous and there is no cooling term.

The hydrodynamical set of equations closes with the energy equation that connects the gas density and pressure and the fluid's internal energy. This equation strongly depends on the type of problem we study. In the literature one can find a variety of general energy equations and equations of state, however we will remain in the context of astrophysical applications where a polytropic equation of state is used to describe the majority of astrophysical fluids. In general

$$P = K\,\rho^{\Gamma}, \quad u = \frac{P}{\Gamma - 1} \tag{2.9}$$

where u is the internal energy of the fluid and Γ is the polytropic index. The set of the last four equations, accompanied by the divergence-free law for the magnetic field, describe a complete set of magnetohydrodynamical equations.

The induction equation (2.4) describes how the magnetic field responds to the motion of the fluid. This reaction is accompanied by forces which are applied on the fluid by the magnetic field. The general form of Lorentz force is

$$\mathbf{F}_L = \frac{\mathbf{j}\times\mathbf{B}}{c}, \tag{2.10}$$

and if we use Faraday's law we get

$$\mathbf{F}_L = \frac{1}{4\pi}(\nabla\times\mathbf{B})\times\mathbf{B} = \frac{1}{4\pi}\left(\mathbf{B}\cdot\nabla\right)\mathbf{B} - \frac{1}{8\pi}\nabla B^2, \tag{2.11}$$

where the Lorentz force is clearly spit into two parts. The first term expresses the *magnetic tension* created by the curving of the field lines. It acts as a restoring force that tries to move the fluid in order to straighten the magnetic field lines. The second term is the gradient of *magnetic pressure*

$$P_{\rm magn} = \frac{B^2}{8\pi} \tag{2.12}$$

which expresses the magnetic energy density. In cases where the magnetic tension is balanced by the gradient of the magnetic pressure, the Lorentz force disappears and the electric current becomes parallel to the magnetic field ($\mathbf{j}\times\mathbf{B} = 0$). This type of magnetic field is called *force-free*.

The most common external force that appears in astrophysical applications of MHD is gravity. Due to the conservative nature of gravity, in a Newtonian environment, the gravitational force can be described by a scalar potential Φ_G with

$$\mathbf{F}_{\rm grav} = -\nabla\Phi_G. \tag{2.13}$$

With the inclusion of the two forces, the equation of motion is written as

$$\rho\frac{\partial \mathbf{v}}{\partial t} + \rho\left(\mathbf{v}\cdot\nabla\right)\mathbf{v} = -\nabla P + \frac{1}{4\pi}\left(\mathbf{B}\cdot\nabla\right)\mathbf{B} - \frac{1}{8\pi}\nabla B^2 - \nabla\Phi_G. \tag{2.14}$$

2.1.1 The Approximation of Ideal Magnetohydrodynamics

In the limit of ideal MHD, in which we assume the fluid to be a perfect conductor, if we also assume non-relativistic velocities, the induction equation (2.4) reduces to

$$\frac{\partial \mathbf{B}}{\partial t} = \nabla\times\left(\frac{\mathbf{v}\times\mathbf{B}}{c}\right), \tag{2.15}$$

while Ohm's law (2.3) becomes

$$\mathbf{E} + \frac{\mathbf{v}\times\mathbf{B}}{c} = 0. \tag{2.16}$$

In this case the electric and magnetic field are perpendicular ($\mathbf{E}\cdot\mathbf{B} = 0$). Taking the divergence of (2.15) we get the evolution of the zero-divergence condition of the magnetic field

$$\nabla\cdot\frac{\partial \mathbf{B}}{\partial t} = \frac{\partial}{\partial t}\left(\nabla\cdot\mathbf{B}\right) = 0, \tag{2.17}$$

which means that the magnetic field must remain divergence free while moving with the fluid. Taking the divergence of Ampere's law ((2.1d)) we get

$$\frac{\partial q}{\partial t} + \nabla\cdot\mathbf{j} = 0, \tag{2.18}$$

which expresses the conservation of charge and in the non-relativistic limit reduces to

$$\nabla\cdot\mathbf{j} = 0, \tag{2.19}$$

The magnetic flux through a surface can be expressed as the "number" of magnetic field lines that penetrate the surface. According to Gauss's theorem, the change in the flux of a magnetic field that enters and exits a closed surface is equal to the volume integral of the divergence of the field within that surface, which from Equation (2.1b) is zero. We can then define *magnetic flux tubes* of constant flux as they are seen in Figure (2.2).

This also implies that the magnetic flux does not depend either on the shape or the area of the surfaces. The single requirement is that the number of field lines be the same. If we start decreasing the area of the surfaces S_1 and S_2 we will eventually reach a point where the flux tube can barely fit a single field line. As a result the flux tubes are considered an extended version of the field lines.

At the foundation of ideal MHD sits Alfvén's theorem (see Figure 2.1; also Alfvén (1942b)), which states that in a magnetized fluid with infinite conductivity, the magnetic flux is conserved with the fluid's motion, or in other words the magnetic field lines remain "frozen" within the fluid and they have to move with it. This can be expressed as

$$\frac{\partial\Phi}{\partial t} = \frac{\partial}{\partial t}\int_C \mathbf{B}\, d\mathbf{S} = 0. \tag{2.20}$$

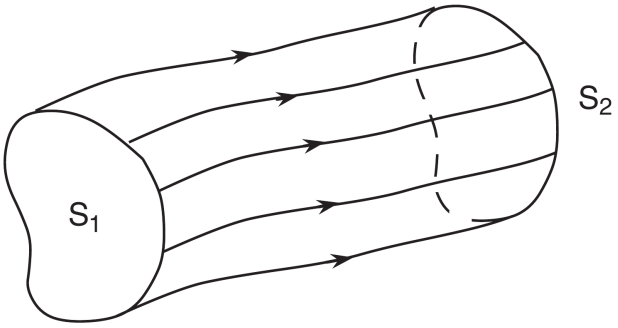

FIGURE 2.2: A magnetic flux tube. The surfaces S_1 and S_2 need not be the same. As long as they are both penetrated by the same numbers of field lines.
Image credit: Goedbloed and Poedts (2004)

2.1.2 The Resistive MHD

In Equation (2.2) we introduced the quantity of electric conductivity σ as a measurement of the resistance of the fluid in the electric currents. In literature, its inverse $\eta = 1/\sigma$ is the *magnetic resistivity*, while $\tilde{\eta} = \eta/\mu_0$ is defined as *magnetic diffusivity* in order to absorb the μ_0 factor. In the following we will use the diffusivity η in the equations.

The main difference between resistive and ideal MHD is that the introduction of resistivity/diffusivity nullifies Alfvén's theorem and allows the magnetic field lines to move with respect to the fluid. As a result, the magnetic flux cannot be conserved, at least not in the same way as it does in ideal MHD. In a resistive magnetic flow, part of the electromagnetic energy is transformed into heat, increasing the internal energy of the fluid with a rate of

$$\frac{de}{dt} = \frac{1}{\sigma} j^2 = \eta j^2. \tag{2.21}$$

This process is commonly referred to as *Ohmic heating*.

More information on how we implement resistivity in our work you can be found in Chapter 3.1.4.

2.1.3 Mean – Field Dynamo Theory

In this section we will present the basic assumptions, descriptions and results of the mean – field dynamo theory. For a more detailed analysis on the foundation of mean – field dynamo theory we recommend Moffatt (1978).

For this section only, we will use $\mathbf{V}$ to describe the fluid velocity and $\mathbf{v}$ for the fluctuating velocity.

The dynamo theory proposes a mechanism to generate and maintain a magnetic field from the kinetic energy of a fluid. Turbulence is the main physical property which is theorized as the generator of the field and it has been studied in a stohastic level by Brandenburg and Subramanian (2005) and Brandenburg, Sokoloff, and Subramanian (2012). Parker (1955) was the first to include the idea of a dynamo – based magnetic field generation in his seminal work and Krause and Raedler (1980) developed it into a complete theory. Their idea is based on the assumption that the physical properties of the magnetized fluid can be split into a

mean and a *varying* part. Pudritz (1981b) and Pudritz (1981a) applied the dynamo theory in the case of thin accretion disks and showed the development of a magnetic field due to the differential rotation of the disk ($\alpha\Omega$ dynamo).

We consider the case of a homogeneous conducting fluid with velocity $\mathbf{V}$, threaded by a magnetic field $\mathbf{B}$, with an electric field $\mathbf{E}$ and a current density $\mathbf{j}$. In general, these quantities show variations in time and space, so it is useful to assume that the large scale behaviour is described by a mean–field (eg. $\mathbf{V_0} = \langle \mathbf{V} \rangle$) while the small scale turbulent behaviour is described by velocity deviations $\mathbf{v}$.

Following Maxwell's equations (2.1) we can produce the induction equation for the general values of $\mathbf{V}$, $\mathbf{B}$, $\mathbf{E}$ and $\mathbf{j}$.

$$\eta \nabla^2 \mathbf{B} + \nabla \times (\mathbf{V} \times \mathbf{B}) - \partial_t \mathbf{B} = 0, \quad \nabla \cdot \mathbf{B} = 0, \tag{2.22}$$

We will express the physical quantities in the form of mean–field and fluctuating values. The splitting is written as

$$\begin{aligned} \mathbf{V} &= \mathbf{V_0} + \mathbf{v} \\ \mathbf{B} &= \mathbf{B_0} + \mathbf{b}, \end{aligned} \tag{2.23}$$

resulting in an induction equation for the averaged values

$$\frac{\partial \mathbf{B_0}}{\partial t} = \nabla \times (\mathbf{V_0} \times \mathbf{B_0}) + \nabla \times \boldsymbol{\mathcal{E}} + \eta \nabla^2 \mathbf{B_0}, \tag{2.24}$$

and for the fluctuating parts

$$\frac{\partial \mathbf{b}}{\partial t} = \nabla \times (\mathbf{V_0} \times \mathbf{b}) + \nabla \times (\mathbf{v} \times \mathbf{B_0}) + \nabla \times \mathbf{G} + \eta \nabla^2 \mathbf{b}, \tag{2.25}$$

where η is the magnetic diffusivity.

$$\boldsymbol{\mathcal{E}} = \langle \mathbf{v} \times \mathbf{b} \rangle, \quad \mathbf{G} = \mathbf{v} \times \mathbf{b} - \langle \mathbf{v} \times \mathbf{b} \rangle \tag{2.26}$$

with $\boldsymbol{\mathcal{E}}$ being the mean electromotive force.

In order to solve the equation we must find a way to express $\boldsymbol{\mathcal{E}}$ in terms of the mean fields. The theory suggests that the mean electromotive force is linearly related to the mean magnetic field, meaning that we can develop $\boldsymbol{\mathcal{E}}$ as a convergent series in the form

$$\mathscr{E}_i = \alpha_{ij} B_{0j} + \beta_{ijk} \frac{\partial B_{0j}}{\partial x_k} + \gamma_{ijkl} \frac{\partial^2 B_{0j}}{\partial x_k \partial x_l} + \ldots, \tag{2.27}$$

where the coefficients α_{ij}, β_{ijk} are pseudo–tensors connected with the $\alpha-$ dynamo and diffusivity respectively. Also, provided that the series is rapidly converging, the high order terms are negligible in comparison with the first two terms.

2.1.3.1 The α–Dynamo

If we isolate the first term, we get the leading component of the electromotive force

$$\mathscr{E}_i^{(0)} = \alpha_{ij} B_{0j}, \tag{2.28}$$

and if we split α_{ij} into a symmetric and anti-symmetric parts the electromotive force becomes

$$\boldsymbol{\mathcal{E}}_i^{(0)} = \alpha_{ij}^{\text{sym}} \mathbf{B_0} + (\mathbf{a} \times \mathbf{B_0}) \tag{2.29}$$

The anti-symmetric part of α_{ij} contributes th the effective mean velocity and acts on the mean magnetic field. The contribution of the symmetric part is revealed more easily if we assume that the velocity field of the fluctuations is isotropic and homogeneous. In this case α_{ij} must be isotropic as well, meaning

$$\alpha_{ij} = \alpha \delta_{ij}, \tag{2.30}$$

while the anti-symmetric part vanishes ($\mathbf{a} = 0$). Combining with Equations (2.28) and (2.3) we get

$$\mathbf{j}^{(0)} = \sigma \boldsymbol{\mathcal{E}}^{(0)} = \sigma \alpha \mathbf{B_0}, \tag{2.31}$$

where sigma is the magnetic resistivity. The appearance of a electric current parallel to the mean magnetic field seems strange since we are used to the induced electric current and magnetic field being perpendicular. The electromotive force that appeared because of the α parameter was named by Steenbeck and Krause (1966) as "the $\alpha-$ effect" and is the protagonist of the mean field dynamo theory. The contribution of the α dynamo helps to close up the circle of magnetic field generation. The existence of a poloidal magnetic field $\mathbf{B_P}$ in a rotating fluid (eg. differentially rotating accretion disk threaded by poloidal magnetic field), induces a toroidal component $\mathbf{B_{\mathfrak{C}}}$. In the case of mean fields, Equation (2.31) generates a toroidal electric current which induces in a poloidal magnetic field.

If the velocity field is not isotropic as we assumed earlier, then the α dynamo parameter can be expressed with values in the three primary spatial dimensions (Ruediger and Kichatinov, 1993) appearing as

$$\alpha_{ij} = \begin{pmatrix} \alpha^{(1)} & 0 & 0 \\ 0 & \alpha^{(2)} & 0 \\ 0 & 0 & \alpha^{(3)} \end{pmatrix} \tag{2.32}$$

resulting in a electromotive force in the form of

$$\boldsymbol{\mathcal{E}}^{(0)} = \left(\alpha^{(1)} B_{01} + \alpha^{(2)} B_{02} + \alpha^{(3)} B_{03}\right) \tag{2.33}$$

2.1.3.2 The β–Diffusivity

If we consider the second term in the right hand side of Equation (2.27), we get

$$\mathscr{E}^{(1)} = \beta_{ijk} \frac{\partial B_{0j}}{\partial x_k}. \tag{2.34}$$

Similar to the α, in the case of isotropic and homogeneous velocity field, the β parameter becomes

$$\beta_{ijk} = \beta \, \varepsilon_{ijk}, \tag{2.35}$$

with β being a scalar parameter. From (2.34) we get

$$\boldsymbol{\mathcal{E}}^{(1)} = \beta \nabla \times \mathbf{B_0} = \beta \mu_0 \mathbf{J_0}, \tag{2.36}$$

where $\mathbf{J_0}$ is the mean current. Also

$$\nabla \times \boldsymbol{\mathcal{E}}^{(1)} = \beta \nabla^2 \mathbf{B_0} \tag{2.37}$$

Equation (2.37) shows that the β parameter has units of magnetic diffusivity resulting in a total diffusivity of $\eta + \beta$. β diffusivity is associated with the notion of a turbulent diffusivity. The random motion induced by the fluctuations of the velocity field results in the mixing of the fluid particles which is expressed as turbulent diffusion.

2.2 Introduction to Black Holes and General Relativity

This chapter presents a small introduction to the theory of General Relativity. It is meant to be nothing but a reminder of the basic principles of the theory and the first developments and applications. Since the topic requires a strong mathematical background the author stresses that this introduction is not meant to replace any specialized book in the subject. However, considering that the black hole physics are an integral part of this work, the existence of such an introduction seems more than justified. All the following is based on the authors knowledge acquired throughout the years as well as information from the holy bible of General Relativity–Misner, Thorne, and Wheeler (1973) and the works of Wald (1984), Weinberg (1972), Lawden (1982), Schutz (1985), and D'Inverno (1992).

2.2.1 Elements of Tensor Calculus

2.2.1.1 The Metric Tensor

General relativity, as a geometric theory of gravity, makes extensive use of mathematical tools developed mainly in the second half of 19^{th} century. Georg Friedrich Bernhard Riemann's contribution to the field of differential geometry laid the foundations for the mathematical development of Einstein's ideas. In the following section we will present a short introduction to the basic elements of differential geometry through the looking glass of general relativity.

Measuring distances is the basic element of any space. For any two points in space we can assign a scalar quantity that expresses the distance between them. As an example, in a Euclidean 3-D space we have two points $A(x,\, y,\, z)$ and $B(x+dx,\, y+dy,\, z+dz)$. Their distance is given as

$$ds^2 = dx^2 + dy^2 + dz^2, \tag{2.38}$$

and similarly in the Minkowski space of special relativity we have

$$ds^2 = -dt^2 + dx^2 + dy^2 + dz^2, \tag{2.39}$$

where we used the signature $(-,+,+,+)$. The above equations can be written in the general form of the linear element

$$ds^2 = g_{ab}dx^a dx^b = \sum_{a,b=1}^{n} g_{ab}dx^a dx^b, \tag{2.40}$$

where the Einstein summation is used for indices a and b. g_{ab} is the *metric tensor* and it can be written as an $n \times n$ symmetric matrix in an n-dimensional space. It expresses the shape of the spacetime continuum which can be altered by the presence of any type of massive object. When the metric tensor can be expressed as function of the coordinates of the space then the space is called *Riemann space*.

The metric tensor belongs in a general category of mathematical objects called tensors. They can be seen as a generalization of scalar and vector objects. In an n-dimensional space, a scalar object has $n^0 = 1$ components and is consider a $0th$ order or rank tensor, a vector

has $n^1 = n$ components and is considered a $1st$ order tensor while a second order tensor has n^2 components. The rank of a tensor is determined by the sum of the upper and lower indices. The metric tensor's rank is 2.

2.2.1.2 Tensor Transformation and Differentiation

If we want to transform a tensor from an initial coordinate system $\{x^\alpha\}$ to another one $\{x'^\alpha\}$ we must follow the rules of coordinate transformation whicht for an (m, k) tensor $T'^{cd\dots}_{ab\dots}$ in an n-dimensional space are

$$T'^{cd\dots}_{ab\dots} = \left(\frac{\partial x^e}{\partial x'^a}\right)\left(\frac{\partial x^f}{\partial x'^b}\right)\dots\left(\frac{\partial x'^c}{\partial x^p}\right)\left(\frac{\partial x'^d}{\partial x^s}\right)\dots T^{ps\dots}_{ef\dots}. \tag{2.41}$$

where $a, b, c, d, e, f, p, s \ldots = 1, 2, \ldots, n$. The main properties of tensors that result from the above transformation law are

- If a tensor is zero in one coordinate system, then it is zero in all coordinate systems.
- If two tensors are equal in a coordinate system, they are equal in all systems
- The form of a tensor equation does not change between coordinate systems.

The last one is a key property in the general theory of relativity.

An important characteristic of tensor objects is that the results of differentiation must also be a tensor. In the case of scalar object f the derivative as we know it satisfies Equation (2.41), so

$$\partial'_a f = \frac{\partial f}{\partial x'^a} = \frac{\partial f}{\partial x^b}\frac{\partial x^b}{\partial x' a} = \frac{\partial x^b}{\partial x'^a}\,\partial_b f. \tag{2.42}$$

It becomes clear that the derivative of a scalar object is a $1st$ order tensor (vector). Problems arise when we try to differentiate vectors and higher order tensors. In this case the transformation does not work (in general) which means that we need to find another way to express the derivatives of tensors. We define the *covariant derivative* of a covariant vector v_a as

$$\nabla_b v_a = \partial_b v_a - \Gamma^a_{bc} v_c, \tag{2.43}$$

where Γ^a_{bc} is the *affine connection*, a *non-tensor* quantity. As a result, the covariant derivative of a vector is a $2nd$ order tensor. In Riemann spaces the affine connection can be written as a function of the metric tensor of the space and its components, called *Christoffel symbols*

$$\Gamma^a_{bc} = \frac{1}{2} g^{ad}\left(\partial_c g_{db} + \partial_b g_{dc} - \partial_d g_{bc}\right), \tag{2.44}$$

and because of the symmetry of the metric tensor they satisfy $\Gamma^a_{bc} = \Gamma^a_{cb}$. The covariant derivative can help us define the concept of parallel transport of a vector along a curve. If $t^a = dx^a/d\lambda$ is the tangent along a curve C with λ its affine parameter, the vector v^a is said to be parallel transported if

$$t^a \nabla^a v^b = 0. \tag{2.45}$$

2.2.1.3 Geodesic Equation

Using Equation (2.43) we get

$$\frac{dv^a}{d\lambda} + t^b \Gamma^a_{bc} v^c = 0 \tag{2.46}$$

A *geodesic curve* is the straightest possible line one can follow in a curved geometry. So the geodesic curve will have a tangent vector which is parallel propagated along itself. In other words

$$t^a \nabla_a t^b = 0. \tag{2.47}$$

From Equation (2.46) and the definition $t^a = dx^a / d\lambda$ we get

$$\frac{d^2 x^a}{d\lambda^2} + \gamma^a_{bc} \frac{dx^b}{d\lambda} \frac{dx^c}{d\lambda} = 0 \tag{2.48}$$

which is the equation of geodesic curve. Among all the curves we can draw between two points in a Riemann space, the geodesic curve will always follow the shortest path. The geodesic curves are very important in general relativity because in gravitationally curved spacetime, they define the paths objects follow. From physical mechanisms like gravitational lensing we know that the light does not always follow what we perceive as the path of a straight line, but its route can be curved by gravitationally strong objects. This path, however, is always described by the geodesic equation (if there are no other forces affecting it), which in the general case is not a straight line.

2.2.1.4 Riemann Tensor

The introduction of Christoffel symbols leads to the definition of the *curvature tensor* or *Riemann tensor*

$$R^a_{bcd} = -\partial_d \Gamma^a_{bc} + \partial_c \Gamma^a_{bd} - -\Gamma^e_{bc} \Gamma^a_{ed} + \Gamma^e_{bd} \Gamma^a ec. \tag{2.49}$$

Using the metric tensor we can write Riemann tensor in its full covariant form

$$R_{abcd} = g_{ae} R^e_{bcd}. \tag{2.50}$$

In any Riemann space, in a local geodesic frame where $\Gamma^a_{bc} = 0$, because of the above relation the Riemann tensor can be written as

$$R_{abcd} = \frac{1}{2} \left(\partial_b \partial_c g_{ad} + \partial_a \partial_d g_{bc} - \partial_b \partial_d g_{ac} - \partial_a \partial_c g_{bd} \right). \tag{2.51}$$

with the symmetry properties

$$R_{abcd} = R_{cdab}, \quad R_{abcd} = -R_{bacd} = -R_{abdc}, \quad \text{and} \quad R_{a[bcd]} = 0. \tag{2.52}$$

Furthermore, the Riemann tensor satisfies two important identities.

$$2\nabla_{[a} \nabla_{b]} v_c = R_{abcd} v^d \tag{2.53}$$

are the *Ricci identities* that define the curvature of the spacetime and its connection with the gravitational field, and

$$\nabla_e R_{abcd} + \nabla_d R_{abec} + \nabla_c R_{abde} = 0 \tag{2.54}$$

is the *Biachi identity*.
By contracting the Riemann tensor we get the *Ricci tensor*

$$R^a_b = R^c_{acb} = g^{cd} R_{dacb}. \tag{2.55}$$

By contracting the Ricci tensor we end up with the *Ricci scalar object* which expresses the "average" curvature of the spacetime.

2.2.1.5 Connecting to General Relativity

All that we mentioned until now is nothing but a small drop in the sea of differential geometry and curved spaces. These ideas predated Einstein's work as mathematical theories. In 1916 Einstein published the general form of the field equations (Einstein, 1916). His main idea was that the curvature of the spacetime is directly connected with the energy-momentum that is contained in the spacetime itself. For the simple case of an ideal fluid the energy-momentum tensor can be written as

$$T_{ab} = (\rho + u + P) u_a u_b + P g_{ab}. \tag{2.56}$$

where here ρ expresses the total mass density, u is the internal energy, P is the pressure of the fluid and $u^a = dx^a/ds$ is the 4-velocity. All he needed then was a quantity to express the curvature of the spacetime. He knew that since T_{ab} is a $2nd$ order symmetric tensor, the curvature needed something similar. It turns out that the ideal candidate for that is a combination of the Ricci tensor and the scalar Ricci quantity

$$G_{ab} = R_{ab} + \frac{1}{2} R g_{ab}. \tag{2.57}$$

what we call today the *Einstein tensor*. With that the Einstein field equations can be written as

$$G_{ab} = R_{ab} + \frac{1}{2} R g_{ab} = \frac{8\pi G}{c^4} T_{ab} \tag{2.58}$$

Because of Equation (2.54)

$$\nabla^b G_{ab} = 0. \tag{2.59}$$

The Einstein tensor is used in the field equation of General Relativity and it expresses the curvature of the spacetime which is attributed to the existence of matter/energy in the area. Furthermore, Equation (2.59) ends up as an expression of the conservation of energy and momentum.

One of the applications of General Relativity is in Cosmology. The Einstein equations can be used to created models concerning the universe itself. In the early days of General Relativity, the notion that the universe is static was well established in the cosmological

scientific community. Einstein (1917) in his calculations used a extra term in the Einstein tensor in order to balance the effects of gravity and achieve the expected static universe.

$$G_{ab} = R_{ab} + \frac{1}{2}Rg_{ab} + \Lambda g_{ab} = \frac{8\pi G}{c^4}T_{ab} \tag{2.60}$$

After Hubble's discovery (Hubble, 1929) of the expanded universe, he abandoned that idea and the *cosmological constant* Λ was taken as zero for the next decades. In 1998 however, Perlmutter et al. (1999) and Riess et al. (1998) discovered that the universe's expansion is accelerating and the cosmological constant was one of the modifications used to "fix" the theoretical models to match the observations.

2.2.2 The Black Hole

Here we will show some of the basic characteristics of the black hole. For more information we refer the reader to the works of Misner, Thorne, and Wheeler (1973), Frolov and Novikov (1998), Raine and Thomas (2005), and Romero and Vila (2014).

2.2.2.1 The Schwarzschild Solution

The first solution of Einstein's equations came from Karl Schwarzschild in 1916. He solved the equations and provided the form of the metric tensor describing the geometry of the spacetime outside a point mass object (Schwarzschild, 1916). The line element for the Schwarzschild space time is

$$ds^2 = \left(1 - \frac{2GM}{rc^2}\right)c^2dt^2 - \left(1 - \frac{2GM}{rc^2}\right)^{-1}dr^2 - r^2\left(d\theta^2 + \sin^2\theta d\phi^2\right) \tag{2.61}$$

where, M is the mass of the central object, G is the gravitational constant and (t, r, θ, ϕ) are the in Boyer-Lindquist spherical coordinates.

[From now on we will adopt the geometric unit system of general relativity where the speed of light in vacuum c and the gravitational constant G are set equal to unity, $c = G = 1$. Furthermore, a different length is defined that is equal to $R_{\rm g} = GM/c^2$ and corresponds to a time unit of $t_{\rm g} = GM/c^3$. In this system the Schwarzschild metric is written as]

$$ds^2 = \left(1 - \frac{2}{r}\right)c^2dt^2 - \left(1 - \frac{2}{r}\right)^{-1}dr^2 - r^2\left(d\theta^2 + \sin^2\theta d\phi^2\right) \tag{2.62}$$

This solution describes the spacetime *outside* a spherically symmetric massive object.

In the case of the point mass object the metric shows two singularities, one at $r = 0$ and one at $r = \frac{2GM}{c^2} = 2R_{\rm g}$. However, only the first one is has a physical meaning. The second one defines the *Schwarzschild radius*, which will reside in the interior of any "normal" astrophysical object. It appears as a singularity in the metric because of the Boyer-Lindquist coordinate system. With proper transformations we can have coordinate systems where the Schwarzschild radius is not a singularity. As an example, the Schwarzschild radius for the Sun is at approximately $3\,km$ and for the Earth is at $9\,mm$. In these cases, since the Schwarzschild

metric describes the spacetime outside the object, the singularity at the Schwarzschild radius does not create any problems in the calculations.

There is however an astrophysical object where the Schwarzschild radius is outside the surface. The *black hole* is an area of spacetime where the gravitational field is so strong that nothing can escape it. For a non-rotating black hole the Schwarzschild metric is used to describe the surrounding spacetime. The boundary of the black hole is the Schwarzschild radius and it is called the *event horizon.* The *photon radius* is the surface where the light starts traveling in circles around the black hole. The *innermost stable circular orbit (ISCO)* is the closest radius outside a black hole where a particle can have a stable orbit.

Outside of the ISCO particles will follow different orbits depending on their initial conditions. The equations of motion can be derived from the conservation of energy and angular momentum and they result in motions in a constant plane. For the Schwarzschild black hole we can write the equation of motion for such particles as an equation for an 1-dimensional motion of particles in an effective potential V_{eff}. The equation of motion is

$$E^2c^2 = \left(\frac{dr}{d\tau}\right)^2 + V_{\text{eff}}^2 \tag{2.63}$$

where E is the energy of the particle, τ is the proper time and

$$V_{\text{eff}} = \sqrt{(1+L^2)\left(1-\frac{2r}{r}\right)} \tag{2.64}$$

with L being the angular momentum of the particle in units of mc and $r_{\text{g}} = GM/c^2$ being the gravitational radius. By taking the extrema of the effective potential we get

$$r = \frac{L^2}{2} \pm \frac{1}{2}L\sqrt{L^2-12} \tag{2.65}$$

The energy of the particle defines whether the orbit will be bound ($E < 0$) or unbound ($E > 0$). For $L^2 < 12R_{\text{g}}$ there are no extrema in the effective potential, which means that the particles with negative energy end up in the black hole while particles with positive energy can escape to infinity (Figure 2.3, top panel, red line).

For $L^2 > 12R_{\text{g}}$ the effective potential has two extrema– V_{eff}^+ (minimum corresponding to r_+) and V_{eff}^- (maximum corresponding to r_-)–that, depending on the particle's energy, define regions with different orbits for the particles (Figure 2.3, top panel, brown, cyan and magenta lines).

- $E > V_{\text{eff}}^-$. The particle does not have enough angular momentum to stay in a closed orbit and it will inevitably fall inside the black hole
- $V_{\text{eff}}^- > E > 0$. The particle's angular momentum is low enough to be trapped by the gravitational potential but its energy is positive and it gets scattered away by the black hole.
- $V_{\text{eff}}^+ < E < 0$. The particle is trapped in open elliptical orbits between two radii. In Newtonian gravity this would be a closed elliptical orbit.
- $E = V_{\text{eff}}^+$ or $E = V_{\text{eff}}^-$. The particle is in circular orbit around the black hole. The $E = V_{\text{eff}}^+$ orbits is stable while the $E = V_{\text{eff}}^-$ is unstable.

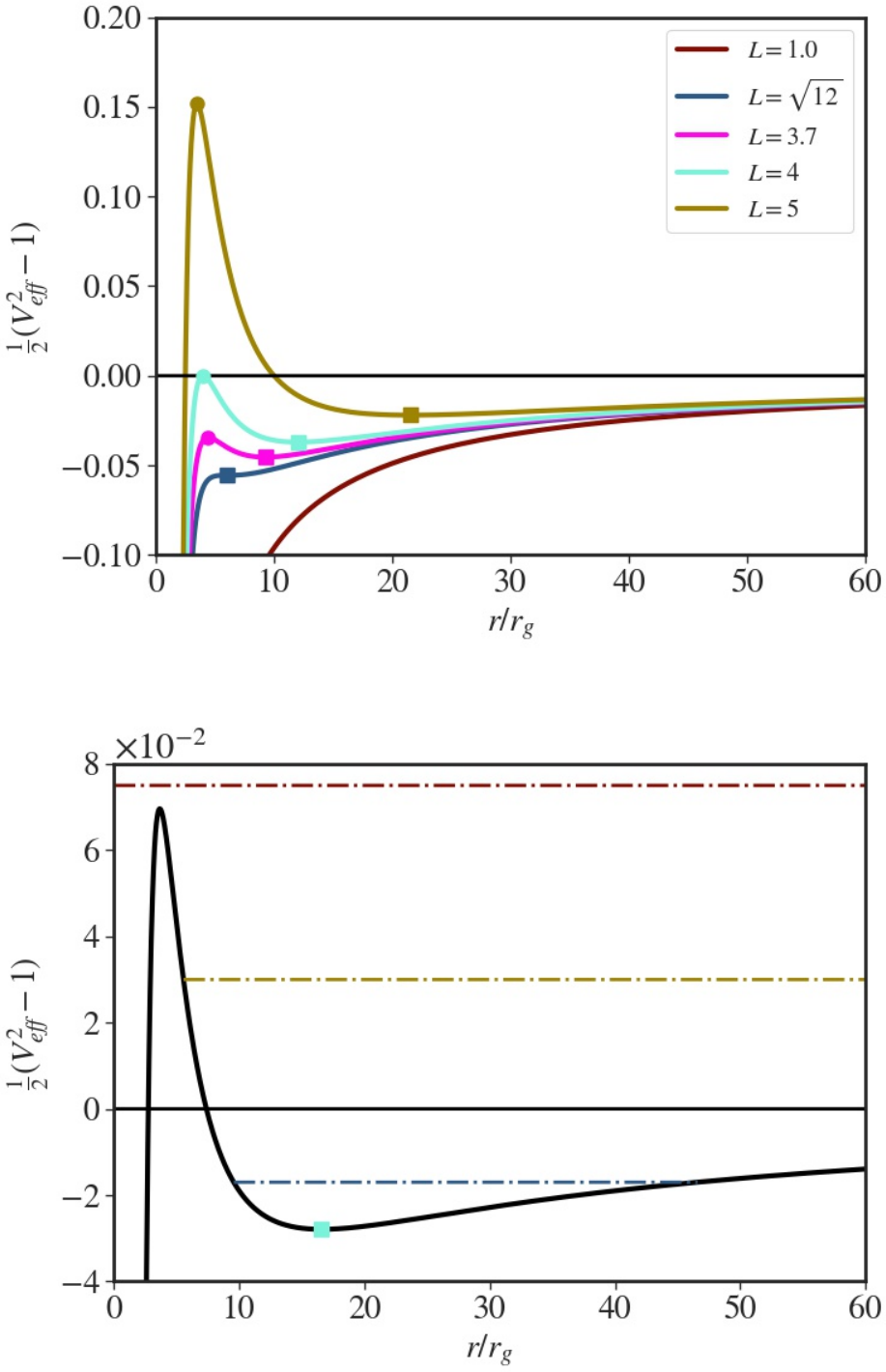

FIGURE 2.3: Effective potential of the particle motion around a Schwarzschild black hole. In the top panel we show the effective potential for different values of the particle's specific angular momentum. The circles show the position of the unstable circular orbit $(r_-,\ V_{\rm eff}^-)$ and the squares show the position of the stable one $(r_+,\ V_{\rm eff}^+)$. For the case of $L=\sqrt{12}$ the two coincide in the ISCO. In the bottom panel we show an example of the possible orbits of particles with different energy but the same specific angular momentum $L=4.5$. From top to bottom the dotted lines show the cases of $E>V_{\rm eff}^-$, $V_{\rm eff}^->E>0$, $V_{\rm eff}^+<E<0$ and $E=V_{\rm eff}^+$ respectively.

These cases can be seen in the bottom panel of Figure 2.3.

For $L^2 = 12R_g$ the effective potential has no local extrema and the equation gives one double root which corresponds to the ISCO $r_{ISCO} = 6r_g$ (Figure 2.3, top panel, blue line).

Repeating the same calculation for the photons we get an effective potential

$$V_{ph} = \frac{L_{ph}^2}{r^2}\left(1 - \frac{2}{r}\right) \tag{2.66}$$

and the equation of motion is given from (2.63). By taking the radial derivative of the photon effective potential we get that

$$\frac{dV_{ph}}{dr} = 0 \rightarrow r = 3R_g \tag{2.67}$$

which coincides with the photon sphere radius we mentioned before. Because $\left.\frac{d^2V_{ph}}{dr^2}\right|_{r=3R_g} < 0$ the circular photon orbits are unstable. The photon effective potential has its maximum value at the photon radius $V_{ph}^{max} = L^2/27R_g$. If the energy of the photon is greater than the V_{ph}^{max} then the photon will be captured by the black hole. If $E_{ph} < V_{ph}^{max}$ we can have photons that are scattered by the black hole, changing their straight path.

2.2.2.2 The Kerr Spacetime

Schwarzschild's solution describes perfectly the spacetime outside a static spherical object. The natural next step is to find a description for a rotating object. In the end, this was much harder than it initially seemed. It took 47 years for such a solution to appear and it was Roy Kerr in 1963 who announced it in the First Texas Symposium on Relativistic Astrophysics (Kerr, 1963). Outside of the small community of theoretical astrophysicists and mathematicians who were working for years on such a solution, the announcement was met with little interest. It took about a decade for the people to realize that Kerr's solution was integral to the explanation of "hot" astronomical topics such as the recently discovered quasars.

The Kerr line element is slightly more complicated than the Schwarzschild one and describes the spacetime around a rotating massive object. In Boyer-Lindquist coordinates it can be written as

$$ds^2 = g_{tt}dt^2 + 2g_{t\phi}dtd\phi - g_{\phi\phi}d\phi^2 - \frac{\Sigma}{\Delta}dr^2 - \Sigma d\theta^2 \tag{2.68a}$$

$$g_{tt} = c^2 - \frac{2GMr}{\Sigma} \tag{2.68b}$$

$$g_{t\phi} = \frac{2GMar\sin^2\theta}{c^2\Sigma} \tag{2.68c}$$

$$g_{\phi\phi} = \frac{\left(r^2 + a^2/c^2\right)^2 - \Delta a^2\sin^2\theta/c^2}{\Sigma}\sin^2\theta \tag{2.68d}$$

$$\Sigma = r^2 + a^2\cos^2\theta/c^2 \tag{2.68e}$$

$$\Delta = r^2 - 2GMr/c^2 + a^2/c^2, \tag{2.68f}$$

where $a = J/M$ is the *Kerr spin parameter* connected with the angular momentum of the star J. This metric reduces to the Schwarzschild one for the case of $a = 0$. The Kerr solution is also the unique stationary axisymmetric vacuum solution on par with the Schwarzschild solution.

The event horizon, the point of no return for the black holes, in the case of rotating black hole is determined by $g_{rr} \to \infty$

$$r_{\mathrm{h}} = 1 \pm \sqrt{1^2 - a^2}. \tag{2.69}$$

It becomes clear that the rotating black hole has two surfaces that carry the properties of the event horizon. The outer horizon r_h^+ reduces to the Schwarzschild horizon for $a = 0$ and is well defined only for $a <= 1$. In the case of $a = 1$ we have a maximally rotating black hole. For $a > 1$ neither of the horizons is defined resulting in a naked singularity in the spacetime. Such a solution is at the moment considered to be unphysical (Cosmic Censorship Principle). The inner horizon r_h^- defines a surface which hides the central singularity even from observers that have crossed the outer horizon.

A particle falling radially towards a rotating black hole has zero angular momentum. However, the particle does have an angular motion as well with angular velocity

$$\Omega = \frac{d\phi}{dt} = \frac{\left(2GM/c^2\right) ar}{\left(r^2 + a^2/c^2\right)^2 - a^2/c^2 \Delta \sin^2\theta}, \tag{2.70}$$

in the direction of the rotation of the black hole with the particle's angular momentum remaining zero, since it is conserved. This oxymoron is based on the fact the the $g^{t\phi}$ component of the metric is non-zero in the Kerr solution. We know that $u^\phi = g^{a\phi}u_a = g^{t\phi}u_t + g^{r\phi}u_r + g^{\theta\phi}u_\theta + g^{\phi\phi}u_\phi$. In Schwarzschild black hole all components except $g^{\phi\phi}$ are zero and if initially $u_\phi = 0$ then $u^\phi = 0$ as well. In the Kerr black hole $g^{t\phi}$ is also non-zero resulting in the azimuthal dragging of not only the particle, but of the local inertial frames of reference themselves. At the same time the angular momentum $L_z = u_\phi$ which is zero initially and remains so because of the conservation of angular momentum.

Another consequence of the inertial frame dragging is the need to define a new type of observer who will follow the frame dragging by rotating with an angular velocity Ω while at the same time they retain a zero angular momentum. The *zero angular momentum observers (ZAMOs)* hold their radial and polar coordinates constant and their velocity is

$$(u^a)_{\mathrm{ZAMO}} = \left(\frac{-g_{\phi\phi}}{\Delta \sin^2\theta}\right)^{1/2} (1, 0, 0, \Omega) \tag{2.71}$$

The strength of the frame dragging becomes stronger the closer a particle approaches to the rotating black hole. There is a surface close to the black hole beyond which it becomes impossible to resist the dragging force and any massive particle (not photon) will have to rotate. This surface is the *static limit* of the black hole and is defined by $g_{tt} = 0$. The radius of the static limit is

$$r_{\mathrm{st}} = \frac{GM}{c^2} \pm \left[\left(\frac{GM}{c^2}\right)^2 - \frac{a^2}{c^2}\cos^2\theta\right]^{1/2}. \tag{2.72}$$

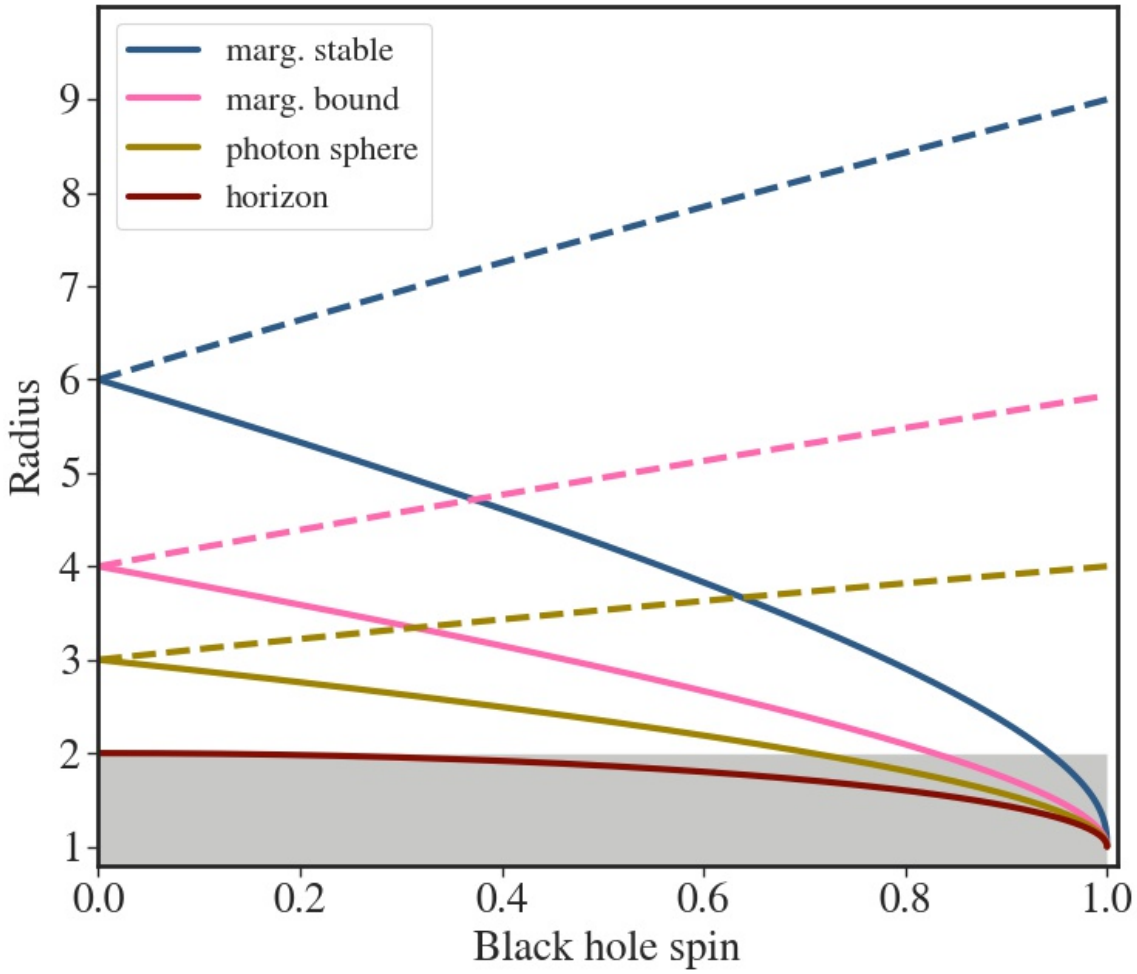

FIGURE 2.4: The radius of the innermost marginally stable orbit, marginally bound orbit, photon sphere and outer horizon as functions of the Kerr parameter a. The solid lines show the orbits for a prograde system of black hole-particle ($a > 0$), while the dashed lines for a retrograde system ($a < 0$). The shaded area marks the radius of the ergosphere in the equatorial plane.

This means there are two static limits, with the outer/positive one being outside the horizon with the exception of the poles where the two surfaces meet, since the static limit surface depends also on the polar angle. In the Schwarzschild case the static limit surface and the event horizon coincide completely.

The radiation emitted by a body at rest close to the black hole will be gravitationally redshifted according to

$$1 + z = \frac{\lambda_\infty}{\lambda_r} \tag{2.73}$$

where z is the gravitational redshift and λ_r and λ_∞ are the wavelengths of the radiation as emitted by the body and as measured by an observer at infinity. Since the metric relates the time of the observer at infinity t with the local time of the body τ, the ratio of wavelengths is proportional to the ratio of the period of the wave and as a result to the time intervals of the two frames. The surface where the wavelength of the radiation is redshifted to infinity is

$$1 + z = \frac{\lambda_\infty}{\lambda_r} = \frac{dt}{d\tau} = \sqrt{g_{tt}}. \tag{2.74}$$

this means that the static limit works also as the *infinite redshift surface*.

The equations of motion for a particle show some special cases of circular orbits in the equatorial plane of a rotating black hole. The first one is the *innermost (marginally) stable orbit* $r_{\rm ms}$ which in the case of Schwarzschild black hole reduces to the ISCO. Bardeen, Press, and Teukolsky (1972) showed that the $r_{\rm ms}$ is given by

$$r^{\pm}_{\rm ms} = \frac{GM}{c^2}\left[3 + Z_2 \mp \sqrt{(3 - Z_1)\,(3 + Z_1 + 2Z_2)}\right], \tag{2.75a}$$

$$\text{with} \qquad Z_1 = 1 + \sqrt[3]{1 - a^2}\left(\sqrt[3]{1 + a} + \sqrt[3]{1 - a}\right), \tag{2.75b}$$

$$Z_2 = \sqrt{3a^2 + Z_1^2}, \tag{2.75c}$$

where again we have two orbits satisfying the equations, with the outer orbit $r^+_{\rm ms}$ using the $(-)$ symbol and expressing the co-rotating particle. With the $(+)$ sign we have the $r^-_{\rm ms}$ for the counter-rotating particle. In this orbit the orbital period of the particle is

$$T = 2\pi\left(\frac{r^{3/2}}{m^{1/2}} \pm a\right). \tag{2.76}$$

As an example, in the case of the supermassive black hole in the centre of the M87 galaxy with mass $6.5 \times 10^9 M_\odot$ and an assumed Kerr parameter of $a = 0.5$ the period of a particle in the $r_{\rm ms} = 4.233$ is approximately 21.5 days.

The marginally parabolic orbit in which a particle coming from infinity goes around the black hole and then it is scattered away is called the *marginally bound orbit*. The orbit is given by

$$r^{\pm}_{\rm mb} = 2 \mp a + 2\sqrt{1 \mp a}. \tag{2.77}$$

For a Schwarzschild black hole the marginally bound orbit is at $r_{\rm mb} = 4$.

Finally, the photon sphere radius is a Kerr spacetime is defined as

$$r_{\rm ph}^{\pm} = 2\left[1 + \cos\left(\frac{2}{3}\arccos\left(\mp a\right)\right)\right], \tag{2.78}$$

and for the Schwarzschild case it yields $r_{\rm ph} = 3$. In Figure 2.4 we plot the radius of these orbits as a function of the Kerr parameter for prograde and retrograde systems.

2.3 General Relativistic Mangetohydrodynamics

For the following, we adopt the signature of Misner, Thorne, and Wheeler (1973) for the metric $(-,+,+,+)$ and use geometrized units where $G = c = 1$. Greek letters run for 0,1,2,3 $(t, r, \theta, \phi$)while Latin letters run for 1,2,3 (r, θ, ϕ). Radii are expressed in units of the gravitational radius, $R_{\rm g} = GM/c^2$, while time is in units of light-travel time $t_{\rm g} = GM/c^3$. Vector quantities are denoted with bold letters, while the vector and tensor components are indicated with their respective indices.

We use the "3+1" decomposition of the GRMHD equations, where the time component is separated from the spatial components which are expressed as 3-dimensional manifolds. A detailed analysis of the 3+1 decomposition and the derivation of the GR-(M)HD equations can be found in many published works including Misner, Thorne, and Wheeler (1973), Anile (1989), Baumgarte and Shapiro (2003), Font (2008), Gourgoulhon (2012), and Rezzolla and Zanotti (2013)

The space-time is described by the metric $g_{\mu\nu}$ in Kerr-Schilds coordinates with $g \equiv det(g_{\mu\nu})$. A zero angular momentum observer frame (ZAMO) frame exists in the space-like manifolds moving only in time with velocity $n_\mu = (-\alpha, 0, 0, 0)$ where $\alpha = 1/\sqrt{-g^{tt}}$ is the lapse function. The gravitational shift is $\beta^i = \alpha^2 g^{ti}$.

In order to achieve the splitting of the spacetime all tensor and vector quantities must me projected into the spatial manifolds via the metric

$$\gamma_{\mu\nu} = g_{\mu\nu} + n_\mu n_\nu \tag{2.79}$$

In Equation (2.56) we introduced the stress-energy tensor in the case of an astrophysical fluid. If this fluid is magnetized then the stress-energy tensor obtain a second electromagnetic part. In total the tensor is written as

$$T^{\mu\nu} = T^{\mu\nu}_{fluid} + T^{\mu\nu}_{EM}, \tag{2.80}$$

with

$$T^{\mu\nu}_{EM} = F^{\mu\gamma}F^{\nu}_{\gamma} - \frac{1}{4}g^{\mu\nu}F^{\gamma\delta}F_{\gamma\delta}, \tag{2.81}$$

being the electromagnetic part while the fluid part is given by Equation (2.56). F^{ab} is the anti-symmetric Faraday tensor associated with the electromagnetic field and ${}^*F^{ab}$ its dual

(Maxwell tensor). The Maxwell equations shown in (2.1) are simplified in covariant form as

$$\nabla^*_\nu F^{\mu\nu} = 0, \tag{2.82a}$$
$$\nabla_\nu F^{\mu\nu} = I^\mu, \tag{2.82b}$$

where $I^a = (qu^\mu, \mathbf{J})$ is the electric 4-current. Choosing a reference frame that is co-moving the fluid we can write the Faraday and Maxwell tensors as

$$F^{\mu\nu} = \quad u^\mu e^\nu - e^\mu u^\nu + \epsilon^{\mu\nu\alpha\beta} u_\alpha b_\beta, \tag{2.83a}$$
$${}^*F^{\mu\nu} = -u^\mu b^\nu + b^\mu u^\nu + \epsilon^{\mu\nu\alpha\beta} u_\alpha e_\beta, \tag{2.83b}$$

where the electric and magnetic field in the comoving system are measured as

$$e^\mu = F^{\mu\nu} u_\nu, \tag{2.84a}$$
$$b^\mu = {}^* F^{\mu\nu} u_\nu \tag{2.84b}$$

and the anti-symmetric Levi-Civita symbol is used

$$\epsilon_{\alpha\beta\gamma\delta} = \sqrt{-g}[\alpha\beta\gamma\delta], \tag{2.85a}$$
$$\epsilon^{\alpha\beta\gamma\delta} = -\frac{1}{\sqrt{-g}}[\alpha\beta\gamma\delta]. \tag{2.85b}$$

The magnetic and electric field as measured by the normal observer are defined as

$$\mathscr{B}^i = n^*_\mu F^{\mu\nu} = \alpha^* F^{it}, \tag{2.86a}$$
$$\mathscr{E}^i = n_\nu F^{\mu\nu} = -\alpha F^{it}. \tag{2.86b}$$

Then the electromagnetic part of the energy-momentum tensor becomes

$$T^{\mu\nu}_{EM} = (b^2 + e^2)\left(u^\mu u^\nu + \frac{g^{\mu\nu}}{2}\right) - b^\mu b^\nu - e^\mu e^\nu - u_\alpha e_\beta b_\gamma \left(u^\mu \epsilon^{\nu\alpha\beta\gamma} + u^\nu \epsilon^{\mu\alpha\beta\gamma}\right), \tag{2.87}$$

and if we combine both components we get the total energy-momentum tensor

$$\begin{aligned} T^{\mu\nu} = & \quad \left(\rho + u + p + b^2 + e^2\right) u^\mu u^\nu \\ & + \left(p + \frac{1}{2}(b^2 + e^2)\right) g^{\mu\nu} \\ & - b^\mu b^\nu - e^\mu e^\nu - u_\alpha e_\beta b_\gamma \left(u^\mu \epsilon^{\nu\alpha\beta\gamma} + u^\nu \epsilon^{\mu\alpha\beta\gamma}\right). \end{aligned} \tag{2.88}$$

In the case of ideal MHD the electric field vanishes from the equation because we can always compute it through Ohm's law as it is written in Equation (2.16). In the more general case of non-ideal MHD Ohm's law is given by Equation (2.3). Here we also show its form in

the case of a resistive environment and a mean-field dynamo (see Section 2.1.3). Blackman and Field (2002) connected magnetic helicity and turbulent electromotive force with the dynamo and the amplification of the magnetic field, while Kulsrud (2005) provides a deeper analysis in the turbulent nature of diffusivity and dynamo.

In our case, we adopt the formulation of Bucciantini and Del Zanna (2013) where the α-dynamo term is replace by $\xi = -\alpha$ in order to avoid confusion with the gravitational lapse. Thus, in covariant form in the fluid frame Ohm's law is written as

$$e^{\mu} = \eta j^{\mu} - \xi b^{\mu}, \tag{2.89}$$

where j^{μ} is the electric current density components. In the new generalized environment, the electric field can no longer be calculated by the cross product of fluid velocity and magnetic field and new equations need to be formulated. By setting $\xi = 0$ we get the resistive version of Ohm's law and also by setting $\eta = 0$ we get back into the ideal case $e^{\mu} = 0$. For more details on Ohm's law and its solution see Chapter 3.1 and Appendix A

Along with Maxwell's equations and Ohm's law for the electric and magnetic field we have the hydrodynamic equations. The conservation of particle numbers is

$$\nabla_{\mu}(\rho_0 u^{\mu}) = 0, \tag{2.90}$$

where ρ_0 is the rest mass density and the conservation of energy

$$\nabla_{\mu} T^{\mu}_{\nu} = 0, \tag{2.91}$$

Adopting the equation of state from (2.9) we have a system of equation that describe the motion of a magnetized fluid in a general-relativistic environment.

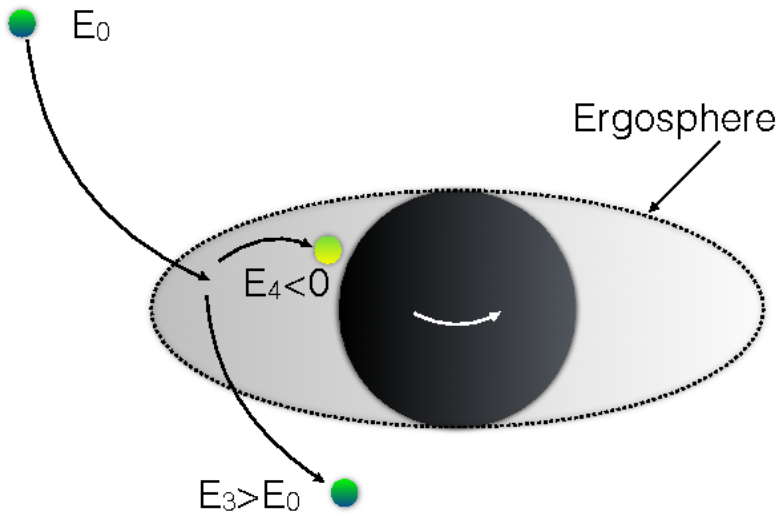

FIGURE 2.5: Schematic depiction of the original Penrose process. The particle falls into the ergosphere and then decays into two particles, one with negative that collapses in the black hole and one with positive energy that escapes outside the ergosphere.
Image credit: Leiderschneider and Piran (2016)

2.4 Jet Launching Mechanisms

In this section we will briefly discuss some of the most common theoretical ideas that have been proposed in the part years as possible jet launching mechanisms.

2.4.1 The Ergosphere and the Blandford-Znajek Mechanism

Inside the region defined by the static limit (Equation (2.72)) and the outer event horizon it is possible for a particle to have negative energy relative to an observer at infinity. This region is called the *ergosphere* and apart from the inescapable rotation from the frame dragging, Penrose (1969) and Penrose (2002) suggested that it can be used in order to extract energy from the black hole. Piran, Shaham, and Katz (1975), Schnittman (2014), and Berti, Brito, and Cardoso (2015) also suggested similar methods of energy extraction based on Penrose's original idea.

For this process, a particle needs to be in a retrograde orbit despite the inescapable frame dragging of the rotating black hole. Assume that for some reason this particle decays into two different particles, one with negative energy and angular momentum that orbits in a retrograde manner and that subsequently falls in the black hole and a second particle with positive energy and angular momentum that manages to escape outside the static limit surface. Since the capture particle had negative energy and angular momentum, it will reduce the energy of the black hole while the surviving particle will exit with more energy

that the initial particle had. As seen by an observer at infinity, this process extracts energy and angular momentum from the black hole. With this mechanism, the black hole can be (hypothetically) used as an energy reservoir.

Besides the obvious mechanical difficulties of applying such an idea in actual black holes, there are also physical ones. To create the Penrose process the decaying particles must split into two fragments, one of which must be rotating counter to the black hole and thus having negative energy. If we do the necessary calculations, we get that a particle right in the marginally stable orbit of an extreme Kerr black hole with $a = 1$ requires a velocity jump of $c/2$ just to reduce its energy to zero. To go to actual negative energy trajectories the required velocity jump must be even larger, thus rendering this process implausible within any astrophysical context.

There is however, a similar mechanism that results in energy extraction from the black hole but it involves the existence of magnetic fields that threads the ergosphere. In this case, rotational energy can be transferred to the magnetic field and then escape in the form of Poynting flux. Blandford and Znajek (1977) created a theory that described a force-free, axisymmetric magnetosphere in equilibrium around a rotating black hole. The magnetic field is created by currents the flow along the rotation of the accretion disk. Solving the Maxwell equations in a relativistic environment (see Chapter 2.3), ignoring the inertia of the fluid, they found that the toroidal vector potential A_ϕ is a possible choice. For that, they used a boundary condition in the event horizon for which the electromagnetic field remains finite as seen by an observer crossing the horizon in free fall. They calculated the total radial energy flow as it is observed at infinity as

$$L \approx 10^{45}\mathrm{ergs}^{-1}\left(\frac{\mathrm{M}}{10^6\mathrm{M}_\odot}\right)^2\left(\frac{\mathrm{a}}{\mathrm{a}_{\max}}\right)^2\left(\frac{\mathrm{B}}{10^4\mathrm{G}}\right)^2. \tag{2.92}$$

This is in the order of magnitude of the energy emitted by AGN $\left(10^{42} - 10^{45}\right)$.

Thorne, Price, and MacDonald (1986) in their book *The Membrane Paradigm*, present the idea that the event horizon is replaced by a rotating conductor of finite resistivity and other well defined properties. Based on that, they were able to study the physics of black holes using just classical physics. Punsly and Coroniti 1990b; Punsly and Coroniti 1990a expressed a criticism over the BZ mechanism based on the idea of the Membrane Paradigm. According to their work, the solution derived describes two different flows, one outflow and one inflow towards the black hole. For the ingoing solution the wind passes through all the MHD characteristic surfaces before it reaches the event horizon which means that it is causally disconnected from the outflowing jet.

Komissarov (2001) and Komissarov (2004) studied the BZ mechanism using GRMHD in the force-free regime in order to study the validity of the BZ mechanism. For the case of an initial split-monopole magnetic field and low values of Kerr parameter, the system ends up in a stable state the resembles the one described in Blandford and Znajek (1977) which was derived as a perturbed solution on the Schwarzschild black hole. The simulations also show that the magnetic field lines that thread the ergosphere are being forced into rotating with the black hole because of frame dragging, while in the Membrane Paradigm, only the ones that cross the horizon are rotating. In this regard, the BZ mechanism is much closer to the Penrose process since they both make use of the ergosphere and its unavoidable frame dragging.

2.4.2 Can the Blandford-Znajek Mechanism Explain All Jets?

The "radio loud/radio quiet dichotomy" in AGN is one of the phenomena wherein the black hole spin plays a strong role. The ratio of the luminosity in the radio and the optical bands is $10^3 - 10^4$ times larger in the radio-loud source than in the radio-quiet ones when compared at constant optical luminosity (Sikora, Stawarz, and Lasota, 2007). A possible explanation for this would be that the jet is driven by some mechanism similar to the BZ mechanism, if we assume that the jets from the radio loud AGN host black holes with large Kerr parameter values. Unfortunately, the quadratic dependence of the BZ luminosity from the spin parameter (see Equation (2.92)) is not enough to explain the disparity in $L_{\rm radio}/L_{\rm opt}$. Hoever, the BZ mechanism is just a first order approximation. Tchekhovskoy, Narayan, and McKinney (2010) did a wide survey of simulation with different spin parameters and found that the dependence of the luminosity on black hole spin steepens as the Kerr parameter reaches its limit at $a = 1$. In more detail,

$$L \sim k\Phi_{\rm tot}^2 \left[\left(\frac{a}{2r_{\rm H}} \right)^2 + \alpha \left(\frac{a}{2r_{\rm H}} \right)^4 + \beta \left(\frac{a}{2r_{\rm H}} \right)^6 \right], \tag{2.93}$$

where $\Phi_{\rm tot}$ is the total poloidal magnetic flux in the jet, k is a constant that depends on the geometry of the magnetic field and $r_{\rm H}$ is the radius of the event horizon. With these additional terms, the variation of the Kerr parameter is enough to explain the difference in the luminosity of the radio loud and quiet AGN.

There is also a discussion on whether the configuration of the magnetosphere around the black hole can affect the energy output of the jet. In a closed magnetosphere, the field lines that thread the black hole bend towards the disk while in an open magnetosphere they connect at infinity. A closed magnetosphere can turn into an open one when there is enough shear developed in the rotating system of black hole and accretion disk. Naturally, the highest amount of shear is expected in the case fast spinning black hole in a retrograde system where the black hole and the accretion disk are rotating in opposite directions. This means that retrograde systems should be more likely to launch jets with the BZ mechanism (Garofalo, 2009; Garofalo, Evans, and Sambruna, 2010). This is based on the idea that the magnetic flux can be trapped by the black hole after it crosses its ISCO as it is advected from the accretion disk (Reynolds, Garofalo, and Begelman, 2006). The result is the formation of a "gap", which is more prominent in the retrograde system because their ISCO is in larger radius. Tchekhovskoy and McKinney (2012) simulated black hole-accretion disk systems with spin parameters of ± 0.9 and they found that the energy extracted from the prograde system is more efficient than that from the retrograde one. They also estimated that $\sim 80\%$ of the total energy outflow is coming from the BZ-powered jet and they found no evidence of the magnetic flux-free gap reported in previous works.

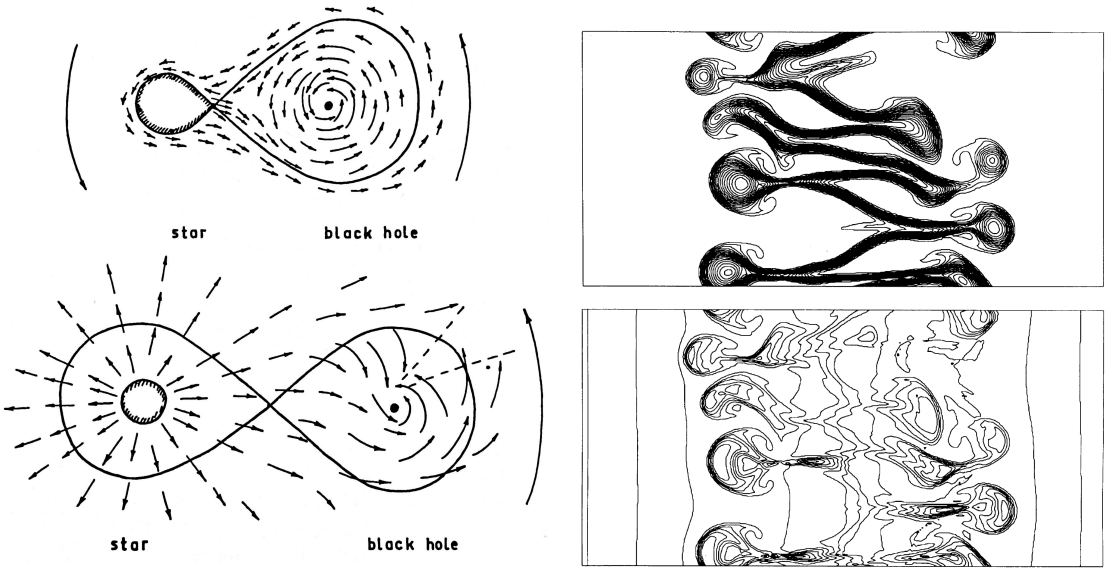

FIGURE 2.6: *left:* Two cases of accretion disk and the effect of magnetorotational instability. *left:* Accretion of gas towards a black hole from a companion star that fills exactly its Roche lobe resulting in accretion through the Lagrange point L1 (*upper*) and from a companion whose size is much smaller that its Roche lobe (*lower*). *right:* The effect of the MRI on the poloidal magnetic field lines (*upper*) and on the angular momentum.
Image credit: Shakura and Sunyaev (1973) and Hawley and Balbus (1991)

2.4.3 The Accretion Disk Model

In order to further investigate the launching of jets we need to address the accretion disk first. The idea of the formation of accretion disks started from the study of binary systems and the flow of gas from one star to the other. During the decades of 1960 and 1970 a model started forming that included the creation of an accretion disk with a collapsed star as central object (Gorbatskii, 1965; Prendergast and Burbidge, 1968; Pringle and Rees, 1972; Shakura, 1973).

In a binary system composed of a black hole and a companion star, if the companion starts ejecting material outwards, part of it will be captured in the strong gravitational field of the black hole. In the rare case where the material flows radially towards the black hole, it will end up crossing the horizon into the black hole without forming any other structures. In the most common case though that the material has some angular momentum, it will start losing it following a spiral trajectory around the black hole. If at some point the centrifugal force starts balancing the gravitational pull, the material will begin rotating in circular orbits forming an accretion disk around the black hole.

Because of the conservation of angular momentum the disk that is formed is dynamically stable, with the material staying in its circular orbits. Unless, there is a way to transfer angular momentum from the inner layers of the disk to the outer ones. In Shakura and Sunyaev (1973), the authors present a full theory for the structure of an accretion disk where the angular momentum transport depends on the values of an α parameter that characterizes the viscosity of the disk. They parameterized the molecular viscosity with α resulting in

$$\nu = \alpha H c_s, \tag{2.94}$$

where ν is the kinematic viscosity, H is the scale high of the disk and c_s is the sound speed. Even though the exact nature of the α parameter is even nowadays not completely understood, Shakura and Sunyaev (1973) realized that this was not necessary to describe the structure of the disk. However, they suggested that the stress between different layers of a magnetized disk along with the generated turbulence are enough to transfer angular momentum outwards.

In 1991, Balbus and Hawley (1991) published a well constructed theory regarding the existence of a shear instability in accretion disks which was already under investigation but was not yet established as an important process in astrophysics (Chandrasekhar, 1960; Acheson and Hide, 1973). The basic idea was that in a differential rotating accretion disk that is threaded by a magnetic field with a poloidal component, if a volume element is moving outwards the field is trying to enforce rigid rotation on it resulting in the element rotating faster than it would do in its new radial position. The faster rotation is accompanied by stronger centrifugal force that drives the element even more outwards further developing the instability.

The nature of the instability resulted in the name magnetorotational instability (MRI). A non-linear increase of the instability can result in the development of turbulent viscosity (Hawley and Balbus, 1991). The characteristic length of turbulent viscosity is the scale of the turbulent eddies which in general is larger than the particle mean free path which is the characteristic scale of molecular viscosity. This means that the turbulent viscosity resulting from the MRI is a much better candidate for the α viscosity of Shakura and Sunyaev (1973).

2.4.4 The Blandford-Payne Mechanism

In 1982, Blandford and Payne (1982) proposed an idea for the launching of outflows from the surface of accretion disks. In their seminal work, they theorized that a wind/jet can be launched from the surface of an rotating accretion disk that is threaded by a magnetic field with the help of the centrifugal force. Alfvén's theorem dictates that in the regime of ideal MHD the fluid elements and the magnetic field lines will be coupled, meaning that any motion of the fluid with drag along the magnetic field as well, and vice versa.

If we consider the case of a thin accretion disk rotating around a central massive object (not necessarily a black hole) that is threaded by a magnetic field with strong poloidal components, as the disk evolves, the magnetic field lines will start rotating rigidly with the disk. A mechanical analog of this is the rotation of an inclined wire loaded with beads. As the wire (or in our case the magnetic field line) rotates, the beads (or fluid elements) rotate along with it at the same angular velocity of the disk that depends on the distance from the central object and source of gravitational forces. The centrifugal force which appears will push the beads that have large distance from the central object (and as a result are less affected by gravity) along the wire accelerating them until they fly outwards.

We consider a point inside the disk with distance R_0 from the central object (at $(0, 0)$ in cylindrical coordinates (R, z)). We can express the above description mathematically by simply comparing the gravitational potential with a "potential" from the centrifugal force. This results in the total potential of a volume element at (R_0, z)

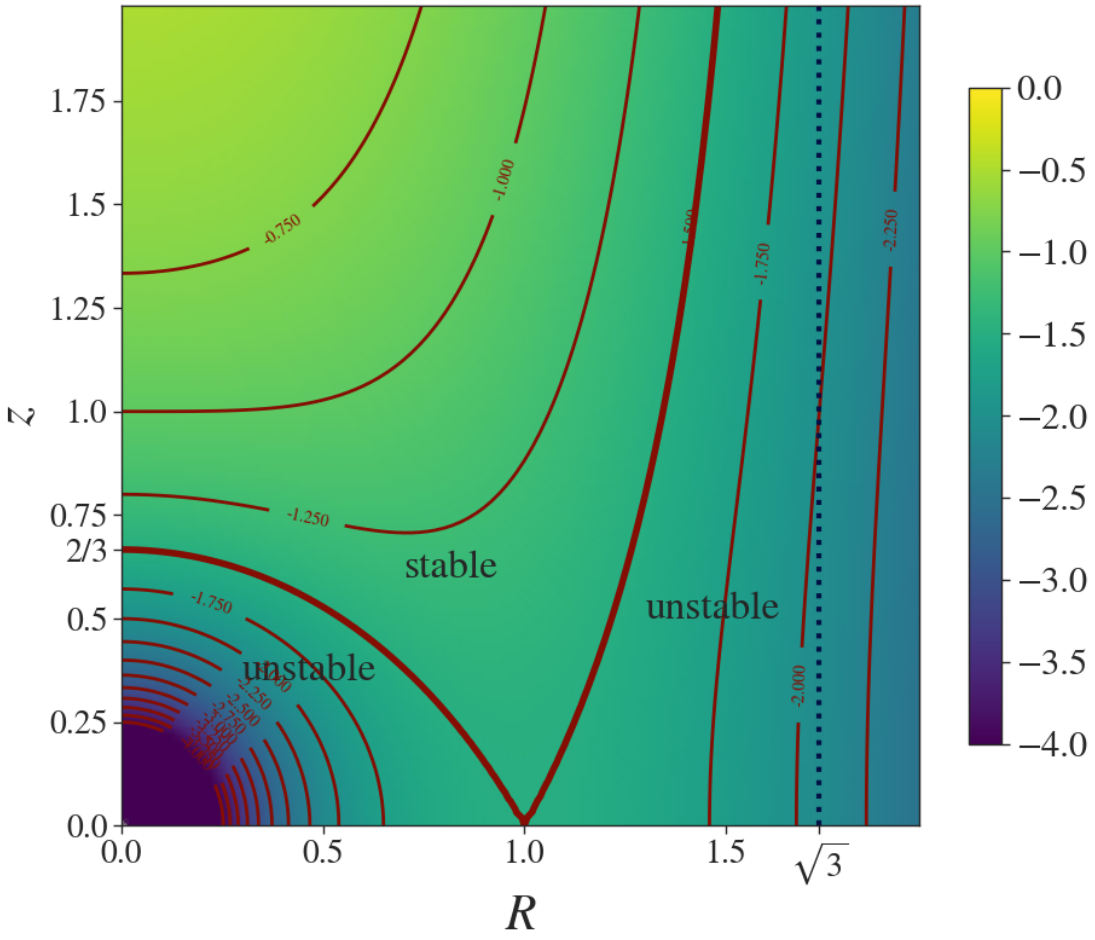

FIGURE 2.7: Isopotential surfaces of potential Φ for the detrimental case of $G = M = R_0 = 1$ for the "bead on a wire" model that is rotating with Keplerian angular velocity and is released from the $(R_0, z) = (1, 0)$ point (cylindrical coordinates). The thick solid line marks the marginally stable potential, while the area above it includes the values of the potential where the volume element at in staying in the disk surface. The stable region also has higher potential values. The dotted line at $R = \sqrt{3}$ is the asymptotic limit of the marginally stable potential. The angle between its right part and the disk surface at the equatorial plane is 60°.

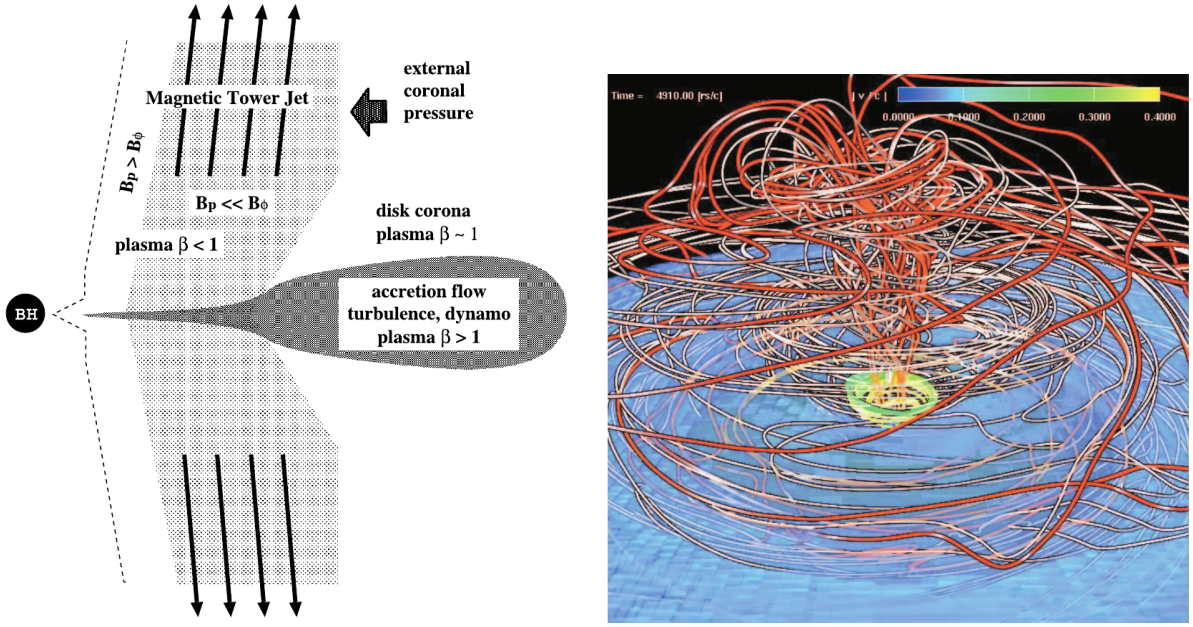

FIGURE 2.8: *left:* Schematic representation of the magnetic tower jet. *right:* Evolved state of magnetic tower simulation. The thick red lines indicate magnetic field lines anchored to the inner part of the disk, while thin white lines indicate the ones anchored in the outer part. The green lines indicate streamlines of the velocity vector. The colorbar shows the total velocity. Image credit: Kato, Mineshige, and Shibata (2004)

$$\Phi(r,z) = -\frac{GM}{R_0}\left[\frac{1}{2}\left(\frac{R}{R_0}\right)^2 + \frac{R_0}{\left(R^2+z^2\right)^{1/2}}\right] \tag{2.95}$$

The force that acts on the volume element when it gets launched from the disk surface is given by the gradient of the potential (2.95) along the direction of the field line. If $\hat{\mathbf{e}}_{\rm fl}$ is the unity vector along the field line, the total force is $\mathbf{F}_{\rm tot} = -\partial\Phi/\partial\hat{\mathbf{e}}_{\rm fl}$. The force perpendicular to this direction is always zero since we work under the assumption that the the field line follows a rigid rotation. In Figure 2.7 we plot the surfaces of constant potential Φ for $G = M = R_0 = 1$. If the unity vector points toward one of the two "unstable" regions, the volume element will either get accreted towards the central object at $(0,0)$ (left hand side unstable region) or get launched from the disk and continue as part of the outflow (right hand side unstable region). The central stable region is where volume element is still bound to the disk surface. The angle between the disk and the right part of the marginally stable surface is 60°, which means that if the magnetic field lines have an angle with the disk surface of less than 60° inclined toward the outer part of the disk, the fluid elements from the disk surface can become unstable and be launched in the form of an outflow.

2.4.5 Magnetic Towers

The idea of the "magnetic tower" jet was introduced first by Lynden-Bell and Boily (1994) and was followed up by Lynden-Bell (1996), Lynden-Bell (2003), and Lynden-Bell (2006)

In its most basic formulation, it includes an accretion disk that is threaded by a poloidal field whose field lines are forming loops with two footpoints anchored to the surface of the disk at different radii. The disk is surrounded by a corona in the force-free state. The differential rotation of the disk induces a twist in the field lines that depends on the difference in the angular velocity between the footpoints. This results in the development of a toroidal magnetic component. As the disk rotates, the magnetic pressure from the toroidal field increases, pushing the poloidal field lines outwards. This continues until there is an equilibrium between the magnetic pressure inside the loops and the external pressure. After that point the lateral expansion of the field lines stops and they expand only vertically in the form of a tower (see Figure 2.8; left). The height of the magnetic tower increases as the disk rotates at an almost constant rate.

Kato, Hayashi, and Matsumoto (2004) performed axisymmetric resistive MHD simulations of a magnetically threaded accretion disk rotating around a neutron star. They find the same magnetic loops that eventually collimate around the central axis when the pressure equilibrium is reached. The velocity of the expansion of the tower is up to $0.1c$. They continued their investigation of magnetic towers in Kato, Mineshige, and Shibata (2004) where they moved to 3D simulations and they studied the effect of the ambient pressure in the development of the jet. If the pressure becomes too large then the whole effect is suppressed and even if the jet gets launched, its ordered structure collapses into a quasi-steady state with a complex nature (see Figure 2.8; right).

Chapter 3

Numerical Details and Test Simulations

For our investigation of the jet launching mechanisms we will use the 3D GRMHD code `HARM3D` (Gammie, McKinney, and Tóth, 2003; Noble et al., 2006; Noble, Krolik, and Hawley, 2009). The code was developed by Scott C. Noble and was based on the original HARM code (Gammie, McKinney, and Tóth, 2003; Noble et al., 2006). In this chapter I will briefly describe the numerical methods used by `HARM3D` and `rHARM3D` and then I will show the special grid we used for the simulations, the boundary and initial conditions, floor values as well as the implementation of diffusivity itself. The chapter ends with some numerical tests that show the effect of diffusivity and confirm its correct implementation. [1]

3.1 Numerical Details of `HARM3D` and `rHARM3D`

`HARM3D` uses a conservative scheme to solve the equation of ideal GRMHD, with the option to switch off the magnetic field for pure hydrodynamic simulations. There is also a large variation of extra physical mechanisms that can be included in simulations including the use of kinematic viscosity, radiative transfer (Noble et al., 2011) and even dynamical spacetime for simulating systems of binary black holes (Bowen et al., 2017; Bowen et al., 2018; Bowen et al., 2019). In `HARM3D` the equations are written following the general form

$$\frac{\partial \boldsymbol{U}(P)}{\partial t} = -\frac{\partial \boldsymbol{F}^i(P)}{\partial x^i} + \boldsymbol{S}(P). \tag{3.1}$$

The primitive variables $\boldsymbol{P}$ consist of the fluid density and energy density, the three components of the velocity and the three components of the magnetic, in a set of 8 variables that are defined in the initial condition of the simulation. The fluxes $F^i(P)$, the set of conserved variables $\boldsymbol{U}(P)$ and their source terms $S(P)$ are calculated from the primitive variables and then evolved following Equation (3.1) which describes the Godunov conservative scheme (Komissarov, 1999). To complete the evolution we need to return from the conserved variable to the primitive ones. This is not as easy as the forward transformation. Noble et al. (2006) constructed several inversion schemes for the original `HARM` code which they also exist in `HARM3D`. Del Zanna, Bucciantini, and Londrillo (2003) developed similar schemers for their special relativistic MHD code. With these schemes the conserved variables are transformed

[1] The contents of this chapter are adapted from Vourellis et al. (2019). The paper is published in the Astrophysical Journal. The author of the thesis run the simulations, analyzed the result and wrote the text for both the published paper and this chapter.

and manipulated in the more numerically stable form of algebraic equations. In the end a Newton-Raphson method is called to solve the equations and return the primitive variables.

We introduced new physics in the code extending it from the ideal into the resistive MHD regime by implementing magnetic diffusivity. Because of the non-zero diffusivity, the electric field is not vanishing anymore (Equation (2.89) requiring a new formulation of the equations. During this, we had to increase the number of primitive (and conservative) variables from 8 to 11 to include the three components of the electric field.

In Section 2.3 we presented the basic equation of (resistive) GRMHD. For implementing them into the code they become

$$\frac{1}{\sqrt{-g}}\partial_\mu\left(\sqrt{-g}\rho u^\mu\right)=0, \tag{3.2a}$$

$$\partial_t\left(\sqrt{-g}T^t_\mu\right)+\partial_i\left(\sqrt{-g}T^i_\mu\right)=\sqrt{-g}T^\kappa_\lambda\Gamma^\lambda_{\mu\kappa}, \tag{3.2b}$$

$$\tag{3.2c}$$

expressing the conservation of mass and energy-momentum respectively. The above equations do not include the electric field and magnetic field. In the case of ideal GRMHD the electric field can be calculated as the cross product of the velocity and the magnetic field (Ohm's law).

To calculate the evolution of the magnetic and electric field we start by taking the temporal and spatial projections separately in Equation (2.82). This results in the derivation of the divergence condition ((2.1b)) and the time evolution for the magnetic field

$$\gamma^{-1/2}\partial_t\left(\gamma^{1/2}\boldsymbol{B}\right)+\nabla\times\left(\alpha\boldsymbol{E}+\boldsymbol{\beta}\times\boldsymbol{B}\right)=0, \tag{3.3}$$

along with Gauss' law for the electric field ((2.1a)) and the time evolution of the electric field

$$\gamma^{-1/2}\partial_t\left(\gamma^{1/2}\boldsymbol{E}\right)-\nabla\times\left(\alpha\boldsymbol{B}-\boldsymbol{\beta}\times\boldsymbol{E}\right)=-\left(\alpha\boldsymbol{J}-q\boldsymbol{\beta}\right), \tag{3.4}$$

where γ is the determinant of the spatial metric as it is defined in Equation (2.79), a and $\boldsymbol{\beta}$ are the scalar lapse and shift vector and $\boldsymbol{J}$, $\boldsymbol{E}$ and $\boldsymbol{B}$ are the spatial vectors of the electric current, electric and magnetic field as they are measured by the normal observer respectively.

From Ohm's law as it is shown in Equation (2.89) we can get

$$F^{\mu\nu}u_\nu=\eta I^\mu+\eta\left(I^\nu u_\nu\right)u^\mu+\xi F^{*\mu\nu}u_\nu. \tag{3.5}$$

Blackman and Field (1993) derived this equation for resistive fluid only but the addition of the dynamo term is straightforward. The source term $I^\nu u_\nu=q_0$ is the electric charge density as measured in the fluid frame (Komissarov, 2007). Solving for time and spatial components separately and using Equation (3.4) to replace the electric current we get

$$\begin{aligned}\gamma^{-1/2}\partial_t\left(\gamma^{1/2}\boldsymbol{E}\right)-\nabla\times\left(\alpha\boldsymbol{B}-\boldsymbol{\beta}\times\boldsymbol{E}\right)+\left(\alpha\boldsymbol{v}-\boldsymbol{\beta}\right)q&\\ =-\alpha\Gamma\left[\boldsymbol{E}+\boldsymbol{v}\times\boldsymbol{B}-\left(\boldsymbol{E}\cdot\boldsymbol{v}\right)\boldsymbol{v}\right]/\eta+&\\ +\xi\alpha\Gamma\left[\boldsymbol{B}-\boldsymbol{v}\times\boldsymbol{E}-\left(\boldsymbol{B}\cdot\boldsymbol{v}\right)\boldsymbol{v}\right]/\eta.&\end{aligned} \tag{3.6}$$

We discretize the time evolution of the electric field and after some "minor" algebraic calculations we get

$$\begin{aligned} E^i\left[\tilde{\eta}+\Gamma+\xi^2\frac{(\Gamma^2-1)}{\tilde{\eta}+\Gamma}\right] &= -\epsilon^{ijk}\tilde{v}_j B_k+\tilde{\eta}\left[Q^i+\frac{\tilde{v}^i(Q^k\tilde{v}_k)}{\Gamma\tilde{\eta}+1}\right] \\ &+\xi\left[\Gamma B^i-\frac{\tilde{\eta}\tilde{v}^i}{\Gamma\tilde{\eta}+1}(B^k\tilde{v}_k)\right] \\ &-\xi\left\{\frac{\tilde{\eta}\epsilon^{ijk}\tilde{v}_j Q_k+(\Gamma^2-1)B^i-(\tilde{v}^j B_j)\tilde{v}^i}{\Gamma+\tilde{\eta}}\right\} \\ &-\xi^2\frac{\Gamma\epsilon^{ijk}\tilde{v}_j B_k}{\Gamma+\tilde{\eta}} \\ &+\xi^2\tilde{v}^i\left\{\frac{\Gamma\tilde{\eta}Q^k\tilde{v}_k+\xi B^k\tilde{v}_k}{(\Gamma\tilde{\eta}+1)(\Gamma+\tilde{\eta})}\right\}, \end{aligned} \tag{3.7}$$

where

$$Q^i = E^i+\Delta t\left[-\left(\alpha v^i-\beta^i\right)q+\epsilon^{ijk}\partial_j\left(\alpha B_k-\epsilon_{klm}\beta^l E^m\right)\right], \tag{3.8a}$$

$$q = \gamma^{-1/2}\partial_k\left(\gamma^{1/2}E^k\right), \tag{3.8b}$$

$$\tilde{\eta} = \frac{\eta}{\alpha\Delta t}. \tag{3.8c}$$

For a extensive derivation of Equation (3.7) please refer to Appendix A.

Unfortunately, the electric field evolution equation shows signs of *stiffness*, meaning that for certain intervals the solution becomes unstable resulting in unphysically high numbers. The non-stiff part of the electric field, that does not include any diffusive terms, is calculated separately as Q^i. In Equation (3.8a) the electric field E^i represent the total electric field as it was calculated in the previous time step. For the stiff part we implemented the same solver as the one in Qian et al. (2017), where an additional fixed-point iteration method is used inside the Newton-Raphson method that solves the final algebraic equations. The fixed-point iteration continues until the values of the electric field have converged with the desired accuracy.

The parallelization of the code gave us a very big advantage in comparison with our previous works (Qian et al., 2017; Qian, Fendt, and Vourellis, 2018) where our simulations where restricted to serial runs. The additional calculations from the introduction of resistivity and especially the extra loop for the calculation of the electric field, encumber the speed of the code. Using the parallel capabilities of `rHARM3D` we were able to run the simulations within the time frame of a week (depending on the lifetime of the simulation). The simulations shown in the following chapters were performed using the MPI (Message Passing Interface)-parallel version of the code mainly in MPIA's `ISAAC` cluster but also in the MPG's `COBRA` and `DRACO` clusters.

3.1.1 Numerical Grid

Depending on our problem setup, we apply a different numerical grid. The original grid of `HARM` applying modified Kerr-Schild coordinates is used for our test simulations of diffusivity

and for the dynamo simulations in Chapter 6.

For our resistive GRMHD simulations we decided to construct a stretched grid in order to shift the outer boundary condition as far out as possible. This grid is an extension of the original HARM grid and is based on the hyper-logarithmic grid of Tchekhovskoy, McKinney, and Narayan (2009). With that we may concentrate cells close to the black hole in the radial direction and concentrate cells close to the equatorial plane or the polar axis in the polar direction, allowing us to resolve the turbulent disk and the polar jet at the same time. Furthermore, with such a scheme the outer boundary is causally disconnected from the inner simulated area of interest close to the black hole or the disk.

In the hyper-logarithmic grid the radial coordinate is split into two parts. The first part follows a logarithmic scaling as in the original HARM code (Gammie, McKinney, and Tóth, 2003). Beyond a transition radius $R_{\rm tr}$, the grid becomes substantially more scarce, up to the outer radius $R_{\rm out}$.

Physical and numerical radial coordinates translate as

$$r(x_1) = \exp\left[\frac{1}{2}x_1 + 4H\ (x_1 - x_{1_{\rm tr}})^4\right], \tag{3.9}$$

where x_1 is the uniformly spaced numerical radial coordinate and $x_{1_{\rm tr}}$ is the transition radius (corresponding to $R_{\rm tr}$). The function $H = H(x_1 - x_{1_{\rm tr}})$ is a step function that is equal to unity for $x_1 > x_{1_{\rm tr}}$ and vanishes otherwise. In Figure 3.1 we show the relation between the numerical and the physical radial coordinates.

The physical and numerical polar coordinates are connected by

$$\theta(x_2) = \theta_{\rm start} + x_2\theta_{\rm length} - h_{\rm slope}\sin(4\pi x_2), \tag{3.10}$$

where θ and x_2 are the physical and numerical polar coordinates, respectively, while $\theta_{\rm start}$ denotes the starting angle and $\theta_{\rm length} = \pi - 2\theta_{\rm start}$ the angular length of the coordinate in radians. The factor $h_{\rm slope}$ governs how many grid cells are focused toward the equatorial plane and toward the symmetry axis. We note that these coordinates are slightly different from the original HARM code, where the choice of focusing coordinates and the increase of resolution for the polar coordinate are only possible toward the equatorial plane.

Our typical maximum resolution in the polar coordinate is $\Delta\theta = 0.00625$ along the polar axis and in the equatorial plane, while the minimum resolution is $\Delta\theta = 0.025$ at 45°. The radial coordinate is best resolved close to the horizon, where $\Delta r_{r=2} = 0.02$, and is radially decreasing with $\Delta r_{r=10} = 0.1$, $\Delta r_{r=50} = 0.5$, and $\Delta r_{r=100} = 1$.

3.1.2 Boundary Conditions

For our simulations we use outflow boundary conditions in the inner and outer radial boundary. The values of the primitive variables are copied from the boundary cells to the ghost cells. At the same time we make sure that there is no inflow from the boundaries by checking that the velocity is pointing outward at each boundary cell. As an extra measure in the inner boundary, we make sure we have 10 cells of our grid inside the black hole event horizon in order to prevent numerical effects from propagating outside of it.

Furthermore, one of the reasons we modified our numerical grid into the hyper-logarithmic version we described before is because we wanted to have the outer boundary as far away

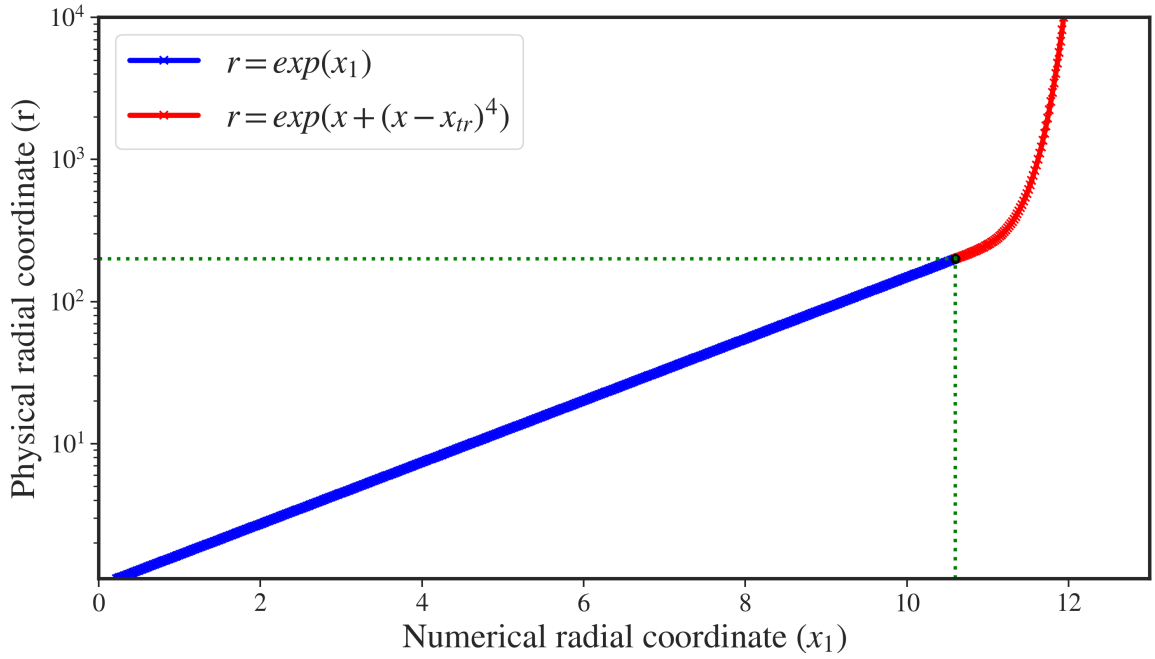

FIGURE 3.1: Interrelation between the numerical and physical radial coordinates for the stretched grid. Up to a transition radius $(x_{\rm tr}, R_{\rm tr})$, we use a simple logarithmic grid (blue), beyond which the grid transits into a hyper-logarithmic scaling (red).

from the disk as possible. Before adopting the hyper-logarithmic grid, we had noticed a collimation effect in the magnetic field lines that we had deemed as artificial (see Appendix B in Qian, Fendt, and Vourellis (2018)). By selecting an outer radius of $R_{\rm out} = 10000$, we make sure that the outer boundary stays causally disconnected from the disk. In the axial boundary we impose axisymmetric boundary conditions where the vector values are being reflected along the small cutout in both axes.

3.1.3 Initial Conditions

The initial disk density distribution is described by a nonrelativistic vertical equilibrium profile, such as applied in Sheikhnezami et al. (2012),

$$\rho(r,\theta) = \left[\frac{\Gamma-1}{\Gamma}\frac{r_{in}}{r}\frac{1}{\epsilon^2}\left(\sin\theta + \epsilon^2\frac{\Gamma}{\Gamma-1}\right)\right]^{1/(\Gamma-1)}, \tag{3.11}$$

slightly modified to fit into our code. Here $r_{\rm in}$ is the initial inner disk and $\epsilon = H/r$ is the initial disk aspect ratio as is defined by the vertical equilibrium of a disk with a local pressure scale height $H(r)$. The pressure and internal energy are given by the polytropic equation of state $p = K\rho^{\Gamma}$ and Equation 2.9, where K is the polytropic constant. For the polytropic exponent we will use different values for different simulations as specified in the sections below.

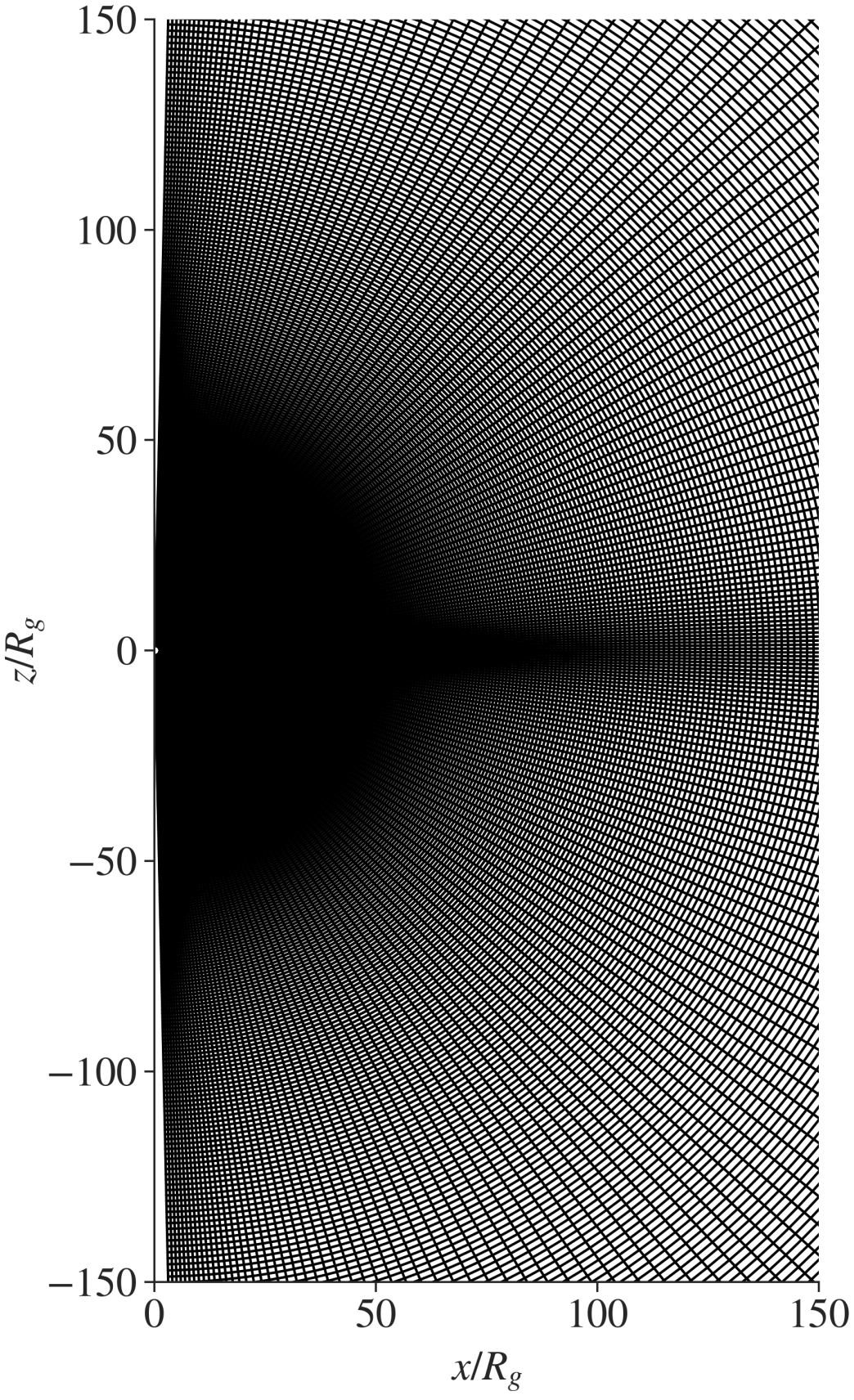

FIGURE 3.2: Numerical grid up to radius $r = 200$.

Around the disk we prescribe an initial corona. For the choice of a polytropic index of $\Gamma = 4/3$, the disk has a finite outer radius much smaller than the outer radius of the stretched grid. Furthermore, the upper and lower disk surfaces do not follow lines of constant polar angle as implied by Eq. (3.11). The initial coronal density and pressure are given by

$$\rho_{\rm cor} \propto r^{1/(1-\Gamma)}, \qquad p_{\rm cor} = K_{\rm cor}\rho_{\rm cor}^{\Gamma}. \tag{3.12}$$

The coronal temperature is chosen to be much higher than the disk temperature, $K_{\rm cor} >> K$. This implies a density jump between disk and corona but a pressure equilibrium along the disk surface. More specifically, for our simulation we chose $K = 0.001$ for the disk initial condition and $K = 1$ for the initial corona. The corona collapses instantly the moment the simulation starts, and part of it is also expelled by the initial ejections from the disk, meaning that the values are quickly replaced by the floor values of the simulation (see Sect. 3.1.5). However, the polytropic equation $P = K\,\rho^{\Gamma}$ is not enforced in any step of the code except the initial condition. The code uses Equation 2.9 to connect pressure and internal energy, which means that entropy and temperature are free to change.

The disk is given an initial orbital velocity following Paczyński and Wiita (1980),

$$\tilde{u}^{\phi} = r^{-3/2}\left(\frac{r}{r - R_{\rm PW}}\right), \tag{3.13}$$

where $R_{\rm PW}$ is a constant of choice, here equal to the gravitational radius $R_{\rm g}$. This approximation is applied in the ϕ-component of the fluid velocity u^{ϕ}.

In the resistive GRMHD simulations the disk is initially threaded by a large-scale poloidal magnetic field, implemented via the magnetic vector potential A_{ϕ} following $B = \nabla \times A_{\phi}$. In most cases we use the inclined field profile suggested by Zanni et al., 2007,

$$A_{\phi}(r,\theta) \propto (r\sin\theta)^{3/4}\frac{m^{5/4}}{\left(m^2 + \tan^{-2}\theta\right)^{5/8}}. \tag{3.14}$$

The parameter m determines the initial inclination of the field, which plays an important role for the magnetocentrifugal launching of disk winds (Blandford and Payne, 1982). The magnetic field strength is then normalized by choice of the plasma-$\beta = p_{\rm gas}/p_{\rm magn}$.

3.1.4 The Magnetic Diffusivity

The simulations presented in this work apply a scalar function for the magnetic diffusivity that is constant in time. The diffusivity is assumed to be of turbulent nature, thus much larger than the microscopic resistivity, and thought to be generated by the magnetorotational instability (MRI; Balbus and Hawley 1991). In general, the magnetic diffusivity distribution is chosen such that it resembles a magnetized diffusive disk within an ideal-MHD wind and jet area.

We apply a magnetic diffusivity profile, as it is typically used in jet-launching simulations (see, e.g. Zanni et al. 2007; Sheikhnezami et al. 2012; Qian, Fendt, and Vourellis 2018), i.e.

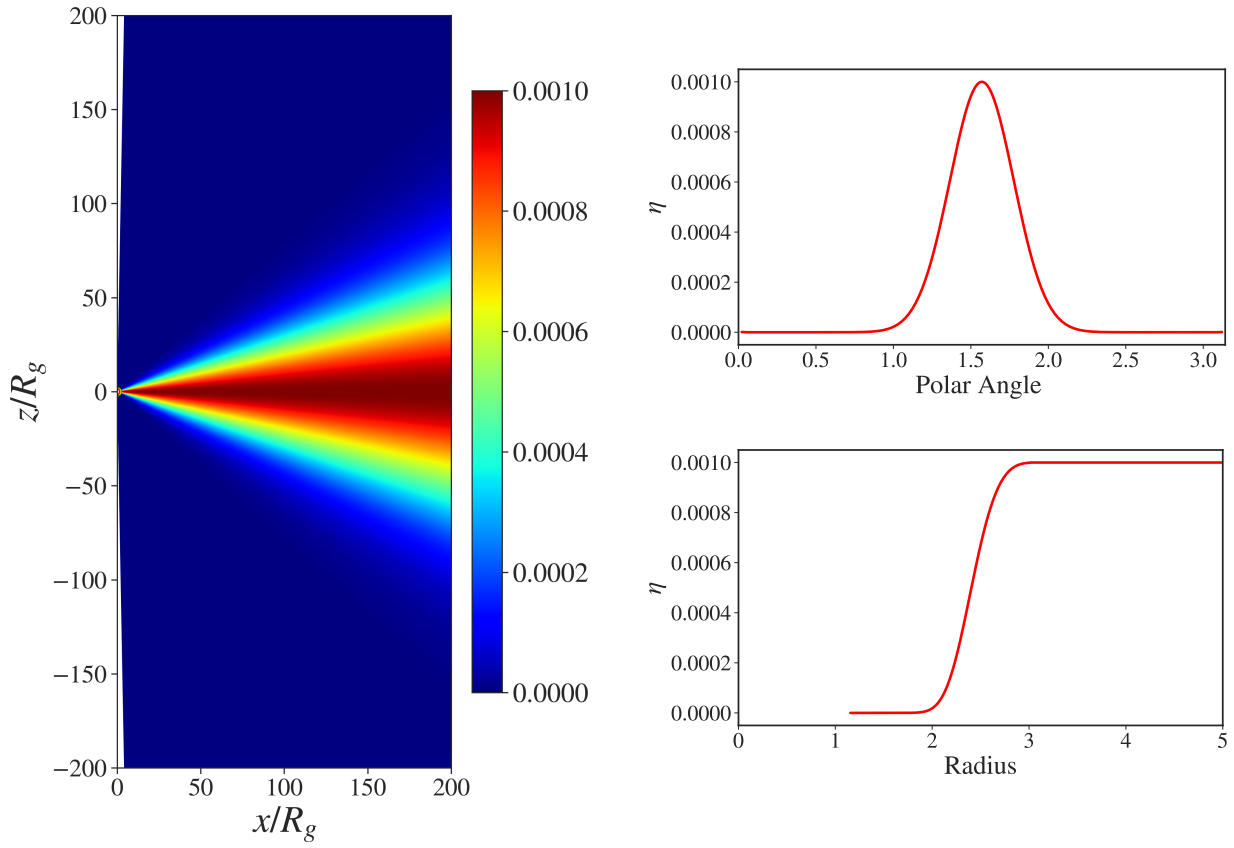

FIGURE 3.3: Distribution of the magnetic diffusivity. Along the equatorial plane, the diffusivity saturates to a constant value η_0, while in the polar angular direction it follows a Gaussian profile. For $r < 3$, the profile drops smoothly until it meets the event horizon.

a Gaussian profile along the polar angle with a maximum at the initial disk midplane,

$$\eta(r,\theta) = \eta_0 \exp\left[-2\left(\frac{\alpha}{\alpha_\eta}\right)^2\right], \tag{3.15}$$

where η_0 is the level of diffusivity along the equatorial plane, $\alpha = \pi/2 - \theta$ is the angle toward the disk midplane and $\alpha_\eta = \arctan(\chi \times \epsilon)$ is the angle that measures the scale height of the diffusivity profile. The parameter χ compares the scale height of the diffusivity profile with the disk pressure scale height. This profile – as artificial as it might seem – focuses the high diffusivity values in the equatorial plane, allowing for a highly resistive material and for a lowly resistive to asymptotically ideal-MHD disk wind and jet. Since we take resistivity as a result of turbulence, we expect higher diffusivity in the highly turbulent areas of the interior of the disk.

Initially, we also considered an anisotropic resistivity profile with different values of η affecting the poloidal and toroidal components of the magnetic field. According to Ferreira (1997) such a profile would help stabilize the disk evolution reaching a stationary state. In contrast to Zanni et al. 2007; Murphy, Ferreira, and Zanni 2010, and Sheikhnezami et al. (2012), who applied an anisotropic diffusivity in their simulations, in our case the disk loses its mass rather quickly, mainly due to the disk wind. This rapid mass loss is actually

minimizing the stabilization effect by an anisotropic magnetic diffusivity. Furthermore, the initial ejections created by the absence of equilibrium between the disk and the black hole delay the reach of a stationary condition even more. Based on that, we decided that the introduction of anisotropic diffusivity would not contribute much in the stability of the the disk.

When testing the performance of our code, we found that the simulations become more stable when we apply a low background diffusivity (1000 times lower than in the disk) along the rotational axis. We thus apply an exponentially decreasing profile along the axial boundary within six grid cells. As this axial diffusivity is confined within an opening angle of $< 3.5°$, it does not affect the physics of the jet launching. We also apply an exponential decrease in the radial diffusivity profile from radius $r = 3$ toward the horizon, resulting in a smooth transition from the high disk diffusivity to the ideal-MHD black hole environment. Figure 3.3 shows the 2D distribution, as well as the radial and angular profiles of η.

For the magnitude of the magnetic diffusivity η_0 we apply a range of values, $\eta_0 = 10^{-10} \dots 10^{-2}$ (in code units). These values correspond to some kind of standard parameters applied in the literature in diffusive MHD simulation in GR (Bucciantini and Del Zanna, 2013; Bugli, Del Zanna, and Bucciantini, 2014; Qian et al., 2017; Qian, Fendt, and Vourellis, 2018), in nonrelativistic simulations (Casse and Keppens, 2002; Zanni et al., 2007; Sheikhnezami et al., 2012; Stepanovs and Fendt, 2014), but have been modeled concerning strength and spatial distribution also by direct simulations, e.g. by Gressel (2010).

Magnetic diffusivity also affects the time step of the simulations. Since the code is solving the GRMHD equations using an explicit scheme, the time step is limited by the characteristic velocit of the magnetized fluid. In the additional case of resistive MHD, the diffusive time scale must be taken into consideration. For a grid size Δx the diffusive time step Δt_η must be

$$\Delta t_\eta < \frac{(\Delta x)^2}{\eta}. \tag{3.16}$$

This means that the level of magnetic diffusion we add in the simulation will also affect its computational cost.

Here we emphasize another important impact of physical resistivity: It suppresses the MRI (Fleming, Stone, and Hawley, 2000; Longaretti and Lesur, 2010). Overall, we do not expect to detect any MRI being resolved in our disk structure. As discussed in Qian et al. (2017), the diffusion rate will be of order $k^2\eta$ (Fleming, Stone, and Hawley, 2000), with the wavenumber k. From Balbus and Hawley (1991) we know that the MRI grows only in a certain range of wavenumbers $k \in [0, k_{\max}]$, in the linear MRI regime – depending on whether the numerical grid may resolve certain wavelengths and whether certain wavelengths will fit into the the disk pressure scale height. Furthermore, there exists a wavenumber k_{MRI} for which the MRI growth rate reaches a maximum (see Hawley and Balbus 1992 for the case of a Keplerian disk). A certain number of MRI modes can therefore be damped out when $k^2_{\mathrm{MRI}}\eta$ is comparable to the maximum growth rate of MRI. Moreover, for a large enough η, it is even possible to damp out most of the MRI modes in the linear evolution of MRI.

In Qian et al. (2017) a thorough investigation of resistive effects on the accretion rate of an initial Fishbone & Moncrief (Fishbone and Moncrief, 1976) torus was presented. They could show that for this setup for $\eta \lesssim 10^{-3}$ the MRI seemed to be completely damped, while for lower η the onset of the MRI and thus of massive accretion was substantially delayed.

This result was claimed to be consistent with Longaretti and Lesur (2010), demonstrating that the growth rate of the MRI substantially decreases with $1/\eta$ beyond a critical diffusivity.

In addition to the point that we do not expect the MRI to play a role in our simulations owing to the disk resistivity, we also note that we consider a thin disk that is thread by a strong magnetic field. Thus, angular momentum transport is dominated by the torque of the magnetic lever arm.

Other consequences of considering a magnetic diffusivity are physical reconnection of the magnetic field and also physical ohmic heating. Both effects are present in our simulations, and we will discuss their impact on the accretion-ejection system accordingly.

3.1.5 The Density Floor Model

As typical for any MHD code, `rHARM3D` cannot work in vacuum. This is a problem also for relativistic MHD codes, in particular for their inversion schemes, so usually a floor model is applied to circumvent numerical problems when the initial disk corona collapses.

Depending on the model setup, we apply a different floor model for the density and pressure. Note that in particular in our approach that applies a large-scale initial disk magnetic flux, we potentially deal with a high magnetization $\propto B^2/\rho$ and / or low plasma-*beta* $\propto P/B^2$ at large radii. Thus, for simulations on a large grid, we choose a floor profile following a broken power law. For the density we apply

$$\rho_{\rm flr}(r) \propto \left[\left(\frac{r}{r_0}\right)^{1/(1-\Gamma_1)} + \left(\frac{r}{r_0}\right)^{1/(1-\Gamma_2)}\right], \tag{3.17}$$

while the internal energy follows

$$u_{\rm flr}(r) \propto \left[\left(\frac{r}{r_0}\right)^{\Gamma_1/(1-\Gamma_1)} + \left(\frac{r}{r_0}\right)^{\Gamma_2/(1-\Gamma_2)}\right], \tag{3.18}$$

with $\Gamma_1 = 4/3$ and $\Gamma_2 = 2$, and where r_0 marks the transition radius between the two power laws with typically $r_0 = 10\,R_{\rm g}$ (see Figure 3.4). With that we implement higher floor values for large radii in order to avoid a too high magnetization. Close to the black hole we apply the same floor profile as in the original `HARM` code.

3.1.6 Characteristic Quantities of the Simulations

Here we define a number of physical quantities, that will later be used to characterize the evolution in different simulations. The mass contained in a disk-shaped area between radii r_1 and r_2 and between surfaces of constant angle θ_1 and θ_2 is calculated as

$$M_{\rm disk} = 2\pi \int_{r_1}^{r_2} \int_{\theta_1}^{\theta_2} \rho(r,\theta)\,\sqrt{-g(r,\theta)}\,d\theta\,dr, \tag{3.19}$$

where $\sqrt{-g}$ is the square root of the determinant of the metric. The mass flux through a sphere of radius R between angles (θ_1, θ_2) is

$$\dot{M}(R) = 2\pi \int_{\theta_1}^{\theta_2} \rho(R,\theta)\,u^r(R,\theta)\,\sqrt{-g(R,\theta)}\,d\theta. \tag{3.20}$$

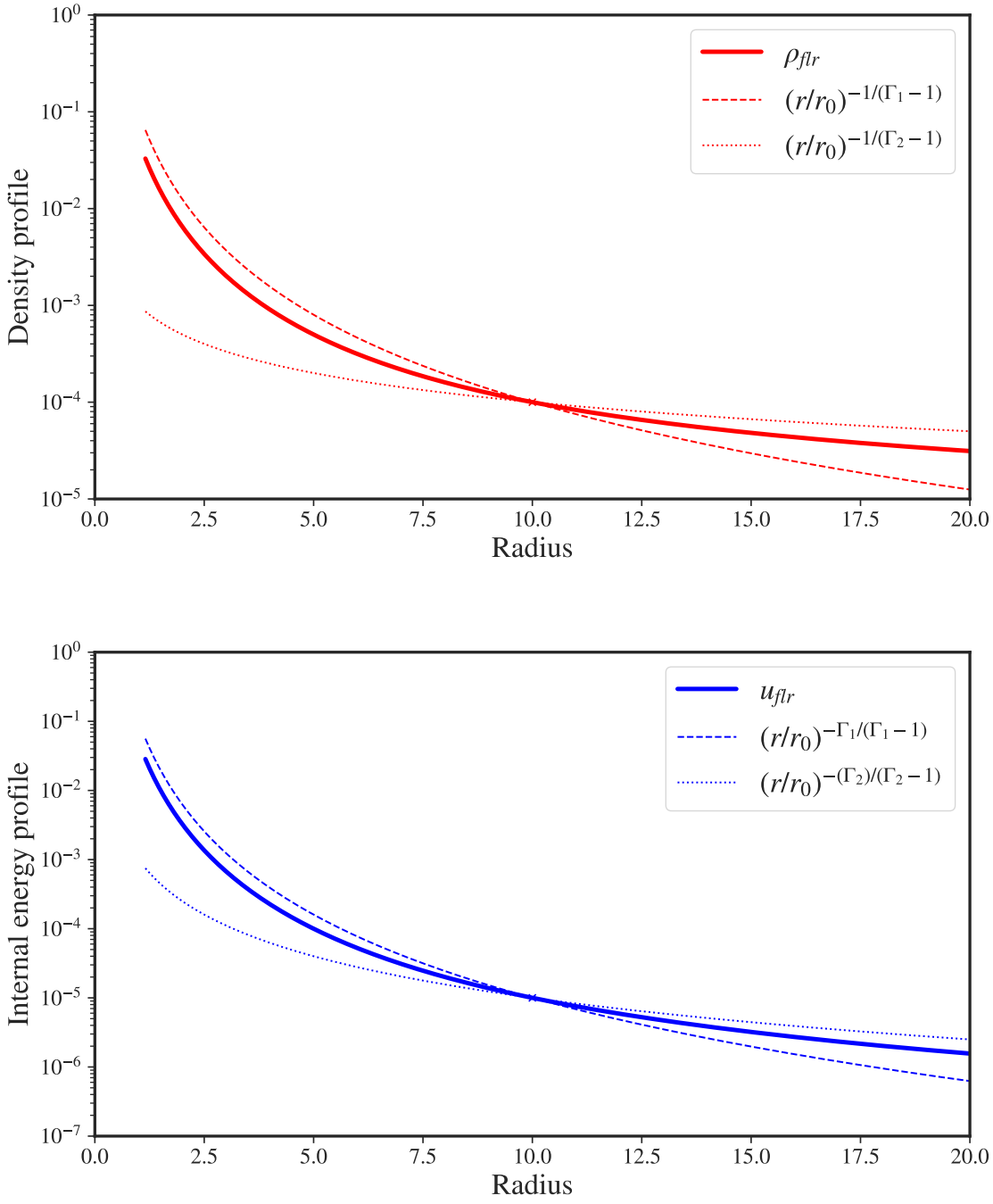

FIGURE 3.4: Floor model used in the science simulations. The radial density (top) and internal energy (bottom) distributions are calculated as broken power laws.

Similarly, we calculate the mass flux in θ-direction considering the u^θ component and the area element $\sqrt{-g(R,\theta)}\, d\phi dr$. This is in particular used to calculate the disk wind mass flux from the disk surface, considering two surfaces with a constant opening angle Θ that is

chosen to be similar to the initial disk density distribution. We thus obtain

$$\dot{M}(\Theta) = 2\pi \int_{r_1}^{r_2} \rho(r,\Theta)\, u^{\theta}(r,\Theta)\, \sqrt{-g(r,\Theta)}\, dr. \tag{3.21}$$

The Poynting flux per solid angle is defined as

$$\begin{aligned} F_{\rm EM}(r,\theta) &= -T^{r}_{t} \\ &= -\left[\left(b^2+e^2\right)\left(u^r u_t + \frac{1}{2} g^r_t\right) - b^r b_t - e^r e_t \right. \\ &\left. -u_\beta e_\gamma b_\delta \left(u^r \epsilon^{\beta\gamma\delta}_t + u_t \epsilon^{r\beta\gamma\delta}\right)\right]. \end{aligned} \tag{3.22}$$

By integration along the polar angle we obtain the flux through a sphere of radius R,

$$\dot{E}_{\rm EM}(R) = 2\pi \int_0^{\pi} \sqrt{-g(R,\theta)}\, F_{\rm EM}(R,\theta)\, d\theta. \tag{3.23}$$

The corresponding electromagnetic flux is

$$\begin{aligned} F_{\rm EM}(r,\theta) &= -T^{\theta}_{t} \\ &= -\left[\left(b^2+e^2\right)\left(u^\theta u_t + \frac{1}{2} g^\theta_t\right) - b^\theta b_t - e^\theta e_t \right. \\ &\left. -u_\beta e_\gamma b_\delta \left(u^\theta \epsilon^{\beta\gamma\delta}_t + u_t \epsilon^{\theta\beta\gamma\delta}\right)\right]. \end{aligned} \tag{3.24}$$

By integration along the radius, we obtain the flux through a surface of constant angle Θ,

$$\dot{E}_{\rm EM}(\Theta) = 2\pi \int_{r_1}^{r_2} \sqrt{-g(r,\Theta)}\, F_{\rm EM}(r,\Theta)\, dr. \tag{3.25}$$

The poloidal Alfvén Mach number is $M_{\rm A,p} = \left[h\rho u_{\rm P}^2 B_{\rm P}^{-2}\right]^{1/2}$ (see also Qian, Fendt, and Vourellis 2018), where $h \equiv \Gamma/(\Gamma-1)(P/\rho)+1$ is the specific enthalpy of the fluid. Alfvénic Mach numbers $M_{\rm A,p} < 1$ imply that the magnetic energy is dominating the kinetic energy of the fluid and that the dynamics of the outflow is most likely governed by the strong magnetic field in that area.

3.2 Test Simulations Considering Magnetic Diffusivity

In order to verify the implementation of magnetic diffusivity into `HARM3D`, we have performed two test simulations. Our tests are similar to those applied by Qian et al. (2017). In the first test we follow the diffusion of a parallel magnetic field in a rectangular box through for different strength of the magnetic diffusivity and compare it with the time-dependent analytic solution to the diffusion equation. The second test problem is a classic shock tube that allows us also to check how magnetic diffusivity affects the shock-capturing abilities of the code.

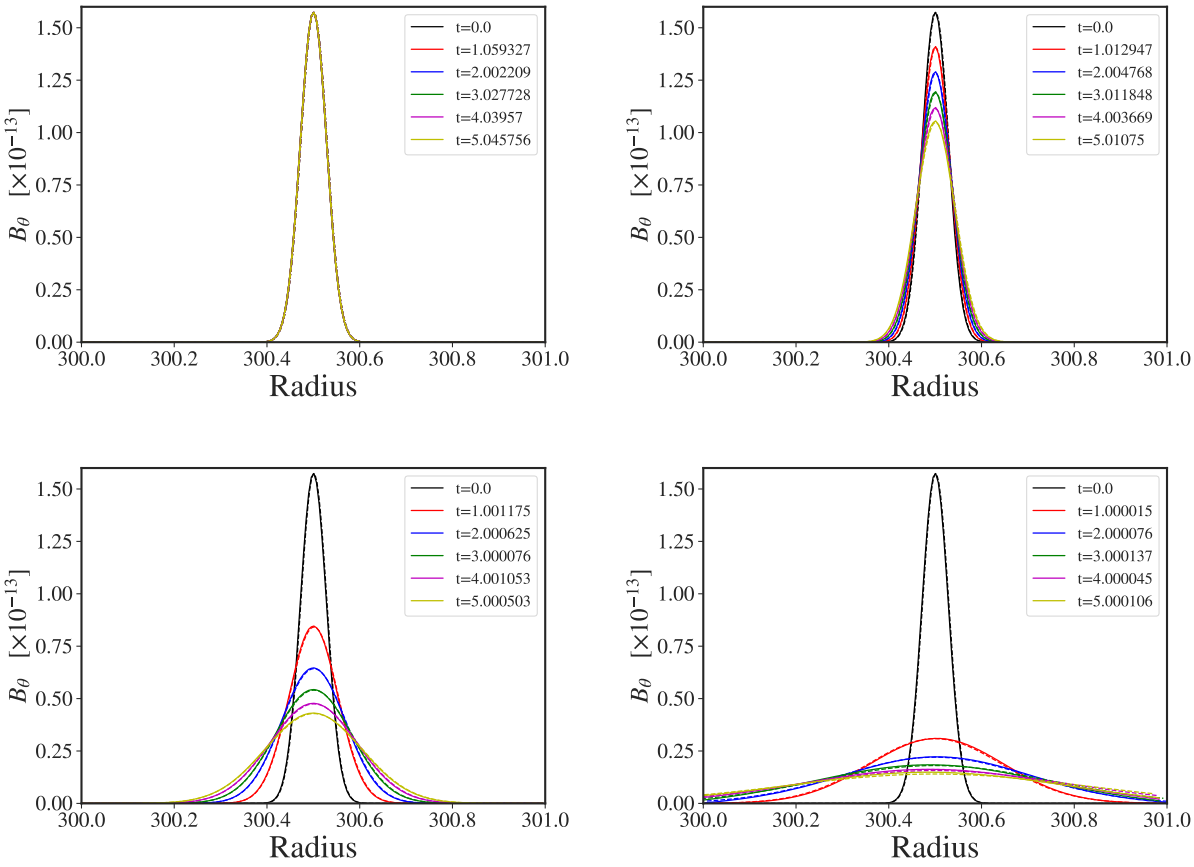

FIGURE 3.5: Diffusive decay of a vertical magnetic field. Evolution of the θ-component of the magnetic field for simulation runs applying four values for the magnetic diffusivity, $\eta = 10^{-12}$ (top left), $\eta = 10^{-4}$ (top right), $\eta = 10^{-3}$ (bottom left), and *box2* with $\eta = 10^{-2}$ (bottom right). Each color represents a different time step t in the simulation. Solid lines show simulation results, while dashed lines show the analytical solution.

3.2.1 Diffusive Decay of a Vertical Field

The setup for the simulations treating the diffusive decay of a vertical field considers a hydrostatic gas distribution located in an almost rectangular box that is threaded by a weak magnetic field. A uniform magnetic diffusivity is applied for the whole box and is the only parameter affecting the magnetic field evolution. Applying different levels of magnetic diffusivity, we compare the simulated evolution of the magnetic field with the analytic solution. As in Qian et al. (2017), we find an almost perfect match.

3.2.1.1 Numerical Setup

The box simulations are performed in a 256^2 grid in a small sector of our domain space, along the equatorial plane, extending by Δr in radius and $\Delta\theta$ in latitude. By choosing a large-enough radius r_0 to place the box ($\Delta r << r_0$), we establish that its shape is as close as possible to a perfect square, with a side length $r \in [r_0 - \Delta r/2, r_0 + \Delta r/2]$, and

a latitude $\Delta\theta$ that corresponds to a z-direction side Δz, where $z = r\sin(\pi/2-\theta)$ and $\theta \in [\pi/2-\Delta\theta/2, \pi/2+\Delta\theta/2]$.

A relativistic gas is applied in the area of the box with a polytropic index of $\gamma = 4/3$. The gas is in hydrostatic equilibrium with radial profiles of density $\rho(r) = C\, r^{\alpha}$ and pressure $p(r) = \beta\, \rho^{\gamma_{\rm G}}$, where $\alpha = 1/(1-\gamma_{\rm G})$, $\beta = 1/(1-\alpha)$ and C denotes a proper normalization constant. This profile balances the gravitational force at large distances from the black hole (where GR effects are negligible). The magnetic field is uniform in θ-direction. In the r-direction it follows a (time-dependant) Gaussian profile

$$B_\theta(r,\tilde{t}) = \frac{1}{\sqrt{\tilde{t}}}\exp\left(-\frac{(r-r_0)^2}{4\eta\tilde{t}}\right). \tag{3.26}$$

We apply a very high plasma-β, $\beta_{HM} = 10^8$ in order to establish a weak magnetic field that does not initiate any advection of magnetic flux. The time variable $\tilde{t} = t_0 + t$ is connected with the code running time t with the parameter t_0 which basically normalizes the Gaussian profile. Finally, we are using outflow boundary conditions in all four boundaries of the box.

3.2.1.2 Simulation Runs

We have placed the simulation box far from the black hole at a radius $r_0 = 300.5$ with a side length of $\Delta r = 1 \approx \Delta z$. At this distance the shape of our box is quite close to square as $\Delta r << r_0$. We follow the magnetic field evolution as given initially by Equation 3.26 along the equatorial plane. We run a series of simulations for different strengths of magnetic diffusivity. In Figure 3.5 we compare the simulation results (solid lines) with the analytic solution (dashed lines).

For simulation *box12* with $\eta = 10^{-12}$ there is barely any change in the magnetic field distribution and the simulation perfectly matches the ideal-MHD limit. Note that for the very high resolution applied in these simulations, also the numerical diffusivity is low[2]. As we increase the magnetic diffusivity (*box4, box3, box2*) to the values of $\eta = 10^{-2}$, the magnetic field decays - faster for higher diffusivity. Overall, the initial field distribution decays following exactly the analytical solution.

However, for high levels of the magnetic diffusivity, $\eta > 0.1$, the code fails. In this case the magnetic field has completely lost its initial Gaussian distribution, which poses a limit in the values of diffusivity we are allowed to use in our simulation.

3.2.2 Diffusive Shock Tube Test

Following Qian et al. (2017) we perform a series of tests with our resistive code based on the classical 1D shock tube test that demonstrates the shock-capturing capability of the code. We employ a computational domain that extends for $x \in [298.75, 302.25]$ in the limit of Minkowski space-time using Cartesian coordinates with 4000 cells to reduce the effect of numerical diffusion. The initial condition of the test follows the setup of Dumbser and Zanotti (2009) and Bucciantini and Del Zanna (2013). We implement a discontinuity in the density of the gas, in the gas velocities, and in the magnetic field; thus,

[2]See Qian et al. (2017) for an assessment of the numerical diffusivity of `HARM-2D`

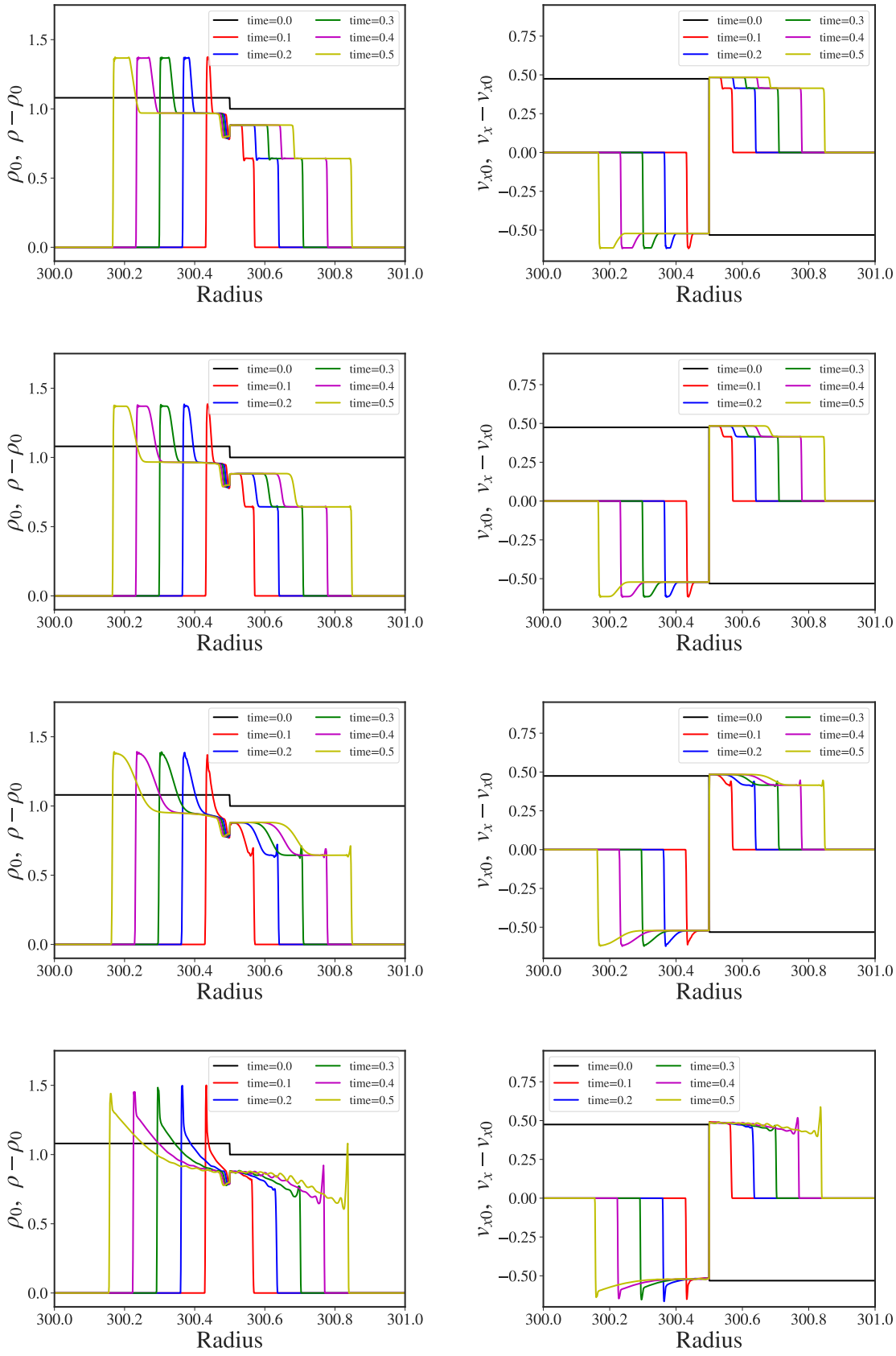

FIGURE 3.6: Time evolution of the classic 1D shock tube test. Shown are gas density (left) and horizontal velocity (right) for different levels of magnetic diffusivity, $\eta = 10^{-2}, 10^{-1}$ (from top to bottom). The initial conditions for ρ_0 and V_{x0} are denoted by black lines, while colored lines denote the evolution for five consecutive times steps.

$$(\rho,p, v^x, v^y, v^z, B^x, B^y, B^z) = (1.08, 0.49, 0.4, 0.3, 0.2, 2.0, 0.3, 0.3) \tag{3.27}$$

for $x < 300.5$ and

$$(\rho,p, v^x, v^y, v^z, B^x, B^y, B^z) = (1.0, 1.0, -0.45, -0.2, 0.2, 2.0, -0.7, 0.5) \tag{3.28}$$

for $x > 300.5$, The initial electric field is set to the ideal-MHD value. The boundary condition at the ends of the tube is fixed to the initial values (Dirichlet boundary conditions). For the equation of state we choose a polytropic index $\gamma = 5/3$.

In Figure 3.6 we show the evolution of the discontinuity in gas density and horizontal velocity for different values of magnetic diffusivity. We note that in all cases we see the distinct features that result from the breaking of the initial discontinuity and the velocity values describe accurately the behavior of the gas density. The left-going rarefaction wave has a negative velocity and moves faster than the compound wave that follows it. The contact discontinuity propagates with the same speed as the compound wave, which also appears in the density distribution, while the discontinuity moves slowly away from it's initial position at $x = 0$. The discontinuity is followed by a slowly moving shock front and a fast-moving rarefaction wave, both with positive velocities.

In Figure 3.7 we compare the distribution of gas density and vertical magnetic field for different levels of magnetic diffusivity. We see that for $\eta < 10^{-4}$ there is little difference between the simulations.

3.3 Summary

In this chapter, we have extended the newly developed resistive GRMHD code `rHARM` (Qian et al., 2017) to a parallel version by implementing magnetic resistivity in `HARM3D`. This will allow us to apply our models of jet launching from thin accretion disks to longer time scales and larger spatial scales, also considering a higher numerical resolution.

First, we refer to the numerical solution of the resistive GRMHD equations and we explain the transition from the ideal `HARM3D` to the resistive `rHARM3D` We also show the analytic derivation of the electric field evolution equation used in the inversion scheme.

We presented a detailed description of the new numerical grid which allows us to extend the outer boundary the very large radii with little extra computational cost. We also described the initial conditions used for many of the thin disk simulations that follow in the next chapters as well as the boundary conditions used in the code. Next we describe the numerical model and distribution used for the magnetic resistivity. The prescription allows for maximum diffusion of the magnetic field on the equatotial plane and close to it as well us for smooth transition to lower values as we leave the disk surface and approach the black hole. The density and pressure floor model is described next, whose importance is also indicated as they important for a large part the outflows we observe.

We proceed by presenting two test for the model of diffusivity. A series of magnetic field decay test where we simulate the evolution of magnetic field and the effect of diffusivity on

it. We compare the simulation results with the analytical solution and we find very good agreement in as well as an upper limit of diffusivity above which the code fails to converge. We also run the resistive version of the classical 1D shock tube simulations where we test the limits of the code in treating shocks. The results are in agreement with similar tests in the literature and the also confirm the aforementioned upper limit in diffusivity.

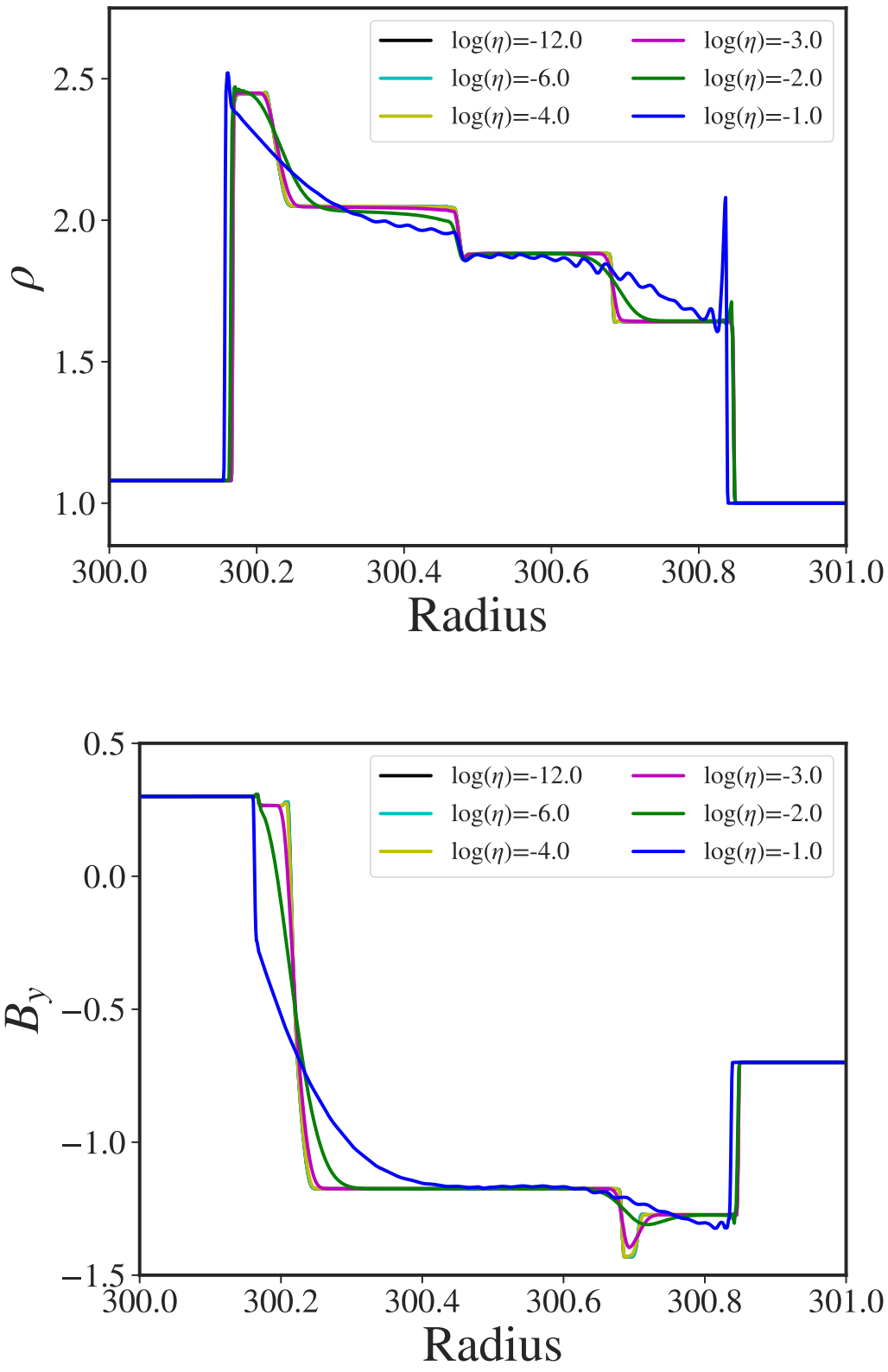

FIGURE 3.7: Diffusive shock tube test. Shock longitudinal structure in density (top) and perpendicular magnetic field (bottom) at time $t = 0.5$ for different levels of magnetic diffusivity, $\eta = 10^{-12}$ (black line, ideal MHD), $\eta = 10^{-6}$ (cyan), $\eta = 10^{-4}$ (yellow), $\eta = 10^{-3}$ (magenta), $\eta = 10^{-2}$ (green), and $\eta = 10^{-1}$ (blue). Note that for $\eta < 10^{-4}$ the lines are overlapping.

Chapter 4

Investigating the Outflows of Thin Accretion Disks

In this chapter we will perform a detailed analysis of our reference simulation. We will study both the disk accretion and the outflows with a focus on the outflows ejected from the accretion disk and the region of the black hole. We will analyze the accretion and ejection mass flux and the electromagnetic energy output of the jet. [1]

4.1 A Reference Simulation

In the following we will first describe the details of our reference simulation that will be used to compare our parameter runs for characteristic properties of the source. The reference simulation runs for 9000 $t_{\rm g}$ corresponding to approximately 67 disk orbits at the initial inner disk radius. In Figure 4.1 we show the evolution of the density distribution, the poloidal magnetic field lines, and the poloidal velocity field up to time $t = 8000$.

4.1.1 Initial Conditions

The distributions for the initial density, pressure, angular velocity, and magnetic vector potential are given by Equations (3.11), (2.9), (3.13), and (3.14). For the disk rotation (3.13) we impose a factor of 0.95 in order to treat a sub-Keplerian disk. For the disk gas law we apply $\Gamma = 4/3$ and $K = 0.001$. For a Kerr parameter of $a = 0.9$, the horizon is located at $r = 1.4358$ and the innermost stable circular orbit (ISCO) at $r = 2.32088$.

For the numerical grid we choose a transition radius $R_{\rm tr} = 200$ and an outer grid radius $R_{\rm out} = 10^4$. The initial inner disk radius $r_{\rm in} = 7$ is outside the ISCO in order to avoid possible initial ejections of gas, as the initial disk is not in force equilibrium within GR. At this radius the initial angular velocity of the disk is $\Omega_{\rm r_{in}} \approx 0.047$, thus slightly lower than the Keplerian value $\Omega_K \approx 0.052$, and corresponding to an orbital period of $T_{\rm r_{in}} \approx 135$.

The initial corona is given by Eq. (3.12) with $K_{\rm cor} = 1$, resulting in a higher coronal entropy. The initial magnetic field structure follows Eq. (3.14) with $m = 0.6$. The magnetic field strength is fixed by the choice of the plasma-$\beta = 10$ at the initial inner disk radius. The magnetic diffusivity profile is given by Eq. (3.15) with $\chi = 3$ and $\eta_0 = 0.001$ (see Figure 3.3).

[1] The contents of this chapter are adapted from Vourellis et al. (2019). The paper is published in the Astrophysical Journal. The author of the thesis run the simulations, analyzed the result and wrote the text for both the published paper and this chapter.

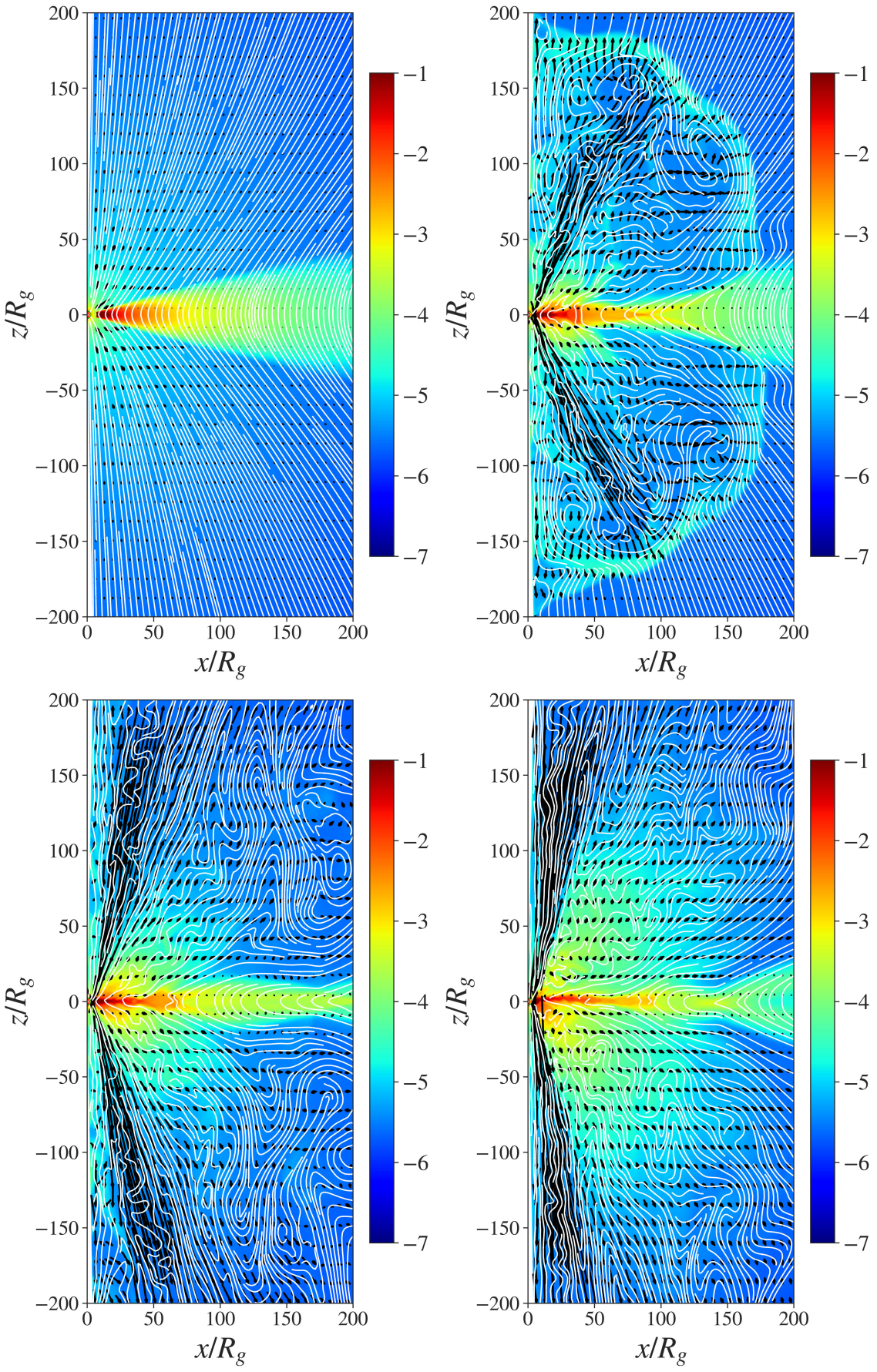

FIGURE 4.1: Snapshots of our reference simulation. Shown is the density distribution (in log scale) at times $t = 0$, 1000, 2000, 4000, 6000, and 8000. The poloidal magnetic field lines are shown (white lines), while the poloidal velocity field is represented by the black arrows.

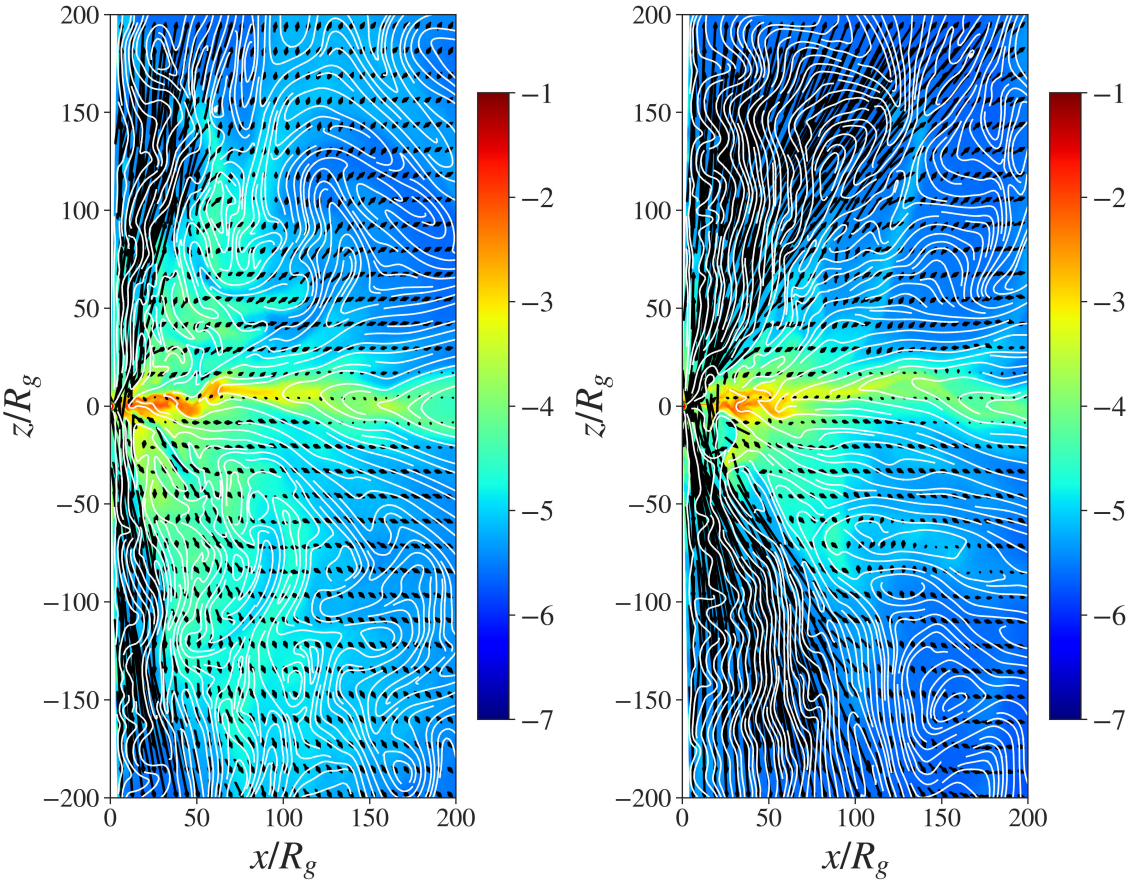

FIGURE 4.1: Snapshots of our reference simulation (cont.)

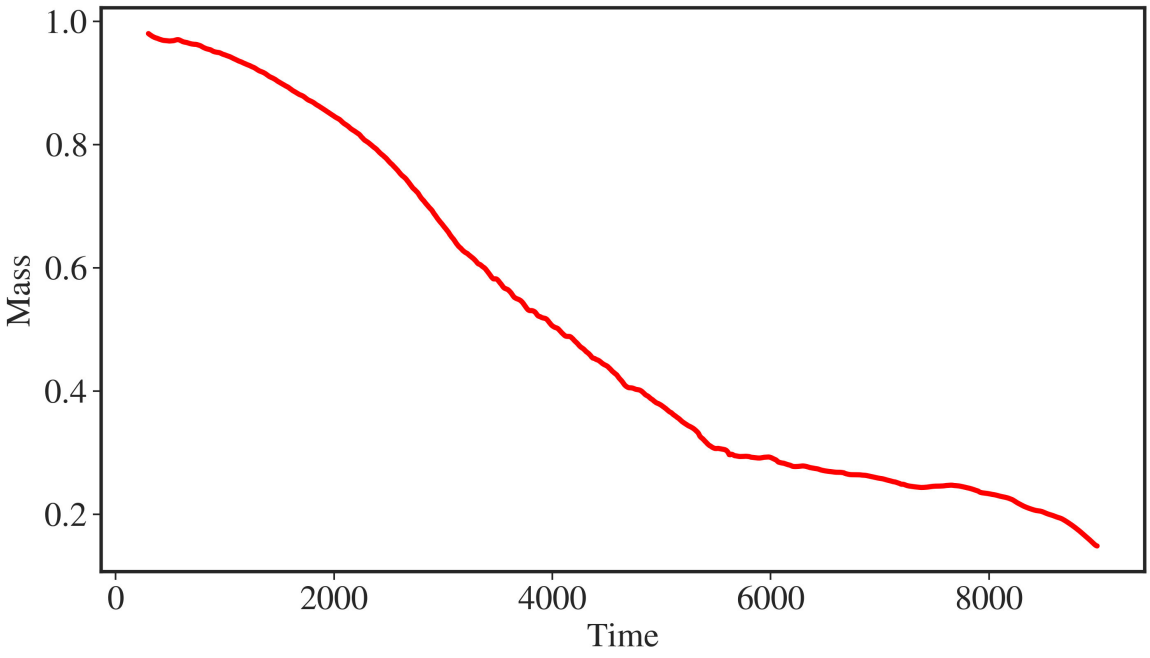

FIGURE 4.2: Evolution of the disk mass in our reference simulation measured in a reference area as described in the text. The mass is normalized to the initial disk mass.

4.1.2 Evolution of Disk Mass and Disk Accretion

As the disk evolves, accretion sets in and the inner disk radius changes to lower values, extending down to $r \approx 3$ right outside of the ISCO after having completed more than 200 rotations at this radius. Since the shape of the disk changes constantly, it is difficult to measure the total disk mass. One option is to measure the mass within a disk area defined by the inner surface located at $r = 3$, an outer surface at $r = 100$, and the surfaces of constant opening angle of $\theta \approx 80°$ and $\theta \approx 100°$. The disk mass is then obtained by integrating the mass density in the disk area as specified above [2].

The evolution of the disk mass is shown in Figure 4.2. Since the disk is not in equilibrium, there is a rapid change in the innermost part of the disk that causes a small initial increase. We understand that the extra mass for the disk arises from the initial corona, which immediately starts to collapse, and by that squeezes and relaxes the inner disk until a quasi-equilibrium is reached at $t \approx 300$. After that, the disk mass decreases steadily until $t \approx 5500$, when the slope of the disk mass evolution changes. This is mainly due to changes in the disk outflow. Note that by the end of the simulation the disk has lost more than 80% of its initial mass.

Figure 4.3 shows the normalized accretion rates measured through three different radii, $r = 2$, 4 and 13, and integrated over the disk scale height. Close to the horizon, measured at radius $r = 2$, the accretion rate is first negligible, mainly because of the absence of disk material in that radius. After $t = 3000$, accretion rate increases. Note that by now the inner disk radius, located initially at $r = 7$, has moved closer to the black hole, populating that area with dense disk material. The enhanced accretion level is accompanied by substantial accretion spikes. However, the underlying base accretion rate seems to decrease as the disk loses mass. The accretion mass flux in the inner area is of the order of 10^{-4}.

After $t = 6000$ and until the end of the simulation, the innermost area around $r = 2$ becomes almost empty again, with the exception of a thin stream of material that is connecting the disk with the black hole. It looks like that at this point in time all material close to the black hole has fallen into it, but has not been replenished by disk material from larger radii. As a result, accretion at $r = 2$ is halted completely[3] for a substantial period of time, until it is temporarily restarted by disk material that has newly arrived (accreted) from larger radii. This relaunch of accretion is indicated by the spikes in the accretion rate at late times.

Similar to $r = 2$, at radius $r = 4$ accretion is not significant until $t = 1500$, while it gradually increases afterward until $t = 3000$. In the following strong accretion phase ($t \in [3000, 6000]$), there is also a significant amount of material moving outward. In the inner part of the disk, just outside the ISCO, the gas is actually moving in both directions, radially inward and outward, thus indicating the turbulent character of the motion. The highly turbulent nature of the inner accretion flow is shown in Figure 4.4. The figure demonstrates the rapid change in density and velocity within short time. Note the strong gradient in velocity at the ergosphere (yellow line; dark blue indicates high infall speed).

Since the average accretion rate at radius $r = 4$ is similar to that measured at $r = 2$, we conclude that the accretion mass flux is conserved and, thus, no outflow is ejected from this

[2]The disk mass and mass flux are normalized by the mass of the *initial* disk material included in the disk area as specified above

[3]with the exception of the floor density accretion

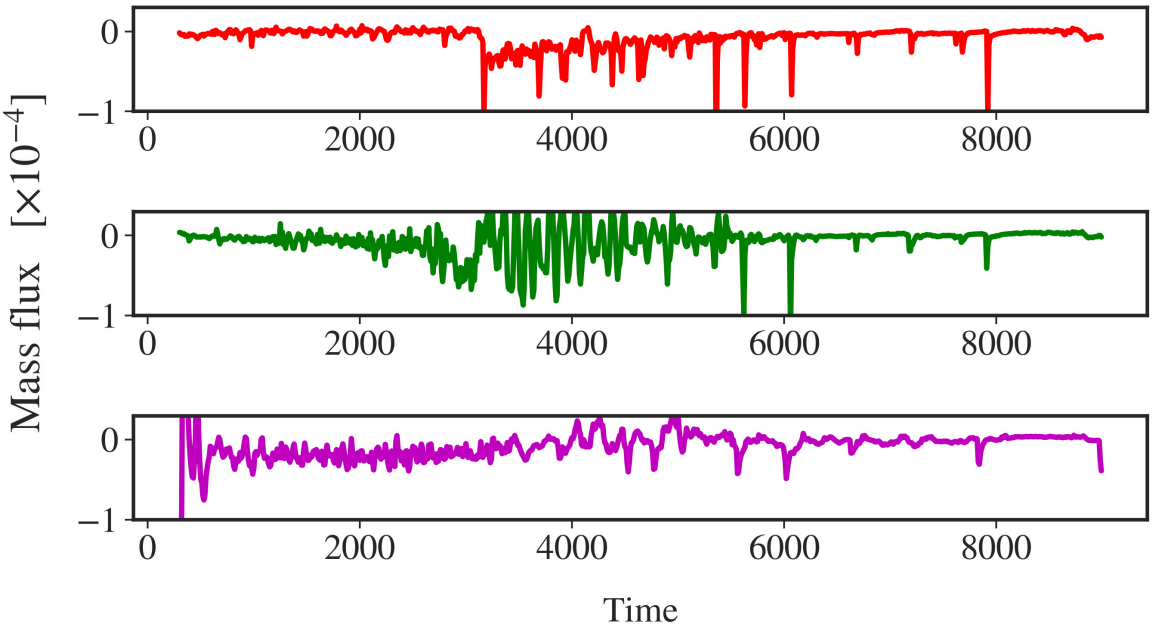

FIGURE 4.3: Accretion rate measured in three different radii ($r = 2,\ 4,\ 13$, top to bottom) for the duration of the simulation. The mass flux was integrated between 80° and 100° using the negative values of radial velocity.

area close to the black hole. Even farther out, at radius $r = 13$, the accretion process looks quite different. The accretion rate is again of an order of magnitude similar to smaller radii. The accretion spikes that are seen at lower radii now are replaced with much broader time periods of high mass accretion, indicating a slower change to the accretion rate.

However, we still detect a few accretion spikes during the third phase of evolution. In fact, the accretion spikes that are observed at $r = 13$ are subsequently followed by spikes at $r = 4$ and $r = 2$. We measure a time delay between the spikes at $r = 13$ and $r = 4$ varying between $\Delta t = 75$ and $\Delta t = 40$. The time delay between the spikes at $r = 4$ and $r = 2$ is $\Delta t \simeq 10$. [4] An approximate average accretion velocity can be defined by dividing the distance traveled by the fluid by the time delay of the spikes. For the three major spikes appearing at radius $r = 2$ at $t = [5630, 6070, 7920]$ we measure a similar velocity from radius $r = 4$ to radius $r = 2$ of 0.2 for all three spikes. For the pattern speed of the spikes from $r = 13$ to $r = 4$ we measure velocities of 0.12, 0.225, and 0.16, respectively. These values derived for the pattern speed agree well with the radial velocity that we observe in this area of the disk.

At late stages of the simulation (between $t = 6000$ and 9000) we notice a decline in the accretion rate at all three radii. This is accompanied by the opening of a larger gap between the horizon and the inner disk, meaning that the inner disk radius moves out. At this time, the disk has already lost 70% of its mass. During this period, the disk accretion becomes disconnected from the black hole. We interpret this as follows. Due to the decrease of density and pressure (following accretion and ejection of disk material), this area becomes magnetically dominated. The strong magnetization leads to the structure of a magnetically

[4] This is also the time sequence for our data dumps, so we cannot provide a higher time resolution for the pattern speed of the spikes.

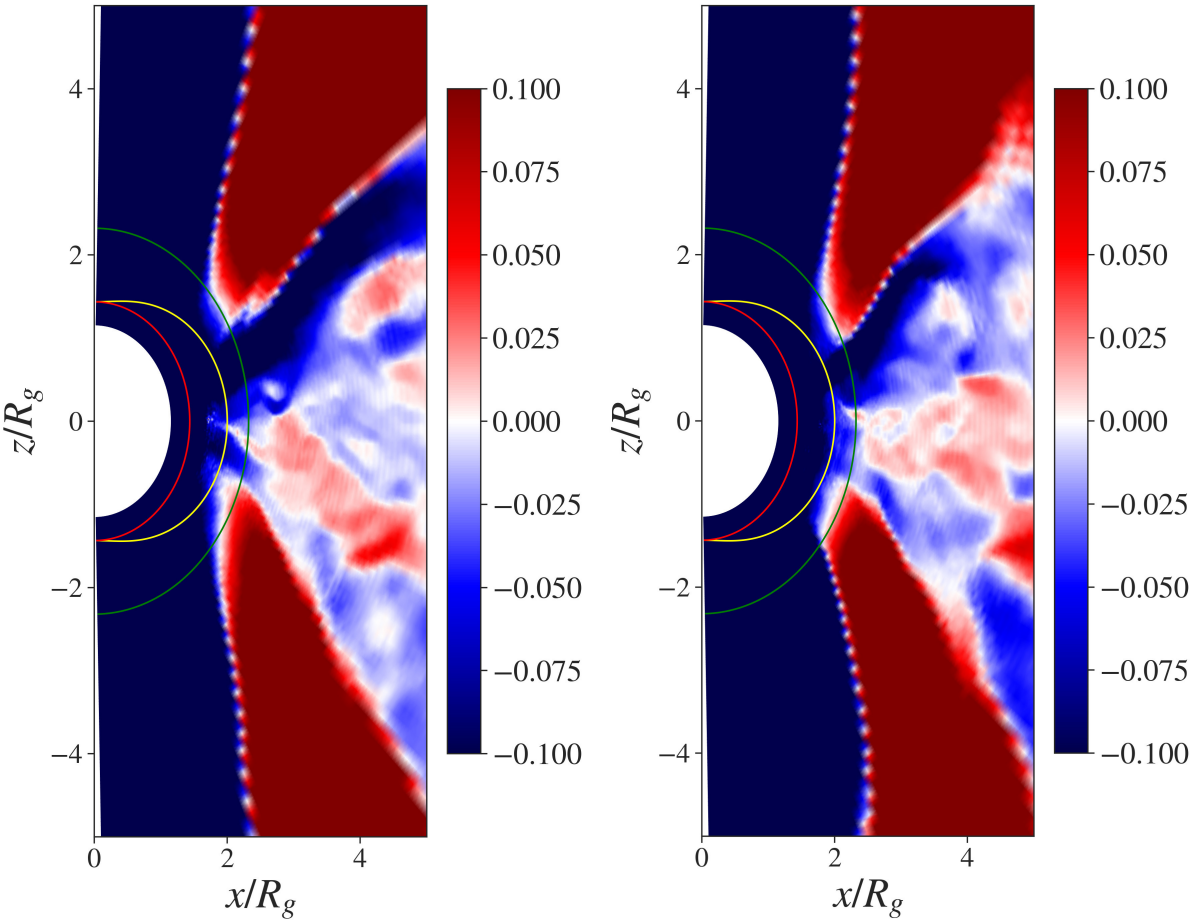

FIGURE 4.4: Turbulent dynamic structure of the inner disk. Shown is the radial velocity distribution at a short time interval, at $t = 3800$ (left) and at $t = 3850$ (right). Positive and negative velocities indicate the turbulent nature of the inner disk area. The red semicircle marks the horizon, the yellow line marks the ergosphere, and the green line indicates the radius of the ISCO.

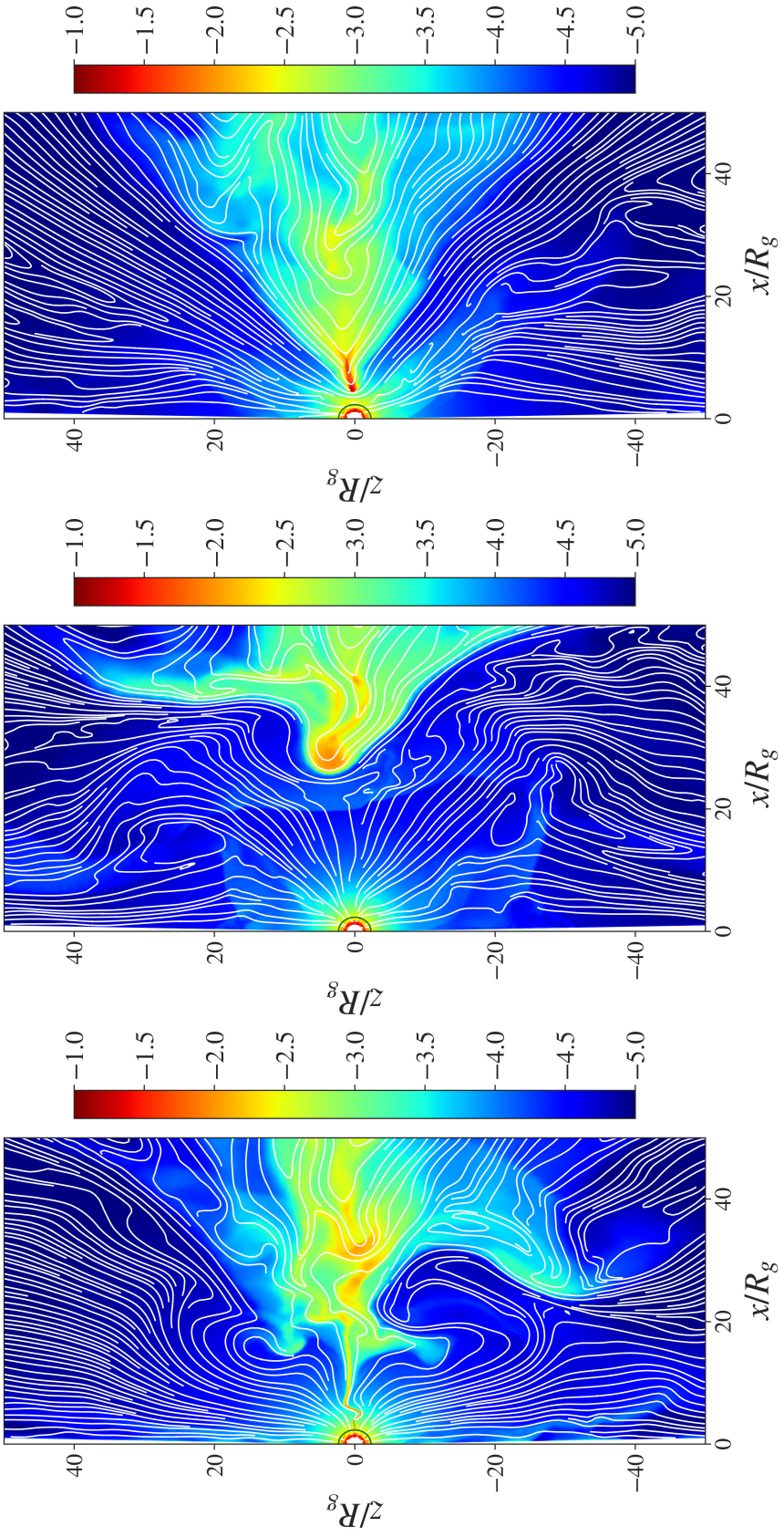

FIGURE 4.5: Snapshots of of our reference simulation. Shown is the density distribution (log scale) at times $t = 8000$, 8500, and 9000. The poloidal magnetic field lines are shown (white lines). At late times the accretion disk disconnects from the black hole, which results in halting of mass accretion and ejection of the BZ jet.

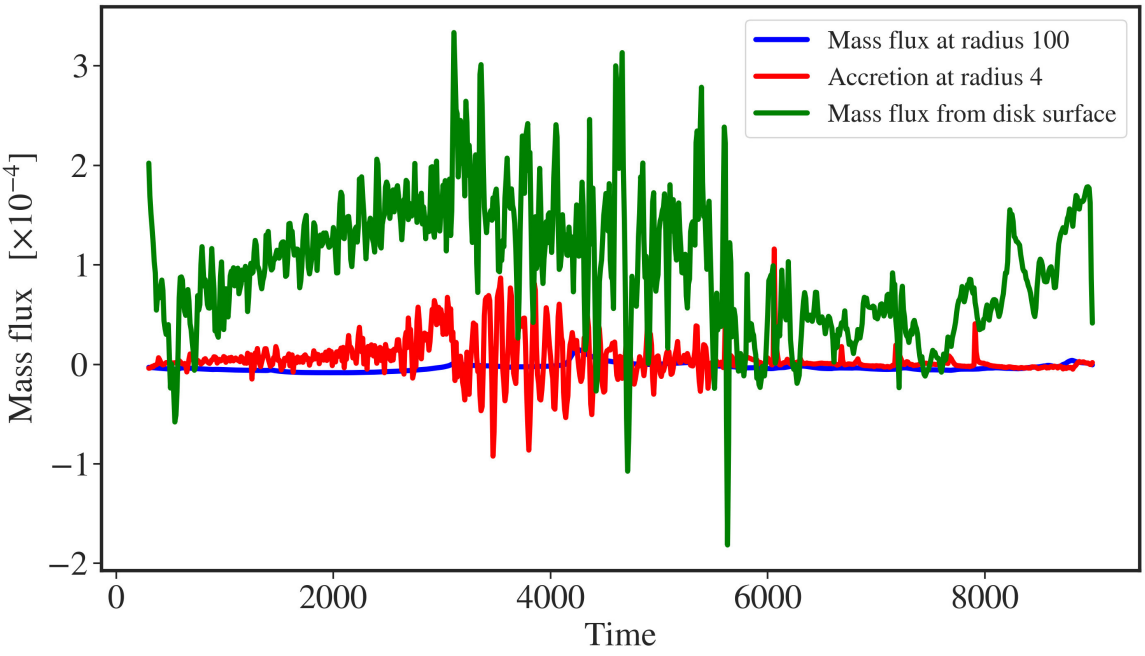

FIGURE 4.6: Integrated mass flux through the outer disk at $r = 100$ (blue), through the inner disk radius at $r = 3$ (red), and through the disk surfaces (green).

arrested disk (MAD; see Igumenshchev, Narayan, and Abramowicz (2003)). When the magnetic flux is advected to the black hole respectively to the rotational axis, the magnetization in this area decreases again, and accretion restarts (see Fig.4.5).

Finally, in Figure 4.6 we display the mass fluxes vertical to the surfaces of constant opening angles ($\theta = 80°, 100°$) that approximate the surfaces of the initial disk density distribution. We see that the mass fluxes of accretion and radial outflow along the disk are comparable. However, both are dominated by the vertical mass loss from the disk surface. The low accretion rate is comparable to an MAD structure (Tchekhovskoy, Narayan, and McKinney, 2011) and due to the strong disk magnetic field, a strong outflow is launched, but at the same time the accretion rate decreases. Obviously, also the strength of magnetic diffusivity plays a role (see our comparison study below). We may conclude that most of the mass that the disk is losing is due to the strong disk wind that is launched.

We note that since a substantial disk wind is present during the whole simulation, the wind mass-loss rate is changing. The wind mass flux increases until about $t = 3000$ and then decreases again until $t = 6000$. In the late stages of the simulation the wind mass flux is highly variable. These two different phases of wind ejection seem to correspond to similar phases in the disk accretion, visible in Figure 4.3 (middle panel), which shows large variations in the mass accretion rate, or in Figure 4.2, which indicates a change in the disk mass evolution at $t = 3000$.

In order to double-check our mass flux integration, we have measured the total mass loss of the disk with two different methods. First, we integrate all mass flux, leaving the surfaces of the disk area as specified previously. Second, we calculate the mass loss from the mass evolution of the disk (see Figure 4.2). Figure 4.7 compares the time evolution of the two measurements. Essentially, both show excellent agreement, confirming our methods to determine the evolution of the disk.

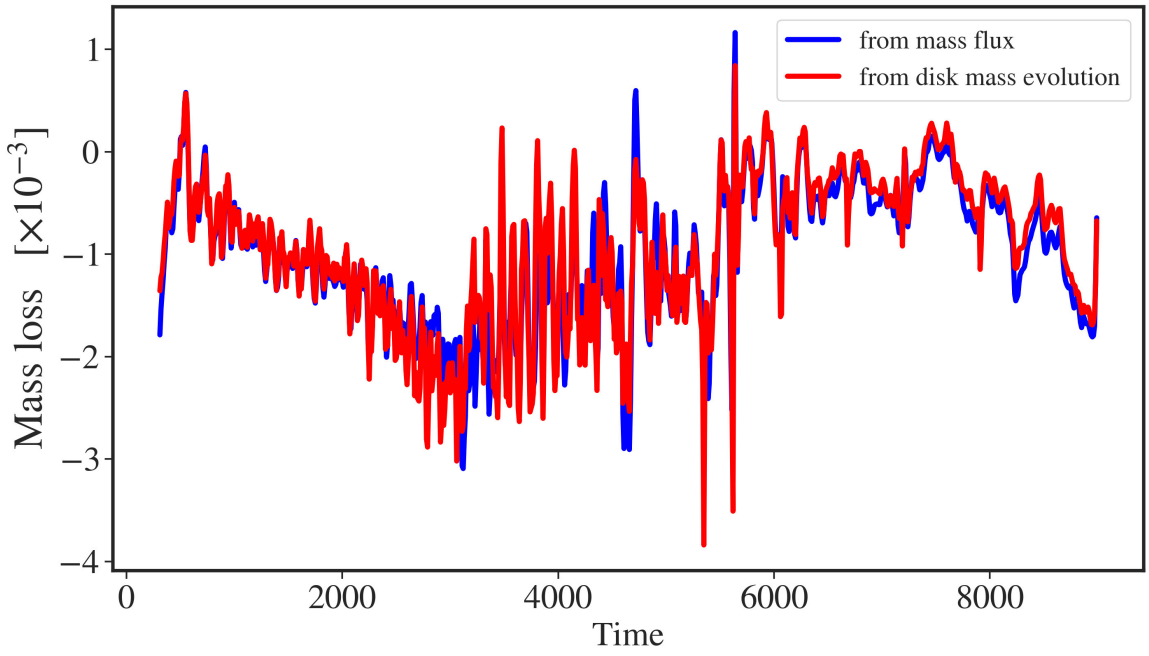

FIGURE 4.7: Comparison of the disk mass loss as calculated directly from the disk mass evolution (red) and from the outflow mass flux (blue). Both curves coincide, demonstrating the robustness of our integration tools.

The mass loss remains negative for the majority of the simulation, with small exceptions of momentary mass increase especially in the later stages. On average, we have a mass-loss rate of the order of $10^{-3}/t_{\rm g}$. The rate of mass loss, however, changes a lot, following a repeating pattern similar to the one appearing in the vertical mass flux from the disk surface, demonstrating that the large mass loss is due to the disk wind. Based on Figure 4.6, if we integrate over time, we find that out of a total of 85% of the disk mass lost during the simulation, approximately 73% is from the disk wind, 10% is from accretion to the black hole, and 2% is across the outer disk radius.

4.1.3 Outflow from the Black Hole Magnetosphere

The most prominent feature of our reference simulation (as visible in Figure 4.1) is the outflow that develops from the area around the black hole. It starts around $t = 1000$ with the advection of magnetic flux toward the black hole. The field lines that enter the ergosphere are being twisted and turned along the toroidal direction, creating eventually a jet toward the polar direction, according to the BZ mechanism (Blandford and Znajek, 1977). Up to $t = 3000$, this jet has been fully developed, and it enters a quasi-steady state until the end of the simulation ($t = 9000$), even though its strength still depends on the advection of the magnetic flux and, through that, on the accretion rate of the disk. The jet is identified by a parabolic-shaped funnel of high-velocity fluid that originates from the area around the black hole and moves almost parallel (in the later stages) to the symmetry axis toward the outer parts of our domain.

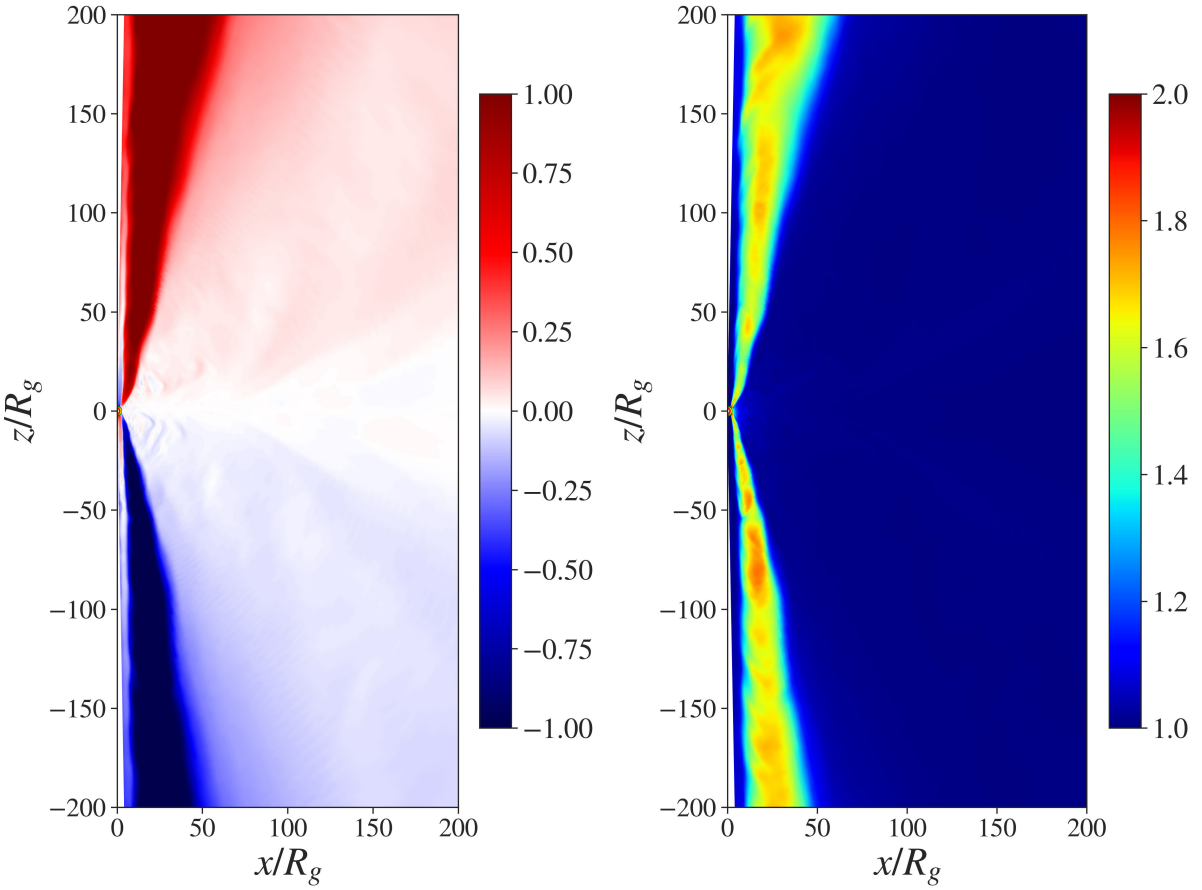

FIGURE 4.8: Vertical component of the velocity and the Lorentz factor on a subgrid of 200 R_g.

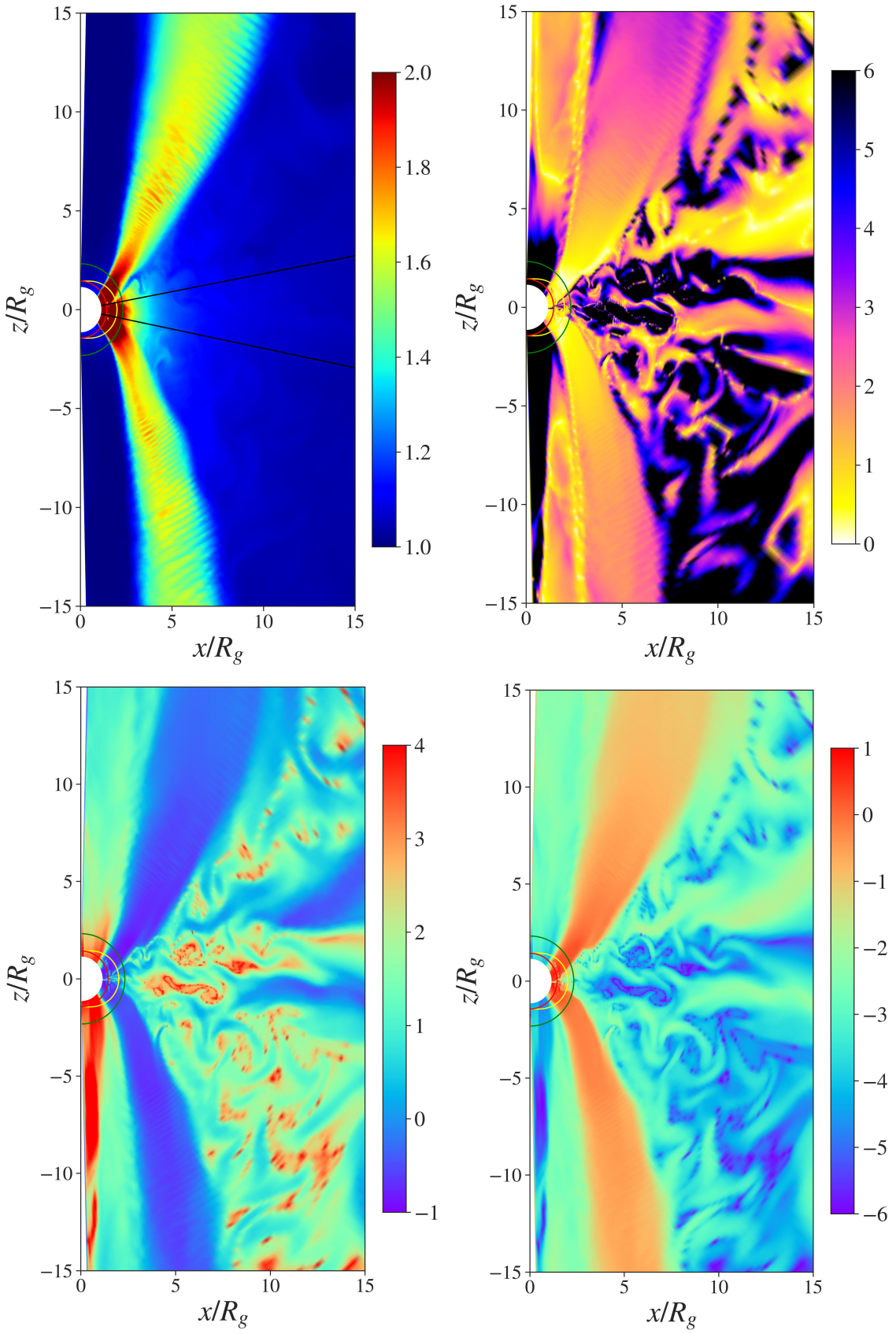

FIGURE 4.9: Magnetohydrodynamic accretion-ejection structure close to the black hole, $r < 15$ at $t = 4000$. Shown is the Lorentz factor (left), the poloidal Alfvén Mach number (log scale; second from left), the plasma-β (log scale; second from right), and the magnetization ρ/B^2 (log scale; right). The high Alfvén Mach number indicates flows that are dominated by kinetic energy, regardless of the highly magnetized area. The red semicircle marks the horizon, the yellow line marks the ergosphere, and the green line indicates the radius of the ISCO.

The jet funnel can be seen clearly in Figure 4.8, where we plot the z-component of the fluid frame velocity and the Lorentz factor at time $t = 4000$. The jet seems to consist of fast-moving inner parts with $\gamma \approx 1.8$, a moderately fast moving envelope with $\gamma \approx 1.5$, and the outer part where the Lorentz factor values stay below $\gamma = 1.3$. The fast-moving inner parts seem discontinuous, and we can clearly distinguish 2-3 knots of high velocity in larger radii ($r > 50$), while closer to the black hole the high values of Lorentz factor seem to have a more continuous distribution (see Figure 4.9).

We select four radii, $r \approx 4,\ 12,\ 52$, and 75, where high-velocity knots appear. In Figure 4.10 we see how the radial velocity, the mass flux, and the electromagnetic energy flux (Poynting flux) per solid angle are distributed along the polar angle in these radii. In general, the Poynting flux distribution follows the high-velocity areas, proving that the jet funnel has a strong electromagnetic component. The mass flux in the funnel area does not show a significant increase in comparison with the disk wind area and the disk, where the mass density is considerably higher, since the accelerated material consists primarily of floor density values.

Figure 4.9 shows the Lorentz factor, the poloidal Alfvén Mach number, the plasma-β and the magnetization over an area of 15 $R_{\rm g}$ at time $t = 4000$. The highly magnetized funnel coincides with the high-velocity area of the jet. It starts as a sub-Alfvénic flow right outside of the ISCO; however, even though in the area of the funnel is highly magnetized (plasma-$\beta \approx 1,\ B^2/\rho \approx 1$), the flow is accelerated quickly to super-Alfvénic speed, indicating that it is dominated by kinetic energy.

4.1.4 Evolution of the Poynting Flux

We now examine the electromagnetic energy fluxes (Poynting flux) of our reference simulation. In Figure 4.11 we show the evolution of the integrated Poynting flux through a surface at radius $r = 100$. We further split our integration domain into the following three areas. The first region is between $0^\circ < \theta < 25^\circ$ and mainly covers the funnel region hosting the relativistic jet from the black hole magnetosphere. The disk wind area (covering larger polar angles) is split into two more regions (see also our Sect. 4.1.5). This is a region between $25^\circ < \theta < 65^\circ$, where the B_ϕ-dominated disk wind evolves and a region between $65^\circ < \theta < 80^\circ$, where the poloidal magnetic field dominates. [5] The chosen separation does not exactly follow the direction of the funnel, as the geometry of the funnel flow changes with time. However, it is a good approximation for the average location of the funnel, especially in higher radii. Note that even though the majority of the (bent) funnel jet is inside the opening angle we have just defined, at $r \approx 2-4$ it is rooted closer to the equatorial plane, resulting in very low values of Poynting flux measured for the launching region and higher values for the disk wind regions (see also Figure 4.10).

The three phases of the disk evolution can also be seen in the evolution of the Poynting flux of the jet funnel. In the beginning, the flux remains almost constant, but after $t = 3000$ it drastically increases, indicating the development of a strong jet. This is mainly due to the advection of magnetic field and energy toward the black hole, along with the mass accretion from the disk. Beyond $t = 6000$ – due to the high disk mass loss – the variability in the accretion rate triggers the Poynting flux, leading to strong variations in the funnel and in most of the disk wind.

[5] Section 4.1.5 discuss the different types of disk wind extensively.

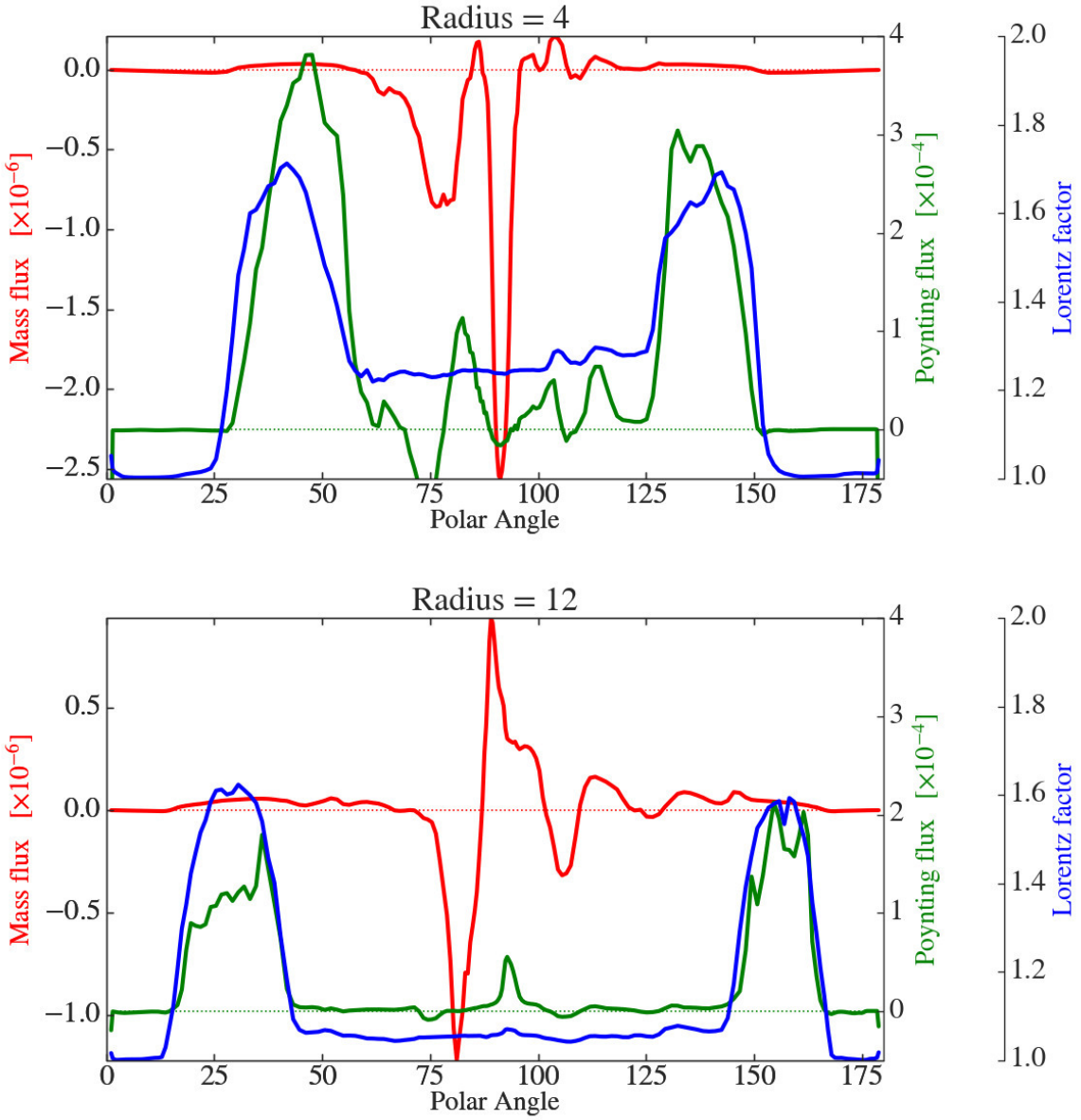

FIGURE 4.10: Comparison of the angular distribution of mass flux (red), Poynting flux per solid angle (green), and Lorentz factor (blue) for the reference simulation at $t = 4000$ at four radii, $r = 4, 12, 52$ and 75. Negative mass flux indicates accretion toward the black hole. The BZ-driven jet funnel is clearly distinguished by the peaks in Lorentz factor and electromagnetic energy flux. For increasing radii, the mass flux increases, demonstrating the matter-dominated disk wind. In low radii, between the rotational axis $\theta = 0, 180$ and the jet funnel floor density material falls toward the black hole.

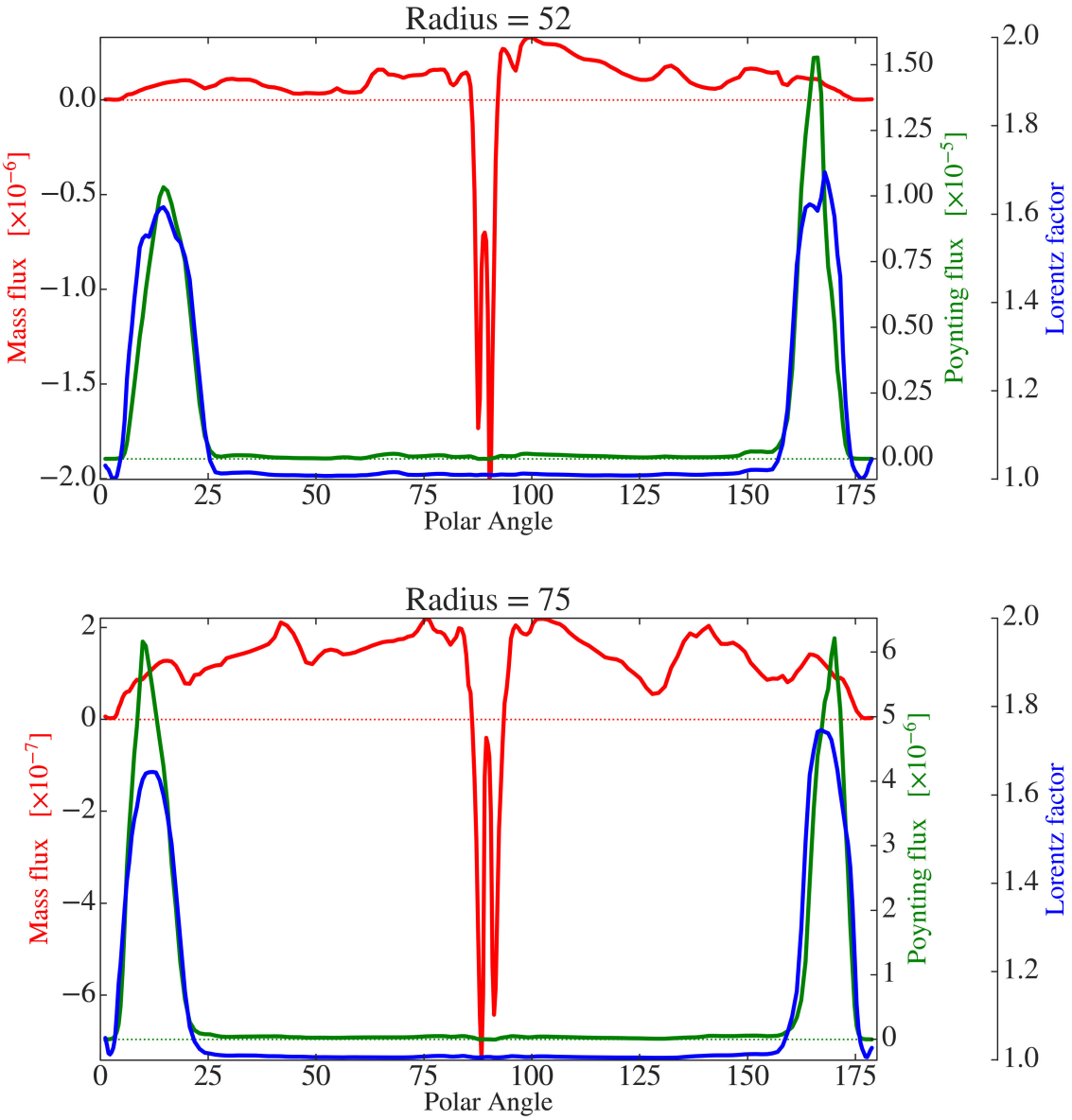

FIGURE 4.10: Comparison of the angular distribution of mass flux, Poynting flux, and Lorentz factor (cont).

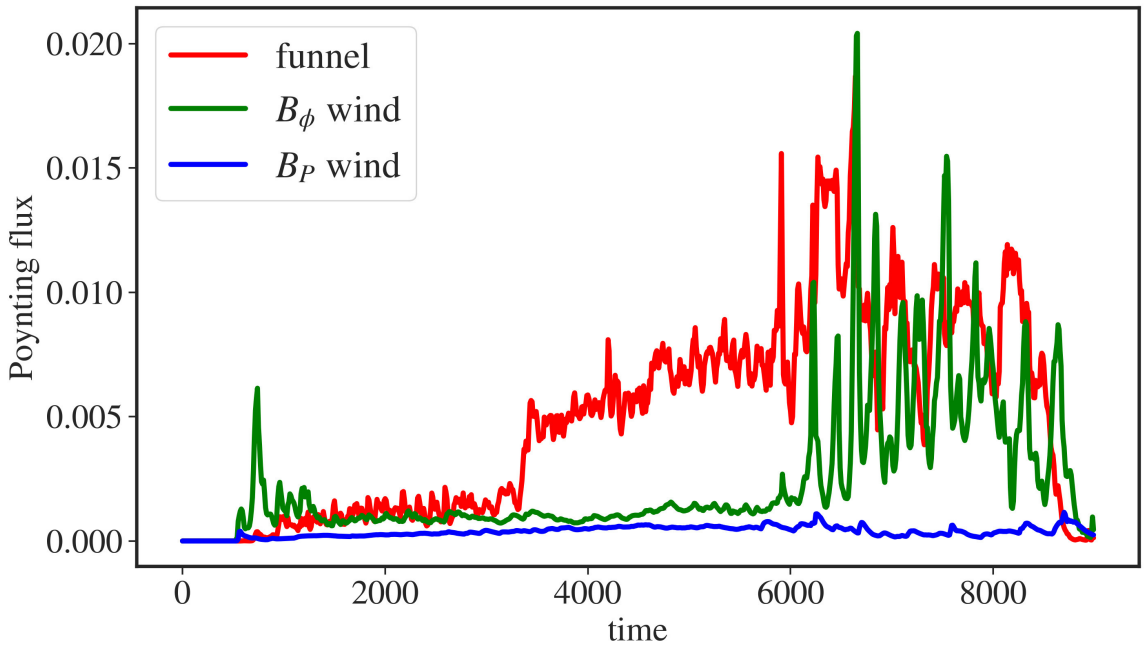

FIGURE 4.11: Evolution of the total Poynting flux for our reference simulation at radius $r = 100$. We split our domain into three regions. The first is between $0° < \theta < 25°$, expressing the Poynting flux from the relativistic jet funnel (red). The second is between $25° < \theta < 65°$, which includes the B_ϕ-dominated disk wind (green). The third is between $65° < \theta < 80°$, which includes the B_P-dominated disk wind (blue).

For the disk wind, at small radii the associated Poynting flux shows a steady increase with time. However, this is again an artifact due to integration area that cannot follow the bent geometry of the funnel flow. Also, the base of the funnel flow is partly extending beyond the chosen integration domain (limited to 25°). It is thus not accounting, for the initial funnel Poynting flux, but contributing to the Poynting flux we measure for the wind. This is indicated clearly in Figure 4.10. At larger distances, the Poynting flux remains at low levels, now following the true geometry of the disk wind. For the B_P-dominated disk wind the Poynting flux has very low but still positive values in the outer radii.

Table 5.1 shows the time-averaged Poynting flux measured at radius $r = 100$ for the three previously mentioned angular regions. As probably expected, the higher values of Poynting flux are detected in the jet funnel, about two times larger than the corresponding flux in the disk wind. The B_ϕ-dominated disk wind also drives a Poynting flux about six times larger than the flux in the B_P-dominated disk wind. In total, the electromagnetic energy output of the disk is led mainly by the Poynting-dominated jet from the black hole. where we also detect the highest velocities.

This seems to contradict earlier results (Qian, Fendt, and Vourellis, 2018) indicating a disk wind substantially contributing to the total electromagnetic flux. We think that the reason for this difference is mainly the shorter live time of the simulation in Qian, Fendt, and Vourellis (2018), in particular for the simulation with high spin. This is visible in Figure 4.11 where we see that for early times $t \simeq 500$ the Poynting flux of the B_ϕ-dominated wind (green

curve) dominates the inner jet.

4.1.5 The Accretion Disk Wind

The origin of accretion disk winds has been studied in the context of both AGNs and YSOs. Numerous works have investigated the launching mechanisms, especially in the nonrelativistic regime (Casse and Keppens, 2002; Zanni et al., 2007; Sheikhnezami et al., 2012; Stepanovs and Fendt, 2014). It has become clear since the seminal work of Ferreira (1997) that the magnetic resistivity is a key parameter for the investigation of the disk wind since it allows the gas to penetrate the magnetic field lines and thus allows for both (i) advection toward the black hole and (ii) mass loading the disk wind.

In a strong disk magnetic field, magnetocentrifugally accelerated outflows can be driven once the material is lifted from the disk plane into the launching surface, usually located around the magnetosonic surface. Qian et al. (2017) and Qian, Fendt, and Vourellis (2018) have extended the study of disk winds to the general relativistic regime. However, they have found that - in contrary to nonrelativistic disks - it is mainly the pressure gradient of the toroidal magnetic field that launches of disk winds, while the energy output by the disk wind can indeed be comparable to the BZ outflow launched by the BH. In addition (or rather as a consequence), disk winds from relativistic disks are quite turbulent and do not evolve in the smooth outflow structures that are known from nonrelativistic cases. In this section we continue the analysis of the disk outflows, extending their study to (physically) larger grids of higher resolution.

4.1.5.1 General Overview

In Figures 4.12 and 4.13 we present the velocity structure, the Alfvén Mach number, and the plasma-β for different areas of the disk wind. In order to emphasize the dynamic range of the disk wind, we restrict the velocity plots to $v_{\rm p} < 0.1c$.

The plots of radial velocity (Figure 4.12 left, and Figure 4.13 top) nicely demonstrate the wind launching surface where the radial velocity changes sign, thus indicating the transition from accretion to ejection. The total poloidal velocity vectors start from inside the disk, where accretion dominates, and then continue across zero-velocity surface into the disk wind. The radial disk wind velocity increases as the wind leaves the disk surface, reaching up to $u^r = 0.1c$ and following the magnetic field lines. Our vectors clearly demonstrate the connection between disk accretion and wind ejection.

In Figure 4.13 we show the poloidal Alfvén Mach number $M_{\rm A,p}$. The Alfvén surface is located slightly above the disk surface (which we defined by $u^r = 0$), implying that the fluid leaves the disk surface with sub-Alfvénic speed, $M_{\rm A,p} < 1$. However, it quickly accelerates to super-Alfvénic velocity. This is a major difference from the nonrelativistic launching simulations we have cited above, where the extension of the sub-Alfvénic regime is more comparable to the self-similar solution described by Blandford and Payne (1982), in which the flow in the area close to the disk is magnetically dominant, with matter accelerated along the field lines by the magnetic stress (or so-called *magnetocentrifugally*). The flow then consecutively passes the Alfvén and the fast-magnetosonic surface, before it becomes collimated by magnetic tension.

That mechanism may work as well for relativistic jets has been suggested by numerical simulations by Porth and Fendt (2010), however without considering the launching process out of the accretion disk. In our reference simulation, the picture is quite different, with an Alfvén surface much closer to the disk surface. The flow reaches super-Alfvénic speed of $M_{\mathrm{A,p}} > 5$ already in the altitude of $z < 10$ from the disk midplane. Thus, we conclude that we do not find evidence for a large BP-driven region of the disk wind, and the outflow is most probably driven by the magnetic pressure gradient of the toroidal field, thus as a so-called magnetic tower (Lynden-Bell, 1996).

We also need to compare the magnetic pressure to the gas pressure. This is done in Figure 4.13 where we present the distribution of plasma-β in the area of the disk. Inside the disk, we find plasma-$\beta > 100$ (as prescribed by our initial condition), but as we move away from the disk surface, the plasma-β quickly starts decreasing to values between 10 and 1 or even lower. This finding supports the idea of a magnetic-pressure-driven disk wind.

Interestingly, we find that the disk wind separates into two components considering the plasma-β. There is an inner component of the disk wind that develops from the innermost part of the accretion disk ($r \lesssim 10$). This wind component has a rather high gas density and pressure, resulting in high poloidal plasma-β and low magnetization, $B^2/\rho \sim 0.0001$. The second wind component originates from larger radii, and it is dominated by the poloidal magnetic field. We will first describe the inner wind component.

4.1.5.2 B_ϕ-dominated Disk Wind

Considering the strength of the magnetic field components, we see that the toroidal field dominates the poloidal magnetic field. This is shown in Figure 4.13 where we plot the ratio $|B_\phi/B_{\mathrm{P}}|$. In particular, the wind from the inner disk carries a toroidal field 10 times larger than the poloidal component. We believe that this results from the fact that at this time the innermost part of the disk has completed a larger number of orbits: at time $t = 4000$ and at $r = 5$ we have almost 50 orbits, compared to about 18 at $r = 10$ and only 10 at $r = 15$. Hence, simply the twist of the originally poloidal magnetic field may induce such a strong toroidal field component. If the simulation would evolve further, we expect this area of a toroidaly dominated magnetic field to grow along the disk.

We find that the radial velocity of the disk wind is not homogeneously distributed but contains patches of negative speed. These patches coincide with areas of strong toroidal velocity, which usually accompanies the toroidal magnetic field in the super-Alfvénic flow regime (Figure 4.13, bottom right panel).

The turbulent nature of the wind seems to damp down as the wind moves farther away from its source. Unsteady, super-Alfvénic outflows are well known from nonrelativistic simulations. For example, Sheikhnezami et al. (2012) observe a similar structure for the overall disk wind in high plasma-β simulations. These outflows are dominated by the toroidal magnetic field component, also known as tower jets (see below), and are accelerated by the vertical toroidal magnetic field pressure gradient. However, in our simulations we notice that this turbulent outflow layer has a certain, rather narrow opening angle. If we assume that the extent of this layer defines a characteristic length, we may also assume that the extension of this structure in the ϕ-direction may be similar, possibly hinting to a series of outflow tubes around the disk. Interestingly, Britzen et al. (2017) have recently suggested that such

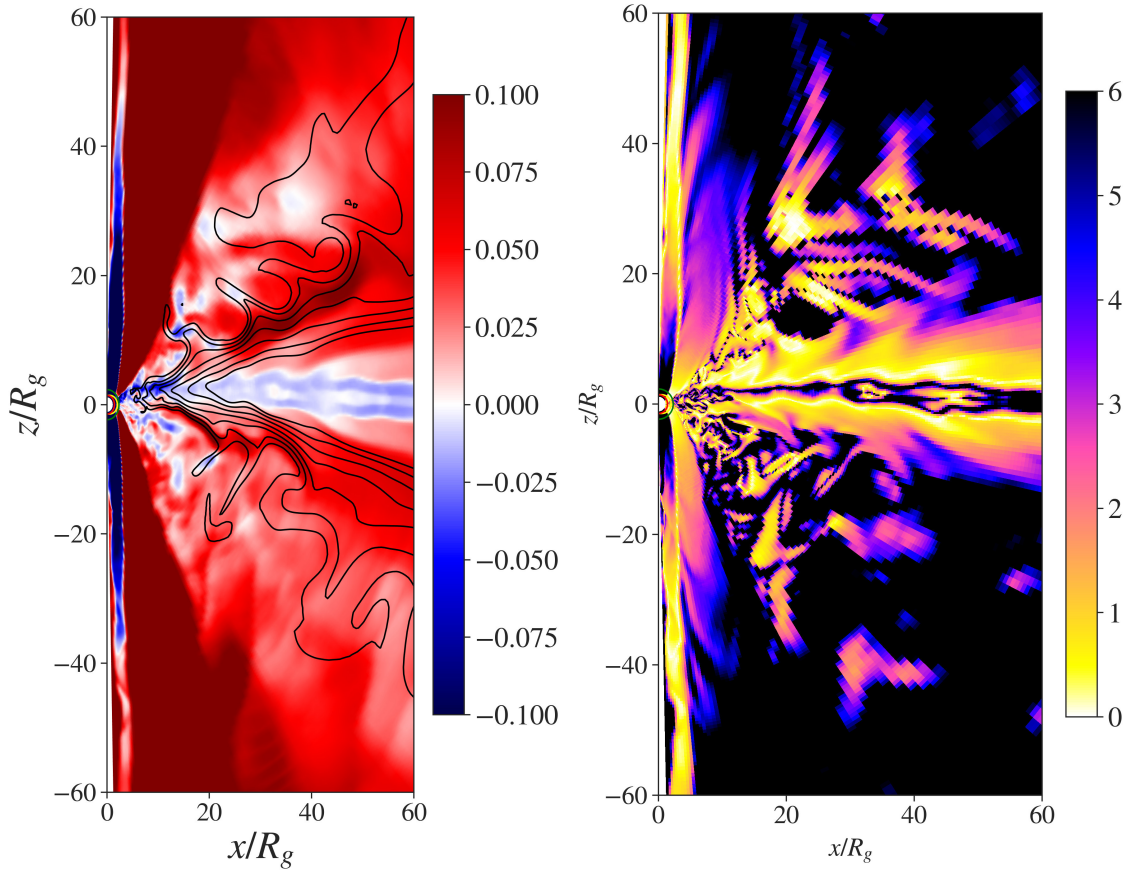

FIGURE 4.12: Reference simulation *sim0*. Shown are the radial velocity (left), with superimposed contours of the vector potential (black lines), and the Alfvén Mach number (right), both at time $t = 4000$.

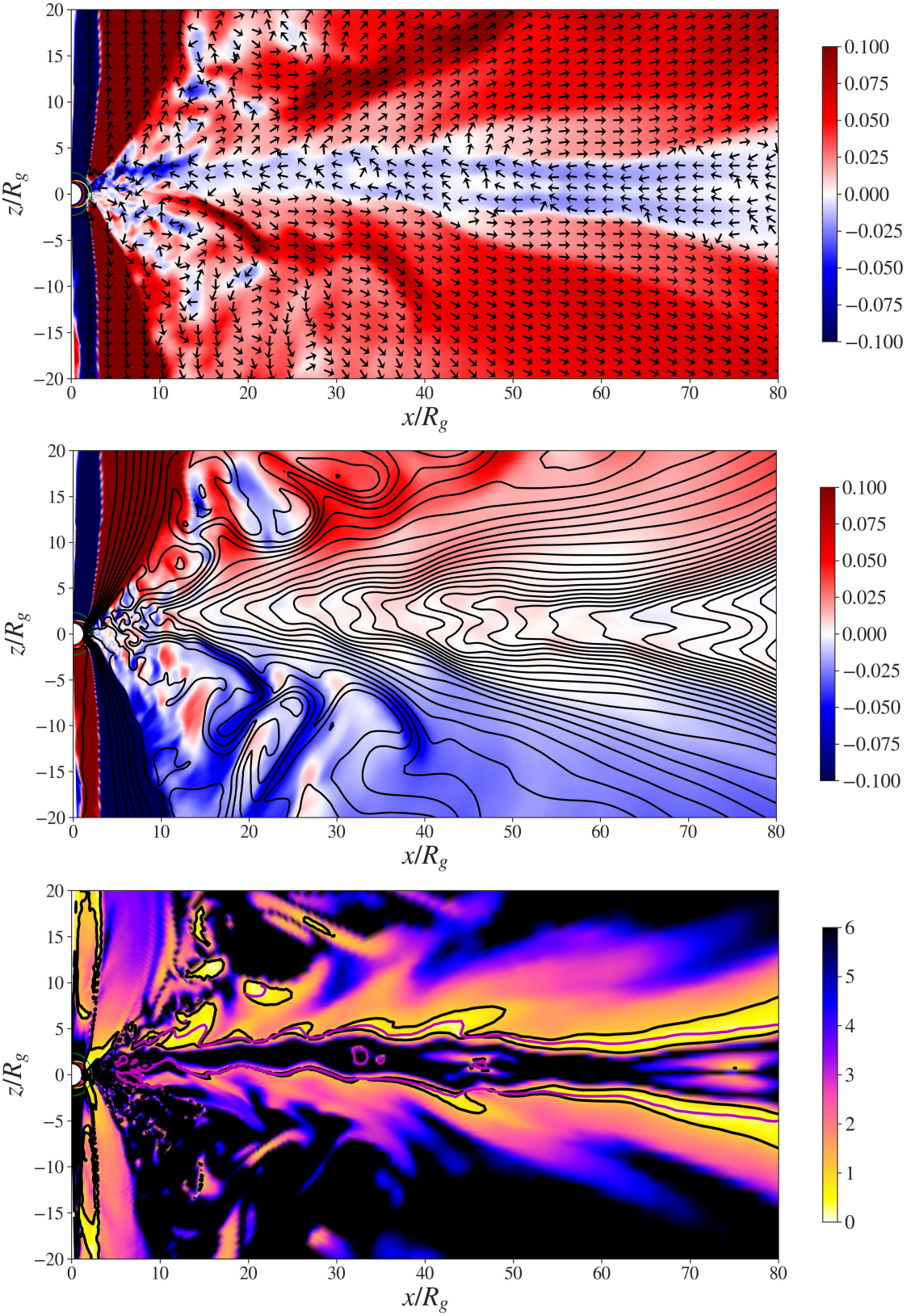

FIGURE 4.13: Snapshots of the disk area for different physical variables for simulation *sim0* at time $t = 4000$. We show the radial velocity (colors) with poloidal velocity (black arrows), the vertical velocity (colors) with magnetic field lines (black lines), the poloidal Alfvén Mach number superimposed with the Alfvén surface (black lines), the plasma-β, the ratio between the toroidal and poloidal magnetic field components $|B_\phi/B_{\rm P}|$ (log scale) and the ratio between toroidal and poloidal velocity $|u_\phi/u_{\rm P}|$ (log scale). The white line defines the area where u^r changes sign, $u^r = 0$.

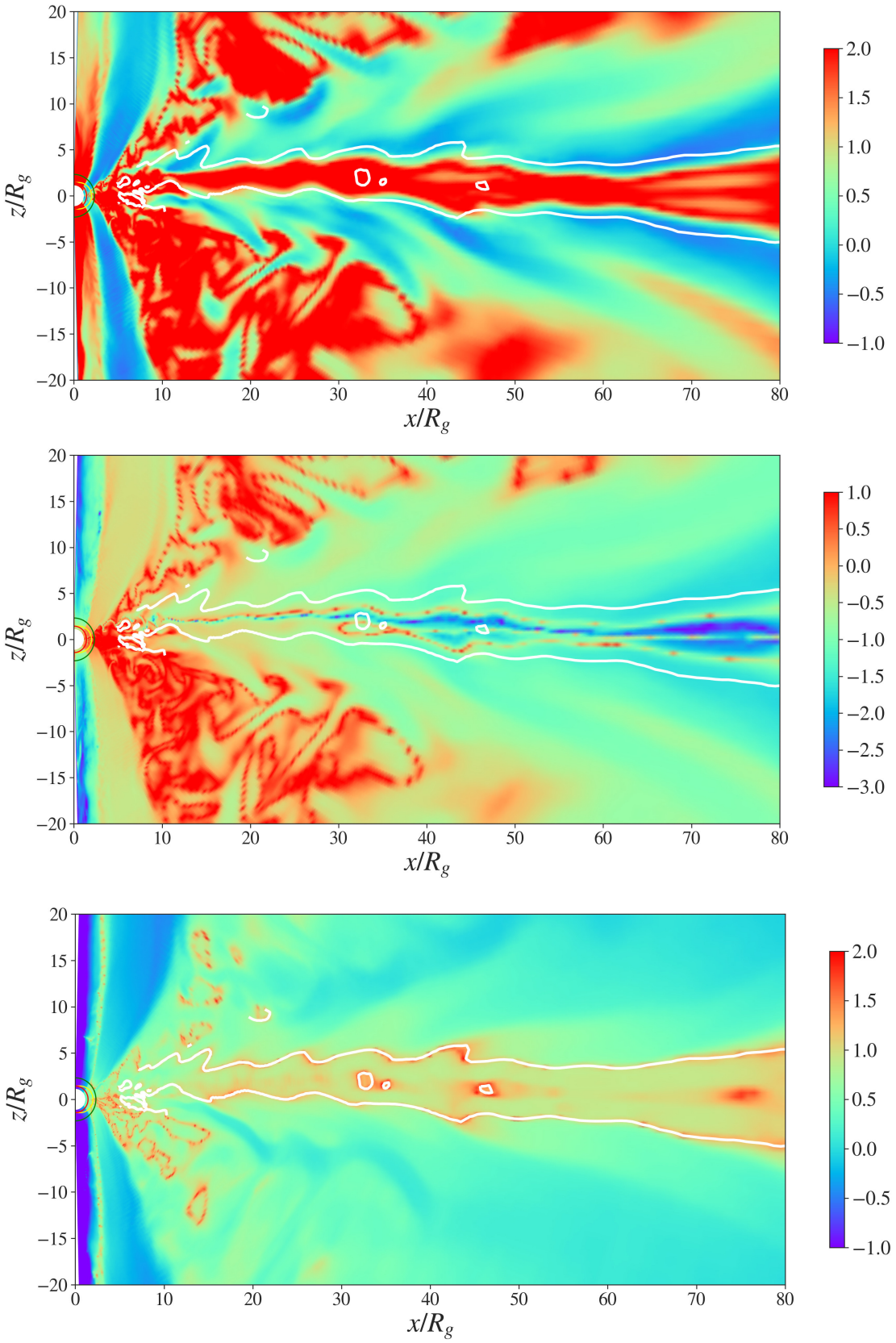

FIGURE 4.13: Snapshots of the disk area for different physical variables for simulation *sim0* at time $t = 4000$ (cont).

turbulent loading of jet channels may happen in M87, leading to large-scale episodic wiggling of the overall jet structure.

In Figure 4.13(top right) we show the z-component of the velocity, where we can distinguish a number of "branches" with values higher than in the adjacent area. These branches are actually part of the B_ϕ-dominated disk wind. They seem to stay connected to the surface of the disk from where they are originally launched and then continue through the B_ϕ-dominated wind following the poloidal magnetic field lines. The footpoint of the branches coincides with highly magnetized disk areas. This might explain the acceleration within the branches - on the other hand, when this material enters the B_ϕ-dominated wind, the plasma-β *increases* without weakening the acceleration. We note that the strong V_z component pushes the disk wind material toward the boundaries of the funnel outflow. As for an alternative scenario, we may think of a magnetic-pressure-driven radial outflow that drags the poloidal field with it, thus stretching it into a radially aligned poloidal field distribution.

4.1.5.3 B_p-dominated Disk Wind

We now discuss the second wind component that originates in the outer, main body of the disk. Here, for radii $r \gtrsim 10$, the $|B_\phi/B_\mathrm{P}|$ ratio decreases with radius and the poloidal field starts to dominate. This outer wind becomes launched almost parallel to the magnetic field lines (see velocity streamlines and poloidal field lines in Figure 4.13), and it retains that direction as well for larger distances. The vertical velocity component is substantially lower compared to the inner disk wind, implying a weaker acceleration despite the higher magnetization. When comparing the local escape speed with the local poloidal velocity of the disk wind, we find that the disk wind is launched with sub-escape velocity. However, the wind becomes further accelerated to $u_\mathrm{P} > u_\mathrm{esc}$ and becomes eventually fast enough to escape the gravity of the black hole.

In Figure 4.13 (first panel), we notice that in the area where the disk wind develops the wind tends to follow the radial direction in general. However, in Section 4.1.2 above we quantified the launching of the disk wind as mass flux escaping the disk surface in the polar direction (θ-component of the velocity). Thus, after being launched vertically from the disk surface, the wind further develops into a kind of radial outflow. This overall picture connecting between the launching in polar direction and the radial outflow can be verified by calculating the mass fluxes through the respective boundaries.

4.1.5.4 Connecting the Vertical and Radial Disk Wind

Following the considerations of the disk wind toward the end of Section 4.1.2, we show in Figure 4.14 the disk wind mass fluxes, only in this case we are interested in the situation at smaller radii, where the disk outflow is stronger. We calculate the mass fluxes vertical to surfaces of constant opening angle of $\theta = 80°, 100°$ that approximate the opening angle of the initial disk density distribution. We integrate the mass fluxes in the range $r = [4,\ 100]$ where we also separate between infall (motion toward the disk surface) and outflow (motion away from the disk surface), thus providing the net vertical fluxes. We find that the disk wind seems to increase for $0 < t < 3000$ while it decreases for $3000 < t < 6000$; overall we measure an average mass flux of $\langle \dot{M} \rangle = 9.72 \times 10^{-5} M_{0,\mathrm{disk}}$. The variations in the mass flux

during the second phase are much stronger; this is consistent with a similar behavior in the accretion rate (see Section 4.1.2 and Figure 4.3).

A similar behavior is observed in the radial mass fluxes. These increase or decrease with radius, depending on the phase during the simulation. Simultaneously, this is visible as an increase or decrease, respectively, in the mass load of the disk wind. Note that the latter we can also observe by measuring the difference in the two mass fluxes. The overall time-averaged mass flux is $\langle \dot{M} \rangle = 4.56 \times 10^{-5} M_{0,\mathrm{disk}}$ across a spherical surface at $r = 100$. The difference in the two mass fluxes is deposed as mass in the area of the disk wind increasing its density. Taking into account this mass sink, as well as all mass fluxes through the surfaces of the integration area, we find a good agreement between the radial and the disk wind fluxes for small time intervals. The remaining difference is due to the jet funnel that is constantly loaded by the floor model for the density and that naturally contributes to the radial mass fluxes and also increases the mass load in the radial wind.

Our detection of a B_ϕ-dominated disk wind confirms the results of Qian, Fendt, and Vourellis (2018), who interpreted their results in terms of a tower jet (Ustyugova et al., 1995; Lynden-Bell, 1996). However, the whole disk wind in Qian, Fendt, and Vourellis (2018) is entirely dominated by the B_ϕ, while in our simulation it is restricted to the disk wind from the inner disk only. As our new simulations have a higher resolution, Qian, Fendt, and Vourellis (2018) may have not been able to resolve the inner part of the disk wind properly.

4.1.5.5 Magnetic Reconnection and Ohmic Heating

Since the disk evolves in a resistive environment, we expect the generation of ohmic heating, which will affect the internal and magnetic energy in the disk. As we do not use radiative transfer, we cannot directly compare the energetics of ohmic heating with the emitted radiation.

However, we can attempt an estimation of the generated heating. For the reference simulation, we calculated an approximation of ohmic heating as $\eta \vec{J}^2$ and compared it with the internal and magnetic energy of the fluid. We separated the area into two parts – the first one is from $r = 5$ to $r = 20$, and the second one is from $r = 20$ to $r = 50$. Since the resistivity is concentrated to the accretion disk (and thus the ohmic heating), we also constrain the area between 5° above and below the equatorial plane. The ohmic heating is mostly generated from the inner part of the disk, as the magnetic field gradients ($j \propto B$) are largest over there.

We find that up to time $t = 5000$ ohmic heating generates a total energy of 1.5×10^{-4} (in code units). This is somewhat higher than the total magnetic energy in this disk area but substantially lower than the internal energy of the disk. At larger radii, from $20 < r < 50$ the ohmic heating rate is even lower, making it overall negligible in comparison with the magnetic and internal energy.

Another physical mechanism that contributes to the heating of our fluid is magnetic reconnection. It has been shown (de Gouveia dal Pino and Lazarian, 2005; de Gouveia Dal Pino, Piovezan, and Kadowaki, 2010) that in AGNs the magnetic reconnection episodes that occur mostly in the inner disk and the black hole magnetosphere can heat up the disk material and at the same time accelerate the ejected disk wind.

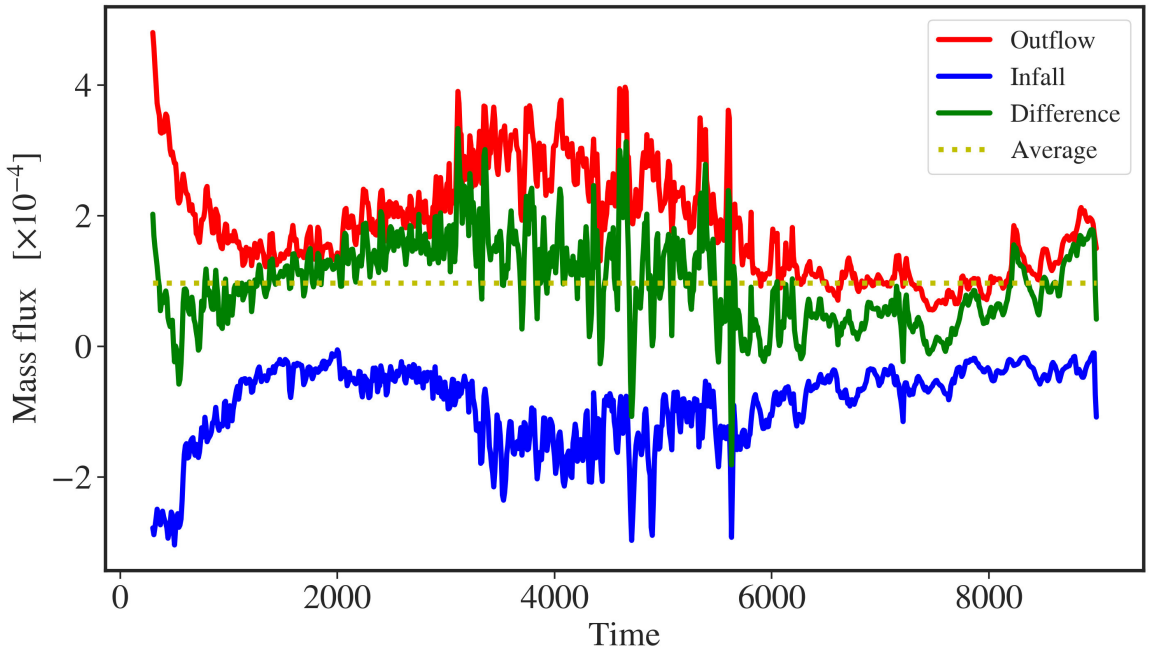

FIGURE 4.14: Mass fluxes in the reference simulation *sim0*. Shown are the outflow (red) and the inflow (blue) mass fluxes integrated along a constant opening angle (considered as the initial "disk surface") as a function of time. Mass flux away from (toward) the equatorial plane is counted as positive (negative). The difference of the two contributions is shown in green, while the average is shown by the yellow line.

4.2 Summary

As a reference simulation we applied the code for a setup considering a black hole with Kerr parameter $a = 0.9$ together with a disk magnetic diffusivity profile that follows a Gaussian distribution over the polar angle. We have investigated the physics of the accretion-ejection mechanism between the disk and the launched wind while focusing somewhat on the nature of the outflows and the development of the disk wind.

We provide a detailed study of the MHD characteristics of the disk-wind structure. A thin disk exists until accretion and disk wind have depleted the initial mass reservoir of the disk. We resolve the disk surface were accretion of material is turned into ejection. The Alfvén surface of the disk wind is close to the disk surface - the disk wind is thus launched with sub-Alfvénic speed, but quickly accelerated to super-Alfvénic velocities. The counter-rotating disk seems to develop a different accretion mode with layered accretion in the upper disk levels.

Two different types of disk winds were identified. The first one arises from the inner part of the disk $r \lesssim 10$ and is dominated by the toroidal magnetic field component, while carrying a large part of the mass flux. This type of disk wind has many similarities with the wind investigated by Qian, Fendt, and Vourellis (2018) where it was identified as a tower jet (Lynden-Bell, 1996). In contrast to Qian, Fendt, and Vourellis (2018) we observe a second type of disk wind. This feature is launched from the larger radii, and is dominated by the poloidal magnetic field. So far we believe that this is mainly due to the fact that the outer

disk is less evolved in comparison with the inner part. The B_ϕ-dominated disk wind shows higher radial mass flux even though it is not as highly magnetized.

Chapter 5

Dependence of Disk Outflows on Black Hole Spin and Diffusivity

In this chapter, will now compare our reference run *sim0* with a number of simulations that apply different black hole spin and magnetic diffusivity (see Table 5.1). Black hole rotation is an important part of the BZ mechanism and in the following we will study its effect in the outflowing electromagnetic energy. Resistivity has a strong effect the the diffusion of the magnetic field as well as in the accretion of disk material. We expect high diffusivity to allow material from the outer part of the disk to be accreted easier and then feed the outflows.[1]

5.1 Accretion-Ejection and Black Hole Rotation

We now discuss how the dynamical evolution of accretion-ejection interrelates with the black hole rotation, i.e. the Kerr parameter a. We first concentrate on the disk accretion. Figure 5.1 shows the disk accretion rates at $r \approx 2$ for the simulation runs *sim1*, *sim2* and *sim0*, each normalized with the mass of the respective initial disks.

While for *sim0* the accretion rate in the first stages of the evolution ($t \in [0, 3000]$) is constant and very low, for slower-rotating black holes the accretion rate shows a noticeable increase. Also, this first stage, which looks different from the later evolution, lasts longer in the case of $a = 0.9$. We think that this is due to the fact that the horizon ($r = 2$), and the ISCO ($r = 6$) are located closer to the initial disk radius. Therefore, it take less time to bring disk material to the ISCO, from which it falls to the horizon. At later stages, all simulations show a similar behavior, with only the accretion spikes in *sim0* being slightly stronger.

On average, for the duration of the simulation, the normalized accretion rate at $r = 2$ for the Schwarzschild black hole is slightly higher, $\langle \dot{M} \rangle = -1.59 \times 10^{-5} M_{0,\mathrm{disk}}$, while for the case of $a = 0.9$ we find $\langle \dot{M} \rangle = -7.49 \times 10^{-6} M_{0,\mathrm{disk}}$. Specifically, the three systems accrete 18.4%, 17.3%, and 11% of their initial disk mass into the black hole for the duration of the simulations.

[1] The contents of this chapter are adapted from Vourellis et al. (2019). The paper is published in the Astrophysical Journal. The author of the thesis run the simulations, analyzed the result and wrote the text for both the published paper and this chapter.

TABLE 5.1: Mass and energy fluxes for simulations applying different black hole spin a and diffusivity η_0. The average mass fluxes in units of 10^{-5} are measured over the whole simulation period and are normalized by the initial disk mass. The average Poynting fluxes are in code units of 10^{-3}. The average vertical wind mass flux is integrated along the radius vector along 80° or 100° up to $r = 100$. The average radial wind flux is integrated along a spherical surface at $r = 100$. Note that simulations *sim3, sim5, sim6* end before $t = 6000$. The columns show from left to right the simulation run ID; the spin parameter a; the maximum diffusivity η_0; the average accretion rate at $r = 2$, $\langle \dot{M}_{\rm acc} \rangle$; the average vertical mass flux $\langle \dot{M}_\theta \rangle$; the average total radial mass flux $\langle \dot{M}_r \rangle$ ($0_\circ < \theta < 80°$); the average mass flux in the jet funnel $\langle \dot{M}_r \rangle_{\rm fun}$ ($0° < \theta < 25°$); the average mass flux in the B_ϕ-dominated disk wind $\langle \dot{M}_r \rangle_{B_\phi}$ ($25° < \theta < 65°$); the average mass flux in the B_p-dominated disk wind $\langle \dot{M}_r \rangle_{B_{\rm P}}$ ($65° < \theta < 80°$); the electromagnetic energy flux in the funnel $\langle \dot{E}_{\rm EM} \rangle_{\rm fun}$ ($0° < \theta < 25°$); the electromagnetic energy flux in the B_ϕ-dominated disk wind $\langle \dot{E}_{\rm EM} \rangle_{B_\phi}$ ($25° < \theta < 65°$); the electromagnetic energy flux in the B_p-dominated disk wind $\langle \dot{E}_{\rm EM} \rangle_{B_{\rm P}}$ ($65° < \theta < 80°$); Values in parentheses show the percentage of each individual radial mass flux over the total radial mass flux.

Run	a	η_0	$\langle \dot{M}_{\rm acc} \rangle$	$\langle \dot{M}_\theta \rangle$	$\langle \dot{M}_r \rangle$	$\langle \dot{M}_r \rangle_{\rm fun}$	$\langle \dot{M}_r \rangle_{B_\phi}$	$\langle \dot{M}_r \rangle_{B_{\rm P}}$	$\langle \dot{E}_{\rm EM} \rangle_{\rm fun}$	$\langle \dot{E}_{\rm EM} \rangle_{B_\phi}$	$\langle \dot{E}_{\rm EM} \rangle_{B_{\rm P}}$
sim0	0.9	0.001	-0.75	9.72	4.15	1.02 (25)	2.40 (58)	0.73 (16)	4.89	2.38	0.38
sim1	0	0.001	-1.59	6.20	1.83	0.26 (14)	1.02 (56)	0.55 (30)	0.44	0.55	0.23
sim2	0.5	0.001	-1.57	7.51	2.88	0.67 (23)	1.57 (54)	0.64 (22)	2.87	1.29	0.32
sim3	-0.9	0.001	-1.27	5.77	4.88	0.96 (20)	3.48 (71)	0.44 (9)	3.00	4.52	0.21
sim4	0.9	0.01	-0.53	5.61	3.17	0.79 (25)	1.94 (61)	0.44 (14)	1.82	1.93	0.19
sim5	0.9	0.0001	-1.24	12.8	3.70	1.43 (39)	1.81 (49)	0.46 (12)	4.11	1.93	0.24
sim6	0.9	10^{-10}	-1.24	11.6	3.04	1.37 (45)	1.33 (44)	0.33 (10)	4.17	1.72	0.25

In Figure 5.2 we compare the disk wind that is launched from the disk surface. The disk mass flux is in general positive with few exceptions[2], meaning that there is a substantial mass injection from the disk into the outflow.

Following the same method as described toward the end of Section 4.1.5.4 we measure a normalized mass flux for the disk wind of $\langle \dot{M} \rangle = 6.2 \times 10^{-5} M_{0,\mathrm{Disk}}$ for the case of $a = 0$, a flux of $\langle \dot{M} \rangle = 7.41 \times 10^{-5} M_{0,\mathrm{Disk}}$ for the case of $a = 0.5$, and a flux of $\langle \dot{M} \rangle = 9.72 \times 10^{-5} M_{0,\mathrm{Disk}}$ for the case of $a = 0.9$. This implies that the three accretion-ejection systems accumulate a mass loss of 49%, 62.3%, and 80.7% of their initial disk mass by the disk wind. The cases $a = 0$ and $a = 0.9$ differ by almost 30% in the disk wind mass flux. For the radial fluxes there is a similar increase by 178% between the simulations applying $a = 0$ and the $a = 0.9$ (see Table 5.1). Thus, as an overall trend we find that the disk wind mass flux increases for higher black hole spin.

We understand that this is due to the ejection of mass that is launched from the innermost radii of disk accretion for high a (see Figure 4.3, middle panel). These ejections, and thus positive radial mass fluxes inside the disk, do not appear for the cases of low spin $a = 0$ and $a = 0.5$, for which accretion dominates, and which result in an overall lower disk wind ejection rate (see in Figure 5.2). There is also the interplay between the evolution of the disk structure in respect to the distribution of magnetic diffusivity. As the ISCO radius is affected by the Kerr parameter, the disk is located completely inside the high diffusivity area for $a = 0$, while part of the inner radii has lower diffusivity for the case of $a = 0.9$.

Note that the radius $r = 3$ is just outside the ISCO for simulation *sim0*, but inside the ISCO for *sim1* and *sim2*, which we think explains why no ejection is visible in the case of the latter two simulations. In order to check this hypothesis, we also measured the mass flux at $1R_{\mathrm{g}}$ and $2R_{\mathrm{g}}$ outside of the ISCO for each of our simulations. Only in simulation *sim0* does a positive mass flux from this radius appear, subsequently contributing to the increased mass flux we measure in the disk corona.

We further investigate the radial mass fluxes through a surface of radius $r = 100$. We find that the increase in the mass flux is much higher than in the vertical fluxes. We have also analyzed the radial mass flux of the disk wind by comparing the fluxes in three domains of the outflow (see Table 5.1 for numerical values). The innermost flow area is from 0° to 25°, and it indicates the mass flux in the Poynting-dominated jet. The adjoined area from 25° to 65° covers the B_ϕ-dominated wind launched in the innermost disk. The third domain from 65° to 80° contains the mass flux from the B_{P}-dominated disk wind. Obviously, we also include the fluxes from the lower hemisphere.

We recognize that our choice for the limits in the polar angle will not always coincide perfectly with the physical part of the flow we want to study. This holds especially in the earlier and later times of the simulations when both the jet and the disk wind are strongly evolving, either further being developed (early) or are dying off because of the disk mass loss (late). For the Poynting-dominated jet, the floor density model that dominates this area obviously determines most of the mass flux .

Comparing the simulations, we find that the relative contribution of the B_ϕ-dominated disk wind to the overall mass flux is similar for simulations *sim1*, *sim2* and *sim0* - even though in absolute values the wind mass flux increases with black hole spin. The relative contribution of the B_ϕ and the B_{P}-dominated disk winds, however, depends on on the black hole spin. In the case of a Schwarzschild black hole the B_ϕ-dominated disk wind contributes

[2]Most of the negative flux occurrences appear in the late stages of *sim1*

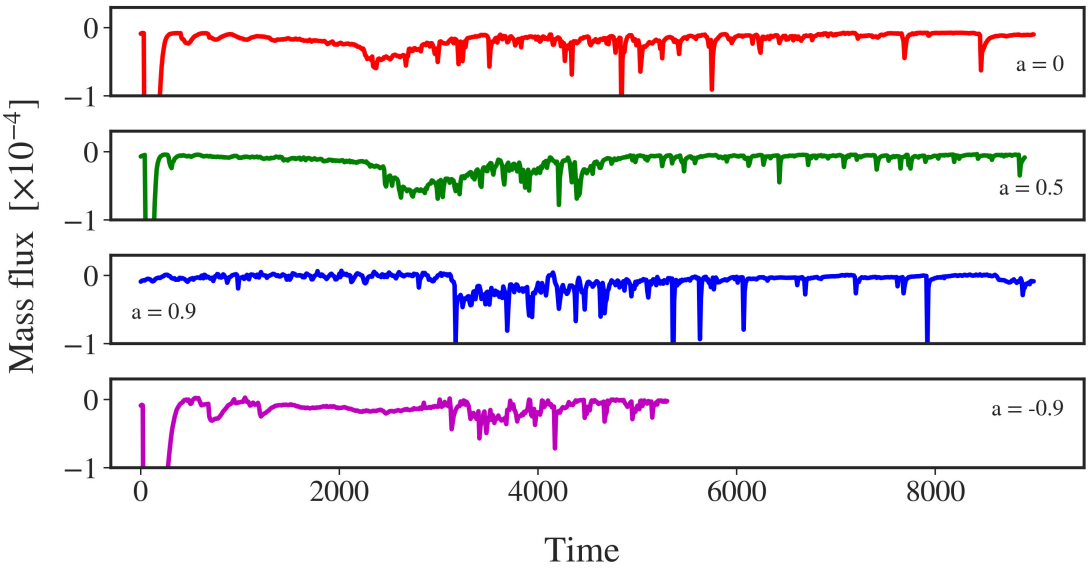

FIGURE 5.1: Accretion rate and black hole spin. Comparison of the accretion rates measured at $r \approx 2$ for simulation runs applying a Kerr parameter $a = 0$ (*sim1*, red), $a = 0.5$ (*sim2*, green), $a = 0.9$ (*sim0*, blue), and $a = -0.9$ (*sim3*, magenta).

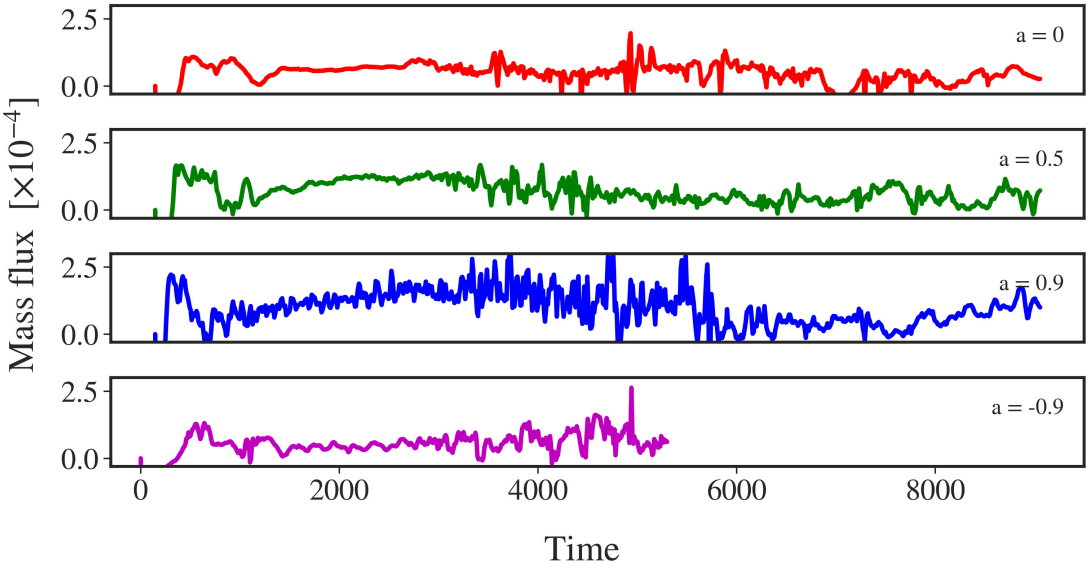

FIGURE 5.2: Ejection rate and black hole spin. Comparison of the vertical mass fluxes associated with the disk wind for simulation runs applying a Kerr parameter $a = 0$ (red), $a = 0.5$ (green), and $a = 0.9$ (blue), and $a = -0.9$ (magenta), integrated along the surfaces of constant angle at 80° and 100°.

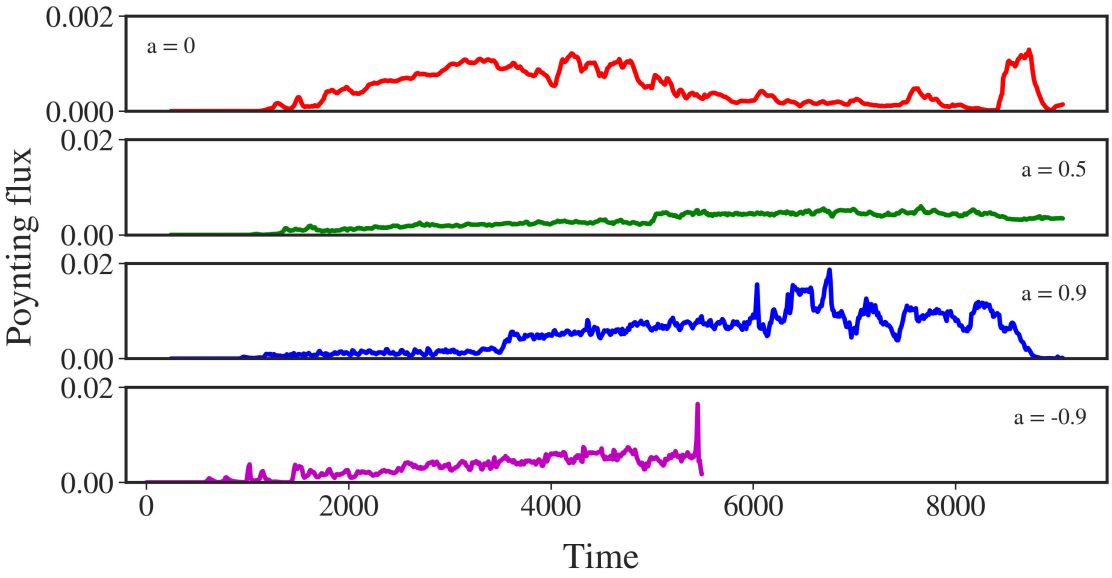

FIGURE 5.3: Poynting flux and black hole spin. Comparison of the radial Poynting fluxes at $r = 100$ for simulation runs applying a Kerr parameter $a = 0$ (*sim1*, red), $a = 0.5$ (*sim2*, green), $a = 0.9$ (*sim0*, blue), and $a = -0.9$ (*sim3*, magenta). Note that simulation *sim1* is scaled 10 times lower than the others.

65% to the total disk wind mass flux, while for the case of $a = 0.9$ the contribution is at 77%. For the counterrotating black hole the contribution increases to 89% while it shows the strongest wind also in absolute values. We conclude that the black hole rotation increases, not only the disk outflow mass flux in general but also contributes substantially in the B_ϕ-dominated disk wind as it is generated from the inner part of the disk.

Finally, we compare the Poynting flux in our simulations. Figure 5.3 shows the time evolution of the Poynting flux through a surface at $r = 100$ in the area of the funnel flow for the four different cases of black hole spin. There is a clear trend that the Poynting flux from the jet funnel increases with spin parameter. The highest Poynting flux appears in the reference simulation with $a = 0.9$. For simulation *sim1* the flux is substantially (factor 10) lower than for the simulation with a rotating black hole. Also, in *sim1* the absence of black hole rotation results in a relatively higher flux from the disk wind. A question arises on what drives the Poynting flux from a nonspinning black hole. We believe that this Poynting flux is driven by the rapidly rotating (infalling) material that is just outside the horizon in a fashion similar to the BZ mechanism. The magnetic field lines are twisted by the rotating disk, creating a jet with smaller electromagnetic energy flux.

5.1.1 A Counterrotating Black Hole

We now investigate how a counterrotating black hole affects the overall jet launching. It has been suggested that the efficiency of the BZ process in prograde systems is slightly higher compared to retrograde black hole-torus systems (Tchekhovskoy and McKinney, 2012). Here we extend this analysis for resistive GRMHD and for thin accretion disks. We have set up

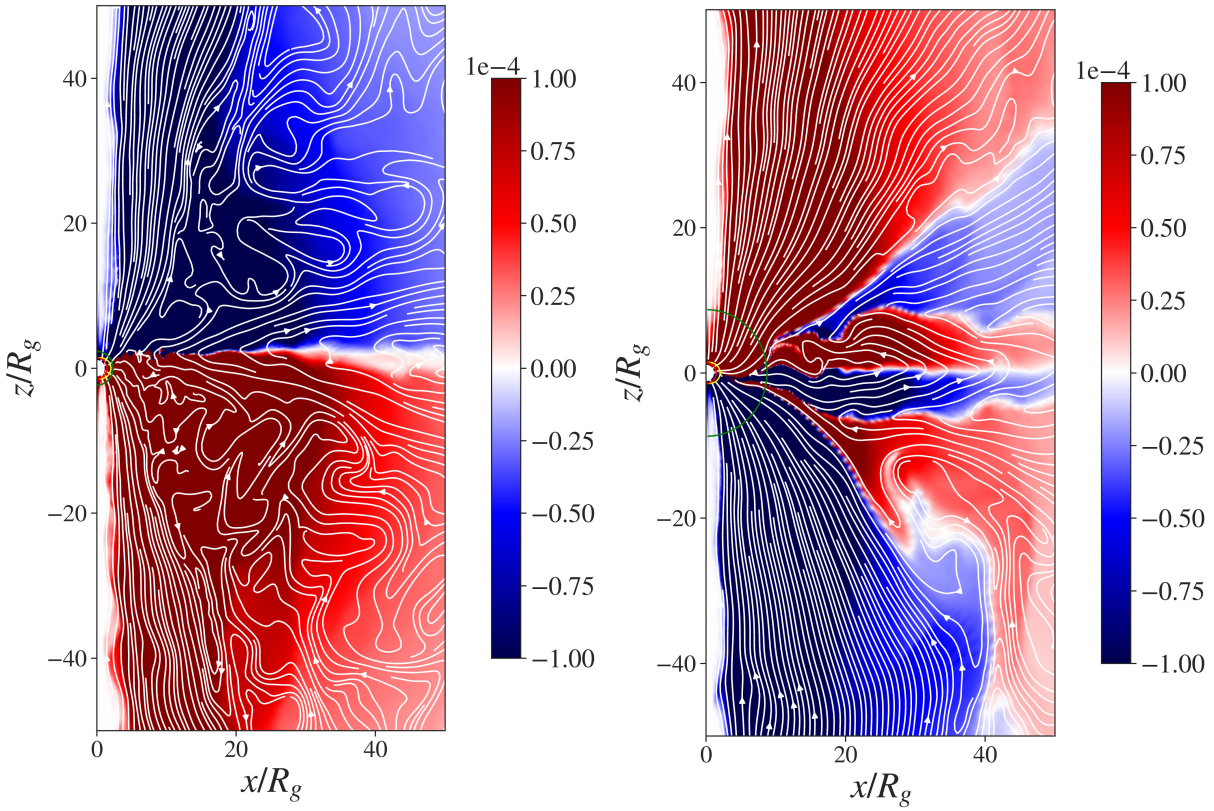

FIGURE 5.4: Counterrotating black hole. Comparison of the toroidal magnetic field component for simulation *sim0* with $a = 0.9$ (left) and *sim3* with $a = -0.9$ (right) at $t = 4000$. The white lines show poloidal magnetic field lines.

simulation run *sim3* with a negative Kerr parameter $a = -0.9$, but otherwise identical to our reference simulation.

A first comparison shows the accretion rate at radius $r = 2$ (see Figure 5.1) and the disk wind mass flux (see Figure 5.2) for both simulations. For $a = -0.9$ the ISCO is located at $r \approx 8.7$. As a result, since the inner radius of the initial disk is located farther in at $r = 7$, accretion toward the black hole starts immediately with a sudden infall of the disk area inside ISCO. Furthermore, the disk immediately looses a substantial fraction of mass, about 30% until $t = 300t_g$. Afterward, the disk structure adjusts such that its inner radius remains outside the ISCO and the normal – slow – accretion begins as soon as angular momentum is removed from the disk material.

All simulations start with an initial setup with $B_\phi = 0$. However, by the rotation of the footpoints of the field lines (accretion disk or space time) a toroidal field is induced. In the prograde simulations, the B_ϕ in the disk wind and the black hole magnetosphere have the same sign since both the disk and the black hole have rotate in the same direction. At the equatorial plane B_ϕ changes sign (see Figure 5.4, left panel), since the magnetic field lines are anchored at infinity.

In contrast, for the case of retrograde black hole rotation, simulation *sim3*, the B_ϕ in the black hole magnetosphere and in the outflow launched from there is induced with the opposite sign compared to the disk wind (see Figure 5.4, right panel), resulting in another boundary layer with $B_\phi = 0$ appearing between the jet funnel and the disk wind.

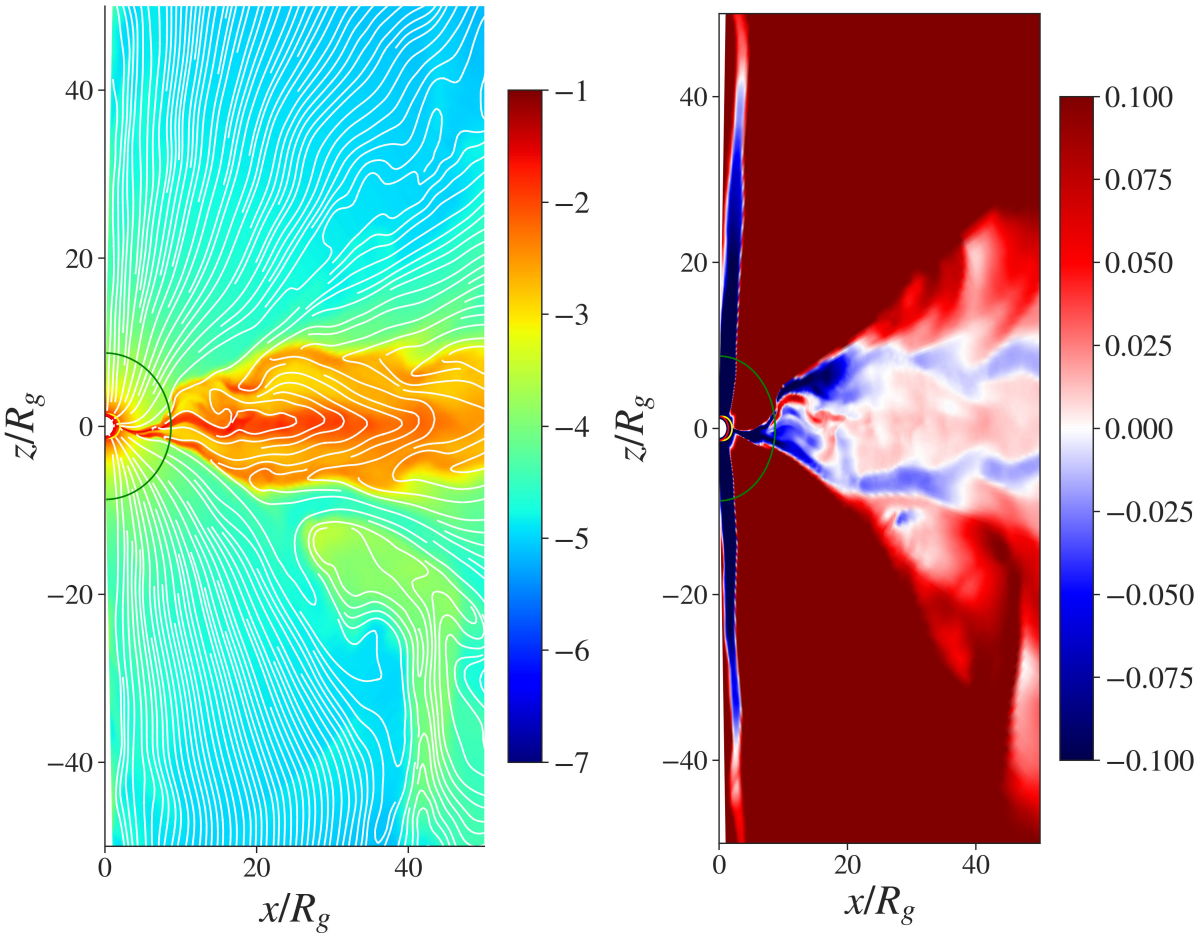

FIGURE 5.5: Counterrotating black hole. Density (log scale, left) and radial velocity (right) for simulation *sim3* with $a = -0.9$ at $t = 4000$.

While we expect (and find) the black hole-driven outflow to have a different sign for negative Kerr parameter, we would expect the disk wind to have B_ϕ with the same sign for positive and negative Kerr parameter, again with $B_\phi = 0$ and a change of sign at the equatorial plane. However, to our surprise, we find that in the disk area close to the inner disk radius the B_ϕ changes sign three times (instead of only once; see Figure 5.4). In fact, the B_ϕ in the wind above the disk surface is directed *opposite* to the B_ϕ below the disk surface[3]. Along the disk surface $B_\phi = 0$.

This also affects the poloidal component of the magnetic field (mainly the radial component), as it is visible purely from the shape of the field lines. The change of sign in B_ϕ close to the equatorial plane is intrinsically connected to the type of accretion: Figure 5.5 shows the radial velocity for simulation *sim3* and clearly indicates that inside the disk some material is moving *outward*, while accretion happens along the surface layers of the disk. For the case of prograde rotation, accretion is mainly along the equatorial plane. This unexpected behavior, however, does not affect the overall accretion rate.

For simulation *sim3* with $a = -0.9$ we find – similar to the prograde case – an outgoing Poynting flux, which is indicative of Blandford-Znajek launching. The Poynting flux in the funnel area increases with time, with a time average value of $\langle \dot{E}_{\rm EM} \rangle = 3 \times 10^{-3}$ at radius $r = 100$. For comparison, the Poynting flux at $r = 100$ for the prograde simulation *sim0* is $\langle \dot{E}_{\rm EM} \rangle = 4.89 \times 10^{-3}$. Furthermore, the Poynting flux from the disk wind appears to be stronger than the one from the funnel having a time average of $\langle \dot{E}_{\rm EM} \rangle = 4.52 \times 10^{-3}$ at $r = 100$. We do not find significant differences in the electromagnetic energy emitted within the funnel flow between the prograde and retrograde simulations.

It would have been interesting to follow the retrograde setup for a longer time, but the simulation stopped at $t \approx 5500$, most probably due to the high mass loss and also the complex magnetic field and velocity structure.

Although we find for the retrograde black hole rotation a few remarkable and also unexpected features that can be astrophysically interesting, we do not want to overinterpret, as we think that the retrograde case is not likely realized in nature. Retrograde black hole rotation may be realized by galaxy mergers with accompanied binary black hole mergers, but not from pure disk accretion. Similarly, counterrotating black hole-disk systems may be expected from specific initial conditions for neutron star mergers and thus may affect the subsequent gamma ray burst activity.

5.2 Impact of Magnetic Diffusivity

MRI is thought to be the main driver of turbulence in accretion disks (Balbus and Hawley, 1991; Balbus and Hawley, 1998). The feasibility of the MRI has been demonstrated also in GRMHD simulations (Penna et al., 2010; McKinney, Tchekhovskoy, and Blandford, 2012). Overall, turbulence results in a dissipative effect for the magnetic field, which we express through a mean magnetic diffusivity, in analogy to the α-effect for turbulent viscosity (Shakura and Sunyaev, 1973).

In contrast with ideal MHD, the disk material is now able to move across the magnetic field (lines) while accreting toward the black hole. The advection of magnetic flux is reduced owing to the weaker coupling between magnetic field and mass. It is thus worth investigating

[3]Of course similar for the upper and lower hemisphere respectively

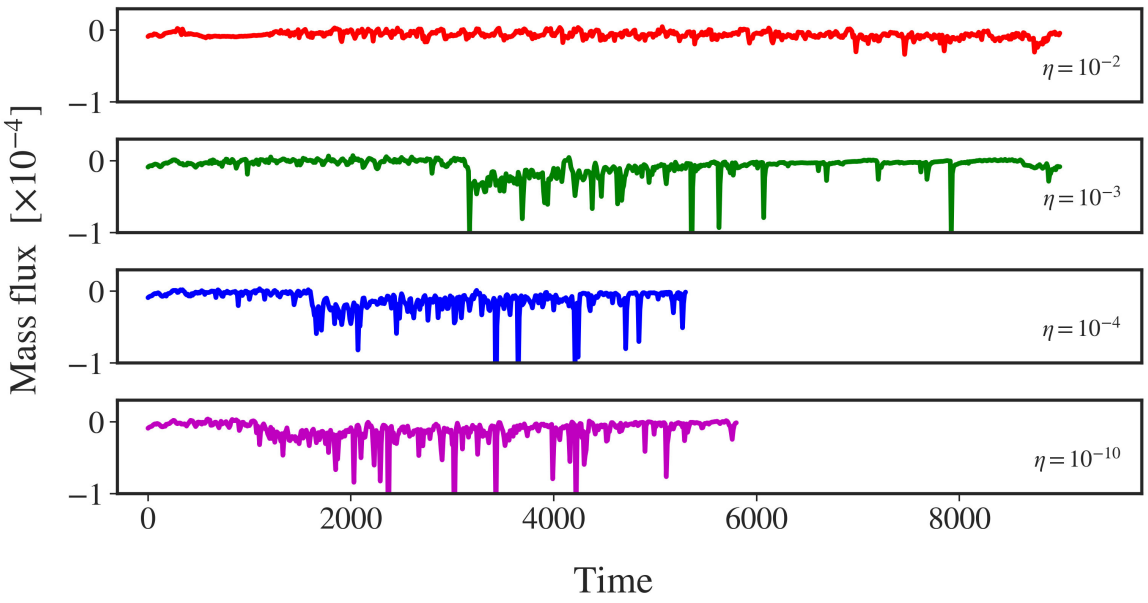

FIGURE 5.6: Accretion rate and resistivity. Comparison of the accretion rates measured at $r \approx 2$ for the simulation runs with $\eta_0 = 10^{-2}$ (*sim4*, red), $\eta_0 = 10^{-3}$ (*sim0*, green), $\eta_0 = 10^{-4}$ (*sim5*, blue), and $\eta_0 = 10^{-10}$ (*sim6*, magenta).

the effect of diffusivity on the accretion-ejection mechanism and the launching of outflows and jets. As described above, we have implemented a background diffusivity fixed in time and space that mainly follows the disk structure (see Sect. 3.1.4).

In the following we focus on varying the strength of the disk magnetic diffusivity. Further studies considering the scale height or the radial profile need to be done, as it has been worked out for nonrelativistic studies of jet-launching simulations (see, e.g. Sheikhnezami et al. (2012) and Stepanovs and Fendt (2014)).

We have run three further simulations, that are identical to our reference simulation but consider $\eta_0 = 10^{-2}$ (*sim4*), 10^{-4} (*sim5*), and 10^{-10} (*sim6*), respectively (see Table 5.1). We observed that a higher magnetic diffusivity stabilizes the simulation run, and simulation *sim4* runs until $t = 15000$. Simulations with lower diffusivity levels were terminating earlier, however still providing enough information for a comparison.

In Figure 5.6 we compare the accretion rate at radius $r = 2$ for different levels of magnetic diffusivity. For simulation *sim4* with the highest level of diffusivity we notice an almost constant (in comparison with the other simulations) accretion rate without any spikes. Still some spikes start appearing after $t = 9000$ when we plot the long-term accretion evolution of *sim4* even though the background accretion does not change much. Overall, for this simulation we cannot identify the three phases of accretion rate we found in the reference simulation, even with the longer simulation time.

For lower levels of diffusivity the evolution of the accretion rate has more similarities to simulation *sim0*. We identify similar phase changes to those we detected in our reference simulation; however, unfortunately the simulations stop before they reach a time scale that is comparable to that of the reference simulation. Even in this case, though, for *sim5* the second phase starts at $t \approx 1600$, while for *sim6* it starts at $t \approx 1100$; however it is not as

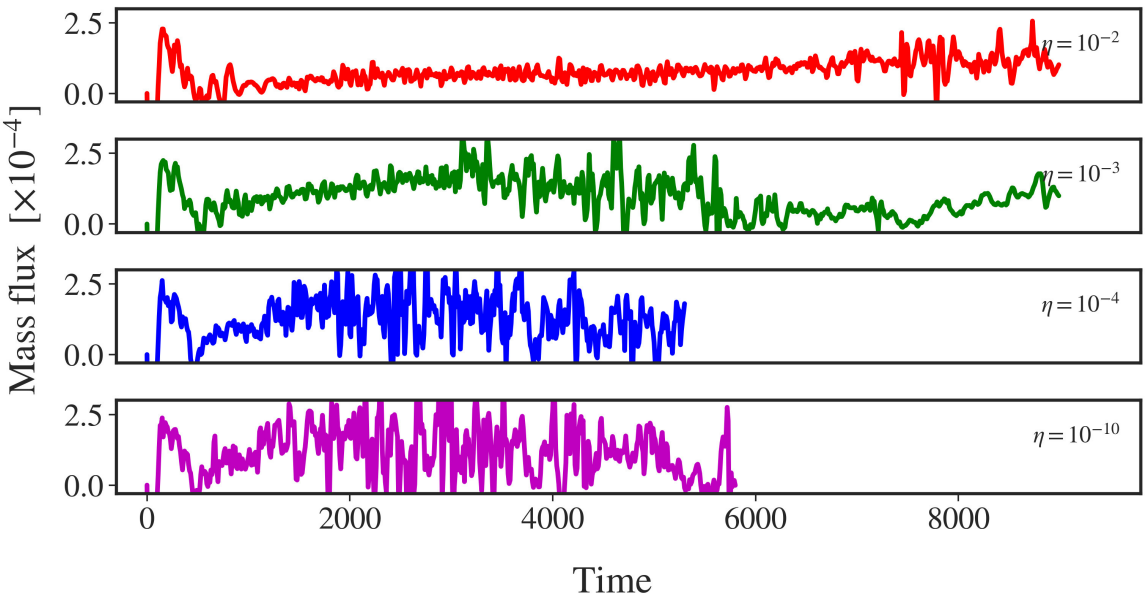

FIGURE 5.7: Ejection rate and resistivity. Comparison of the mass flux associated with the disk wind for the simulation runs with $\eta_0 = 10^{-2}$ (*sim4*, red), $\eta_0 = 10^{-3}$ (*sim0*, green), $\eta_0 = 10^{-4}$ (*sim5*, blue), and $\eta_0 = 10^{-10}$ (*sim6*, magenta), integrated along the surfaces of constant angle at 80° and 100°.

clear as in the reference simulation.

For the vertical flux of the disk wind we observe a similar behavior – a larger disk wind mass flux resulting for lower levels of diffusivity (see Figure 5.7). It therefore seems that high diffusivity reduces the efficiency for the magnetic field to a launch disk wind. This is straightforward to understand and has been observed in nonrelativistic simulations (Sheikhnezami et al., 2012): for a magnetic driving of outflows (Blandford-Payne or magnetic pressure driven) a strong coupling between magnetic field and matter is essential.

For the radial mass flux we detect a different behavior. A high radial mass flux appears for the reference simulation with $\eta_0 = 0.001$, while for both higher and lower diffusivity levels the mass flux decreases to approximately similar levels. The area where we find the B_ϕ-dominated wind has a lower diffusivity level than the equatorial plane, but for simulation *sim4* it is still significant enough to weaken the wind. The area of the B_ϕ-dominated wind increases with the increase of diffusivity.

Finally, we investigate the Poynting fluxes for the different levels of diffusivity. Figure 5.8 shows the Poynting flux through the jet funnel at radius $r = 100$ for various η. The flux increases in time for all cases; however, comparing simulation *sim4* (largest η) with the reference simulation, the increase is much slower. Simulations *sim5* and *sim6* show again very similar behavior following the trend we observed in the accreting and vertical mass fluxes. Also, in the case of *sim4* the flux from the disk wind is slightly stronger than the flux from the jet funnel.

The previous findings hint at preferred levels of diffusivity (or a preferred level of turbulence) that supports the launching of a disk wind. For higher diffusivity, the coupling between matter and field may not be efficient enough for launching, while for lower levels of

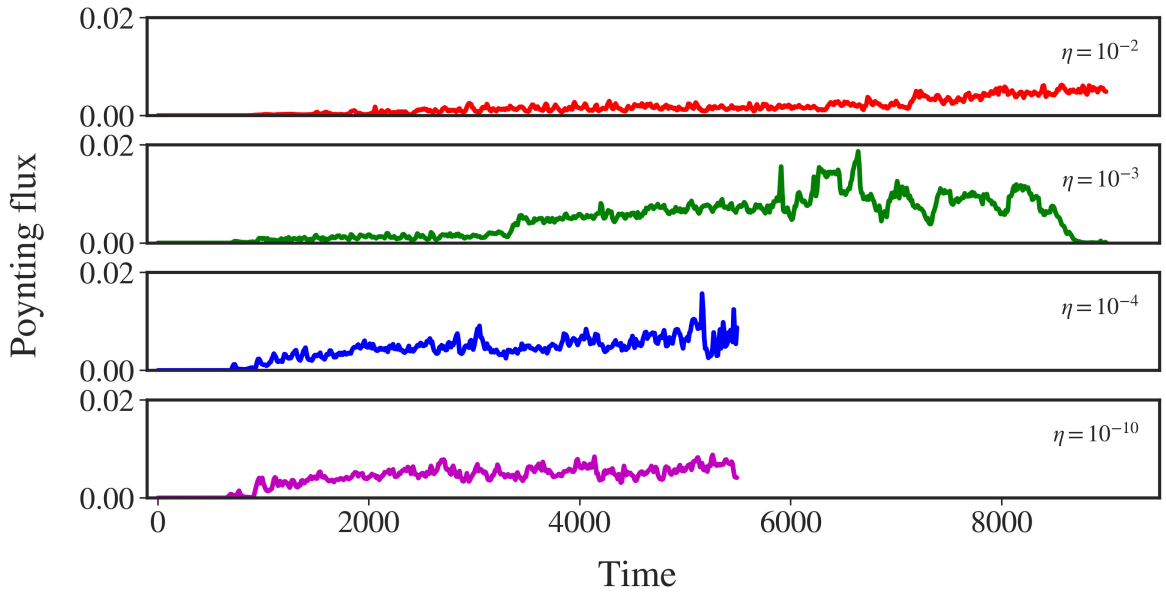

FIGURE 5.8: Poynting flux and resistivity. Comparison of the radial Poynting fluxes at $r = 100$ in the jet funnel for simulation runs applying diffusivity $\eta_0 = 10^{-2}$ (*sim4*, red), $\eta_0 = 10^{-3}$ (*sim0*, green), $\eta_0 = 10^{-4}$ (*sim5*, blue), and $\eta_0 = 10^{-10}$ (*sim6*, magenta).

diffusivity the mass loading becomes inefficient.

What is the mechanism behind these findings of a threshold value for the magnetic diffusivity of $\eta = 10^{-3}...10^{-2}$ where the flow becomes smooth and never MAD-like? We believe that is is the interplay between magnetic reconnection, magnetic diffusion, and ohmic heating that governs the disk structure at these scales. Magnetic reconnection destroys magnetic flux that is needed to launch strong outflows. It also generates turbulence to the flow. We would thus expect a high resistivity to weaken the outflow launching. On the other hand, a higher resistivity enables a more efficient mass loading of the outflow. Thus, a smaller resistivity would decrease the mass load of the outflow but potentially may produce outflows with higher speed (for the same magnetic flux available). Ohmic heating of the launching area would, in contrast, increase the mass loading (in classic MHD steady-state theory the mass load is determined by the sound speed at the launching radius).

Overall, our simulations seem to follow these trends. For low resistivity, resistive mass loading becomes less efficient, assisted by low ohmic heating. For high resistivity, reconnection weakens the outflow. For a critical resistivity in between, outflow launching becomes most efficient.

5.3 The Direction of Electric Field

In ideal MHD the electric field is always directly calculated from Ohm's law and for that reason it is often omitted even though it is the main contributor in the acceleration of charged particles along the magnetic field lines. We mentioned before that the introduction of resistivity creates the necessity to evolve the electric field with the other physical quantities.

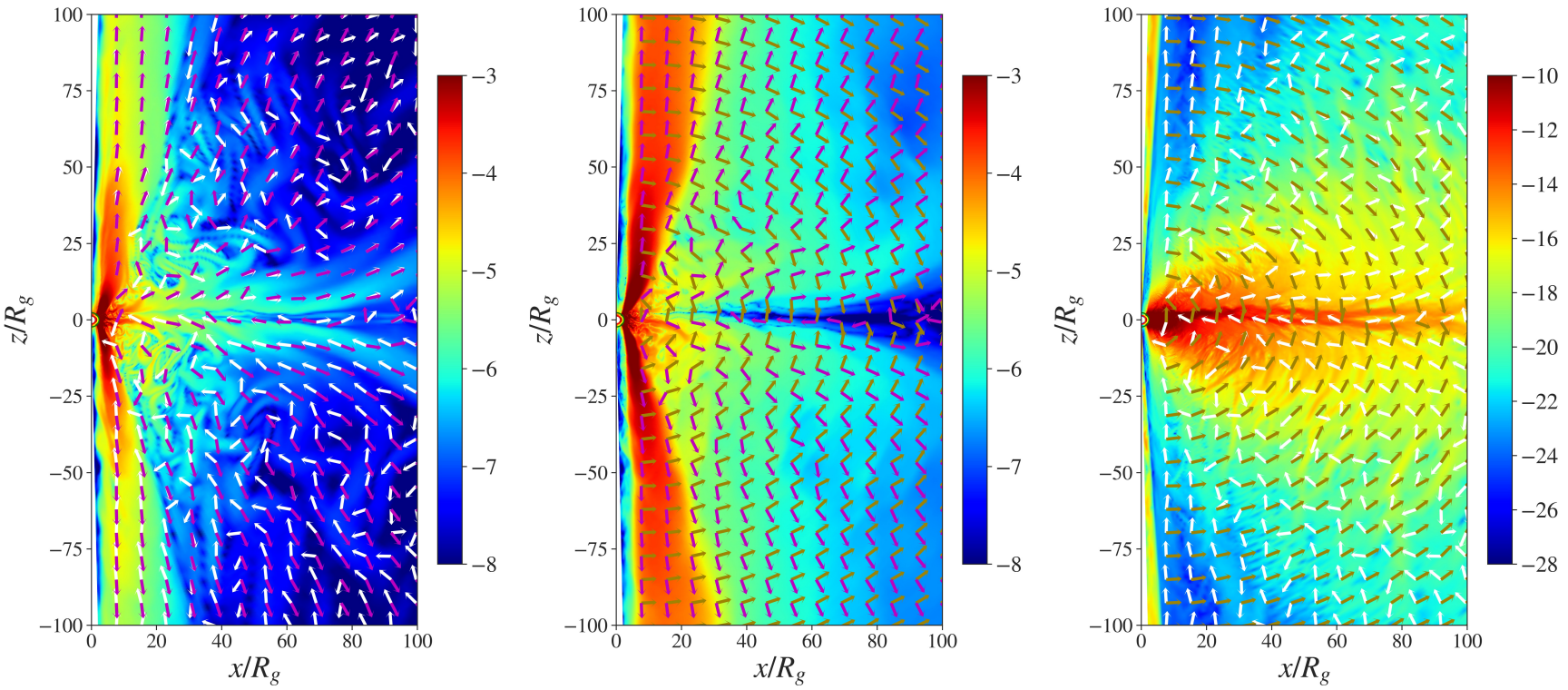

FIGURE 5.9: The three components of the poloidal electric field, $\boldsymbol{B}_p \times \boldsymbol{v}_\phi$ (left), $\boldsymbol{B}_\phi \times \boldsymbol{v}_p$ (middle)+ $\eta \boldsymbol{J}_p$ (right) for the reference simulation *sim0* at $t = 4000$. The arrows show the direction of the poloidal components of velocity (magenta), magnetic (white) and electric field (brown). In the funnel and disk wind area the dominant component is $\boldsymbol{B}_\phi \times \boldsymbol{v}_p$ and in there the electric field is almost perpendicular to $\boldsymbol{v}_p$, while in the disk area and the launching area of the disk wind the $\boldsymbol{B}_p \times \boldsymbol{v}_\phi$ term is dominant and the electric field is perpendicular to $\boldsymbol{B}_p$.

In this section we will take a look in the structure of the often ignored electric field and the information it provides us with.

The poloidal electric field can be written as a combination of the poloidal and azimuthal components of the magnetic field, fluid velocity and electric current

$$\boldsymbol{E}_p = \boldsymbol{B}_p \times \boldsymbol{v}_\phi + \boldsymbol{B}_\phi \times \boldsymbol{v}_p + \eta \boldsymbol{J}_p, \tag{5.1}$$

where $\boldsymbol{J}_p = \boldsymbol{J}_r + \boldsymbol{J}_\theta$ (for an analytical derivation please refer to Appendix B). There are three components in the above equation affecting the value and direction of the poloidal electric field differently. In case the values of those three components vary greatly, the values and, more importantly, the direction of the poloidal electric field will be determined mainly by the dominant components.

In Figure 5.9 we see these three components plotted over the same scale for comparison for the reference simulation *sim0* at $t = 4000$. The cross products can be approximated by simple value multiplication since the poloidal and azimuthal vectors are always perpendicular. In the same figure we also plot the poloidal vector for the fluid velocity, electric and magnetic field. We see that the values of the $\boldsymbol{B}_p \times \boldsymbol{v}_\phi$ is in general lower that the value of the $\boldsymbol{B}_\phi \times \boldsymbol{v}_p$ component, mainly in the jet funnel and the developed disk wind. However, inside the disk and in the just launched disk wind the $\boldsymbol{B}_p \times \boldsymbol{v}_\phi$ is dominating. As a result, the electric field seems to follow the direction perpendicular to either the poloidal velocity or the poloidal magnetic field (and of course any intermediate case) depending on the values of those components. The toroidal velocity and magnetic field become comparatively strong only close to the black hole. The $\eta \boldsymbol{J}_p$ term is not strong enough to affect the direction of electric field even for higher values of diffusivity.

From simulations of steady state solutions we know that the poloidal electric field must be perpendicular to the poloidal magnetic field and can be expressed by

$$\boldsymbol{E}_p = \frac{r\Omega^F}{c} B_p \boldsymbol{n} = \frac{r}{r_L} B_p \boldsymbol{n}, \tag{5.2}$$

where Ω^F is the angular velocity of the field lines, $r_L = c/\Omega^F$ is the light cylinder radius (the radius where the angular velocity of the field lines surpasses the speed of light) and $\boldsymbol{n} = \boldsymbol{B}_p / B_p \times \hat{\boldsymbol{e}}_\phi$ is the direction of the poloidal electric field (Porth and Fendt, 2010).

In Figure 5.9 we also compare the direction of the three poloidal vectors for velocity (pink arrows), magnetic (white arrows) and electric field (brown arrows). In the outflow that is launched from the surface of the disk the poloidal velocity is mostly radial and since it is the major contributor in the value of the dominating component $\boldsymbol{b}_\phi \times \boldsymbol{v}p$ the vector of the poloidal electric field is perpendicular to it (see arrows of Figure 5.9, middle panel). The same applies in the case of the axial jet funnel as well. The direction of the poloidal magnetic field is much more variable than the velocity. In the disk wind it does not follow any particular direction and the expected perpendicularity with the poloidal electric field does not apply.

Exception to this is the axial jet funnel where the two vectors are almost perfectly perpendicular (see arrows of Figure 5.9, right panel). This also means that the poloidal velocity and magnetic field vectors should be (anti)parallel in the axial jet funnel of the (south)north hemisphere (see arrows of Figure 5.9, left panel). This means that the steady state condition we described before can only apply in the axial jet funnel, while in the disk

wind field and fluid do not follow a smooth evolution probably die to the different types of disk wind we described in Chapter 4.

In the jet funnel, since the poloidal velocity and magnetic field are parallel we can approximate that

$$\boldsymbol{v}_p = \kappa \boldsymbol{B}_p, \tag{5.3}$$

with κ having positive and negative values depending on the hemisphere. In general, the values of poloidal velocity are a few orders of magnitude larger than the values of the poloidal magnetic field, which means that $\kappa \sim 10^3 - 10^5$. From Equation (5.1) we get

$$\begin{aligned} \boldsymbol{E}_p &= \boldsymbol{B}_p \times \boldsymbol{v}_\phi + \boldsymbol{B}_\phi \times \boldsymbol{v}_p + \eta \boldsymbol{J}_p \\ &= \boldsymbol{B}_p \times \boldsymbol{v}_\phi + \boldsymbol{B}_\phi \times \kappa \boldsymbol{B}_p + \eta \boldsymbol{J}_p \\ &= \boldsymbol{B}_p \times (\boldsymbol{v}_\phi - \kappa \boldsymbol{B}_\phi) + \eta \boldsymbol{J}_p, \end{aligned} \tag{5.4}$$

which satisfies the steady state condition of $\boldsymbol{E}_p \perp \boldsymbol{B}_p$.

5.4 Summary

We compare the accretion rates for different black hole spin parameters. For the same level of magnetic diffusivity ($\eta_0 = 0.001$), we find for increasing spin the accretion rate decreases close to the horizon. At the same time, the accretion rate increases, and with it the mass flux of the launched disk wind in both the polar direction (launching) and radial direction (acceleration) increase as well. This result comes in contrast with previous works (Qian, Fendt, and Vourellis, 2018) where the connection between accretion and disk wind was much stronger.

We compare the accretion rates for different levels of magnetic diffusivity. For the same black hole spin we find that increasing diffusivity lowers the accretion rate, and results in a decrease in the mass flux of the disk wind launched from the disk surface. The radial mass fluxes show only small differences that do not allow us to say beyond any doubt if they are affected by the changes in diffusivity. Definitely, a weaker coupling between matter and magnetic field, induced by the increase in magnetic diffusivity, affects both accretion rate and mass loading of the wind in a similar way.

The electromagnetic energy flux that is carried by different parts of the outflow is dominated by the flux of the jet funnel. This flux in the jet funnel is highly affected by the black hole rotation as this part of the outflow driven by the BZ mechanism. We find that the disk and the Poynting-dominated outflows are strongly connected as the level of magnetic diffusivity does affect the electromagnetic flux in the jet as well – in spite of the fact that the diffusivity close to the horizon is negligible. Similar to the peak in the mass fluxes for the disk wind, the Poynting flux reaches a peak value for $\eta_0 = 10^{-3}$. We believe that this critical level for the resistivity is a result of the interplay between re-connection decreasing the magnetic flux launching the outflow and magnetic diffusion and ohmic heating, both increasing the mass flux.

The simulation of a counter-rotating black hole revealed an interesting feature. The retrograde rotation induces additional field reversals in the toroidal component of the magnetic field in the inner disk area. In this case, the accretion is supported mainly from the surface

material of the inner disk area (where $B_\phi = 0$), though without significantly affecting the accretion rate itself.

Finally, we take a look in the direction of the poloidal electric field vector in comparison the the poloidal velocity and the poloidal magnetic field vectors. We find that the velocity is the major contributor in the value and the direction of the electric field. In the jet funnel where velocity and magnetic field are parallel we find the electric field perpendicular to both, whereas in the disk wind the electric field stay perpendicular mostly to the poloidal velocity.

Chapter 6

Magnetic Dynamo in Accretion Disks and Tori

In the previous chapters we studied the launching of jets and in the simulations we performed we always used a poloidal magnetic field that threaded the disk as part of the initial conditions. The origins of such magnetic fields are generally unknown, however there are theoretical models that show the magnetic field can be generated from the turbulence in the fluid (see Chapter 2.1.3) In this chapter we will attempt to show simulations of fully dynamical development and evolution of a magnetic field generated by a mean–field dynamo in a general relativistic environment. We follow the closure discovered by Bucciantini and Del Zanna (2013) which we implemented into `HARM3D`. First, we introduce our method and the initial conditions for the simulation and then we apply them in the case of accretion tori and thin disks.

6.1 Dynamo Action

In Section 2.1.3 we showed on a theoretical level how the mean–field dynamo theory can lead to the generation of magnetic fields. In order to apply this idea in a simulation we need to put in an astrophysical context. Turbulence is the main candidate for the generation of the magnetic field. The MRI (Balbus and Hawley, 1991) is one of the potential candidates for the turbulent dynamo (Brandenburg et al., 1995). Pudritz (1981b), Pudritz (1981a), and Stepinski and Levy (1988) showed generation of magnetic field from dynamo in accretion disks. Campbell, Papaloizou, and Agapitou (1998) studied the advection of dynamo generated magnetic field and the bending of the field lines due to advection, while Campbell (1999) showed that the 60° angle required for the launching of disk winds according to Blandford and Payne (1982) is reduced to 20° in the case of a magnetic field with curved field lines and a finite thin disk.

The extension of our resistive code used in the simulations of the previous chapters to include dynamo is relatively straightforward. The forward and inverse scheme for the primitive and conserved variables is the same as the one described in Chapter 3.1, while we use the full Equation (3.7) in order to include the term depending on the ξ parameter.

The ratio between the α or ξ value and the diffusivity defines the *dynamo number.* In the case of the Newtonian simulations utilizing a thin accretion disk (Bardou et al., 2001; von Rekowski et al., 2003; Stepanovs and Fendt, 2016) the dynamo number is defined as

$$D_\alpha = |R_\alpha R_\omega| = \frac{\alpha H}{\eta}\frac{SH^2}{\eta} \tag{6.1}$$

where the two fractions represent the Reynold's numbers from the α effect and the differential rotation respectively. H is a measure of the scale height of the disk and S is a measure of the shear due to the differential rotation.

In the case of tori in general relativistic environment, Bugli, Del Zanna, and Bucciantini (2014) are using the point of highest density in the "centre" of the torus as a measure of the scale height and the difference in the angular velocity between the inner torus radius and the point of maximum density as a measure of the shear. This translates to

$$D_\xi = \left|R_\xi R_\omega\right| = \frac{\xi R_{\rho_{\max}}}{\eta}\frac{\Delta\Omega R^2_{\rho_{\max}}}{\eta} \tag{6.2}$$

From the Newtonian simulations we know that in order to develop a poloidal magnetic field in the form of a dipole, the prescribed dynamo distribution must change sign in the equatorial plane. Specifically, (Rekowski, Rüdiger, and Elstner, 2000) mention that the α parameter must be negative in the upper hemisphere. However, in our code, this does not happen immediately. We noticed that if we prescribe either an initial toroidal field that changes sign in the equator or has any change in their value in the θ direction, and/or a ξ dynamo distribution that changes sign in the equatorial plane as well, the poloidal field that is created in the first steps of the simulation is quadrupolar. The only means by which a purely dipolar poloidal field can be created is by prescribing an initial toroidal field and a ξ distribution that keeps the same sign in both hemispheres.

As mentioned before, our code was based on the mean-field dynamo closure discovered by Bucciantini and Del Zanna (2013). Between the test simulations they provide and the application by Bugli, Del Zanna, and Bucciantini (2014) they only show the poloidal field in the neutron star dynamo test in Section 5.2.4 of Bucciantini and Del Zanna (2013). In this case the ξ dynamo is constant and has the same sign in the whole grid and the initial toroidal field has the same sign inside the neutron star, resulting in a dipolar poloidal field. After trying many different combinations, we can verify that the only one that results in the generation of a dipolar poloidal field is

- when the initial toroidal field keeps the same sign in both hemispheres and
- when the ξ distribution has a constant value in the θ direction and keeps the same sign in both hemispheres.

In the classical MHD regime the induction equation of a system that includes η diffusivity and α dynamo can be written as

$$\partial_t \boldsymbol{B} = \nabla \times (\boldsymbol{v} \times \boldsymbol{B}) + \nabla \times (\alpha \boldsymbol{B}) + \nabla \times \nabla \times (\eta \boldsymbol{B})\,. \tag{6.3}$$

In general, η and α are tensors. Only in the case where they are constant they can be moved outside of the derivatives. The closure derived by Bucciantini and Del Zanna (2013) and used in our work assumes only isotropy in diffusivity and dynamo without requiring the values to be constant. This however does not fully work since we can see clear indications that any dependence of the on the values of dynamo affects the polarity of the generated poloidal

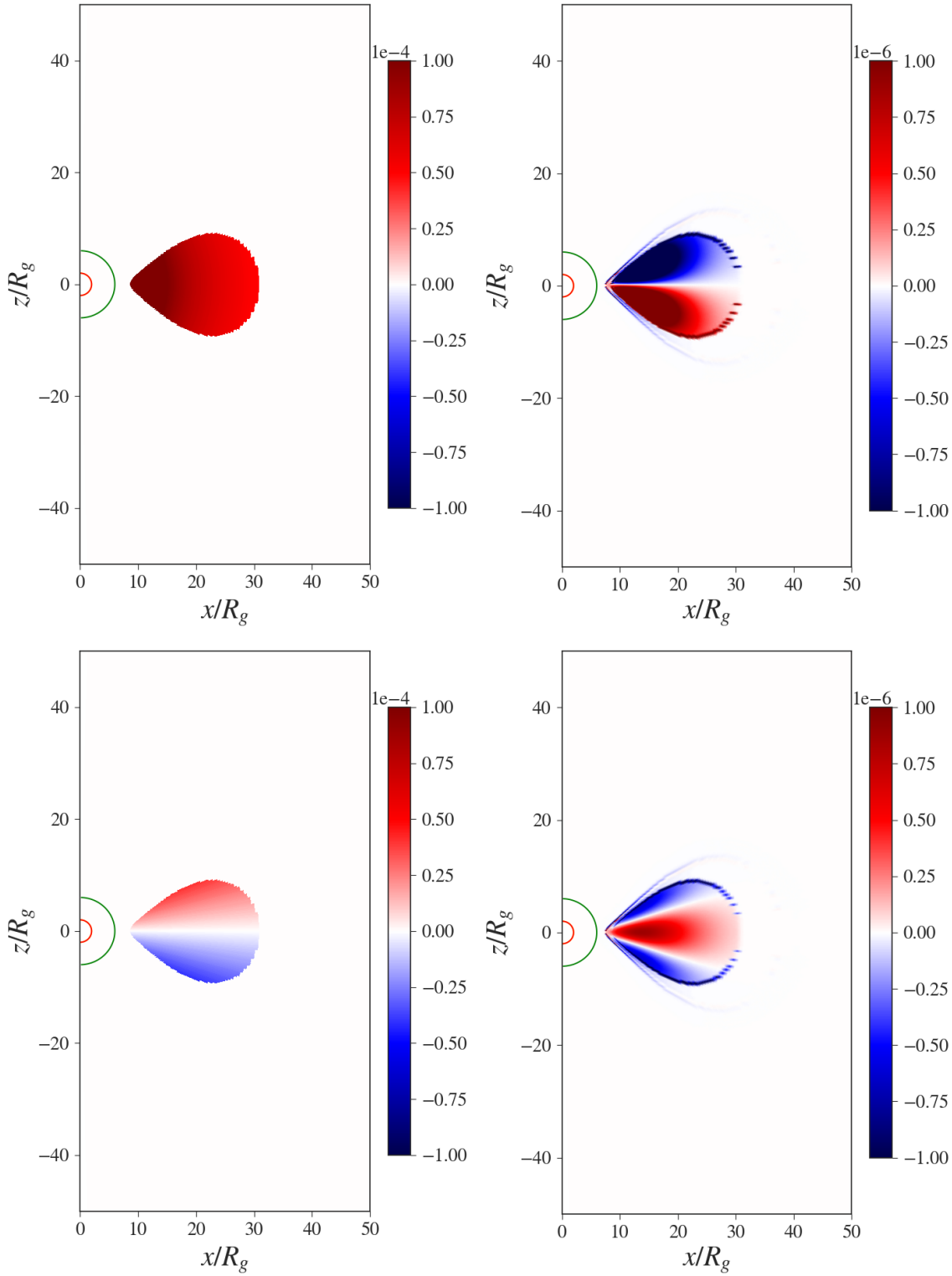

FIGURE 6.1: Distribution of ξ dynamo with radial (upper left) and angular dependence (lower left) and the resulting radial component of the magnetic field B_r (right panels). Only in the case of angular dependence on the dynamo the magnetic field shows a quadrupolar form. The initial condition used is a toroidal field with the same sign in both hemispheres.

magnetic field. In Figure 6.1 we show an example of the dynamo distribution affecting the polarity of the magnetic field.

6.1.1 The Quenching Prescription

If the dynamo is left to act unchecked its non-linear nature will result in the exponential increase of the magnetic field strength. A very strong magnetic field can suppress physical processes such as the MRI which are considered sources of the turbulence in the disk. With the repression of turbulence the dynamo will also be suppressed resulting in a weakened generated field. In the absence of a turbulence model, the dynamo quenching must be done artificially by enforcing lower ξ values when certain criteria apply (e.g. low plasma-β).

As an example, Bardou et al. (2001) implement a back-reaction on the α dynamo from the magnetic field by making α depend on the values of $\boldsymbol{B}$. Fendt and Gaßmann (2018) used a diffusivity model where the dynamo was quenched by increasing the magnetic diffusivity, which also provides for a more physical approach. However, the rate in which diffusivity and dynamo affect the magnetic field are very different. Depending on the dynamo number, ξ can show an exponential increase while η can dampen the magnetic field with a rate close to linear. Thus, if the dynamo number is too large, the change in diffusivity might not be enough and an artificial quenching must be used. Furthermore, increasing diffusivity decreases the timestep resulting in an increase in the computational cost for the simulation.

In our models, we implement a quenching mechanism that calculates the magnetization of the fluid and when the magnetization becomes too large, the quenching is applied by reducing the value of the ξ parameter. The quenching prescription follows Bardou et al. (2001) with

$$\xi_q = \xi \frac{1}{1 + \beta_{eq}/\beta}, \tag{6.4}$$

where ξ_q is the quenched dynamo and β_{eq} is the equipartition plasma-β.

However, we encountered an issue with the MPI parallelization of the code. Initially we wanted to take average values of magnetization over a region of cells and the apply the quenching in them, however, this meant that either all these cells should belong in the same process/core or we should find a way to communicate the values between the processes. The second option would require heavy work with the parallel aspect of the code with which we were not very familiar, so we choose the first option which also had a downside. It was restricting us into using small number of cores for the simulations in order to have a large area of the disk in one core. We compromised in running the simulation with parallel splitting only in the radial direction. In this way, each process was a set of "semicircles" with 256 cells in the θ direction and only 4 or 5 in the radial direction. Still, this arrangement resulted in more time consuming simulations.

The values of diffusivity, dynamo and Kerr parameter for each simulation can be seen in Table 6.1.

6.2 A Dynamo-Generated Poloidal Field in an Accretion Torus

For our simulations we choose to simulate the evolution of the magnetic field as it is developed inside a toroidal disk. This choice is motivated by the fact that we want to avoid the initial collapse we often see when simulating thin disks. For that we choose the equilibrium solution introduced by Abramowicz, Jaroszynski, and Sikora (1978) and Fishbone and Moncrief (1976). Since the torus is an equilibrium solution of the spacetime, some of its characteristics depend on the rotation of the black hole. For the case of a Schwarzschild black hole $a = 0$, we choose an inner radius for the torus at $r_{\rm in} = 6$ and a point of maximum density at $r_{\rm max} = 15$. The simulation grid extends from just inside the event horizon of the black hole to a radius of $r = 80$. The torus is surrounded by an artificial atmosphere, namely a set of floor values in the density and pressure. We use the distribution described in Section 3.1.5. The torus is surrounded by a corona of low density and pressure and is prescribed with a poloidal or toroidal magnetic field. The toroidal field is located inside the torus, following it density distribution and its is normalized based on the choice of plasma-β. Since we are interested in the generation of magnetic field we choose a very high plasma-$\beta \sim 10^6$ for our seed toroidal field.

For the simulations that appear in this chapter we go back to the original numerical grid of the code, without the hyper-logarithmic component we implemented. The purpose of the hyper-logarithmic grid was to solve boundary issues with the applied poloidal field. However, in the dynamo simulations, the poloidal field is generated from the torus and does not cross the boundary. The grid size used in all following simulations is 256×256. The simulations are taking place in a resistive environment. Magnetic diffusivity will act against the dynamo and will dampen the generated field. We also expect diffusivity to be higher in the areas with higher turbulence. The profile we choose follows the density distribution of the torus with constant value outside of it.

For the dynamo, we choose a distribution where the dynamo works inside the torus but in a smaller area. With this choice we make sure that there is no dynamo outside of the torus or in its outer layers where diffusivity is low, which would result in very high dynamo numbers.

6.2.1 Using a Constant Dynamo Distribution

In Figure 6.2 we show the initial distributions of density, B_ϕ, η and ξ. For the definition of the total dynamo number we will use Equation (6.2), where both the ξ and the ω dynamo numbers are defined for every cell separately but only inside the initial torus distribution. The reason is that the magnetic diffusivity drops to $\sim 10^{-10}$ outside of the torus resulting in very large ω dynamo number.

When the simulations starts, the poloidal magnetic field appears immediately inside the torus in the area where B_ϕ and dynamo coexist. As the simulation runs, the field starts increasing in value due to the dynamo while advecting towards the black hole following partially the accretion of the torus. Simultaneously, diffusivity is trying to dampen the magnetic field. In the end, the D_ξ determines where the field is amplified or dampened. Since ξ is constant, the profile of diffusivity decides the value of R_ξ. As an example of their

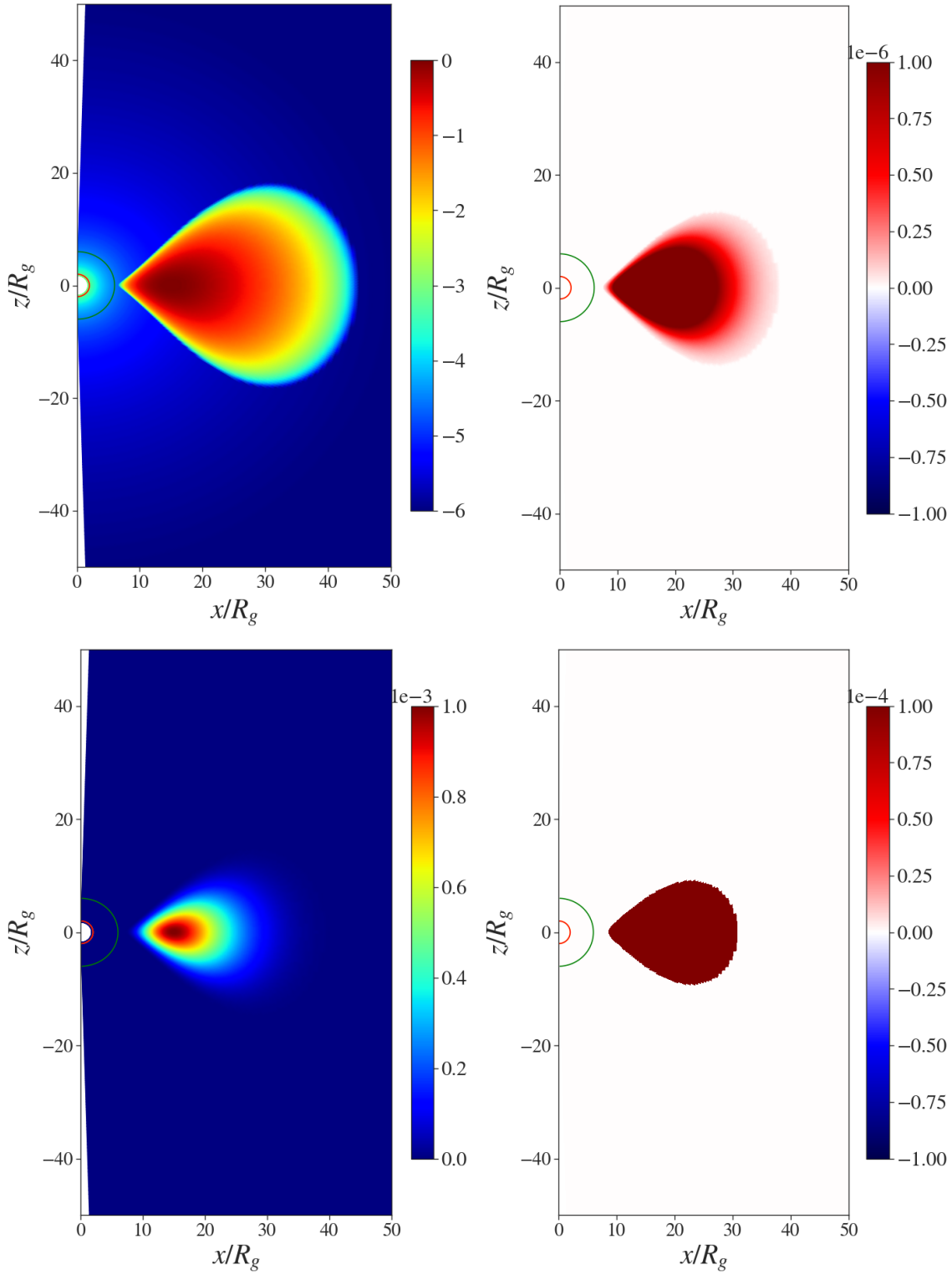

FIGURE 6.2: Initial conditions for our reference simulation. Shown are the initial distributions of density (logscale; upper left), toroidal magnetic field B_ϕ (linear scale; upper right), diffusivity η (linear scale; lower left) and dynamo ξ (linear scale; lower right).

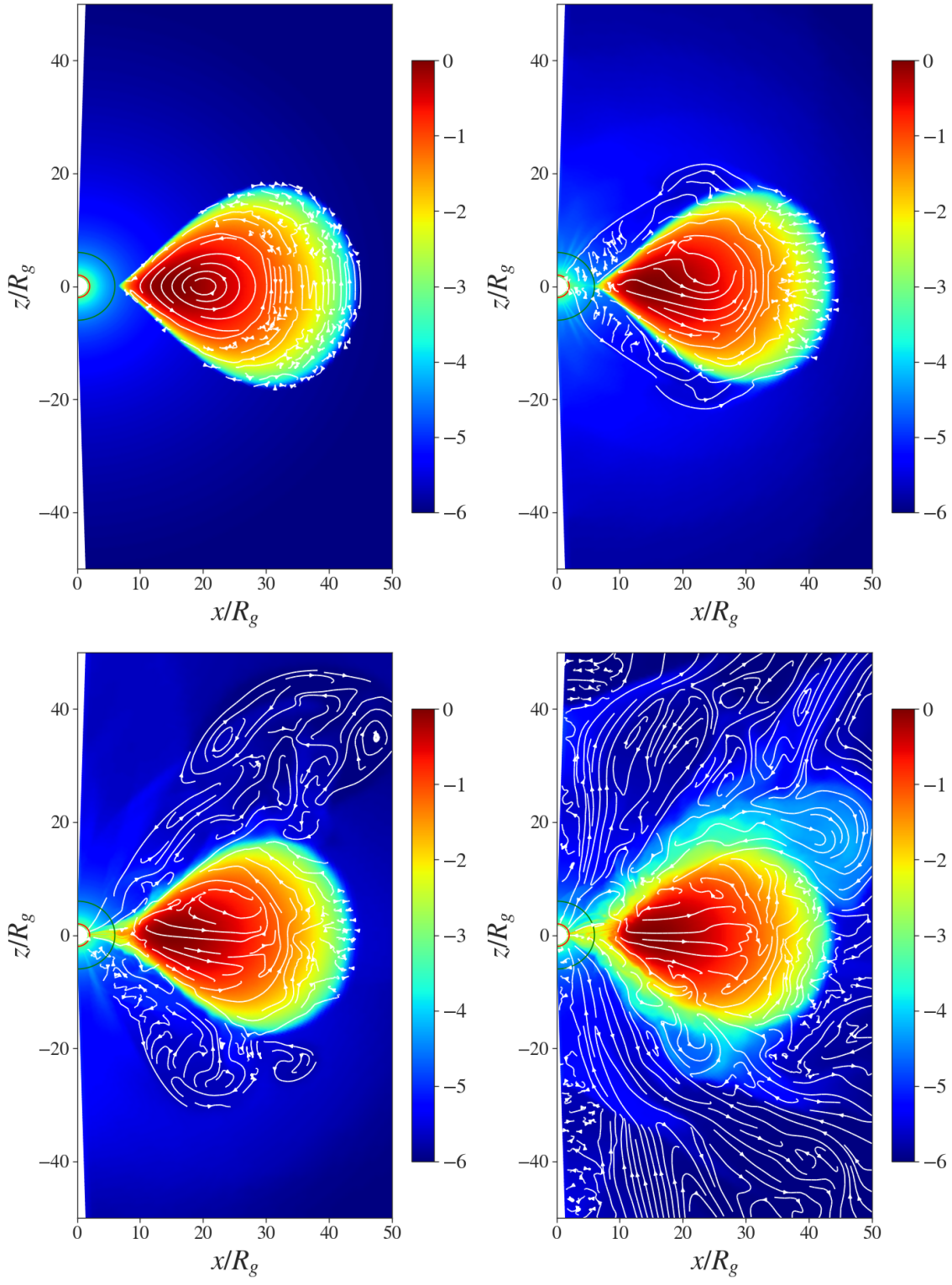

FIGURE 6.3: Generation of dipolar poloidal field. The color gradient shows the density distribution in log scale and the white lines show the poloidal magnetic field. The initial condition starts with a toroidal field with high plasma-$\beta \sim 10^6$. The poloidal field appears immediately in the area where dynamo exists ($t = 1$, upper left) and it evolves through $t = 1000, 2000$ and 3500. This corresponds in approximately 10 rotations of the point of maximum density at $R_{\rho_{\max}} = 15$.

TABLE 6.1: Details of the dynamo simulations. The first column shows the type of simulation (*dip* and *quad* are torus simulations with a dynamo the generates an initial dipolar and quadrupolar structure respectively and *thin* are thin disk simulations). The initial field column refers to the type of seed magnetic field used in the simulations (B_T for toroidal field and B_P for poloidal). The + or − sign shows the sign of the field in the two hemispheres. β_0 is the plasma-β value of the seed field. a, η_0 and ξ_0 are the Kerr parameter, maximum diffusivity and maximum dynamo parameter respectively, while the dynamo distribution is described in the next column. The final column shows whether the simulation used dynamo quenching or not.

Run	Initial field	β_0	a	η_0	ξ_0	ξ distribution	Quenching
dip0	B_T (+)	10^6	0	10^{-3}	10^{-3}	positive, constant	no
dip1	B_T (+)	10^6	0	10^{-3}	10^{-3}	positive, constant	yes
quad1	B_T (+)	10^6	0	10^{-3}	10^{-3}	positive, θ–dependence	no
quad2	B_T (+)	10^6	0	10^{-3}	10^{-3}	positive/negative, θ–dependence	no
quad3	B_T (+)	10^6	0.9	10^{-3}	10^{-3}	positive, θ–dependence	no
quad4	B_T (+)	10^6	0	10^{-3}	2×10^{-3}	positive, θ–dependence	no
quad4.1	B_T (+)	10^6	0	10^{-3}	2×10^{-3}	positive, θ–dependence	yes
thin1	B_T (+)	10^6	0	10^{-3}	10^{-3}	positive, constant	no
thin2	B_T (+)	10^6	0	10^{-3}	2×10^{-3}	positive, constant	no
thin3	B_P (±)	10^6	0	10^{-3}	10^{-3}	positive, constant	no
thin4	B_P (±)	10^6	0	10^{-3}	4×10^{-3}	positive, constant	no

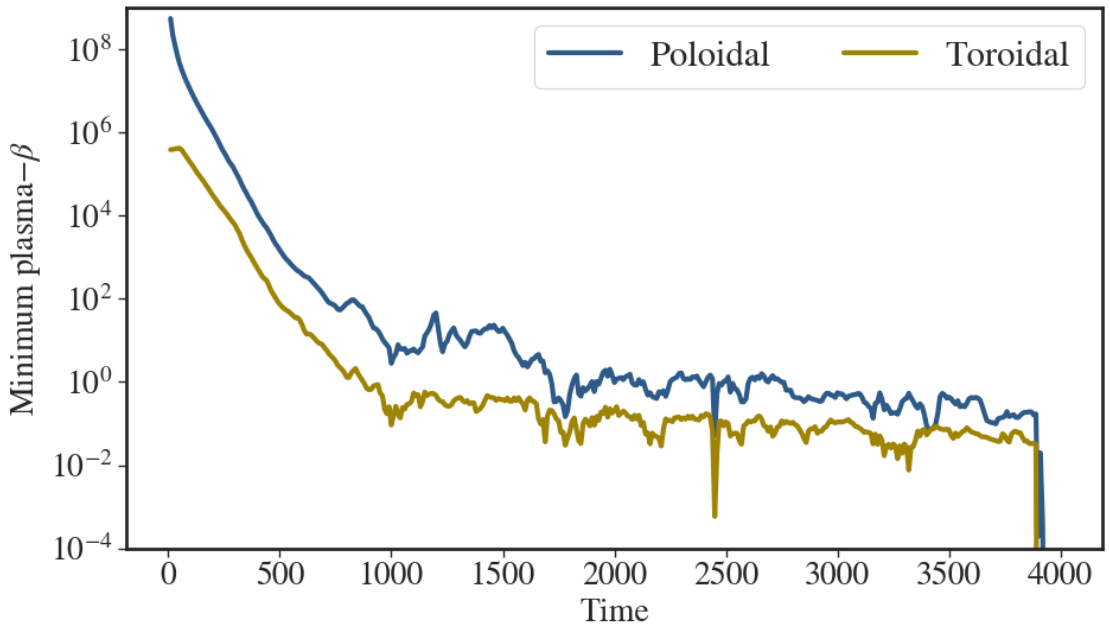

FIGURE 6.4: Minimum value of the plasma-β for the toroidal and poloidal components of the magnetic field in the area where dynamo works during the evolution of the simulation. At $t = 3900$ there is a sudden drop in the plasma-β (increase in the magnetic field) which marks the failure of the code.

values, in the center of the torus the numbers are $R_\xi \sim 15$ while its maximum values reaches $R_\xi \sim 150$ in the boundaries of the dynamo distribution.

In Figure 6.3 we see the snapshots of the evolution of the poloidal magnetic field. As mentioned before, in the beginning, the field lines are restricted in the area where $\xi \neq 0$. However, they are eventually dragged along with the material that is accreted towards the black hole. At time $t = 2000$, as the dynamo has been working for approximately 6 rotations of the torus center, we see a low strength outflow being launched from the inner part of the torus. The magnetic field lines follow the low density fluid showing the first indications of the development of a jet. The launching point of the outflow is barely inside of the ISCO and can be attributed to the presence of the strong toroidal magnetic field we see in the close atmosphere of the inner part of the torus. This strong toroidal field, which has been amplified by the ω effect of the dynamo, can increase the magnetic pressure and push material and poloidal field outwards (Lynden-Bell, 1996). The material accelerated by the outflow consists mainly of the floor values used by the code as background environment. At this point the plasma-β of the magnetic field is approximately 1 inside the ISCO and between 10 and 100 in the area of the outflow.

The poloidal field continues to grow up to $t \sim 3800$, but then the field becomes too strong, resulting in a failure of convergence for the code. At that time, both the toroidal and the poloidal components of the field have spread into the greatest part of the grid while the plasma-β has reached values between $0.01 - 0.1$ inside the ISCO and around 1 in the outflow. In Figure 6.4 we see the evolution of the minimum value of plasma-β inside the torus. In the area where the outflow is launched from, the plasma-β is approximately 10 times lower.

6.2.1.1 The Structure of the Magnetic Field

The initial condition of the toroidal component of the magnetic field follows the density profile while keeping a positive sign in both hemispheres. We know that such a field is very difficult to exist in astrophysical disks however, as we mentioned before, it is necessary to produce a dipolar poloidal field. However, a toroidal field is also produced by the ω effect when the newly created poloidal field starts rotating, inducing an extra toroidal component on top of the initial one. The induced toroidal field changes sign in the equatorial plane keeping the positive values in the upper hemisphere (where the poloidal field is negative). This results in a gradual change in the toroidal field inside the torus, where the initial condition is replaced by the newly generated field. At time $t = 1000$, the change in sign has already appeared in the border of the area with non-zero dynamo values (and poloidal field) and it keeps spreading, gradually changing the sign of the toroidal field in the lower hemisphere. At time $t = 2000$ this transformation has mostly finished with a toroidal field that changes sign in the equatorial plane.

The generated poloidal field is dominated by its radial component, which decides the direction of the field lines. One of the problems of the generated field is that even though initially it emerges as a perfect dipole, with negative values in the upper hemisphere and positive ones in the lower hemisphere, eventually it changes into a form of alternating positive and negative stripes each other resulting in the creation of closed loops of field lines. This layering effect of the radial magnetic field component affects the toroidal field, as a similar behavior is seen in later stages. The layered behavior of the generated field starts

at around $t = 500 - 800$ where the dipole that was initially produced starts to change as positive B_r values appear in the upper hemisphere, which was initially only negative. This occurs in similar ways in all components of both the magnetic and the electric field. At around $t = 1000$, a new layer appears in the B_r with negative values that alternate the previously produced positive values in the upper hemisphere. This procedure continues for the whole duration of the simulation and eventually results in a completely layered magnetic field. These layers always appear in the inner part of the torus where the ξ dynamo number is also higher and always inside of the previously appeared layer. The reason for this is, at the moment of writing this thesis, unknown.

6.2.2 Simulation with Dynamo Quenching

To test the effect of our dynamo quenching scheme we run simulation *dip1*, which is similar to *dip0* with the exception of the dynamo distribution that extends into the whole initial torus distribution. In order to compensate for larger dynamo area we applied a dynamo quenching mechanism according to Equation (6.4). The simulation shared many similarities with *dip0* including the growth of the magnetic field, which for simulation *dip1* happens quite earlier.

For the quenching we chose an equipartition plasma-$\beta_{eq} = 1000$ in order to start the quenching before the magnetic field becomes to strong and crash the simulation. However, we were not able to avoid that even with the early quenching we used. In Figure 6.5, we see the plasma-β and the dynamo parameter ξ as it is being quenched in the inner part. Even though the values of plasma-$\beta \sim 0.1$ around the black hole, the quenching is happening only in the inner part of the disk, which is probably the main reason it was not very effective. A quenching mechanism that will use information from the whole torus/disk via the implemented parallelization would be able to quench the dynamo more effectively and extend the "lifetime" of the simulation.

6.2.3 Using θ–depended Dynamo Distribution

As we mentioned previously, any dependence of the dynamo distribution from the polar angle will create an quadrupolar poloidal field. We will present two simulations where we try to reproduce outflows from a dynamo generated by a quadrupolar field. In simulation *quad1*, we use a dynamo distribution that keeps the same sign in the two hemispheres but with the aforementioned polar angular dependence. Since the dynamo is supposed to vanish in the equatorial plane we choose to use a prescription similar to the one used by Stepanovs and Fendt (2016) imposing a sinusoidal function over the polar angle θ resulting in increasing values as we divert from the equatorial plane (see Figure 6.6).

As the simulation evolves, the magnetization in the surface of the torus, where the dynamo number is higher, increases, resulting in the appearance of low velocity outflows. The newly generated field is advented towards the black hole increasing its magnetic pressure and energy. The plasma-β plot in Figure 6.6 shows the strength of the poloidal magnetic pressure in comparison with the fluid pressure. From inside the ISCO, poloidal field lines are extended outwards creating a path for accelerating material. High velocities are observed only in the lower hemisphere jet (counter-jet) where the Lorentz factor values are around 2 while the upper hemisphere jet (jet) is restricted to lower velocities $\sim 0.2c$.

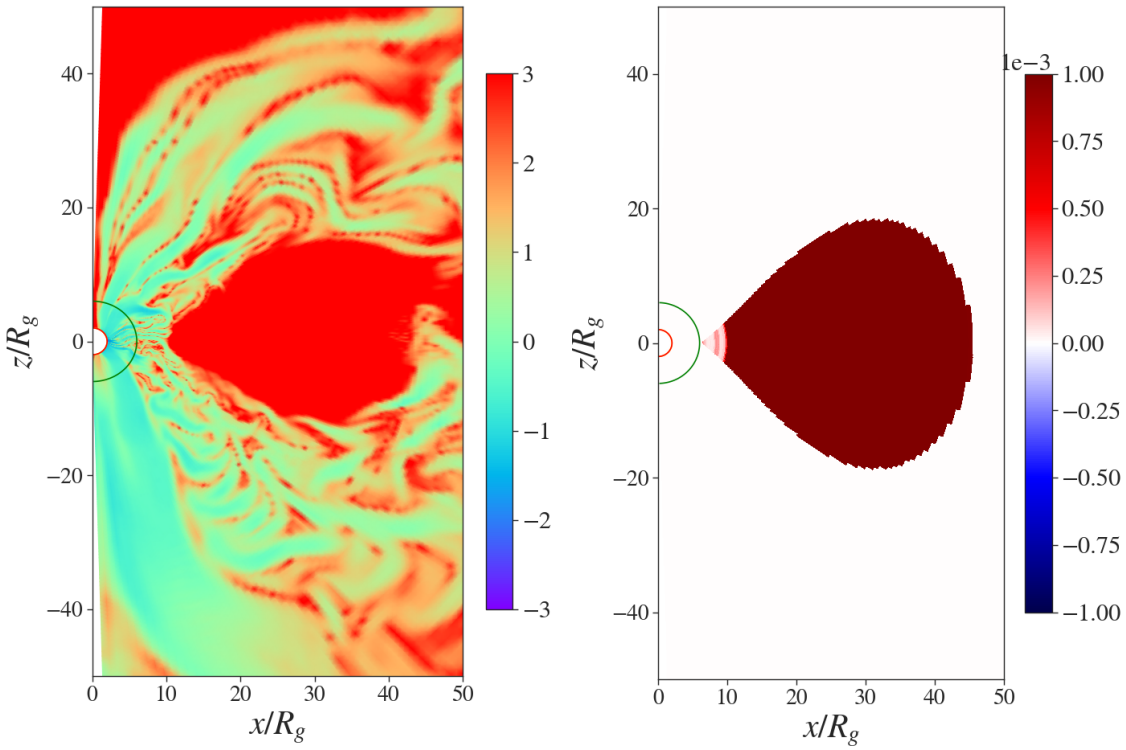

FIGURE 6.5: Plasma-*beta* and ξ dynamo at time $t = 2400$ for simulation *dip1*. Even though the ejection from the inner part of the system is with strong magnetization, the quenching in only happening in the inner part of the dynamo sitribution.

Similar to the case of the constant dynamo, the generated field appears in layers of different signs inside the torus which increase the complexity of its initial quadrupolar nature. In the jet area, however, a dipolar component appears. The structure still has some of the layers but the dipolar nature is quite prominent. The dipole nature magnetic field allows the field line to open outwards aiding the development of a jet.

The structure of the jet and counter jet is similar when it comes to their shape, length and collimation. When they were initially developed, they also had similar velocities. As evolution continues, the counter-jet starts developing higher velocities that its counterpart. A possible explanation can be found in the electric field structure. In Figure 6.6 we also see the values of the radial electric field component E_r. There is a clear difference in the structure of the electric field between the two hemispheres. In the upper hemisphere, the structure appears chaotic with positive and negative values of the field appearing next to each other. There is a region that is dominated by a positive electric field but the values are not very strong in comparison with the lower hemisphere. Here, there is a clear region where strong negative values of electric field dominate and this region coincides with the high-velocity outflow region.

6.2.4 Other Torus Simulations

In simulation *quad2* we add another feature in the dynamo prescription. We demand the positive values to be restricted in the upper hemisphere and the lower hemisphere to have

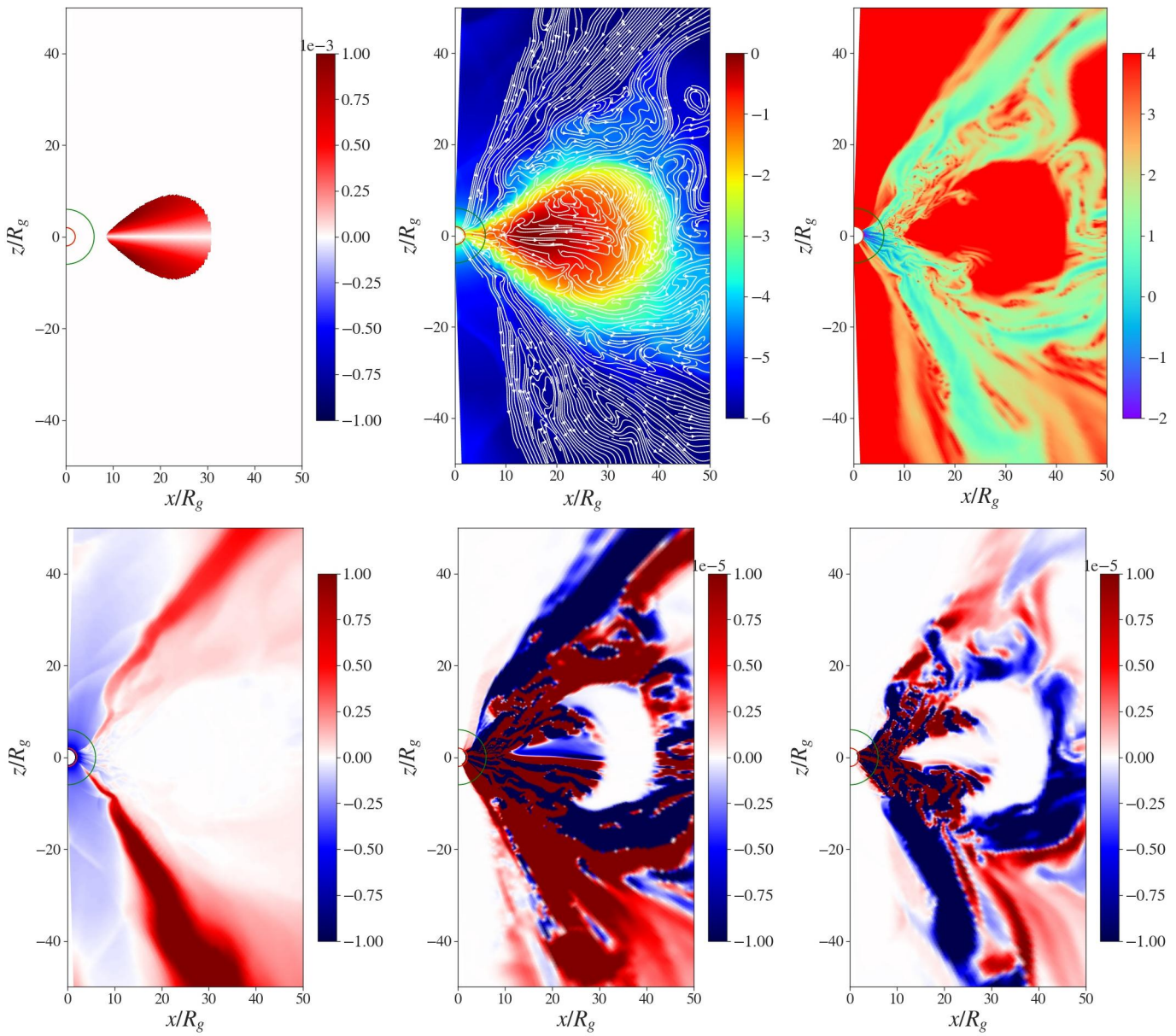

FIGURE 6.6: State of simulation *quad1* at time $t = 4800$. *Top left:* Dynamo distribution. *Top middle:* Logarithm of fluid density and poloidal magnetic field lines. *Top right:* Logarithm of poloidal plasma-β. *Bottom left:* Radial fluid velocity u^r. *Bottom middle:* Radial magnetic field B_r. *Bottom right:* Radial electric field E_r.

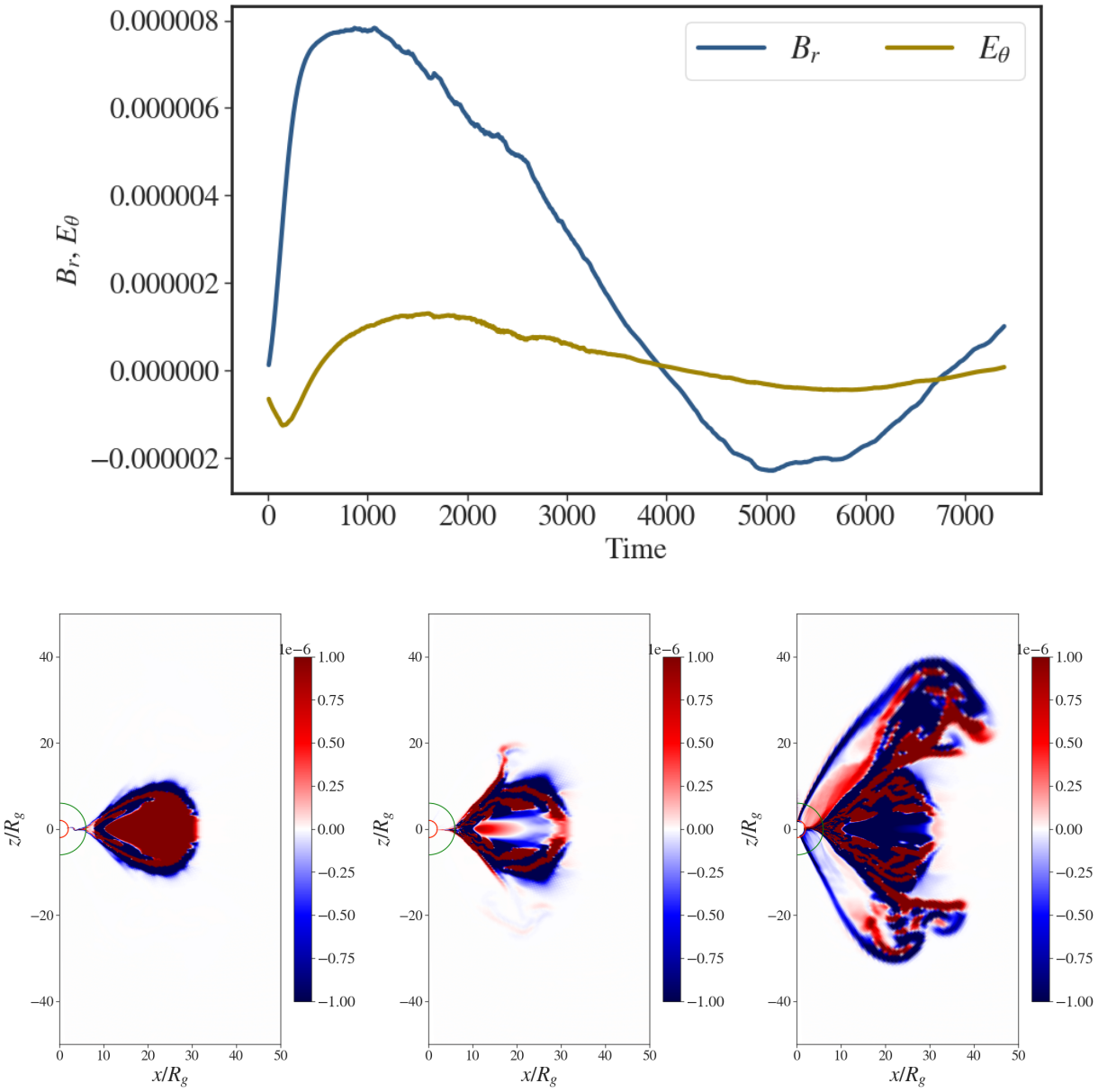

FIGURE 6.7: *Top:* The values of the radial magnetic field and polar electric field components in a cell inside the torus ($R \sim 17, \theta = 90°$) for simulation *quad2*. *Bottom:* Snapshots of the radial component of the magnetic field B_r at three different times $t = 2000,\ 3700,\ 5500$. The changes in the sign of B_r inside the torus are clearly visible.

negative values of ξ. In the equatorial plane the dynamo vanishes and the angular dependence remains as in simulation *quad1*.

The evolved torus looks much different than that in simulation *quad1*. The sign-alternating layers appear again inside the torus in later times and in general the changes in the simulation appear to happen at lower rate. However, this has nothing to do with the time scale of the simulation. The quadrupolar structure of the generated poloidal field is much stronger and persists for much longer times. Outflows develop in the surface of the torus and from the black hole but they are weaker than the ones we saw in simulation *quad1*.

An important feature observed in simulation *quad2* is how the radial magnetic field component B_r changes sign inside the torus. In Figure 6.7 we show the values of B_r and E_θ at radius $r \sim 17$ in the equatorial plane along with 3 snapshots of B_r, where the change in the sign is seen clearly for a large region inside the torus. This effect does not appear for the other two simulations with different dynamo distributions. Simulation *quad1* has some variations in the signs of B_r and E_θ but does not show the clear periodical variation that simulation *quad2* does. Simulation *dip0* shows absolutely no change in the signs of B_r and E_θ.

Simulation *quad3* is the same as *quad1* but with a Kerr parameter of $a = 0.9$. The rotating spacetime accelerated the evolution of the outflow resulting in the generation of a relativistic jet at time $t \sim 1900$. In the same time, simulation *quad1* with $a = 0$ had barely started showing any signs of outflow (see Figure 6.8). The rotating space time also accelerated the growth of the generated magnetic field. By the time the simulation crashed ($t \sim 2000$), the poloidal plasma-β in the accretion nozzle outside the marginally stable orbit was $\beta \sim 10$ which is within the limits of magnetization the code can handle. However, it dropped to much lower values very fast resulting in crashing the simulation.

Simulation *quad4* is also based on *quad1* but with slightly increased base values for the dynamo ($\xi_0 = 0.002$). From its early stages of evolution the difference in the strength of the generated magnetic field was significant. At time $t = 1500$, a jet-like outflow had been developed with branches that extended outwards and fluid velocities up to $\sim 0.2c$. The simulation crashed much sooner than its parent ($t \sim 2200$) and by that time the outflows had extended into the largest part of the grid with velocities up to $\sim 0.6c$.

Simulation *quad4.1* combines simulation *quad4* with the quenching mechanism we also prescribed in simulation *dip1* (see Equation (6.4)). The simulation *quad4.1* lasted for slightly longer than its parent simulation due to the quenching, which however, was again not enough to stop the simulation from crashing.

6.3 A Dynamo-Generated Poloidal Field in a Thin Disk

6.3.1 From a Toroidal Seed Field

As a next application we will use thin disks with the same hydrodynamical initial conditions (density, velocity, etc.) used in the previous chapters (see Chapter 3.1.3). The simulation grid is also the same as the one used in the previous dynamo simulations (256×256, logarithmic in r). Inside the disk we utilize either a toroidal or a poloidal magnetic field. The toroidal field is similar to the one we used in the torus simulations, with positive values in both

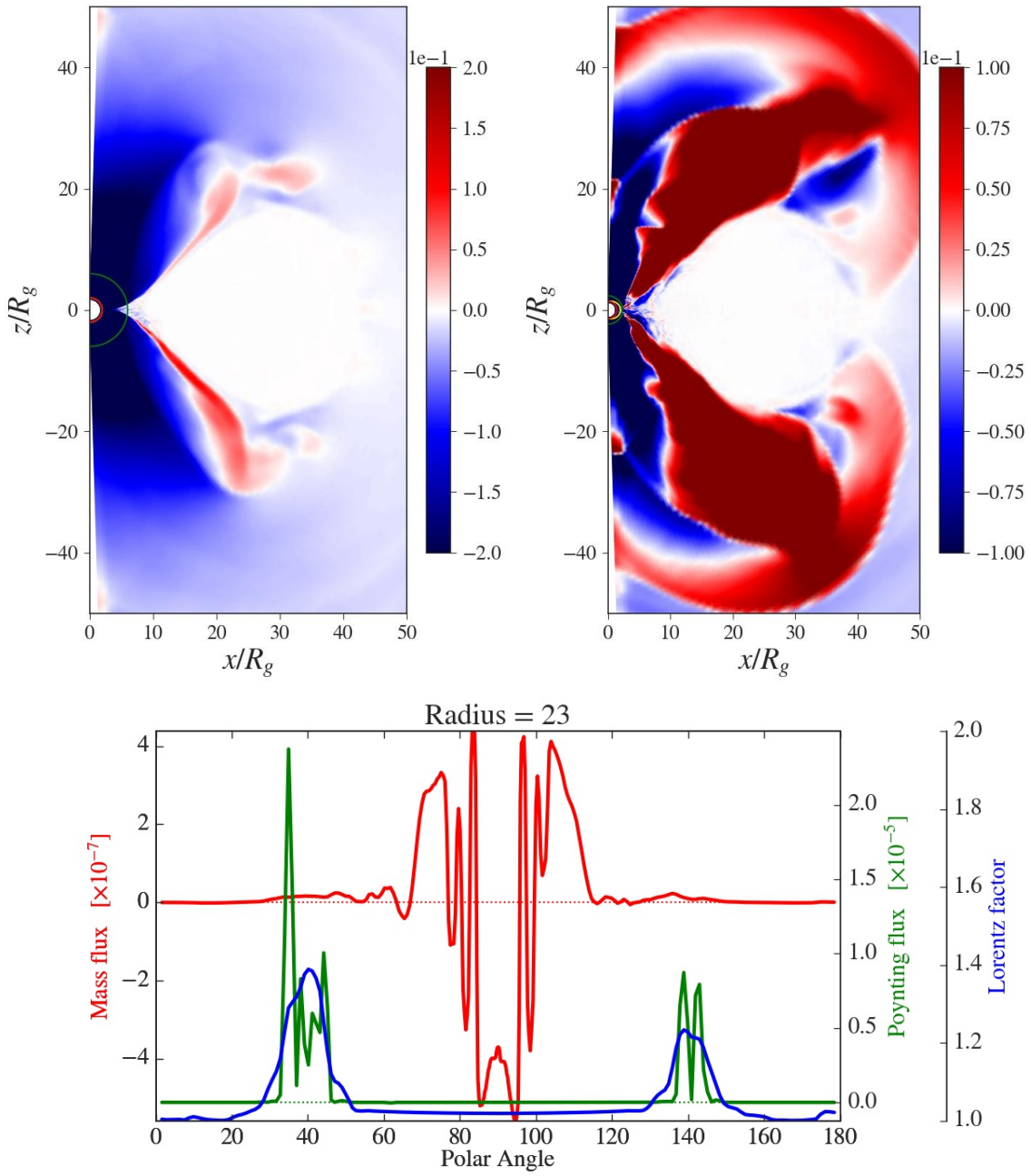

FIGURE 6.8: *Top:* Velocity comparison of the developed outflow at $t = 1900$ in simulations *quad1* (left) and *quad3* (right). The rotating black hole of simulation *quad3* allows for faster evolution of the torus and magnetic field amplification. *Bottom:* Mass flux (red), Poynting flux (green) and Lorentz factor (blue) over the polar angle at radius $r \sim 23$ for simulation *quad3*.

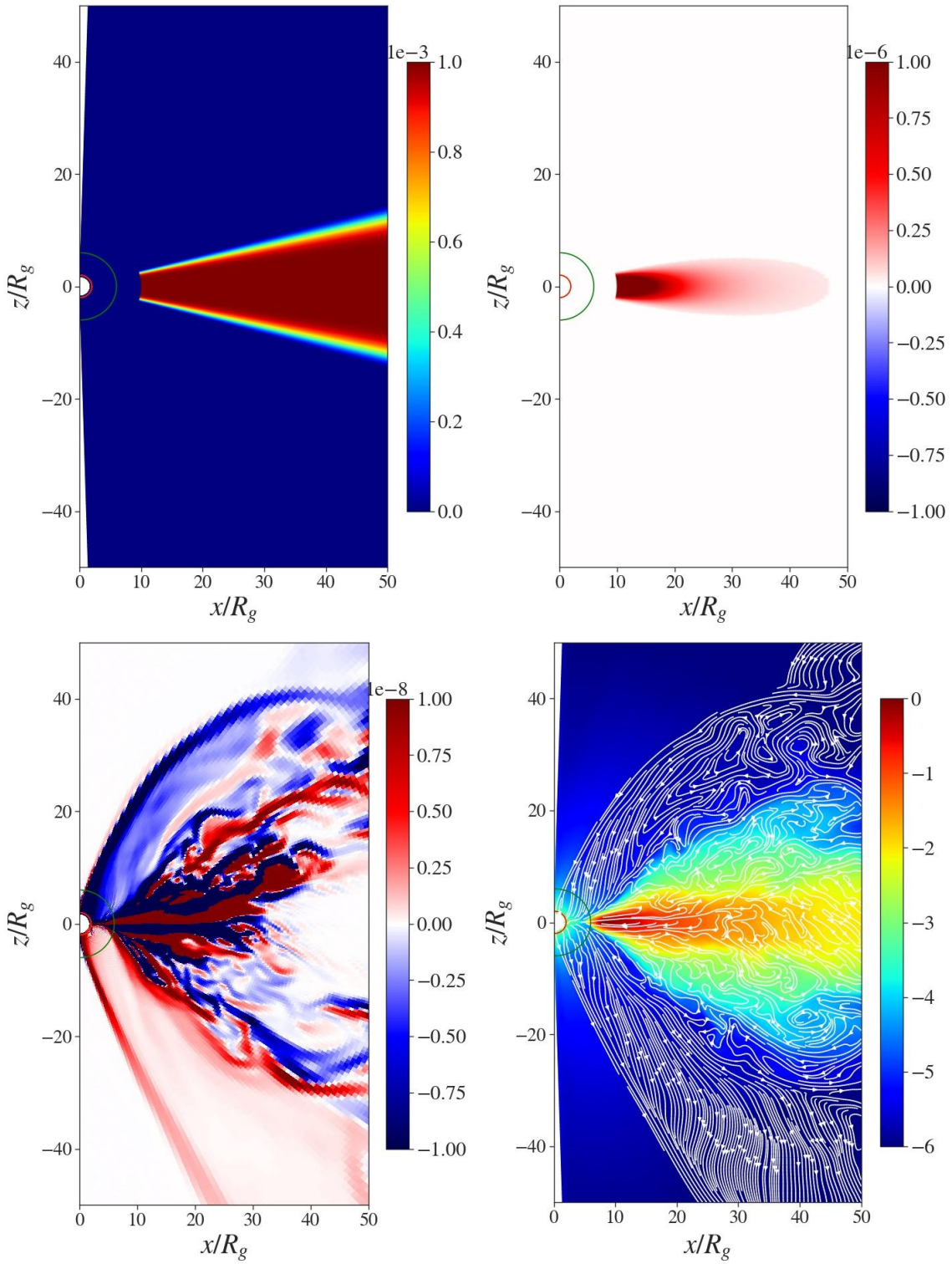

FIGURE 6.9: Initial conditions and evolution of simulation *thin1*. *Top left:* Distribution of magnetic diffusivity. The value is constant inside the disk and the drops steeply in the disk surface. *Top right:* Initial condition for the toroidal magnetic field component. *Bottom left:* Radial component of the magnetic field B_r. *Bottom right:* Fluid density in logarithmic scale with the poloidal magnetic field lines.

hemispheres (see Figure 6.9). The poloidal field has a purely radial component with positive and negative values in the upper and lower hemispheres and is completely confined inside the initial disk distribution. The inner radius of the disk is set to $r = 10$, quite outside the ISCO of the Schwarzschild black hole. For diffusivity we use a new profile that gives a constant value of $\eta = 0.001$ inside the disk with a steep drop to low values in the disk surface (see Figure 6.9). Our goal is to develop a dipolar poloidal field, thus for the dynamo we use a constant value of $\xi = 0.001$ inside the disk and zero in the surrounding corona.

In the bottom panels of Figure 6.9 we also see the values of the radial magnetic field component and the logarithm of the fluid density with poloidal magnetic field lines at time $t = 2500$. The magnetic field structure looks similar to that from the torus simulations even though the values are significantly lower. The distribution of diffusivity is partially responsible for this since it is constant inside the disk and contributes against the generation of a strong magnetic field. When the field is generated inside the disk, it is advected towards the black hole, while keeping its dipolar structure. Inside the disk, layers with different signs appear eventually resulting in the chaotic structure of field lines.

In Figure 6.10 we see the evolution of the minimum values of plasma-β inside the disk for the toroidal and poloidal components. In the beginning, both field components grow due to the $\alpha\omega$ effect, however, after time $t \sim 2000$ the poloidal field stops increasing (with the exception of some variations) and keeps an average value of $\sim 10^5$ for the minimum plasma-β. A similar behavior appears in the torus simulations (see Figure 6.4), with the plasma-β maintaining its gradual decrease albeit with a much flatter slope. Both simulations do not use any quenching mechanism so such a behavior is quite peculiar.

For simulation *thin1*, the poloidal plasma-β starts increasing around time $t \sim 2000$. At the same time, the accretion rate, which until that point was quite strong starts decreasing. If we take a look at the poloidal magnetic field inside the disk and along the equatorial plane we can see that until $t \sim 2000$ the profile is quite flat up to radius $r \sim 30$. The flatness of the poloidal field results in the increase of the magnetic diffusion because the magnetic resistivity, which in turn changes the slope of the poloidal field profile, as we can see in the bottom panel of Figure 6.11. The dynamo that operates in the disk is not strong enough to counter the diffusive effect resulting in the continuous increase and decrease in the values of plasma-β.

On Table 6.1 we see the different simulation we run with the thin disk prescription. In simulation *thin3* we used a poloidal field as an initial condition keeping however the low magnetization of the disk in the same levels as with simulation *thin1*.

6.3.2 From a Poloidal Seed Field

A low-magnetization poloidal magnetic field as a seed in dynamo simulation has been used previously in Newtonian/special relativistic simulations (Stepanovs, Fendt, and Sheikhnezami, 2014; Fendt and Gaßmann, 2018). In our case, since the the thin disk is not in equilibrium with the black hole, from the beginning of the simulation the disk will try to adjust in the gravitational environment of the black hole. This causes deviation of the seed field from the perfectly radial structure. These deviations, however, are minimal and significantly smaller that the magnetic field that is generated by the dynamo.

Simulations *thin3* and *thin4* are using the poloidal seed field and the only difference between them is the value of the dynamo parameter, which for simulation *thin4* is 4 times

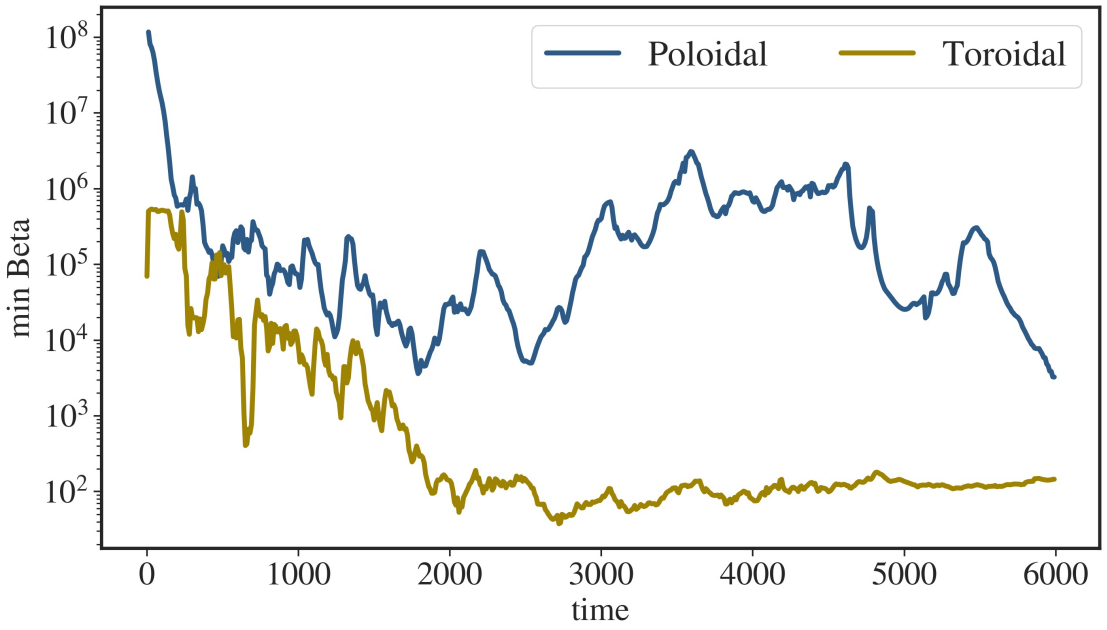

FIGURE 6.10: Minimum value of the plasma-β for the toroidal and poloidal components of the magnetic field in the area where dynamo works during the evolution of simulation *thin1*.

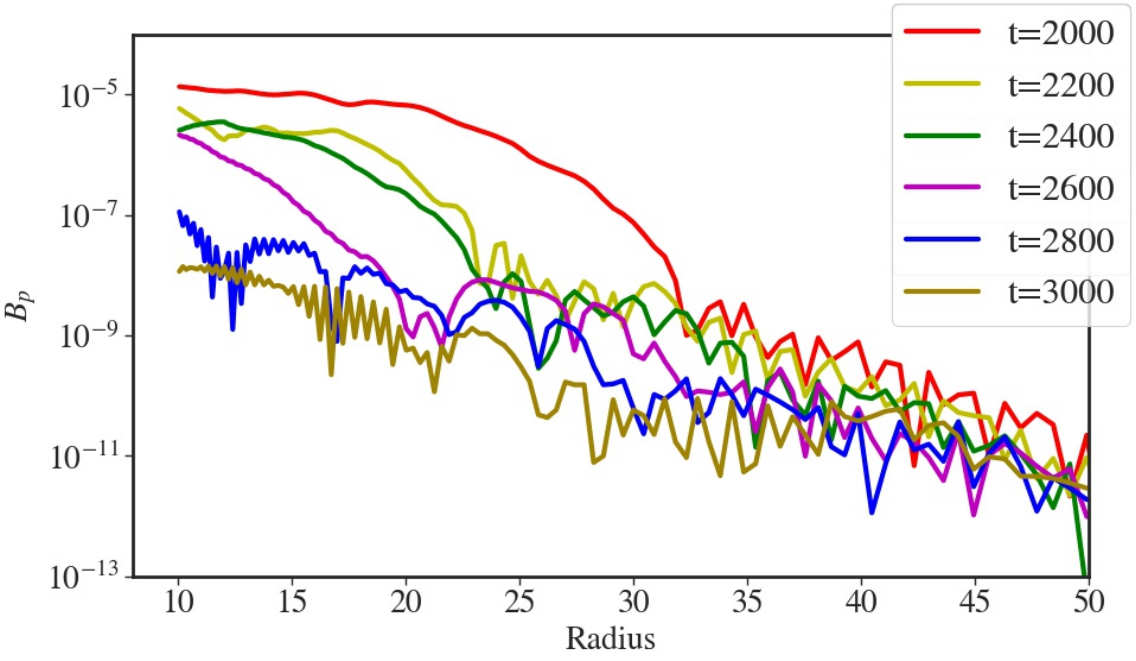

FIGURE 6.11: Evolution of the radial profile in the equatorial plane of the poloidal field for simulation *thin1*.

larger. The evolution of the simulations are very different. Simulation *thin3* the poloidal magnetic field appears underdeveloped probably because the dynamo is not strong enough to counter the diffusive effects of η. On the other side, for simulation *thin4*, the magnetic field is much stronger (at least 4 orders of magnitude). In Figure 6.12 we compare the radial magnetic field at time $t = 6000$ for simulations *thin3* and *thin4*, and we show the density distribution, magnetic field lines and radial velocity for simulation *thin4*.

On a first glance, simulation *thin4* looks similar to our reference simulation from Chapter 4 it is in our immediate plans to analyze it further in order to compare the outflows we observe.

6.4 Summary

In this chapter we presented a fully dynamical generation of magnetic field by a mean–field dynamo and the subsequent evolution of accretion disks and tori around a black hole in a GRMHD environment using `rHARM3D`.

We discussed the implementation of mean–field dynamo in the code and the differences we encountered when testing the structure of the generated field, main the case of a dynamo distribution that changes sign in the equatorial plane and has some kind of dependence from the polar angle. According to our results, the poloidal field that is generated by such a dynamo has a strong quadrupolar structure, contrary to the results of Rekowski, Rüdiger, and Elstner (2000) in Newtonian simulations. After running several simulation we saw that this initial quadrupolar field inside the torus is quickly replace by a structure of many layers of different sign alternating with each other. However, outside of the torus, if the simulation runs long enough, a dipolar component of magnetic field develops and becomes a conduit for the generation of a jet (e.g. *quad2*). In the same simulation we also detected a slow change of sign in the torus interior which might be connected with the dynamo prescription we used.

Both with the the torus and the disk simulation we tried to show that the induced magnetic field is capable of launching jets. We detected relativistic velocities coming either from the surface of the disk/torus or from the inner, almost axial jet. Unfortunately, we did not succeed into producing long running simulations with a rotating black hole, however, simulation *quad3* with $a = 0.9$ show a quickly developed jet coming from the black hole magnetosphere with a significant component of electromagnetic energy flux.

For specific simulations we also prescribed a dynamo quenching mechanism to control the growth of magnetic field. The quenching is happening based on the magnetization of the fluid in each cell which is then compare with a preset equipartition value. We encountered problems with the implementation into the code, which were partially solved on the expense of slower running simulations. The mechanism works and succeeds into extending the “lifetime” of the simulations, however, only temporarily.

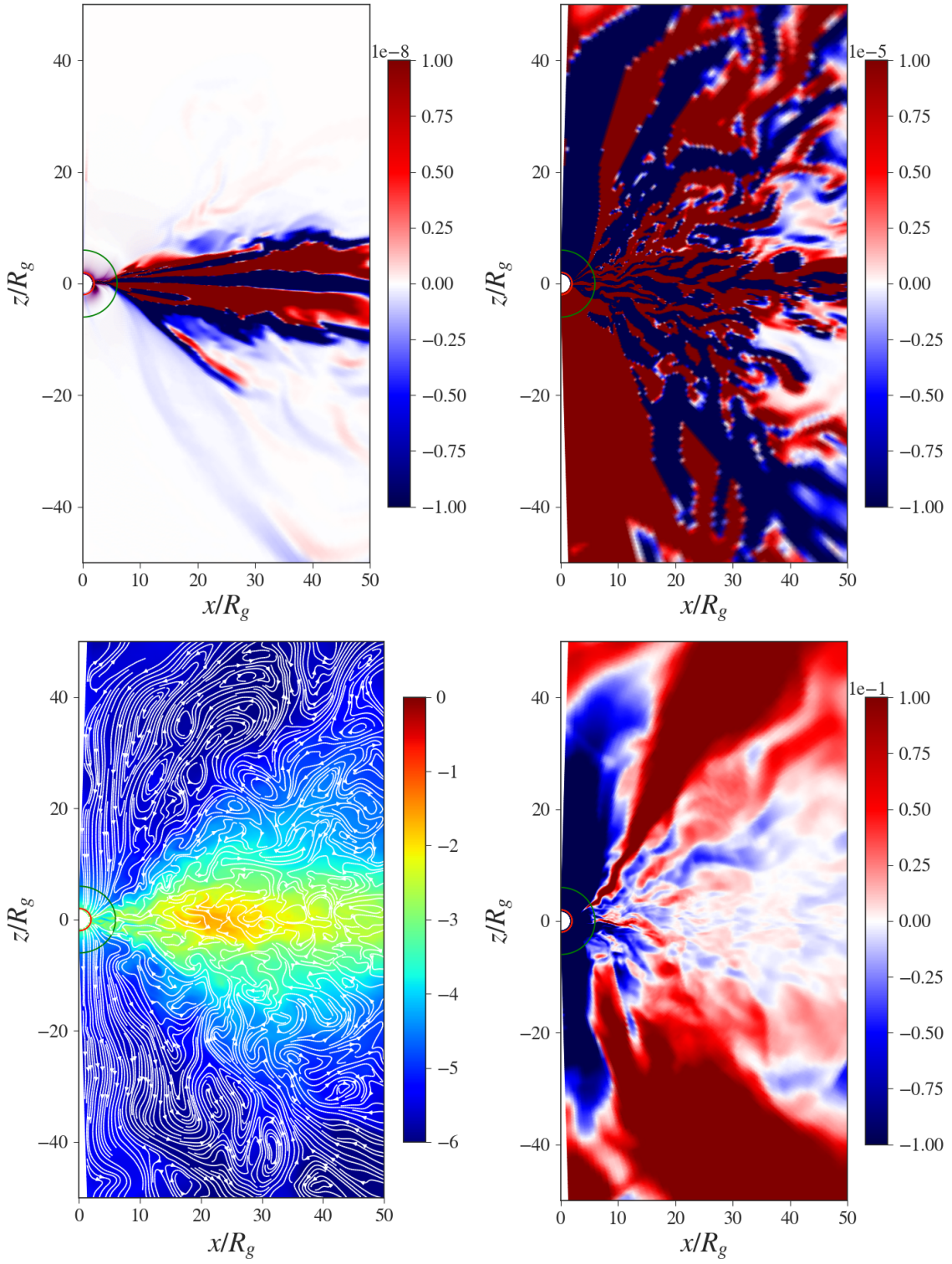

FIGURE 6.12: *Top:* Radial magnetic field component at time $t = 6000$ for simulations *thin3* (left) and *thin4* (right). Notice the different order of magnitude in the colorbar values for the two simulations. *Bottom:* Density contours with poloidal field lines and the radial velocity component u^r at time $t = 6000$ for simulation *thin4*.

Appendix A

Solving the Dynamo Equations

A.1 Convection Term

For historical reference Ohm's law for a relativistic plasma is derived by Blackman and Field (1993) where the also introduce a convection term $j^\tau U_\tau U^\mu$

$$F^{\mu\nu}U_\nu = \eta_r j^\mu + j^\tau U_\tau U^\mu. \tag{A.1}$$

We will start our calculation with the same equation in its more "modern" form as it appears in Palenzuela et al. (2009) and Bucciantini and Del Zanna (2013) in contravariant form

$$I^\mu + (I^\nu u_\nu)\, u^\mu = \sigma F^{\mu\nu} u_\nu, \tag{A.2}$$

where

$$I^\mu = qn^\mu + J^\mu \tag{A.3}$$

is the 4-current as seen by the normal observer.

In this frame, where the observer has a 4-velocity n^μ, we have

$$E^\mu = F^{\mu\nu} n_\nu, \tag{A.4a}$$
$$B^\mu = F^{*\mu\nu} n_\nu, \tag{A.4b}$$

as the electric and magnetic field. This frame is chosen so that $E^0 = B^0 = J^0 = 0$. The convection term $I^\mu u_\mu$ can be written as

$$I^\mu u_\mu = I^0 u_0 + I^i u_i, \tag{A.5}$$

with the following components

$$I^0 = qn^0 + J^0 = q\frac{1}{\alpha} = \frac{q}{\alpha}, \tag{A.6a}$$
$$I^i = qn^i + J^i = -q\frac{\beta^i}{\alpha} + J^i, \tag{A.6b}$$
$$u_0 = \Gamma(n_0 + v_0) = \Gamma(-\alpha + v_0), \tag{A.6c}$$
$$u_i = \Gamma(n_i + v_i) = \Gamma v_i, \qquad \text{since } n_\mu = (-\alpha, 0). \tag{A.6d}$$

Combining them all together we get

$$\begin{aligned} I^\mu u_\mu &= I^0 u_0 + I^i u_i \\ &= \Gamma\frac{q}{\alpha}(-\alpha + v_0) + (q\frac{\beta^i}{\alpha} + J^i)\Gamma v_i \\ &= -\Gamma q + \Gamma\frac{q}{\alpha}v_0 - \Gamma\frac{q}{\alpha}\beta^i v_i + \Gamma J^i v_i \\ &= \Gamma(-q + J^i v_i) + \Gamma\frac{q}{\alpha}v_0 - \Gamma\frac{q}{\alpha}\alpha^2 g^{ti} v_i, \qquad \text{since } \beta^i = \alpha^2 g^{ti} \\ &= -\Gamma(q - J^i v_i) + \Gamma\frac{q}{\alpha}v_0 - \Gamma q\alpha v^0 \\ &= -\Gamma(q - J^i v_i) + \Gamma\frac{q}{\alpha}v_0, \\ &= -q_0 \end{aligned} \tag{A.7}$$

In Komissarov (2007) and Bucciantini and Del Zanna (2013) is mentioned that $I^\mu u_\mu = -q_0$ as the electric charge density in the fluid frame. Only Bucciantini and Del Zanna (2013) calculate the q_0 in the normal observer frame and they mention it as $q_0 = \Gamma(q - J^i v_i)$, however we can see that is not the case. It is probably just a typo on their side.

A.2 Ampere's Equation

The Faraday and Maxwell tensors in the normal observer frame are written as

$$F^{\mu\nu} = n^\mu E^\nu - E^\mu n^\nu + \epsilon^{\mu\nu\lambda\kappa} B_\lambda n_\kappa, \tag{A.8a}$$

$$F^{*\mu\nu} = n^\mu B^\nu - B^\mu n^\nu - \epsilon^{\mu\nu\lambda\kappa} E_\lambda n_\kappa. \tag{A.8b}$$

and the Maxwell equations are

$$\nabla_\mu F^{\mu\nu} = -I^\nu, \tag{A.9a}$$

$$\nabla_\mu F^{*\mu\nu} = 0. \tag{A.9b}$$

with

$$I^\mu = q n^\mu + J^\mu, \tag{A.10a}$$

$$\tag{A.10b}$$

For $\nu = 0 = t$

$$\nabla_\mu \left[n^\mu E^0 - E^\mu n^0 + \epsilon^{\mu 0\lambda\kappa} B_\lambda n_\kappa \right] = -I^0, \tag{A.11a}$$

$$\nabla_\mu \left[-E^\mu n^0 + \epsilon^{\mu 0\lambda 0} B_\lambda n_0 \right] = -q n^0 - J^0, \tag{A.11b}$$

$$\nabla_\mu \left[-E^\mu n^0 \right] = -q n^0, \tag{A.11c}$$

$$\nabla_\mu E^\mu = q. \tag{A.11d}$$

For $\nu = i = (r, \theta, \phi)$

$$\nabla_\mu \left[n^\mu E^i - E^\mu n^i + \epsilon^{\mu i \lambda \kappa} B_\lambda n_\kappa \right] = -I^i, \tag{A.12a}$$

$$\nabla_\mu \left[n^\mu E^i + E^\mu \frac{\beta^i}{\alpha} + \epsilon^{\mu i \lambda 0} B_\lambda n_0 \right] = -qn^i - J^i, \tag{A.12b}$$

$$\nabla_\mu \left[n^\mu E^i + E^\mu \frac{\beta^i}{\alpha} - \epsilon^{\mu i \lambda 0} B_\lambda \alpha \right] = q\frac{\beta^i}{\alpha} - J^i. \tag{A.12c}$$

In the left hand side, for $\mu = 0 = t$ we get

$$\nabla_0 \left[n^0 E^i \right] = \nabla_t \left(\frac{E^i}{\alpha} \right), \tag{A.13}$$

and for $\mu = j$ we get

$$\nabla_j \left[n^j E^i + E^j \frac{\beta^i}{\alpha} + \epsilon^{j i \lambda 0} B_\lambda \alpha \right] = \nabla_j \left[-E^i \frac{\beta^j}{\alpha} + E^j \frac{\beta^i}{\alpha} + \epsilon^{0 j i \lambda} B_\lambda \alpha \right]. \tag{A.14}$$

Putting them back to Equation (A.12c) we get

$$\nabla_t \left(\frac{E^i}{\alpha} \right) + \nabla_j \left(-E^i \frac{\beta^j}{\alpha} + E^j \frac{\beta^i}{\alpha} + \epsilon^{0 j i \lambda} B_\lambda \alpha \right) = q\frac{\beta^i}{\alpha} - J^i, \tag{A.15}$$

$$g^{-1/2} \left[\partial_t \left(g^{1/2} \frac{E^i}{\alpha} \right) - \partial_j \left(g^{1/2} E^i \frac{\beta^j}{\alpha} \right) + \partial_j \left(g^{1/2} E^j \frac{\beta^i}{\alpha} \right) + \partial_j \left(g^{1/2} g^{-1/2} [0 j i \lambda] B_\lambda \alpha \right) \right] = q\frac{\beta^i}{\alpha} - J^i, \tag{A.16}$$

$$g^{-1/2} \left[\partial_t \left(\gamma^{1/2} E^i \right) - \partial_j \left(\gamma^{1/2} E^i \beta^j \right) + \partial_j \left(\gamma^{1/2} E^j \beta^i \right) + \partial_j \left([0 j i \lambda] B_\lambda \alpha \right) \right] = \frac{q\beta^i - \alpha J^i}{\alpha}, \tag{A.17}$$

$$\partial_t \left(\gamma^{1/2} E^i \right) + \partial_j \left(\gamma^{1/2} E^j \beta^i - \gamma^{1/2} E^i \beta^j \right) + \partial_j \left([0 j i k] B_k k \alpha \right) = g^{1/2} \frac{q\beta^i - \alpha J^i}{\alpha}, \tag{A.18}$$

$$\partial_t \left(\gamma^{1/2} E^i \right) + \partial_j \left(\gamma^{1/2} (E^j \beta^i - E^i \beta^j) \right) + \partial_j \left([j i k] B_k \alpha \right) = \gamma^{1/2} \left(q\beta^i - \alpha J^i \right), \tag{A.19}$$

$$\partial_t \left(\gamma^{1/2} E^i \right) + \partial_j \left(\gamma^{1/2} (E^j \beta^i - E^i \beta^j) \right) - \partial_j [i j k] (B_k \alpha) = \gamma^{1/2} \left(q\beta^i - \alpha J^i \right). \tag{A.20}$$

Using Krönecker's δ

$$\partial_t \left(\gamma^{1/2} E^i \right) + \partial_j \left(\gamma^{1/2} (\delta^j_m \delta^i_n - \delta^i_m \delta^j_n) E^m \beta^n \right) - \partial_j [i j k] (B_k \alpha) = \gamma^{1/2} \left(q\beta^i - \alpha J^i \right). \tag{A.21}$$

We know that the Levi-Civita symbol is connected with Krönecker's δ with

$$[kmn][kji] = \delta^j_m \delta^i_n - \delta^i_m \delta^j_n. \tag{A.22}$$

$$\partial_t \left(\gamma^{1/2} E^i\right) + \partial_j \left(\gamma^{1/2} [kmn][kji] E^m \beta^n\right) - \partial_j [ijk](B_k \alpha) = \gamma^{1/2} \left(q\beta^i - \alpha J^i\right), \tag{A.23}$$

$$\gamma^{-1/2} \partial_t \left(\gamma^{1/2} E^i\right) + \gamma^{-1/2} [ijk] \partial_j \left(\gamma^{1/2} [knm] E^m \beta^n\right) - \gamma^{-1/2} [ijk] \partial_j (B_k \alpha) = \left(q\beta^i - \alpha J^i\right), \tag{A.24}$$

$$\gamma^{-1/2} \partial_t \left(\gamma^{1/2} E^i\right) + \epsilon^{ijk} \partial_j \left(\epsilon_{knm} E^m \beta^n\right) - \epsilon^{ijk} \partial_j (B_k \alpha) = \left(q\beta^i - \alpha J^i\right), \tag{A.25}$$

$$\gamma^{-1/2} \partial_t \left(\gamma^{1/2} E^i\right) + \epsilon^{ijk} \partial_j \left(\epsilon_{knm} E^m \beta^n - B_k \alpha\right) = \left(q\beta^i - \alpha J^i\right). \tag{A.26}$$

Turning them into vectors we get

$$\gamma^{-1/2} \partial_t \left(\gamma^{1/2} \boldsymbol{E}\right) + \nabla \left(\boldsymbol{\beta} \times \boldsymbol{E} - \alpha \boldsymbol{B}\right) = q\boldsymbol{\beta} - \alpha \boldsymbol{J}, \tag{A.27}$$

which is Equation 20 from Bucciantini and Del Zanna (2013).

A.3 Deriving the Time Evolution of the Electric Field in the Mean–Field Dynamo Closure

We start from Ohm's law, the definition of the electric current density, the 4-current, electric and magnetic field in the frame co-moving with the fluid.

$$\sigma e^\mu = j^\mu + \xi b^\mu, \tag{A.28a}$$
$$j^\mu = I^\mu + (I^\nu u_\nu) u^\mu, \tag{A.28b}$$
$$e^\mu = F^{\mu\nu} u_\nu, \tag{A.28c}$$
$$b^\mu = F^{*\mu\nu} u_\nu, \tag{A.28d}$$

A.3.1 Temporal Projection

We take the case of $\mu = 0 = t$ for the electric field

$$\begin{aligned} e^0 &= F^{0\nu}u_\nu = \left(n^0E^\nu - E^0n^\nu + \epsilon^{0\nu\lambda\kappa}B_\lambda n_\kappa\right)u_\nu \\ &= n^0E^\nu u_\nu + \epsilon^{0\nu\lambda\kappa}B_\lambda u_\nu n_\kappa \\ &= \frac{1}{\alpha}E^\nu u_\nu + \epsilon^{0\nu\lambda 0}B_\lambda u_\nu n_0 \\ &= \frac{E^\nu u_\nu}{\alpha} = \frac{1}{\alpha}\Gamma E^\nu(n_\nu + v_\nu) \\ &= \frac{1}{\alpha}\Gamma\left(E^0(n_0 + v_0) + E^i(n_i + v_i)\right) \\ &= \frac{1}{\alpha}\Gamma E^i v_i, \end{aligned} \tag{A.29}$$

for the magnetic field

$$\begin{aligned} b^0 &= F^{*0\nu}u_\nu = \left(n^0B^\nu - B^0n^\nu - \epsilon^{0\nu\lambda\kappa}E_\lambda n_\kappa\right)u_\nu \\ &= n^0B^\nu u_\nu - \epsilon^{0\nu\lambda\kappa}E_\lambda u_\nu n_\kappa \\ &= \frac{1}{\alpha}B^\nu u_\nu - \epsilon^{0\nu\lambda 0}E_\lambda u_\nu n_0 \\ &= \frac{B^\nu u_\nu}{\alpha} = \frac{B^\nu}{\alpha}\Gamma(n_\nu + v_\nu) \\ &= \frac{1}{\alpha}\Gamma\left(B^0(n_0 + v_0) + B^i(n_i + v_i)\right) \\ &= \frac{1}{\alpha}\Gamma B^i v_i, \end{aligned} \tag{A.30}$$

and for the electric current density

$$\begin{aligned} j^0 &= qn^0 + J^0 + (I^\nu u_\nu)u^0 \\ &= \frac{q}{\alpha} + (I^\nu u_\nu)u^0 \\ &= \frac{q}{\alpha} + (I^\nu u_\nu)\Gamma(n^0 + v^0) \\ &= \frac{q}{\alpha} + (I^\nu u_\nu)\frac{\Gamma}{\alpha} \end{aligned} \tag{A.31}$$

because $E^0 = B^0 = J^0 = 0$, the only non-zero component of n_κ is $n_0 = -\alpha$, $n^\nu = (1/a, -\beta^i/a)$ and $\epsilon^{abca} = 0$. Combining them all together in Ohm's law we get

$$\sigma\Gamma\frac{1}{\alpha}E^i v_i = \frac{q}{\alpha} + (I^\nu u_\nu)\frac{\Gamma}{\alpha} + \xi\frac{1}{\alpha}\Gamma B^i v_i, \tag{A.32a}$$

$$\sigma\Gamma E^i v_i = q + \Gamma(I^\nu u_\nu) + \xi\Gamma B^i v_i, \tag{A.32b}$$

$$\sigma\Gamma E^i v_i = q - \Gamma q_0 + \xi\Gamma B^i v_i, \tag{A.32c}$$

$$\Gamma E^i v_i = \eta(q - \Gamma q_0) + \xi\Gamma B^i v_i, \tag{A.32d}$$

which can be written as Equation 30 from Bucciantini and Del Zanna (2013)

A.3.2 Spatial Projection

We take the case of $\mu = i = (r, \theta, \phi)$ for the electric field

$$\begin{aligned}
e^i = F^{i\nu}u_\nu &= \left(n^i E^\nu - E^i n^\nu + \epsilon^{i\nu\lambda\kappa}B_\lambda n_\kappa\right)u_\nu \\
&= -\frac{\beta^i}{\alpha}E^\nu u_\nu - E^i n^\nu u_\nu + \epsilon^{i\nu\lambda 0}B_\lambda n_0 u_\nu \\
&= -\frac{\beta^i}{\alpha}E^k u_k - E^i u_\mu u^\mu - \frac{\epsilon^{ijk}}{\alpha}B_k(-\alpha)u_j \\
&= -\frac{\beta^i}{\alpha}\Gamma E^k(n_k + v_k) - E^i(n_0 u^0 + n_i u^i) + \epsilon^{ijk}B_k\Gamma(n_i + v_j) \\
&= -\frac{\beta^i}{\alpha}\Gamma E^k v_k + E^i\alpha u^0 + \epsilon^{ijk}\Gamma B_k v_j \\
&= -\frac{\beta^i}{\alpha}\Gamma E^k v_k + E^i\alpha\Gamma(n^0 + v^0) + \epsilon^{ijk}\Gamma B_k v_j \\
&= -\frac{\beta^i}{\alpha}\Gamma E^k v_k + E^i\alpha\Gamma\frac{1}{\alpha} + \epsilon^{ijk}\Gamma B_k v_j \\
&= -\frac{\beta^i}{\alpha}\Gamma E^k v_k + \Gamma E^i + \epsilon^{ijk}\Gamma B_k v_j
\end{aligned} \tag{A.33}$$

for the magnetic field

$$\begin{aligned}
b^i = F^{*i\nu}u_\nu &= \left(n^i B^\nu - B^i n^\nu - \epsilon^{i\nu\lambda\kappa}E_\lambda n_\kappa\right)u_\nu \\
&= -\frac{\beta^i}{\alpha}B^\nu u_\nu - B^i n^\nu u_\nu - \epsilon^{i\nu\lambda 0}E_\lambda n_0 u_\nu \\
&= -\frac{\beta^i}{\alpha}B^k u_k - B^i u_\mu u^\mu + \frac{\epsilon^{ijk}}{\alpha}E_k(-\alpha)u_j \\
&= -\frac{\beta^i}{\alpha}\Gamma B^k(n_k + v_k) - B^i(n_0 u^0 + n_i u^i) - \epsilon^{ijk}E_k\Gamma(n_i + v_j) \\
&= -\frac{\beta^i}{\alpha}\Gamma B^k v_k + B^i\alpha u^0 - \epsilon^{ijk}\Gamma E_k v_j \\
&= -\frac{\beta^i}{\alpha}\Gamma B^k v_k + B^i\alpha\Gamma(n^0 + v^0) - \epsilon^{ijk}\Gamma E_k v_j \\
&= -\frac{\beta^i}{\alpha}\Gamma B^k v_k + B^i\alpha\Gamma\frac{1}{\alpha} - \epsilon^{ijk}\Gamma E_k v_j \\
&= -\frac{\beta^i}{\alpha}\Gamma B^k v_k + \Gamma B^i - \epsilon^{ijk}\Gamma E_k v_j
\end{aligned} \tag{A.34}$$

and for the electric current density

$$\begin{aligned}
j^\mu = I^i + (I^\nu u_\nu)u^i &= qn^i + J^i + (I^\nu u_\nu)\Gamma(n^i + v^i) \\
&= J^i - \frac{\beta^i}{\alpha}q + (I^\nu u_\nu)\Gamma(v^i - \frac{\beta^i}{\alpha})
\end{aligned} \tag{A.35}$$

because $E^0 = B^0 = J^0 = v^0 = 0$ only the spatial components of $E^\nu u_\nu$ survive, $n^\nu u_\nu = n^\nu g_{\mu\nu} u^\mu = u_\mu u^\mu$. Also for the Levi-Civita pseudo-tensor

$$\begin{aligned}\epsilon^{i\nu\lambda 0} &= g^{-1/2}[i\nu\lambda 0] = g^{-1/2}(-[0i\nu\lambda]) = -g^{-1/2}[0ijk] = -g^{-1/2}[ijk] = -(\alpha^2\gamma)^{-1/2}[ijk] = \\ &= -\frac{1}{\alpha\gamma^{1/2}}[ijk] = -\frac{1}{\alpha\gamma^{1/2}} - \frac{\epsilon^{ijk}}{\gamma^{-1/2}} = -\frac{\epsilon^{ijk}}{\alpha}\end{aligned} \tag{A.36}$$

Combining Equations (A.33) (A.34) and (A.35) in Ohm's law we get

$$\begin{aligned}-\frac{\beta^i}{\alpha}\Gamma E^k v_k + \Gamma E^i + \epsilon^{ijk}\Gamma B_k v_j = \eta\left[J^i - \frac{\beta^i}{\alpha}q + (I^\nu u_\nu)\Gamma(v^i - \frac{\beta^i}{\alpha})\right] \\ + \xi\left[-\frac{\beta^i}{\alpha}\Gamma B^k v_k + \Gamma B^i - \epsilon^{ijk}\Gamma E_k v_j\right]\end{aligned} \tag{A.37}$$

using Equation (A.32b) the equation evolves into

$$\begin{aligned}-\frac{\beta^i}{\alpha}\Gamma E^k v_k + \Gamma E^i + \epsilon^{ijk}\Gamma B_k v_j = \eta J^i - \eta\frac{\beta^i}{\alpha}q + \left[\Gamma E^\nu u_\nu - \eta q - \xi\Gamma B^j v_j\right](v^i - \frac{\beta^i}{\alpha}) \\ + \xi\left[-\frac{\beta^i}{\alpha}\Gamma B^k v_k + \Gamma B^i - \epsilon^{ijk}\Gamma E_k v_j\right],\end{aligned} \tag{A.38}$$

$$\begin{aligned}\cancel{-\frac{\beta^i}{\alpha}\Gamma E^k v_k} + \Gamma E^i + \epsilon^{ijk}\Gamma B_k v_j = \eta J^i - \cancel{\eta\frac{\beta^i}{\alpha}q} + E^\nu u_\nu v^i - \eta q v^i - \xi\Gamma B^j v_j v^i \\ \cancel{- \Gamma E^\nu u_\nu \frac{\beta^i}{\alpha}} + \cancel{\eta q\frac{\beta^i}{\alpha}} + \cancel{\xi\Gamma B^j v_j\frac{\beta^i}{\alpha}} \\ \cancel{-\xi\frac{\beta^i}{\alpha}\Gamma B^k v_k} + \xi\Gamma B^i - \xi\epsilon^{ijk}\Gamma E_k v_j,\end{aligned} \tag{A.39}$$

where we used $E^\nu u_\nu = E^k u_k = E^k(n_k + v_k) = \Gamma E^k v_k$ for the magnetic field respectively and used mute indexes interchangeably. As a result the equation simplifies into

$$\Gamma E^i + \Gamma\epsilon^{ijk} v_j B_k = \eta J^i - \eta q v^i + \Gamma(E^k v_k)v^i - \xi\Gamma(B^k v_k)v^i + \xi\Gamma B^i - \xi\Gamma\epsilon^{ijk} v_j E_k, \tag{A.40}$$

$$\Gamma\left[E^i + \epsilon^{ijk} v_j B_k - (E^k v_k)v^i\right] = \eta\left(J^i - q v^i\right) + \xi\Gamma\left[B^i - (B^k v_k)v^i - \epsilon^{ijk} v_j E_k\right], \tag{A.41}$$

which leads us to Equation 31 from Bucciantini and Del Zanna (2013)

$$\Gamma\left[\boldsymbol{E} - (\boldsymbol{E}\cdot\boldsymbol{v})\,\boldsymbol{v} + \boldsymbol{v}\times\boldsymbol{B}\right] = \eta\left(\boldsymbol{J} - q\boldsymbol{v}\right) + \xi\Gamma\left[\boldsymbol{B} - \boldsymbol{v}\times\boldsymbol{E} - (\boldsymbol{B}\cdot\boldsymbol{v})\,\boldsymbol{v}\right], \tag{A.42}$$

Continuing from Equation (A.41) we change η to σ and multiply by α

$$\alpha\sigma\Gamma\left[E^i + \epsilon^{ijk} v_j B_k - (E^k v_k)v^i\right] = \alpha J^i - \alpha q v^i + \alpha\sigma\xi\Gamma\left[B^i - (B^k v_k)v^i - \epsilon^{ijk} v_j E_k\right], \tag{A.43}$$

$$\alpha\sigma\Gamma\left[E^i+\epsilon^{ijk}v_jB_k-(E^kv_k)v^i\right]-\alpha\sigma\xi\Gamma\left[B^i-(B^kv_k)v^i-\epsilon^{ijk}v_jE_k\right]+\alpha qv^i=\alpha J^i, \tag{A.44}$$

and we subtract $q\beta^i$ in order to form the right hand side of Equation A.26

$$\alpha\sigma\Gamma\left[E^i+\epsilon^{ijk}v_jB_k-(E^kv_k)v^i\right]-\alpha\sigma\xi\Gamma\left[B^i-(B^kv_k)v^i-\epsilon^{ijk}v_jE_k\right]+\alpha qv^i-q\beta^i=\alpha J^i-q\beta^i, \tag{A.45}$$

resulting in

$$\begin{aligned}-\gamma^{-1/2}\partial_t(\gamma^{1/2}E^i)-\epsilon^{ijk}\partial_j\left(\epsilon_{knm}E^m\beta^n-B_k\alpha\right)&=\alpha\sigma\Gamma\left[E^i+\epsilon^{ijk}v_jB_k-(E^kv_k)v^i\right]\\&\quad-\alpha\sigma\xi\Gamma\left[B^i-(B^kv_k)v^i-\epsilon^{ijk}v_jE_k\right]\\&\quad+q(\alpha v^i-\beta^i),\end{aligned} \tag{A.46}$$

$$\begin{aligned}\gamma^{-1/2}\partial_t(\gamma^{1/2}E^i)+\epsilon^{ijk}\partial_j\left(\epsilon_{knm}E^m\beta^n-B_k\alpha\right)&=-\alpha\sigma\Gamma\left[E^i+\epsilon^{ijk}v_jB_k-(E^kv_k)v^i\right]\\&\quad+\alpha\sigma\xi\Gamma\left[B^i-(B^kv_k)v^i-\epsilon^{ijk}v_jE_k\right]\\&\quad-q(\alpha v^i-\beta^i).\end{aligned} \tag{A.47}$$

Turning them into vectors and exchanging η for σ we get

$$\begin{aligned}\gamma^{-1/2}\partial_t(\gamma^{1/2}\boldsymbol{E})+\nabla\times(\boldsymbol{\beta}\times\boldsymbol{E}-\alpha\boldsymbol{B})+q(\alpha\boldsymbol{v}-\boldsymbol{\beta})&=-\alpha\Gamma\left[\boldsymbol{E}+\boldsymbol{v}\times\boldsymbol{B}-(\boldsymbol{E}\cdot\boldsymbol{v})\boldsymbol{v}\right]/\eta\\&\quad+\alpha\xi\Gamma\left[\boldsymbol{B}-(\boldsymbol{B}\cdot\boldsymbol{v})\boldsymbol{v}-\boldsymbol{v}\times\boldsymbol{E}\right]/\eta,\end{aligned} \tag{A.48}$$

which is Equation 32 from Bucciantini and Del Zanna (2013).

A.3.3 Solving the Equation

We absorb the spatial metric in the electric and magnetic field $\gamma^{1/2}E^i=\mathscr{E}^i$, $\gamma^{1/2}B^i=\mathscr{B}^i$. As a result, the evolution of electric field becomes

$$\begin{aligned}\gamma^{-1/2}\partial_t(\mathscr{E}^i)+\epsilon^{ijk}\partial_j\left(\epsilon_{knm}\mathscr{E}^m\beta^n-\mathscr{B}_k\alpha\right)&=-\gamma^{-1/2}\alpha\sigma\Gamma\left[\mathscr{E}^i+\epsilon^{ijk}v_j\mathscr{B}_k-(\mathscr{E}^kv_k)v^i\right]\\&\quad+\gamma^{-1/2}\alpha\sigma\xi\Gamma\left[\mathscr{B}^i-(\mathscr{B}^kv_k)v^i-\epsilon^{ijk}v_j\mathscr{E}_k\right]\\&\quad-q(\alpha v^i-\beta^i),\end{aligned} \tag{A.49}$$

$$\begin{aligned}&\partial_t(\mathscr{E}^i)+\gamma^{-1/2}\epsilon^{ijk}\partial_j\left(\epsilon_{knm}\mathscr{E}^m\beta^n-\mathscr{B}_k\alpha\right)+\gamma^{-1/2}q(\alpha v^i-\beta^i)=\\&\quad=-\alpha\sigma\Gamma\left[\mathscr{E}^i+\epsilon^{ijk}v_j\mathscr{B}_k-(\mathscr{E}^kv_k)v^i\right]+\alpha\sigma\xi\Gamma\left[\mathscr{B}^i-(\mathscr{B}^kv_k)v^i-\epsilon^{ijk}v_j\mathscr{E}_k\right].\end{aligned} \tag{A.50}$$

We set

$$\mathscr{E}^i_{ns}=-\gamma^{-1/2}\epsilon^{ijk}\partial_j\left(\epsilon_{knm}\mathscr{E}^m\beta^n-\mathscr{B}_k\alpha\right)-\gamma^{-1/2}q(\alpha v^i-\beta^i), \tag{A.51}$$

which includes all the *non-stiff* terms of the electric field. The evolution of electric field becomes

$$\partial_t \mathscr{E}^i = \mathscr{E}^i_{ns} - \alpha\sigma\Gamma\left[\mathscr{E}^i + \epsilon^{ijk} v_j \mathscr{B}_k - (\mathscr{E}^k v_k) v^i\right] + \alpha\sigma\xi\Gamma\left[\mathscr{B}^i - (\mathscr{B}^k v_k) v^i - \epsilon^{ijk} v_j \mathscr{E}_k\right], \tag{A.52}$$

We discretize the time derivative of electric field $\partial_t \mathscr{E}^i = \frac{\Delta \mathscr{E}^i}{\Delta t} = \frac{\mathscr{E}^{i(1)} - \mathscr{E}^{i(0)}}{\Delta t}$, where $\mathscr{E}^{i(1)}$ is the current value we want to calculate and $\mathscr{E}^{i(0)}$ the value from the previous time step. All the other terms of Equation (A.52) were calculated in the current time step with the exception of $\mathscr{E}^i_{ns} = \mathscr{E}^{i(0)}_{ns}$. For that reason we will write down the full indexed equation once for reference and then we will drop the time step indices.

$$\begin{aligned}\frac{\mathscr{E}^{i(1)} - \mathscr{E}^{i(0)}}{\Delta t} = \mathscr{E}^{i(0)}_{ns} &- \alpha^{(1)}\sigma^{(1)}\Gamma^{(1)}\left[\mathscr{E}^{i(1)} + \epsilon^{ijk} v^{(1)}_j \mathscr{B}^{(1)}_k - (\mathscr{E}^{k(1)} v^{(1)}_k) v^{i(1)}\right] \\ &+ \alpha^{(1)}\sigma^{(1)}\xi^{(1)}\Gamma^{(1)}\left[\mathscr{B}^{i(1)} - \epsilon^{ijk} v^{(1)}_j \mathscr{E}^{(1)}_k - (\mathscr{B}^{k(1)} v^{(1)}_k) v^{i(1)}\right],\end{aligned} \tag{A.53}$$

$$\begin{aligned}\mathscr{E}^{i(1)} = \mathscr{E}^{i(0)} + \Delta t \mathscr{E}^{i(0)}_{ns} &- \Delta t\alpha\sigma\Gamma\left[\mathscr{E}^i + \epsilon^{ijk} v_j \mathscr{B}_k - (\mathscr{E}^k v_k) v^i\right] \\ &+ \Delta t\alpha\sigma\xi\Gamma\left[\mathscr{B}^i - \epsilon^{ijk} v_j \mathscr{E}_k - (\mathscr{B}^k v_k) v^i\right].\end{aligned} \tag{A.54}$$

We set $Q^i = \mathscr{E}^{i(0)} + \Delta t \mathscr{E}^{i(0)}_{ns}$ with all its values calculated from the previous step. We also absorb in the 3-velocity the Lorentz factor with $\tilde{v}^i = \Gamma v^i$ and $\tilde{v}_i = \Gamma v_i$

$$\begin{aligned}\mathscr{E}^i = Q^i &- \Delta t\alpha\sigma\left[\Gamma\mathscr{E}^i + \epsilon^{ijk}\tilde{v}_j\mathscr{B}_k - (\mathscr{E}^k\tilde{v}_k)\tilde{v}^i/\Gamma\right] \\ &+ \Delta t\alpha\sigma\xi\left[\Gamma\mathscr{B}^i - \epsilon^{ijk}\tilde{v}_j\mathscr{E}_k - (\mathscr{B}^k\tilde{v}_k)\tilde{v}^i/\Gamma\right].\end{aligned} \tag{A.55}$$

In order to solve over the electric field we need to calculate the two terms is which it is involved $\mathscr{E}^k\tilde{v}_k$ and $\epsilon^{ijk}\tilde{v}_j\mathscr{E}_k$. For that, we start by multiplying Equation (A.55) with $\tilde{v}_i$.

$$\begin{aligned}\mathscr{E}^i\tilde{v}_i = Q^i\tilde{v}_i &- \Delta t\alpha\sigma\left[\Gamma\mathscr{E}^i\tilde{v}_i + \epsilon^{ijk}\tilde{v}_j\mathscr{B}_k\tilde{v}_i - (\mathscr{E}^k\tilde{v}_k)\tilde{v}^i\tilde{v}_i/\Gamma\right] \\ &+ \Delta t\alpha\sigma\xi\left[\Gamma\mathscr{B}^i\tilde{v}_i - \epsilon^{ijk}\tilde{v}_j\mathscr{E}_k\tilde{v}_i - (\mathscr{B}^k\tilde{v}_k)\tilde{v}^i\tilde{v}_i/\Gamma\right].\end{aligned} \tag{A.56}$$

$$\begin{aligned}\mathscr{E}^i\tilde{v}_i = Q^i\tilde{v}_i &- \Delta t\alpha\sigma\left[\Gamma\mathscr{E}^i\tilde{v}_i + \cancelto{0}{\epsilon^{ijk}\tilde{v}_j\mathscr{B}_k\tilde{v}_i} - (\mathscr{E}^k\tilde{v}_k)\tilde{v}^i\tilde{v}_i/\Gamma\right] \\ &+ \Delta t\alpha\sigma\xi\left[\Gamma\mathscr{B}^i\tilde{v}_i - \cancelto{0}{\epsilon^{ijk}\tilde{v}_j\mathscr{E}_k\tilde{v}_i} - (\mathscr{B}^k\tilde{v}_k)\tilde{v}^i\tilde{v}_i/\Gamma\right],\end{aligned} \tag{A.57}$$

because if we develop the combination of the cross products they all cancel out.

$$\begin{aligned}\mathscr{E}^i\tilde{v}_i = Q^i\tilde{v}_i &- \Delta t\alpha\sigma\Gamma\mathscr{E}^i\tilde{v}_i + \Delta t\alpha\sigma(\mathscr{E}^k\tilde{v}_k)\tilde{v}^i\tilde{v}_i/\Gamma \\ &+ \Delta t\alpha\sigma\xi\Gamma\mathscr{B}^i\tilde{v}_i - \Delta t\alpha\sigma\xi(\mathscr{B}^k\tilde{v}_k)\tilde{v}^i\tilde{v}_i/\Gamma.\end{aligned} \tag{A.58}$$

We change all k indices to i since they are all mute

$$\mathscr{E}^i\tilde{v}_i + \Delta t\alpha\sigma\Gamma\mathscr{E}^i\tilde{v}_i - \Delta t\alpha\sigma(\mathscr{E}^i\tilde{v}_i)\tilde{v}^i\tilde{v}_i/\Gamma = Q^i\tilde{v}_i + \Delta t\alpha\sigma\xi\Gamma\mathscr{B}^i\tilde{v}_i - \Delta t\alpha\sigma\xi(\mathscr{B}^i\tilde{v}_i)\tilde{v}^i\tilde{v}_i/\Gamma, \tag{A.59}$$

$$\mathscr{E}^i\tilde{v}_i\left[1+\Delta t\alpha\sigma\Gamma-\Delta t\alpha\sigma\tilde{v}^i\tilde{v}_i/\Gamma\right]=Q^i\tilde{v}_i+B^i\tilde{v}_i\left[\Delta t\alpha\sigma\xi\Gamma-\Delta t\alpha\sigma\xi\tilde{v}^i\tilde{v}_i/\Gamma\right], \tag{A.60}$$

$$\mathscr{E}^i\tilde{v}_i\left[\Gamma+\Delta t\alpha\sigma\Gamma^2-\Delta t\alpha\sigma\tilde{v}^i\tilde{v}_i\right]/\Gamma=Q^i\tilde{v}_i+B^i\tilde{v}_i\left[\Delta t\alpha\sigma\xi\Gamma^2-\Delta t\alpha\sigma\xi\tilde{v}^i\tilde{v}_i\right]/\Gamma, \tag{A.61}$$

$$\mathscr{E}^i\tilde{v}_i\left[\Gamma+\Delta t\alpha\sigma\Gamma^2-\Delta t\alpha\sigma(\Gamma^2-1)\right]/\Gamma=Q^i\tilde{v}_i+B^i\tilde{v}_i\left[\Delta t\alpha\sigma\xi\Gamma^2-\Delta t\alpha\sigma\xi(\Gamma^2-1)\right]/\Gamma, \tag{A.62}$$

$$\mathscr{E}^i\tilde{v}_i\left[\Gamma+\Delta t\alpha\sigma\right]/\Gamma=Q^i\tilde{v}_i+B^i\tilde{v}_i\Delta t\alpha\sigma\xi/\Gamma, \tag{A.63}$$

$$\mathscr{E}^i\tilde{v}_i=\Gamma Q^i\tilde{v}_i/\left[\Gamma+\Delta t\alpha\sigma\right]+B^i\tilde{v}_i\Delta t\alpha\sigma\xi/\left[\Gamma+\Delta t\alpha\sigma\right], \tag{A.64}$$

We go back and take the covariant version of Equation (A.55) and form the cross product $\epsilon^{ijk}\tilde{v}_j\mathscr{E}_k$

$$\begin{aligned}\epsilon^{ijk}\tilde{v}_j\mathscr{E}_k=\epsilon^{ijk}\tilde{v}_jQ_k-\Delta t\alpha\sigma\left[\Gamma\epsilon^{ijk}\tilde{v}_j\mathscr{E}_k+\epsilon^{ijk}\tilde{v}_j\epsilon_{kmn}\tilde{v}^m\mathscr{B}^n-(\mathscr{E}^k\tilde{v}_k)\cancel{\epsilon^{ijk}\tilde{v}_j\tilde{v}_k}/\Gamma\right]\times\boldsymbol{v}=0\\+\Delta t\alpha\sigma\xi\left[\Gamma\epsilon^{ijk}\tilde{v}_j\mathscr{B}_k-\epsilon^{ijk}\tilde{v}_j\epsilon_{kmn}\tilde{v}^m\mathscr{E}^n-(\mathscr{B}^k\tilde{v}_k)\cancel{\epsilon^{ijk}\tilde{v}_j\tilde{v}_k}/\Gamma\right]\times\boldsymbol{v}=0,\end{aligned} \tag{A.65}$$

and since $\epsilon^{ijk}\epsilon_{kmn}=-[\delta^m_j\delta^n_i-\delta^n_j\delta^m_i]$

$$\begin{aligned}\epsilon^{ijk}\tilde{v}_j\mathscr{E}_k=\epsilon^{ijk}\tilde{v}_jQ_k-\Delta t\alpha\sigma\left[\Gamma\epsilon^{ijk}\tilde{v}_j\mathscr{E}_k-[\delta^m_j\delta^n_i-\delta^n_j\delta^m_i]\tilde{v}_j\tilde{v}^m\mathscr{B}^n\right]\\+\Delta t\alpha\sigma\xi\left[\Gamma\epsilon^{ijk}\tilde{v}_j\mathscr{B}_k+[\delta^m_j\delta^n_i-\delta^n_j\delta^m_i]\tilde{v}_j\tilde{v}^m\mathscr{E}^n\right],\end{aligned} \tag{A.66}$$

$$\begin{aligned}\epsilon^{ijk}\tilde{v}_j\mathscr{E}_k\left[1+\Delta t\alpha\sigma\Gamma\right]=\epsilon^{ijk}\tilde{v}_jQ_k+\Delta t\alpha\sigma[\delta^m_j\delta^n_i-\delta^n_j\delta^m_i]\tilde{v}_j\tilde{v}^m\mathscr{B}^n\\+\Delta t\alpha\sigma\xi\left[\Gamma\epsilon^{ijk}\tilde{v}_j\mathscr{B}^k+[\delta^m_j\delta^n_i-\delta^n_j\delta^m_i]\tilde{v}_j\tilde{v}^m\mathscr{E}^n\right],\end{aligned} \tag{A.67}$$

$$\begin{aligned}\epsilon^{ijk}\tilde{v}_j\mathscr{E}_k\left[1+\Delta t\alpha\sigma\Gamma\right]=\epsilon^{ijk}\tilde{v}_jQ_k+\Delta t\alpha\sigma[(\tilde{v}^j\tilde{v}_j)\mathscr{B}^i-(\tilde{v}^j\mathscr{B}_j)\tilde{v}^i]\\+\Delta t\alpha\sigma\xi\left[\Gamma\epsilon^{ijk}\tilde{v}_j\mathscr{B}_k+[(\tilde{v}^j\tilde{v}_j)\mathscr{E}^i-(\tilde{v}^j\mathscr{E}_j)\tilde{v}^i]\right],\end{aligned} \tag{A.68}$$

$$\begin{aligned}\epsilon^{ijk}\tilde{v}_j\mathscr{E}_k=\epsilon^{ijk}\tilde{v}_jQ_k/\left[1+\Delta t\alpha\sigma\Gamma\right]+\Delta t\alpha\sigma[(\tilde{v}^j\tilde{v}_j)\mathscr{B}^i-(\tilde{v}^j\mathscr{B}_j)\tilde{v}^i]/\left[1+\Delta t\alpha\sigma\Gamma\right]\\+\Delta t\alpha\sigma\xi\left[\Gamma\epsilon^{ijk}\tilde{v}_j\mathscr{B}_k+[(\tilde{v}^j\tilde{v}_j)\mathscr{E}^i-(\tilde{v}^j\mathscr{E}_j)\tilde{v}^i]\right]/\left[1+\Delta t\alpha\sigma\Gamma\right].\end{aligned} \tag{A.69}$$

We follow from Equation (A.55)

$$\begin{aligned}\mathscr{E}^i = Q^i &- \Delta t\alpha\sigma\Gamma\mathscr{E}^i - \Delta t\alpha\sigma\epsilon^{ijk}\tilde{v}_j\mathscr{B}_k + \Delta t\alpha\sigma(\mathscr{E}^k\tilde{v}_k)\tilde{v}^i/\Gamma \\ &+ \Delta t\alpha\sigma\xi\Gamma\mathscr{B}^i - \Delta t\alpha\sigma\xi\epsilon^{ijk}\tilde{v}_j\mathscr{E}_k - \Delta t\alpha\sigma\xi(\mathscr{B}^k\tilde{v}_k)\tilde{v}^i/\Gamma.\end{aligned} \tag{A.70}$$

Combining with Equations (A.64) and (A.69) we obtain

$$\begin{aligned}\mathscr{E}^i = {} & Q^i - \Delta t\alpha\sigma\Gamma\mathscr{E}^i - \Delta t\alpha\sigma\epsilon^{ijk}\tilde{v}_j\mathscr{B}_k \\ & + \left\{\Gamma Q^k\tilde{v}_k/\left(\Gamma + \Delta t\alpha\sigma\right) + \mathscr{B}^k\tilde{v}_k\Delta t\alpha\sigma\xi/\left(\Gamma + \Delta t\alpha\sigma\right)\right\}\frac{\Delta t\alpha\sigma\tilde{v}^i}{\Gamma} \\ & + \Delta t\alpha\sigma\xi\Gamma\mathscr{B}^i \\ & - \Delta t\alpha\sigma\xi\left\{\frac{\epsilon^{ijk}\tilde{v}_jQ_k}{1+\Delta t\alpha\sigma\Gamma} + \frac{\Delta t\alpha\sigma[(\tilde{v}^j\tilde{v}_j)\mathscr{B}^i - (\tilde{v}^j\mathscr{B}_j)\tilde{v}^i]}{1+\Delta t\alpha\sigma\Gamma}\right. \\ & \qquad \left. + \Delta t\alpha\sigma\xi\frac{\Gamma\epsilon^{ijk}\tilde{v}_j\mathscr{B}_k + [(\tilde{v}^j\tilde{v}_j)\mathscr{E}^i - (\tilde{v}^j\mathscr{E}_j)\tilde{v}^i]}{1+\Delta t\alpha\sigma\Gamma}\right\} \\ & - \Delta t\alpha\sigma\xi(\mathscr{B}^k\tilde{v}_k)\tilde{v}^i/\Gamma,\end{aligned} \tag{A.71}$$

$$\begin{aligned}\mathscr{E}^i + \Delta t\alpha\sigma\Gamma\mathscr{E}^i = {} & Q^i - \Delta t\alpha\sigma\epsilon^{ijk}\tilde{v}_j\mathscr{B}_k + \Delta t\alpha\sigma\xi\left[\Gamma\mathscr{B}^i - (\mathscr{B}^k\tilde{v}_k)\tilde{v}^i/\Gamma\right] \\ & + \frac{\Delta t\alpha\sigma\tilde{v}^i(Q^k\tilde{v}_k)}{\Gamma+\Delta t\alpha\sigma} + \frac{(\Delta t\alpha\sigma)^2\,\xi\tilde{v}^i(\mathscr{B}^k\tilde{v}_k)/\Gamma}{\Gamma+\Delta t\alpha\sigma} \\ & - \Delta t\alpha\sigma\xi\left\{\frac{\epsilon^{ijk}\tilde{v}_jQ_k}{1+\Delta t\alpha\sigma\Gamma} + \frac{\Delta t\alpha\sigma[(\tilde{v}^j\tilde{v}_j)\mathscr{B}^i - (\tilde{v}^j\mathscr{B}_j)\tilde{v}^i]}{1+\Delta t\alpha\sigma\Gamma}\right. \\ & \qquad \left. + \Delta t\alpha\sigma\xi\frac{\Gamma\epsilon^{ijk}\tilde{v}_j\mathscr{B}_k + [(\tilde{v}^j\tilde{v}_j)\mathscr{E}^i - (\tilde{v}^j\mathscr{E}_j)\tilde{v}^i]}{1+\Delta t\alpha\sigma\Gamma}\right\},\end{aligned} \tag{A.72}$$

$$\begin{aligned}\mathscr{E}^i + \Delta t\alpha\sigma\Gamma\mathscr{E}^i = {} & Q^i - \Delta t\alpha\sigma\epsilon^{ijk}\tilde{v}_j\mathscr{B}_k + \Delta t\alpha\sigma\xi\left[\Gamma\mathscr{B}^i - (\mathscr{B}^k\tilde{v}_k)\tilde{v}^i/\Gamma\right] \\ & + \frac{\Delta t\alpha\sigma\tilde{v}^i(Q^k\tilde{v}_k)}{\Gamma+\Delta t\alpha\sigma} + \frac{(\Delta t\alpha\sigma)^2\,\xi\tilde{v}^i(\mathscr{B}^k\tilde{v}_k)/\Gamma}{\Gamma+\Delta t\alpha\sigma} \\ & - \Delta t\alpha\sigma\xi\left\{\frac{\epsilon^{ijk}\tilde{v}_jQ_k + \Delta t\alpha\sigma[(\tilde{v}^j\tilde{v}_j)\mathscr{B}^i - (\tilde{v}^j\mathscr{B}_j)\tilde{v}^i]}{1+\Delta t\alpha\sigma\Gamma}\right\} \\ & - (\Delta t\alpha\sigma\xi)^2\left\{\frac{\Gamma\epsilon^{ijk}\tilde{v}_j\mathscr{B}_k + [(\tilde{v}^j\tilde{v}_j)\mathscr{E}^i - (\tilde{v}^j\mathscr{E}_j)\tilde{v}^i]}{1+\Delta t\alpha\sigma\Gamma}\right\},\end{aligned} \tag{A.73}$$

$$\begin{aligned}\mathscr{E}^i + \Delta t\alpha\sigma\Gamma\mathscr{E}^i = {} & Q^i - \Delta t\alpha\sigma\epsilon^{ijk}\tilde{v}_j\mathscr{B}_k + \Delta t\alpha\sigma\xi\left[\Gamma\mathscr{B}^i - (\mathscr{B}^k\tilde{v}_k)\tilde{v}^i/\Gamma\right] \\ & + \frac{\Delta t\alpha\sigma\tilde{v}^i(Q^k\tilde{v}_k)}{\Gamma+\Delta t\alpha\sigma} + \frac{(\Delta t\alpha\sigma)^2\,\xi\tilde{v}^i(\mathscr{B}^k\tilde{v}_k)/\Gamma}{\Gamma+\Delta t\alpha\sigma} \\ & - \Delta t\alpha\sigma\xi\left\{\frac{\epsilon^{ijk}\tilde{v}_jQ_k + \Delta t\alpha\sigma[(\tilde{v}^j\tilde{v}_j)\mathscr{B}^i - (\tilde{v}^j\mathscr{B}_j)\tilde{v}^i]}{1+\Delta t\alpha\sigma\Gamma}\right\} \\ & - (\Delta t\alpha\sigma\xi)^2\,\frac{\Gamma\epsilon^{ijk}\tilde{v}_j\mathscr{B}_k + [-(\tilde{v}^j\mathscr{E}_j)\tilde{v}^i]}{1+\Delta t\alpha\sigma\Gamma} \\ & - (\Delta t\alpha\sigma\xi)^2\,\frac{(\tilde{v}^j\tilde{v}_j)\mathscr{E}^i}{1+\Delta t\alpha\sigma\Gamma},\end{aligned} \tag{A.74}$$

$$\begin{aligned}\mathscr{E}^i + \Delta t\alpha\sigma\Gamma\mathscr{E}^i + (\Delta t\alpha\sigma\xi)^2 \frac{(\tilde{v}^j\tilde{v}_j)\mathscr{E}^i}{1+\Delta t\alpha\sigma\Gamma} &= Q^i - \Delta t\alpha\sigma\epsilon^{ijk}\tilde{v}_j\mathscr{B}_k + \Delta t\alpha\sigma\xi\left[\Gamma\mathscr{B}^i - (\mathscr{B}^k\tilde{v}_k)\tilde{v}^i/\Gamma\right] \\ &+ \frac{\Delta t\alpha\sigma\tilde{v}^i(Q^k\tilde{v}_k)}{\Gamma+\Delta t\alpha\sigma} + \frac{(\Delta t\alpha\sigma)^2\xi\tilde{v}^i(\mathscr{B}^k\tilde{v}_k)/\Gamma}{\Gamma+\Delta t\alpha\sigma} \\ &- \Delta t\alpha\sigma\xi\left\{\frac{\epsilon^{ijk}\tilde{v}_jQ_k + \Delta t\alpha\sigma[(\tilde{v}^j\tilde{v}_j)\mathscr{B}^i - (\tilde{v}^j\mathscr{B}_j)\tilde{v}^i]}{1+\Delta t\alpha\sigma\Gamma}\right\} \\ &- (\Delta t\alpha\sigma\xi)^2\frac{\Gamma\epsilon^{ijk}\tilde{v}_j\mathscr{B}_k}{1+\Delta t\alpha\sigma\Gamma} \\ &+ (\Delta t\alpha\sigma\xi)^2\frac{(\tilde{v}^j\mathscr{E}_j)\tilde{v}^i}{1+\Delta t\alpha\sigma\Gamma}.\end{aligned} \tag{A.75}$$

The last term contains another $\tilde{v}^j\mathscr{E}_j$ which we will replace with Equation (A.64)

$$\begin{aligned}\mathscr{E}^i\left[1+\Delta t\alpha\sigma\Gamma + (\Delta t\alpha\sigma\xi)^2\frac{(\tilde{v}^j\tilde{v}_j)}{1+\Delta t\alpha\sigma\Gamma}\right] &= Q^i - \Delta t\alpha\sigma\epsilon^{ijk}\tilde{v}_j\mathscr{B}_k + \Delta t\alpha\sigma\xi\left[\Gamma\mathscr{B}^i - (\mathscr{B}^k\tilde{v}_k)\tilde{v}^i/\Gamma\right] \\ &+ \frac{\Delta t\alpha\sigma\tilde{v}^i(Q^k\tilde{v}_k)}{\Gamma+\Delta t\alpha\sigma} + \frac{(\Delta t\alpha\sigma)^2\xi\tilde{v}^i(\mathscr{B}^k\tilde{v}_k)/\Gamma}{\Gamma+\Delta t\alpha\sigma} \\ &- \Delta t\alpha\sigma\xi\left\{\frac{\epsilon^{ijk}\tilde{v}_jQ_k + \Delta t\alpha\sigma[(\tilde{v}^j\tilde{v}_j)\mathscr{B}^i - (\tilde{v}^j\mathscr{B}_j)\tilde{v}^i]}{1+\Delta t\alpha\sigma\Gamma}\right\} \\ &- (\Delta t\alpha\sigma\xi)^2\frac{\Gamma\epsilon^{ijk}\tilde{v}_j\mathscr{B}_k}{1+\Delta t\alpha\sigma\Gamma} \\ &+ (\Delta t\alpha\sigma\xi)^2\frac{\tilde{v}^i}{1+\Delta t\alpha\sigma\Gamma}\left\{\frac{\Gamma Q^k\tilde{v}_k}{\Gamma+\Delta t\alpha\sigma} + \frac{\mathscr{B}^k\tilde{v}_k\Delta t\alpha\sigma\xi}{\Gamma+\Delta t\alpha\sigma}\right\}.\end{aligned} \tag{A.76}$$

We define $\tilde{\eta} = 1/(\sigma\alpha\Delta t)$

$$\begin{aligned}\mathscr{E}^i\left[1+\Gamma/\tilde{\eta} + (\xi/\tilde{\eta})^2\frac{(\tilde{v}^j\tilde{v}_j)}{1+\Gamma/\tilde{\eta}}\right] &= Q^i - \epsilon^{ijk}\tilde{v}_j\mathscr{B}_k/\tilde{\eta} + \xi/\tilde{\eta}\left[\Gamma\mathscr{B}^i - (\mathscr{B}^k\tilde{v}_k)\tilde{v}^i/\Gamma\right] \\ &+ \frac{\tilde{v}^i(Q^k\tilde{v}_k)/\tilde{\eta}}{\Gamma+1/\tilde{\eta}} + \frac{\xi\tilde{v}^i(\mathscr{B}^k\tilde{v}_k)/(\Gamma\eta^2)}{\Gamma+1/\tilde{\eta}} \\ &- \xi/\tilde{\eta}\left\{\frac{\epsilon^{ijk}\tilde{v}_jQ_k + [(\tilde{v}^j\tilde{v}_j)\mathscr{B}^i - (\tilde{v}^j\mathscr{B}_j)\tilde{v}^i]/\tilde{\eta}}{1+\Gamma/\tilde{\eta}}\right\} \\ &- (\xi/\tilde{\eta})^2\frac{\Gamma\epsilon^{ijk}\tilde{v}_j\mathscr{B}_k}{1+\Gamma/\tilde{\eta}} \\ &+ (\xi/\tilde{\eta})^2\frac{\tilde{v}^i}{1+\Gamma/\tilde{\eta}}\left\{\frac{\Gamma Q^k\tilde{v}_k + \mathscr{B}^k\tilde{v}_k\xi/\tilde{\eta}}{\Gamma+1/\tilde{\eta}}\right\}.\end{aligned} \tag{A.77}$$

We multiply by $\tilde{\eta}$

$$\begin{aligned}
\mathscr{E}^i\left[\tilde{\eta}+\Gamma+\tilde{\eta}\left(\frac{\xi}{\tilde{\eta}}\right)^2\frac{(\tilde{v}^j\tilde{v}_j)}{\frac{\tilde{\eta}+\Gamma}{\tilde{\eta}}}\right] &= \tilde{\eta}Q^i-\epsilon^{ijk}\tilde{v}_j\mathscr{B}_k+\xi\left[\Gamma\mathscr{B}^i-(\mathscr{B}^k\tilde{v}_k)\tilde{v}^i/\Gamma\right]\\
&\quad+\frac{\tilde{v}^i(Q^k\tilde{v}_k)}{\Gamma+1/\tilde{\eta}}+\frac{\xi\tilde{v}^i(\mathscr{B}^k\tilde{v}_k)/(\Gamma\tilde{\eta})}{\Gamma+1/\tilde{\eta}}\\
&\quad-\xi\left\{\frac{\epsilon^{ijk}\tilde{v}_jQ_k+[(\tilde{v}^j\tilde{v}_j)\mathscr{B}^i-(\tilde{v}^j\mathscr{B}_j)\tilde{v}^i]/\tilde{\eta}}{1+\Gamma/\tilde{\eta}}\right\}\\
&\quad-\xi^2/\tilde{\eta}\frac{\Gamma\epsilon^{ijk}\tilde{v}_j\mathscr{B}_k}{1+\Gamma/\tilde{\eta}}\\
&\quad+\xi^2/\tilde{\eta}\frac{\tilde{v}^i}{1+\Gamma/\tilde{\eta}}\left\{\frac{\Gamma Q^k\tilde{v}_k+\mathscr{B}^k\tilde{v}_k\xi/\tilde{\eta}}{\Gamma+1/\tilde{\eta}}\right\},
\end{aligned}\tag{A.78}$$

$$\begin{aligned}
\mathscr{E}^i\left[\tilde{\eta}+\Gamma+\xi^2\frac{(\tilde{v}^j\tilde{v}_j)}{\tilde{\eta}+\Gamma}\right] &= \tilde{\eta}Q^i-\epsilon^{ijk}\tilde{v}_j\mathscr{B}_k+\xi\left[\Gamma\mathscr{B}^i-(\mathscr{B}^k\tilde{v}_k)\tilde{v}^i/\Gamma\right]\\
&\quad+\tilde{\eta}\frac{\tilde{v}^i(Q^k\tilde{v}_k)}{\Gamma\tilde{\eta}+1}+\frac{\xi\tilde{v}^i(\mathscr{B}^k\tilde{v}_k)/\Gamma}{\Gamma\tilde{\eta}+1}\\
&\quad-\xi\left\{\frac{\tilde{\eta}\epsilon^{ijk}\tilde{v}_jQ_k+[(\tilde{v}^j\tilde{v}_j)\mathscr{B}^i-(\tilde{v}^j\mathscr{B}_j)\tilde{v}^i]}{\Gamma+\tilde{\eta}}\right\}\\
&\quad-\xi^2\frac{\Gamma\epsilon^{ijk}\tilde{v}_j\mathscr{B}_k}{\Gamma+\tilde{\eta}}\\
&\quad+\xi^2\frac{\tilde{v}^i}{\Gamma+\tilde{\eta}}\left\{\frac{\Gamma\tilde{\eta}Q^k\tilde{v}_k+\mathscr{B}^k\tilde{v}_k\xi}{\Gamma\tilde{\eta}+1}\right\}.
\end{aligned}\tag{A.79}$$

We replace the last $\tilde{v}^j\tilde{v}_j$ we kept until now for symmetry with Γ^2-1

$$\begin{aligned}
\mathscr{E}^i\left[\tilde{\eta}+\Gamma+\xi^2\frac{(\Gamma^2-1)}{\tilde{\eta}+\Gamma}\right] &= \tilde{\eta}Q^i-\epsilon^{ijk}\tilde{v}_j\mathscr{B}_k+\xi\left[\Gamma\mathscr{B}^i-(\mathscr{B}^k\tilde{v}_k)\tilde{v}^i/\Gamma\right]\\
&\quad+\tilde{\eta}\frac{\tilde{v}^i(Q^k\tilde{v}_k)}{\Gamma\tilde{\eta}+1}+\frac{\xi\tilde{v}^i(\mathscr{B}^k\tilde{v}_k)/\Gamma}{\Gamma\tilde{\eta}+1}\\
&\quad-\xi\left\{\frac{\tilde{\eta}\epsilon^{ijk}\tilde{v}_jQ_k+(\Gamma^2-1)\mathscr{B}^i-(\tilde{v}^j\mathscr{B}_j)\tilde{v}^i}{\Gamma+\tilde{\eta}}\right\}\\
&\quad-\xi^2\frac{\Gamma\epsilon^{ijk}\tilde{v}_j\mathscr{B}_k}{\Gamma+\tilde{\eta}}\\
&\quad+\xi^2\tilde{v}^i\left\{\frac{\Gamma\tilde{\eta}Q^k\tilde{v}_k+\xi\mathscr{B}^k\tilde{v}_k}{(\Gamma\tilde{\eta}+1)(\Gamma+\tilde{\eta})}\right\}.
\end{aligned}\tag{A.80}$$

Canceling out the $\gamma^{1/2}$ terms inside the electric and magnetic field we go back to the "normal" symbols and with a little more algebra we get

$$
\begin{aligned}
E^i \left[\tilde{\eta} + \Gamma + \xi^2 \frac{(\Gamma^2 - 1)}{\tilde{\eta} + \Gamma}\right] = & -\epsilon^{ijk}\tilde{v}_j B_k + \tilde{\eta}\left[Q^i + \frac{\tilde{v}^i (Q^k \tilde{v}_k)}{\Gamma\tilde{\eta} + 1}\right] \\
& + \xi\left[\Gamma B^i - \frac{\tilde{\eta}\tilde{v}^i}{\Gamma\tilde{\eta} + 1}(B^k \tilde{v}_k)\right] \\
& - \xi\left\{\frac{\tilde{\eta}\epsilon^{ijk}\tilde{v}_j Q_k + (\Gamma^2 - 1)B^i - (\tilde{v}^j B_j)\tilde{v}^i}{\Gamma + \tilde{\eta}}\right\} \\
& - \xi^2 \frac{\Gamma\epsilon^{ijk}\tilde{v}_j B_k}{\Gamma + \tilde{\eta}} \\
& + \xi^2 \tilde{v}^i \left\{\frac{\Gamma\tilde{\eta}Q^k\tilde{v}_k + \xi B^k \tilde{v}_k}{(\Gamma\tilde{\eta} + 1)(\Gamma + \tilde{\eta})}\right\},
\end{aligned}
\tag{A.81}
$$

which is Equation 35 from Bucciantini and Del Zanna (2013) with the exceptions of the fraction in the second term in the right hand side and the sign in the second to last term. It is probably a typo on their side.

Appendix B

The Direction of the Poloidal Electric Field

In a coordinate system that uses spherical coordinates (r, θ, ϕ) the three components are always perpendicular to each other and their respective unit vectors are connected via

$$\boldsymbol{e}_r = \boldsymbol{e}_\theta \times \boldsymbol{e}_\phi. \tag{B.1}$$

In the case of ideal classical MHD, the electric field vector $\boldsymbol{E}$ is given by Ohm's law which we will repeat here

$$\boldsymbol{E} = -\boldsymbol{v} \times \boldsymbol{B} = \boldsymbol{B} \times \boldsymbol{v} = \begin{bmatrix} \boldsymbol{e}_r & \boldsymbol{e}_\theta & \boldsymbol{e}_\phi \\ B_r & B_\theta & B_\phi \\ v_r & v_\theta & v_\phi \end{bmatrix} \tag{B.2}$$

$$= (B_\theta v_\phi - v_\theta B_\phi)\, \boldsymbol{e}_r - (B_r v_\phi - v_r B_\phi)\, \boldsymbol{e}_\theta + (B_r v_\theta - v_r B_\theta)\, \boldsymbol{e}_\phi \tag{B.3}$$

The electric field can also be written as the sum of its projections in the three coordinate axes

$$\boldsymbol{E} = \boldsymbol{E}_r + \boldsymbol{E}_\theta + \boldsymbol{E}_\phi. \tag{B.4}$$

For the following we will use the radial component as an example with the same procedure being applicable in the polar component as well.

$$\begin{aligned} \boldsymbol{E}_r &= (B_\theta v_\phi - v_\theta B_\phi)\, \boldsymbol{e}_r \\ &= (B_\theta v_\phi - v_\theta B_\phi)\, (\boldsymbol{e}_\theta \times \boldsymbol{e}_\phi) \\ &= B_\theta v_\phi\, (\boldsymbol{e}_\theta \times \boldsymbol{e}_\phi) - v_\theta B_\phi\, (\boldsymbol{e}_\theta \times \boldsymbol{e}_\phi) \\ &= (B_\theta \boldsymbol{e}_\theta \times v_\phi \boldsymbol{e}_\phi) - (v_\theta \boldsymbol{e}_\theta \times B_\phi \boldsymbol{e}_\phi) \\ &= \boldsymbol{B}_\theta \times \boldsymbol{v}_\phi - \boldsymbol{v}_\theta \times \boldsymbol{B}_\phi \\ &= \boldsymbol{B}_\theta \times \boldsymbol{v}_\phi + \boldsymbol{B}_\phi \times \boldsymbol{v}_\theta. \end{aligned} \tag{B.5}$$

Similarly, for the polar component we get

$$\boldsymbol{E}_\theta = \boldsymbol{B}_\phi \times \boldsymbol{v}_r + \boldsymbol{B}_r \times \boldsymbol{v}_\phi \tag{B.6}$$

We define the poloidal unit vector as the one that result from the addition of the radial and angular components, namely

$$\boldsymbol{E}_p = \boldsymbol{E}_r + \boldsymbol{E}_\theta. \tag{B.7}$$

The poloidal vector lies on the same plane as the $\boldsymbol{E}_r$ and $\boldsymbol{E}_{theta}$ but does not have a constant direction as it depends on the values of the other two (if $\boldsymbol{E}_r >> \boldsymbol{E}_\theta$ then the poloidal vector will be almost parallel to the radial one). The total poloidal component of the electric field becomes

$$\begin{aligned}
\boldsymbol{E}_p &= \boldsymbol{E}_r + \boldsymbol{E}_\theta \\
&= \boldsymbol{B}_\theta \times \boldsymbol{v}_\phi + \boldsymbol{B}_\phi \times \boldsymbol{v}_\theta + \boldsymbol{B}_\phi \times \boldsymbol{v}_r + \boldsymbol{B}_r \times \boldsymbol{v}_\phi \\
&= (\boldsymbol{B}_r + \boldsymbol{B}_\theta) \times \boldsymbol{v}_\phi + \boldsymbol{B}_\phi \times (\boldsymbol{v}_r + \boldsymbol{v}_\theta) \\
&= \boldsymbol{B}_p \times \boldsymbol{v}_\phi + \boldsymbol{B}_\phi \times \boldsymbol{v}_p
\end{aligned} \tag{B.8}$$

On a first sight the equation seems strange since we derive the $\boldsymbol{E}_p$ as a cross product that includes $\boldsymbol{B}_p$ and $\boldsymbol{v}_p$, however, as we mentioned before, the poloidal vectors do not have the same direction and the cross product of a poloidal vector with the toroidal gives always a vector in the poloidal plane but with different directions, making the above equation possible.

In the case of resistive MHD, we get the extra term of diffusivity and electric current and the radial and polar component of electric field becomes

$$\boldsymbol{E}_r = \boldsymbol{B}_\theta \times \boldsymbol{v}_\phi + \boldsymbol{B}_\phi \times \boldsymbol{v}_\theta + \eta \boldsymbol{J}_r, \tag{B.9a}$$

$$\boldsymbol{E}_\theta = \boldsymbol{B}_\phi \times \boldsymbol{v}_r + \boldsymbol{B}_r \times \boldsymbol{v}_\phi + \eta \boldsymbol{J}_\theta, \tag{B.9b}$$

from which it is detrimental to show that

$$\boldsymbol{E}_p = \boldsymbol{B}_p \times \boldsymbol{v}_\phi + \boldsymbol{B}_\phi \times \boldsymbol{v}_p + \eta \boldsymbol{J}_p, \tag{B.10}$$

where $\boldsymbol{J}_p = \boldsymbol{J}_r + \boldsymbol{J}_\theta$.

Bibliography

Abbott, B. P. et al. (2017a). "Gravitational Waves and Gamma-Rays from a Binary Neutron Star Merger: GW170817 and GRB 170817A". In: *ApJ* 848, L13, p. L13. DOI: 10.3847/2041-8213/aa920c.

— (2017b). "GW170817: Observation of Gravitational Waves from a Binary Neutron Star Inspiral". In: *Phys. Rev. Lett.* 119 (16), p. 161101. DOI: 10.1103/PhysRevLett.119.161101. URL: https://link.aps.org/doi/10.1103/PhysRevLett.119.161101.

Abramowicz, M., M. Jaroszynski, and M. Sikora (1978). "Relativistic, accreting disks". In: *A&A* 63, pp. 221–224.

Acheson, D. J. and R. Hide (1973). "Hydromagnetics of rotating fluids". In: *Reports on Progress in Physics* 36.2, pp. 159–221. DOI: 10.1088/0034-4885/36/2/002.

Alfvén, H. (1942a). "Existence of Electromagnetic-Hydrodynamic Waves". In: *Nature* 150, pp. 405–406. DOI: 10.1038/150405d0.

— (1942b). "On the existence of electromagnetic-hydrodynamic waves." In: *Ark. Mat., Astron. Fys.* 29, p. 2. DOI: Copyrighted>:(.

Anile, Angelo Marcello (1989). *Relativistic fluids and magneto-fluids : with applications in astrophysics and plasma physics*.

Anninos, Peter, P. Chris Fragile, and Jay D. Salmonson (2005). "Cosmos++: Relativistic Magnetohydrodynamics on Unstructured Grids with Local Adaptive Refinement". In: *ApJ* 635.1, pp. 723–740. DOI: 10.1086/497294.

Asada, K. and M. Nakamura (2012). "The Structure of the M87 Jet: A Transition from Parabolic to Conical Streamlines". In: *ApJ* 745, L28, p. L28. DOI: 10.1088/2041-8205/745/2/L28.

Asada, Keiichi et al. (2014). "Discovery of Sub- to Superluminal Motions in the M87 Jet: An Implication of Acceleration from Sub-relativistic to Relativistic Speeds". In: *ApJ* 781.1, L2, p. L2. DOI: 10.1088/2041-8205/781/1/L2.

Avara, Mark J., Jonathan C. McKinney, and Christopher S. Reynolds (2016). "Efficiency of thin magnetically arrested discs around black holes". In: *MNRAS* 462.1, pp. 636–648. DOI: 10.1093/mnras/stw1643.

Baiotti, L. et al. (2005). "Three-dimensional relativistic simulations of rotating neutron-star collapse to a Kerr black hole". In: *Phys.Rev.D* 71.2, 024035, p. 024035. DOI: 10.1103/PhysRevD.71.024035.

Balbus, S. A. and J. F. Hawley (1991). "A powerful local shear instability in weakly magnetized disks. I - Linear analysis. II - Nonlinear evolution". In: *ApJ* 376, pp. 214–233. DOI: 10.1086/170270.

— (1998). "Instability, turbulence, and enhanced transport in accretion disks". In: *Reviews of Modern Physics* 70, pp. 1–53. DOI: 10.1103/RevModPhys.70.1.

Balick, B. and R. L. Brown (1974). "Intense sub-arcsecond structure in the galactic center." In: *ApJ* 194, pp. 265–270. DOI: 10.1086/153242.

Bardeen, James M. (1970). "Kerr Metric Black Holes". In: *Nature* 226.5240, pp. 64–65. DOI: 10.1038/226064a0.

Bardeen, James M., William H. Press, and Saul A. Teukolsky (1972). "Rotating Black Holes: Locally Nonrotating Frames, Energy Extraction, and Scalar Synchrotron Radiation". In: *ApJ* 178, pp. 347–370. DOI: 10.1086/151796.

Bardou, A. et al. (2001). "The effects of vertical outflows on disk dynamos." In: *Astronomy and Astrophysics* 370, pp. 635–648. DOI: 10.1051/0004-6361:20010267.

Baumgarte, Thomas W. and Stuart L. Shapiro (2003). "General Relativistic Magnetohydrodynamics for the Numerical Construction of Dynamical Spacetimes". In: *ApJ* 585.2, pp. 921–929. DOI: 10.1086/346103.

Berti, Emanuele, Richard Brito, and Vitor Cardoso (2015). "Ultrahigh-Energy Debris from the Collisional Penrose Process". In: *Phys. Rev. Lett.* 114 (25), p. 251103. DOI: 10.1103/PhysRevLett.114.251103. URL: https://link.aps.org/doi/10.1103/PhysRevLett.114.251103.

Biermann, L. (1950). "Über den Ursprung der Magnetfelder auf Sternen und im interstellaren Raum (miteinem Anhang von A. Schlüter)". In: *Zeitschrift Naturforschung Teil A* 5, p. 65.

Bignami, G. F. et al. (1981). "3C 273 revisited : confirmation by COS-B of high energy gamma-ray emission." In: *A&A* 93, pp. 71–75.

Biretta, J. A., W. B. Sparks, and F. Macchetto (1999). "Hubble Space Telescope Observations of Superluminal Motion in the M87 Jet". In: *ApJ* 520.2, pp. 621–626. DOI: 10.1086/307499.

Blackman, Eric G. and George B. Field (1993). "Ohm's law for a relativistic pair plasma". In: *Phys.Rev.Lett.* 71.21, pp. 3481–3484. DOI: 10.1103/PhysRevLett.71.3481.

— (2002). "New Dynamical Mean-Field Dynamo Theory and Closure Approach". In: *Phys.Rev.Lett.* 89.26, 265007, p. 265007. DOI: 10.1103/PhysRevLett.89.265007.

Blandford, R. D. and A. Königl (1979). "Relativistic jets as compact radio sources." In: *ApJ* 232, pp. 34–48. DOI: 10.1086/157262.

Blandford, R. D. and D. G. Payne (1982). "Hydromagnetic flows from accretion discs and the production of radio jets". In: *MNRAS* 199, pp. 883–903. DOI: 10.1093/mnras/199.4.883.

Blandford, R. D. and R. L. Znajek (1977). "Electromagnetic extraction of energy from Kerr black holes". In: *MNRAS* 179, pp. 433–456. DOI: 10.1093/mnras/179.3.433.

Blandford, Roger, David Meier, and Anthony Readhead (2019). "Relativistic Jets from Active Galactic Nuclei". In: *ARA&A* 57, pp. 467–509. DOI: 10.1146/annurev-astro-081817-051948.

Bowen, Dennis B. et al. (2017). "Relativistic Dynamics and Mass Exchange in Binary Black Hole Mini-disks". In: *ApJ* 838.1, 42, p. 42. DOI: 10.3847/1538-4357/aa63f3.

Bowen, Dennis B. et al. (2018). "Quasi-periodic Behavior of Mini-disks in Binary Black Holes Approaching Merger". In: *ApJ* 853.1, L17, p. L17. DOI: 10.3847/2041-8213/aaa756.

Bowen, Dennis B. et al. (2019). "Quasi-periodicity of Supermassive Binary Black Hole Accretion Approaching Merger". In: *ApJ* 879.2, 76, p. 76. DOI: 10.3847/1538-4357/ab2453.

Brandenburg, Axel, Dmitry Sokoloff, and Kandaswamy Subramanian (2012). "Current Status of Turbulent Dynamo Theory. From Large-Scale to Small-Scale Dynamos". In: *Space Sci. Rev.* 169.1-4, pp. 123–157. DOI: 10.1007/s11214-012-9909-x.

Brandenburg, Axel and Kandaswamy Subramanian (2005). "Astrophysical magnetic fields and nonlinear dynamo theory". In: *Phys. Rep.* 417.1-4, pp. 1–209. DOI: 10.1016/j.physrep.2005.06.005.

Brandenburg, Axel et al. (1995). "Dynamo-generated Turbulence and Large-Scale Magnetic Fields in a Keplerian Shear Flow". In: *ApJ* 446, p. 741. DOI: 10.1086/175831.

Britzen, S. et al. (2017). "A swirling jet in the quasar 1308+326". In: *A&A* 602, A29, A29. DOI: 10.1051/0004-6361/201629999.

Broderick, Avery E. and Jonathan C. McKinney (2010). "Parsec-scale Faraday Rotation Measures from General Relativistic Magnetohydrodynamic Simulations of Active Galactic Nucleus Jets". In: *ApJ* 725.1, pp. 750–773. DOI: 10.1088/0004-637X/725/1/750.

Bucciantini, N. and L. Del Zanna (2011). "General relativistic magnetohydrodynamics in axisymmetric dynamical spacetimes: the X-ECHO code". In: *Astronomy and Astrophysics* 528, A101, A101. DOI: 10.1051/0004-6361/201015945.

— (2013). "A fully covariant mean-field dynamo closure for numerical 3 + 1 resistive GRMHD". In: *MNRAS* 428, pp. 71–85. DOI: 10.1093/mnras/sts005.

Bugli, M., L. Del Zanna, and N. Bucciantini (2014). "Dynamo action in thick discs around Kerr black holes: high-order resistive GRMHD simulationsDisk jet ejection in resistive GR-MHD". In: *MNRAS* 440, pp. L41–L45. DOI: 10.1093/mnrasl/slu017.

Burnham, S. W. (1890). "Note on Hind's Variable Nebula in Taurus". In: *MNRAS* 51, p. 94. DOI: 10.1093/mnras/51.2.94.

Campbell, C. G. (1999). "Launching of accretion disc winds along dynamo-generated magnetic fields". In: *MNRAS* 310.4, pp. 1175–1184. DOI: 10.1046/j.1365-8711.1999.03073.x.

Campbell, C. G., J. C. B. Papaloizou, and V. Agapitou (1998). "Magnetic field bending in accretion discs with dynamos". In: *MNRAS* 300.1, pp. 315–320. DOI: 10.1046/j.1365-8711.1998.01910.x.

Casse, F. and R. Keppens (2002). "Magnetized Accretion-Ejection Structures: 2.5-dimensional Magnetohydrodynamic Simulations of Continuous Ideal Jet Launching from Resistive Accretion Disks". In: *ApJ* 581, pp. 988–1001. DOI: 10.1086/344340.

Chandrasekhar, S. (1960). "The Stability of Non-Dissipative Couette Flow in Hydromagnetics". In: *Proceedings of the National Academy of Science* 46.2, pp. 253–257. DOI: 10.1073/pnas.46.2.253.

Cheung, C. C., D. E. Harris, and Ł. Stawarz (2007). "Superluminal Radio Features in the M87 Jet and the Site of Flaring TeV Gamma-Ray Emission". In: *ApJ* 663.2, pp. L65–L68. DOI: 10.1086/520510.

Collin, S. et al. (2002). "Are quasars accreting at super-Eddington rates?" In: *A&A* 388, pp. 771–786. DOI: 10.1051/0004-6361:20020550.

Cowling, T. G. (1933). "The magnetic field of sunspots". In: *MNRAS* 94, pp. 39–48. DOI: 10.1093/mnras/94.1.39.

Curtis, H. D. (1918). "Descriptions of 762 Nebulae and Clusters Photographed with the Crossley Reflector". In: *Publications of Lick Observatory* 13, pp. 9–42.

de Gouveia dal Pino, E. M. and A. Lazarian (2005). "Production of the large scale superluminal ejections of the microquasar GRS 1915+105 by violent magnetic reconnection". In: *A&A* 441.3, pp. 845–853. DOI: 10.1051/0004-6361:20042590.

de Gouveia Dal Pino, E. M., P. P. Piovezan, and L. H. S. Kadowaki (2010). "The role of magnetic reconnection on jet/accretion disk systems". In: *A&A* 518, A5, A5. DOI: 10.1051/0004-6361/200913462.

De Villiers, J.-P. and J. F. Hawley (2003a). "A Numerical Method for General Relativistic Magnetohydrodynamics". In: *ApJ* 589, pp. 458–480. DOI: 10.1086/373949.

De Villiers, J.-P. and J. F. Hawley (2003b). "Global General Relativistic Magnetohydrodynamic Simulations of Accretion Tori". In: *ApJ* 592, pp. 1060–1077. DOI: 10.1086/375866.

De Villiers, J.-P. et al. (2005). "Magnetically Driven Accretion in the Kerr Metric. III. Unbound Outflows". In: *ApJ* 620, pp. 878–888. DOI: 10.1086/427142.

De Villiers, Jean-Pierre, John F. Hawley, and Julian H. Krolik (2003). "Magnetically Driven Accretion Flows in the Kerr Metric. I. Models and Overall Structure". In: *ApJ* 599.2, pp. 1238–1253. DOI: 10.1086/379509.

Deguen, Renaud and Marine Lasbleis (2019). "Fluid Dynamics of Earth's core: geodynamo, inner core dynamics, core formation". In: *arXiv e-prints*, arXiv:1905.10416, arXiv:1905.10416.

Del Zanna, L., N. Bucciantini, and P. Londrillo (2003). "An efficient shock-capturing central-type scheme for multidimensional relativistic flows. II. Magnetohydrodynamics". In: *A&A* 400, pp. 397–413. DOI: 10.1051/0004-6361:20021641.

Del Zanna, L. et al. (2007). "ECHO: a Eulerian conservative high-order scheme for general relativistic magnetohydrodynamics and magnetodynamics". In: *A&A* 473, pp. 11–30. DOI: 10.1051/0004-6361:20077093.

Dent, W. A. (1965). "Quasi-Stellar Sources: Variation in the Radio Emission of 3C 273". In: *Science* 148.3676, pp. 1458–1460. DOI: 10.1126/science.148.3676.1458.

D'Inverno, R. A. (1992). *Introducing Einstein's relativity*.

Dionysopoulou, K., D. Alic, and L. Rezzolla (2015). "General-relativistic resistive magnetohydrodynamic simulations of binary neutron stars". In: *Phys.Rev.D* 92.8, 084064, p. 084064. DOI: 10.1103/PhysRevD.92.084064.

Dionysopoulou, K. et al. (2013). "General-relativistic resistive magnetohydrodynamics in three dimensions: Formulation and tests". In: *Phys.Rev.D* 88.4, 044020, p. 044020. DOI: 10.1103/PhysRevD.88.044020.

Doeleman, S. S. et al. (2012). "Jet-Launching Structure Resolved Near the Supermassive Black Hole in M87". In: *Science* 338, p. 355. DOI: 10.1126/science.1224768.

Dokuchaev, Vyacheslav I. and Natalia O. Nazarova (2019). "The Brightest Point in Accretion Disk and Black Hole Spin: Implication to the Image of Black Hole M87*". In: *Universe* 5.8, p. 183. DOI: 10.3390/universe5080183.

Dolence, Joshua C. et al. (2009). "grmonty: A Monte Carlo Code for Relativistic Radiative Transport". In: *ApJS* 184.2, pp. 387–397. DOI: 10.1088/0067-0049/184/2/387.

Dopita, M. A., R. D. Schwartz, and I. Evans (1982). "Herbig-Haro Objects 46 and 47 - Evidence for bipolar ejection from a young star". In: *ApJ* 263, pp. L73–L77. DOI: 10.1086/183927.

Duez, Matthew D. et al. (2005). "Relativistic magnetohydrodynamics in dynamical spacetimes: Numerical methods and tests". In: *Phys.Rev.D* 72.2, 024028, p. 024028. DOI: 10.1103/PhysRevD.72.024028.

Dumbser, M. and O. Zanotti (2009). "Very high order $P_N P_M$ schemes on unstructured meshes for the resistive relativistic MHD equations". In: *Journal of Computational Physics* 228, pp. 6991–7006. DOI: 10.1016/j.jcp.2009.06.009.

Einstein, A. (1916). "Die Grundlage der allgemeinen Relativitätstheorie". In: *Annalen der Physik* 354, pp. 769–822. DOI: 10.1002/andp.19163540702.

— (1917). "Kosmologische Betrachtungen zur allgemeinen Relativitätstheorie". In: *Sitzungsberichte der Königlich Preußischen Akademie der Wissenschaften (Berlin), Seite 142-152.*

Etienne, Zachariah B. et al. (2015). "IllinoisGRMHD: an open-source, user-friendly GRMHD code for dynamical spacetimes". In: *Classical and Quantum Gravity* 32.17, 175009, p. 175009. DOI: 10.1088/0264-9381/32/17/175009.

Event Horizon Telescope Collaboration et al. (2019). "First M87 Event Horizon Telescope Results. I. The Shadow of the Supermassive Black Hole". In: *ApJ* 875, L1, p. L1. DOI: 10.3847/2041-8213/ab0ec7.

Fanaroff, B. L. and J. M. Riley (1974). "The morphology of extragalactic radio sources of high and low luminosity". In: *MNRAS* 167, 31P–36P. DOI: 10.1093/mnras/167.1.31P.

Fath, E. A. (1909). "The Spectra of Some Spiral Nebulae and Globular Star Clusters". In: *Popular Astronomy* 17, pp. 504–508.

Fendt, Christian and Dennis Gaßmann (2018). "Bipolar Jets Launched by a Mean-field Accretion Disk Dynamo". In: *The Astrophysical Journal* 855.2, 130, p. 130. DOI: 10.3847/1538-4357/aab14c.

Ferreira, J. (1997). "Magnetically-driven jets from Keplerian accretion discs." In: *A&A* 319, pp. 340–359.

Fishbone, L. G. and V. Moncrief (1976). "Relativistic fluid disks in orbit around Kerr black holes". In: *ApJ* 207, pp. 962–976. DOI: 10.1086/154565.

Fleming, T. P., J. M. Stone, and J. F. Hawley (2000). "The Effect of Resistivity on the Nonlinear Stage of the Magnetorotational Instability in Accretion Disks". In: *ApJ* 530, pp. 464–477. DOI: 10.1086/308338.

Font, José A. (2008). "Numerical Hydrodynamics and Magnetohydrodynamics in General Relativity". In: *Living Reviews in Relativity* 11.1, 7, p. 7. DOI: 10.12942/lrr-2008-7.

Fragile, P. Chris et al. (2007). "Global General Relativistic Magnetohydrodynamic Simulation of a Tilted Black Hole Accretion Disk". In: *ApJ* 668.1, pp. 417–429. DOI: 10.1086/521092.

Fragile, P. Chris et al. (2009). "Application of the Cubed-Sphere Grid to Tilted Black Hole Accretion Disks". In: *ApJ* 691.1, pp. 482–494. DOI: 10.1088/0004-637X/691/1/482.

Fragile, P. Chris et al. (2018). "Relativistic, Viscous, Radiation Hydrodynamic Simulations of Geometrically Thin Disks. I. Thermal and Other Instabilities". In: *ApJ* 857.1, 1, p. 1. DOI: 10.3847/1538-4357/aab788.

Frolov, Valeri P. and Igor D. Novikov (1998). *Black hole physics : basic concepts and new developments*.

Gammie, C. F., J. C. McKinney, and G. Tóth (2003). "HARM: A Numerical Scheme for General Relativistic Magnetohydrodynamics". In: *ApJ* 589, pp. 444–457. DOI: 10.1086/374594.

Gammie, Charles F., Stuart L. Shapiro, and Jonathan C. McKinney (2004). "Black Hole Spin Evolution". In: *ApJ* 602.1, pp. 312–319. DOI: 10.1086/380996.

Garofalo, D., D. A. Evans, and R. M. Sambruna (2010). "The evolution of radio-loud active galactic nuclei as a function of black hole spin". In: *MNRAS* 406.2, pp. 975–986. DOI: 10.1111/j.1365-2966.2010.16797.x.

Garofalo, David (2009). "The Spin Dependence of the Blandford-Znajek Effect". In: *ApJ* 699.1, pp. 400–408. DOI: 10.1088/0004-637X/699/1/400.

Garrington, S. T. et al. (1988). "A systematic asymmetry in the polarization properties of double radio sources with one jet". In: *Nature* 331.6152, pp. 147–149. DOI: 10.1038/331147a0.

Giacomazzo, Bruno and Luciano Rezzolla (2007). "WhiskyMHD: a new numerical code for general relativistic magnetohydrodynamics". In: *Classical and Quantum Gravity* 24.12, S235–S258. DOI: 10.1088/0264-9381/24/12/S16.

Giroletti, M. et al. (2012). "The kinematic of HST-1 in the jet of M 87". In: *A&A* 538, L10, p. L10. DOI: 10.1051/0004-6361/201218794.

Goedbloed, J. P. Hans and Stefaan Poedts (2004). *Principles of Magnetohydrodynamics*.

Goldstein, A. et al. (2017). "An Ordinary Short Gamma-Ray Burst with Extraordinary Implications: Fermi-GBM Detection of GRB 170817A". In: *ApJ* 848, L14, p. L14. DOI: 10.3847/2041-8213/aa8f41.

Gorbatskii, V. G. (1965). "Disk-Like Envelopes in Close Binary Systems and Their Effect on Stellar Spectra". In: *Sov. Ast.* 8, p. 680.

Gourgoulhon, Eric (2012). *3+1 Formalism in General Relativity*. Vol. 846. DOI: 10.1007/978-3-642-24525-1.

Gressel, Oliver (2010). "A mean-field approach to the propagation of field patterns in stratified magnetorotational turbulence". In: *MNRAS* 405.1, pp. 41–48. DOI: 10.1111/j.1365-2966.2010.16440.x.

Gubbay, J. et al. (1969). "Variations of Small Quasar Components at 2,300 MHz". In: *Nature* 224.5224, pp. 1094–1095. DOI: 10.1038/2241094b0.

Gugliucci, N. E. et al. (2005). "Dating COINS: Kinematic Ages for Compact Symmetric Objects". In: *ApJ* 622.1, pp. 136–148. DOI: 10.1086/427934.

Guilloteau, S. et al. (2008). "Resolving the circumbinary dust disk surrounding HH 30". In: *A&A* 478, pp. L31–L34. DOI: 10.1051/0004-6361:20079053.

Hargrave, P. J. and M. Ryle (1974). "Observations of Cygnus A with the 5-km radio telescope." In: *MNRAS* 166, pp. 305–327. DOI: 10.1093/mnras/166.2.305.

Haro, G. (1952). "Herbig's Nebulous Objects Near NGC 1999." In: *ApJ* 115, p. 572. DOI: 10.1086/145576.

Hawley, J. F. and S. A. Balbus (1992). "A powerful local shear instability in weakly magnetized disks. III - Long-term evolution in a shearing sheet". In: *ApJ* 400, pp. 595–609. DOI: 10.1086/172021.

Hawley, J. F., L. L. Smarr, and J. R. Wilson (1984a). "A numerical study of nonspherical black hole accretion. I Equations and test problems". In: *ApJ* 277, pp. 296–311. DOI: 10.1086/161696.

— (1984b). "A numerical study of nonspherical black hole accretion. II - Finite differencing and code calibration". In: *ApJS* 55, pp. 211–246. DOI: 10.1086/190953.

Hawley, John F. and Steven A. Balbus (1991). "A Powerful Local Shear Instability in Weakly Magnetized Disks. II. Nonlinear Evolution". In: *ApJ* 376, p. 223. DOI: 10.1086/170271.

Hazard, C., M. B. Mackey, and A. J. Shimmins (1963). "Investigation of the Radio Source 3C 273 By The Method of Lunar Occultations". In: *Nature* 197.4872, pp. 1037–1039. DOI: 10.1038/1971037a0.

Herbig, G. H. (1951). "The Spectra of Two Nebulous Objects Near NGC 1999." In: *ApJ* 113, pp. 697–699. DOI: 10.1086/145440.

Hind, John Russell (1852). "Auszug aus einem Schreiben des Herrn Hind an die Redaction". In: *Astronomische Nachrichten* 35, p. 371. DOI: 10.1002/asna.18530352505.

Hirose, S. et al. (2004). "Magnetically Driven Accretion Flows in the Kerr Metric. II. Structure of the Magnetic Field". In: *ApJ* 606, pp. 1083–1097. DOI: 10.1086/383184.

Homan, Daniel et al. (2018). "Constraints on Particles and Fields from Full Stokes Observations of AGN". In: *Galaxies* 6.1, p. 17. DOI: 10.3390/galaxies6010017.

Hubble, Edwin (1929). "A Relation between Distance and Radial Velocity among Extra-Galactic Nebulae". In: *Proceedings of the National Academy of Science* 15.3, pp. 168–173. DOI: 10.1073/pnas.15.3.168.

Hughes, M. P. (1965). "Radio Brightness Contours of 3C273". In: *Nature* 207.4993, pp. 178–179. DOI: 10.1038/207178a0.

Igumenshchev, I. V., R. Narayan, and M. A. Abramowicz (2003). "Three-dimensional Magnetohydrodynamic Simulations of Radiatively Inefficient Accretion Flows". In: *ApJ* 592, pp. 1042–1059. DOI: 10.1086/375769.

Jansky, Karl G. (1933). "Radio Waves from Outside the Solar System". In: *Nature* 132.3323, p. 66. DOI: 10.1038/132066a0.

Jennison, R. C. and M. K. Das Gupta (1953). "Fine Structure of the Extra-terrestrial Radio Source Cygnus I". In: *Nature* 172.4387, pp. 996–997. DOI: 10.1038/172996a0.

Kato, Y., M. R. Hayashi, and R. Matsumoto (2004). "Formation of Semirelativistic Jets from Magnetospheres of Accreting Neutron Stars: Injection of Hot Bubbles into a Magnetic Tower". In: *ApJ* 600.1, pp. 338–342. DOI: 10.1086/379752.

Kato, Y., S. Mineshige, and K. Shibata (2004). "Magnetohydrodynamic Accretion Flows: Formation of Magnetic Tower Jet and Subsequent Quasi-Steady State". In: *ApJ* 605.1, pp. 307–320. DOI: 10.1086/381234.

Keel, W. C. (1983). "Spectroscopic evidence for activity in the nuclei of normal spiral galaxies." In: *ApJ* 269, pp. 466–486. DOI: 10.1086/161057.

Kerr, Roy P. (1963). "Gravitational Field of a Spinning Mass as an Example of Algebraically Special Metrics". In: *Phys.Rev.Lett.* 11.5, pp. 237–238. DOI: 10.1103/PhysRevLett.11.237.

Kim, J. Y. et al. (2018). "The limb-brightened jet of M87 down to the 7 Schwarzschild radii scale". In: *A&A* 616, A188, A188. DOI: 10.1051/0004-6361/201832921.

Klebesadel, R. W., I. B. Strong, and R. A. Olson (1973). "Observations of Gamma-Ray Bursts of Cosmic Origin". In: *ApJ* 182, p. L85. DOI: 10.1086/181225.

Koide, S., K. Shibata, and T. Kudoh (1999). "Relativistic Jet Formation from Black Hole Magnetized Accretion Disks: Method, Tests, and Applications of a General RelativisticMagnetohydrodynamic Numerical Code". In: *ApJ* 522, pp. 727–752. DOI: 10.1086/307667.

Koide, Shinji et al. (2000). "General Relativistic Simulations of Early Jet Formation in a Rapidly Rotating Black Hole Magnetosphere". In: *ApJ* 536.2, pp. 668–674. DOI: 10.1086/308986.

Komissarov, S. S. (1999). "A Godunov-type scheme for relativistic magnetohydrodynamics". In: *MNRAS* 303, pp. 343–366. DOI: 10.1046/j.1365-8711.1999.02244.x.

— (2001). "Direct numerical simulations of the Blandford-Znajek effect". In: *MNRAS* 326.3, pp. L41–L44. DOI: 10.1046/j.1365-8711.2001.04863.x.

— (2004). "Electrodynamics of black hole magnetospheres". In: *MNRAS* 350.2, pp. 427–448. DOI: 10.1111/j.1365-2966.2004.07598.x.

— (2007). "Multidimensional numerical scheme for resistive relativistic magnetohydrodynamics". In: *MNRAS* 382, pp. 995–1004. DOI: 10.1111/j.1365-2966.2007.12448.x.

Krause, F. and K. H. Raedler (1980). *Mean-field magnetohydrodynamics and dynamo theory.*

Krolik, Julian H., John F. Hawley, and Shigenobu Hirose (2005). "Magnetically Driven Accretion Flows in the Kerr Metric. IV. Dynamical Properties of the Inner Disk". In: *ApJ* 622.2, pp. 1008–1023. DOI: 10.1086/427932.

Kulsrud, Russell M. (2005). *Plasma physics for astrophysics*.

Kulsrud, Russell M. and Ellen G. Zweibel (2008). "On the origin of cosmic magnetic fields". In: *Reports on Progress in Physics* 71.4, 046901, p. 046901. DOI: 10.1088/0034-4885/71/4/046901.

Laing, R. A. and A. H. Bridle (2014). "Systematic properties of decelerating relativistic jets in low-luminosity radio galaxies". In: *MNRAS* 437.4, pp. 3405–3441. DOI: 10.1093/mnras/stt2138.

Larmor, J. (1919). "How could a rotating body such as the sun become a magnet". In: *Report of the British Association for the Advancement of Science*, pp. 159–160.

Lawden, D. F. (1982). *An introduction to tensor calculus, relativity and cosmology /3rd edition/*.

Leiderschneider, Elly and Tsvi Piran (2016). "Maximal efficiency of the collisional Penrose process". In: *Phys.Rev.D* 93.4, 043015, p. 043015. DOI: 10.1103/PhysRevD.93.043015.

Liska, M. et al. (2018). "Formation of precessing jets by tilted black hole discs in 3D general relativistic MHD simulations". In: *MNRAS* 474.1, pp. L81–L85. DOI: 10.1093/mnrasl/slx174.

Lister, M. L. et al. (2016). "MOJAVE: XIII. Parsec-scale AGN Jet Kinematics Analysis Based on 19 years of VLBA Observations at 15 GHz". In: *AJ* 152.1, 12, p. 12. DOI: 10.3847/0004-6256/152/1/12.

Lister, Matthew (2016). "AGN Jet Kinematics on Parsec-Scales: The MOJAVE Program". In: *Galaxies* 4.3, p. 29. DOI: 10.3390/galaxies4030029.

Longaretti, P.-Y. and G. Lesur (2010). "MRI-driven turbulent transport: the role of dissipation, channel modes and their parasites". In: *A&A* 516, A51, A51. DOI: 10.1051/0004-6361/201014093.

Lynden-Bell, D. (1969). "Galactic Nuclei as Collapsed Old Quasars". In: *Nature* 223, pp. 690–694. DOI: 10.1038/223690a0.

— (1996). "Magnetic collimation by accretion discs of quasars and stars". In: *MNRAS* 279, pp. 389–401. DOI: 10.1093/mnras/279.2.389.

— (2003). "On why discs generate magnetic towers and collimate jets". In: *MNRAS* 341.4, pp. 1360–1372. DOI: 10.1046/j.1365-8711.2003.06506.x.

— (2006). "Magnetic jets from swirling discs". In: *MNRAS* 369.3, pp. 1167–1188. DOI: 10.1111/j.1365-2966.2006.10349.x.

Lynden-Bell, D. and C. Boily (1994). "Self-Similar Solutions up to Flashpoint in Highly Wound Magnetostatics". In: *MNRAS* 267, p. 146. DOI: 10.1093/mnras/267.1.146.

Marklund, M. and C. A. Clarkson (2005). "The general relativistic magnetohydrodynamic dynamo equation". In: *Monthly Notices of the Royal Astronomical Society* 358.3, pp. 892–900. DOI: 10.1111/j.1365-2966.2005.08814.x.

Marshall, Megan D., Mark J. Avara, and Jonathan C. McKinney (2018). "Angular momentum transport in thin magnetically arrested discs". In: *MNRAS* 478.2, pp. 1837–1843. DOI: 10.1093/mnras/sty1184.

Maxwell, James Clerk (1865). "VIII. A dynamical theory of the electromagnetic field". In: *Philosophical Transactions of the Royal Society of London* 155, pp. 459–512. DOI: 10.

1098/rstl.1865.0008. URL: http://rstl.royalsocietypublishing.org/content/155/459.short.

McClintock, Jeffrey E. et al. (2006). "The Spin of the Near-Extreme Kerr Black Hole GRS 1915+105". In: *ApJ* 652.1, pp. 518–539. DOI: 10.1086/508457.

McKinney, J. C. (2006a). "General relativistic force-free electrodynamics: a new code and applications to black hole magnetospheres". In: *MNRAS* 367, pp. 1797–1807. DOI: 10.1111/j.1365-2966.2006.10087.x.

— (2006b). "General relativistic magnetohydrodynamic simulations of the jet formation and large-scale propagation from black hole accretion systems". In: *MNRAS* 368, pp. 1561–1582. DOI: 10.1111/j.1365-2966.2006.10256.x.

McKinney, J. C. and C. F. Gammie (2004). "A Measurement of the Electromagnetic Luminosity of a Kerr Black Hole". In: *ApJ* 611, pp. 977–995. DOI: 10.1086/422244.

McKinney, J. C., A. Tchekhovskoy, and R. D. Blandford (2012). "General relativistic magnetohydrodynamic simulations of magnetically choked accretion flows around black holes". In: *MNRAS* 423, pp. 3083–3117. DOI: 10.1111/j.1365-2966.2012.21074.x.

— (2013). "Alignment of Magnetized Accretion Disks and Relativistic Jets with Spinning Black Holes". In: *Science* 339, p. 49. DOI: 10.1126/science.1230811.

McKinney, J. C. et al. (2014). "Three-dimensional general relativistic radiation magnetohydrodynamical simulation of super-Eddington accretion, using a new code HARMRAD with M1 closure". In: *MNRAS* 441, pp. 3177–3208. DOI: 10.1093/mnras/stu762.

McKinney, Jonathan C. and Roger D. Blandford (2009). "Stability of relativistic jets from rotating, accreting black holes via fully three-dimensional magnetohydrodynamic simulations". In: *MNRAS* 394.1, pp. L126–L130. DOI: 10.1111/j.1745-3933.2009.00625.x.

McKinney, Jonathan C., Lixin Dai, and Mark J. Avara (2015). "Efficiency of super-Eddington magnetically-arrested accretion". In: *MNRAS* 454.1, pp. L6–L10. DOI: 10.1093/mnrasl/slv115.

McKinney, Jonathan C. and Ramesh Narayan (2007a). "Disc-jet coupling in black hole accretion systems - I. General relativistic magnetohydrodynamical models". In: *MNRAS* 375.2, pp. 513–530. DOI: 10.1111/j.1365-2966.2006.11301.x.

— (2007b). "Disc-jet coupling in black hole accretion systems - II. Force-free electrodynamical models". In: *MNRAS* 375.2, pp. 531–547. DOI: 10.1111/j.1365-2966.2006.11220.x.

Meliani, Z. et al. (2016). "GR-AMRVAC code applications: accretion onto compact objects, boson stars versus black holes". In: *Classical and Quantum Gravity* 33.15, 155010, p. 155010. DOI: 10.1088/0264-9381/33/15/155010.

Mertens, F. et al. (2016). "Kinematics of the jet in M 87 on scales of 100-1000 Schwarzschild radii". In: *A&A* 595, A54, A54. DOI: 10.1051/0004-6361/201628829.

Misner, C. W., K. S. Thorne, and J. A. Wheeler (1973). *Gravitation*.

Mizuno, Yosuke et al. (2006). "RAISHIN: A High-Resolution Three-Dimensional General Relativistic Magnetohydrodynamics Code". In: *arXiv e-prints*, astro-ph/0609004, astro–ph/0609004.

Moffatt, H. K. (1978). *Magnetic field generation in electrically conducting fluids*.

Murphy, G. C., J. Ferreira, and C. Zanni (2010). "Large scale magnetic fields in viscous resistive accretion disks. I. Ejection from weakly magnetized disks". In: *A&A* 512, A82, A82. DOI: 10.1051/0004-6361/200912633.

Nakamura, Masanori and Keiichi Asada (2013). "The Parabolic Jet Structure in M87 as a Magnetohydrodynamic Nozzle". In: *ApJ* 775.2, 118, p. 118. DOI: 10.1088/0004-637X/775/2/118.

Nakamura, Masanori, David Garofalo, and David L. Meier (2010). "A Magnetohydrodynamic Model of the M87 Jet. I. Superluminal Knot Ejections from HST-1 as Trails of Quad Relativistic MHD Shocks". In: *ApJ* 721.2, pp. 1783–1789. DOI: 10.1088/0004-637X/721/2/1783.

Nakamura, Masanori et al. (2018). "Parabolic Jets from the Spinning Black Hole in M87". In: *ApJ* 868.2, 146, p. 146. DOI: 10.3847/1538-4357/aaeb2d.

Noble, S. C., J. H. Krolik, and J. F. Hawley (2009). "Direct Calculation of the Radiative Efficiency of an Accretion Disk Around a Black Hole". In: *ApJ* 692, pp. 411–421. DOI: 10.1088/0004-637X/692/1/411.

— (2010). "Dependence of Inner Accretion Disk Stress on Parameters: The Schwarzschild Case". In: *ApJ* 711, pp. 959–973. DOI: 10.1088/0004-637X/711/2/959.

Noble, S. C. et al. (2006). "Primitive Variable Solvers for Conservative General Relativistic Magnetohydrodynamics". In: *ApJ* 641, pp. 626–637. DOI: 10.1086/500349.

Noble, Scott C. et al. (2011). "Radiative Efficiency and Thermal Spectrum of Accretion onto Schwarzschild Black Holes". In: *ApJ* 743.2, 115, p. 115. DOI: 10.1088/0004-637X/743/2/115.

Noble, Scott C. et al. (2012). "Circumbinary Magnetohydrodynamic Accretion into Inspiraling Binary Black Holes". In: *ApJ* 755.1, 51, p. 51. DOI: 10.1088/0004-637X/755/1/51.

Novikov, I. D. and K. S. Thorne (1973). "Astrophysics of black holes." In: *Black Holes (Les Astres Occlus)*. Ed. by C. Dewitt and B. S. Dewitt, pp. 343–450.

Ouyed, R. and R. E. Pudritz (1997). "Numerical Simulations of Astrophysical Jets from Keplerian Disks. I. Stationary Models". In: *ApJ* 482, pp. 712–732.

Paczyński, B. and P. J. Wiita (1980). "Thick accretion disks and supercritical luminosities". In: *A&A* 88, pp. 23–31.

Palenzuela, C. et al. (2009). "Beyond ideal MHD: towards a more realistic modelling of relativistic astrophysical plasmas". In: *MNRAS* 394, pp. 1727–1740. DOI: 10.1111/j.1365-2966.2009.14454.x.

Pariev, Vladimir I., Stirling A. Colgate, and J. M. Finn (2007). "A Magnetic α-ω Dynamo in AGN Disks. II. Magnetic Field Generation, Theories, and Simulations". In: *The Astrophysical Journal* 658.1, pp. 129–160. DOI: 10.1086/510735.

Parker, Eugene N. (1955). "Hydromagnetic Dynamo Models." In: *ApJ* 122, p. 293. DOI: 10.1086/146087.

Penna, R. F. et al. (2010). "Simulations of magnetized discs around black holes: effects of black hole spin, disc thickness and magnetic field geometry". In: *MNRAS* 408, pp. 752–782. DOI: 10.1111/j.1365-2966.2010.17170.x.

Penrose, R. (2002). ""Golden Oldie": Gravitational Collapse: The Role of General Relativity". In: *General Relativity and Gravitation* 7, pp. 1141–1165. DOI: 10.1023/A:1016578408204.

Penrose, Roger (1969). "Gravitational Collapse: the Role of General Relativity". In: *Nuovo Cimento Rivista Serie* 1, p. 252.

Perlmutter, S. et al. (1999). "Measurements of Ω and Λ from 42 High-Redshift Supernovae". In: *ApJ* 517.2, pp. 565–586. DOI: 10.1086/307221.

Piran, T., J. Shaham, and J. Katz (1975). "High Efficiency of the Penrose Mechanism for Particle Collisions". In: *ApJ* 196, p. L107. DOI: 10.1086/181755.

Ponomarenko, Yu. B. (1973). "Theory of the hydromagnetic generator". In: *Journal of Applied Mechanics and Technical Physics* 14.6, pp. 775–778. ISSN: 1573-8620. DOI: 10.1007/BF00853190. URL: https://doi.org/10.1007/BF00853190.

Porth, O. (2013). "Three-dimensional structure of relativistic jet formation". In: *MNRAS* 429, pp. 2482–2492. DOI: 10.1093/mnras/sts519.

Porth, O. and C. Fendt (2010). "Acceleration and Collimation of Relativistic Magnetohydrodynamic Disk Winds". In: *ApJ* 709, pp. 1100–1118. DOI: 10.1088/0004-637X/709/2/1100.

Porth, O. et al. (2011). "Synchrotron Radiation of Self-collimating Relativistic Magnetohydrodynamic Jets". In: *ApJ* 737, 42, p. 42. DOI: 10.1088/0004-637X/737/1/42.

Porth, Oliver et al. (2017). "The black hole accretion code". In: *Computational Astrophysics and Cosmology* 4.1, 1, p. 1. DOI: 10.1186/s40668-017-0020-2.

Porth, Oliver et al. (2019). "The Event Horizon General Relativistic Magnetohydrodynamic Code Comparison Project". In: *ApJS* 243.2, 26, p. 26. DOI: 10.3847/1538-4365/ab29fd.

Prendergast, K. H. and G. R. Burbidge (1968). "On the Nature of Some Galactic X-Ray Sources". In: *ApJ* 151, p. L83. DOI: 10.1086/180148.

Pringle, J. E. and M. J. Rees (1972). "Accretion Disc Models for Compact X-Ray Sources". In: *A&A* 21, p. 1.

Pudritz, R. E. (1981a). "Dynamo Action in Turbulent Accretion Discs around Black Holes - Part Two - the Mean Magnetic Field". In: *MNRAS* 195, p. 897. DOI: 10.1093/mnras/195.4.897.

— (1981b). "Dynamo action in turbulent accretion discs around black holes. I - The fluctuations. II - The mean magnetic field". In: *MNRAS* 195, pp. 881–914. DOI: 10.1093/mnras/195.4.881.

Pudritz, R. E. and J. Silk (1989). "The origin of magnetic fields and primordial stars in protogalaxies". In: *ApJ* 342, pp. 650–659. DOI: 10.1086/167625.

Punch, M. et al. (1992). "Detection of TeV photons from the active galaxy Markarian 421". In: *Nature* 358.6386, pp. 477–478. DOI: 10.1038/358477a0.

Punsly, B. and F. V. Coroniti (1990a). "Ergosphere-driven Winds". In: *ApJ* 354, p. 583. DOI: 10.1086/168717.

Punsly, Brian and Ferdinand V. Coroniti (1990b). "Relativistic Winds from Pulsar and Black Hole Magnetospheres". In: *ApJ* 350, p. 518. DOI: 10.1086/168408.

Pushkarev, Alexander et al. (2017). "Linear Polarization Properties of Parsec-Scale AGN Jets". In: *Galaxies* 5.4, p. 93. DOI: 10.3390/galaxies5040093.

Qian, Q., C. Fendt, and C. Vourellis (2018). "Jet Launching in Resistive GR-MHD Black Hole-Accretion Disk Systems". In: *ApJ* 859, 28, p. 28. DOI: 10.3847/1538-4357/aabd36.

Qian, Q. et al. (2017). "rHARM: Accretion and Ejection in Resistive GR-MHD". In: *ApJ* 834, 29, p. 29. DOI: 10.3847/1538-4357/834/1/29.

Raine, Derek and Edwin Thomas (2005). *Black Holes: AN Introduction*. DOI: 10.1142/p409.

Readhead, A. C. S. et al. (1978). "Bent beams and the overall size of extragalactic radio sources". In: *Nature* 276, pp. 768–771. DOI: 10.1038/276768a0.

Readhead, A. C. S. et al. (1996). "The Statistics and Ages of Compact Symmetric Objects". In: *ApJ* 460, p. 612. DOI: 10.1086/176996.

Rees, M. J. (1966). "Appearance of Relativistically Expanding Radio Sources". In: *Nature* 211.5048, pp. 468–470. DOI: 10.1038/211468a0.

— (1971). "New Interpretation of Extragalactic Radio Sources". In: *Nature* 229.5283, pp. 312–317. DOI: 10.1038/229312a0.

Rekowski, M. v., G. Rüdiger, and D. Elstner (2000). "Structure and magnetic configurations of accretion disk-dynamo models". In: *A&A* 353, pp. 813–822.

Remillard, Ronald A. and Jeffrey E. McClintock (2006). "X-Ray Properties of Black-Hole Binaries". In: *ARA&A* 44.1, pp. 49–92. DOI: 10.1146/annurev.astro.44.051905.092532.

Reynolds, Christopher S., David Garofalo, and Mitchell C. Begelman (2006). "Trapping of Magnetic Flux by the Plunge Region of a Black Hole Accretion Disk". In: *ApJ* 651.2, pp. 1023–1030. DOI: 10.1086/507691.

Rezzolla, Luciano and Olindo Zanotti (2013). *Relativistic Hydrodynamics*.

Riess, Adam G. et al. (1998). "Observational Evidence from Supernovae for an Accelerating Universe and a Cosmological Constant". In: *AJ* 116.3, pp. 1009–1038. DOI: 10.1086/300499.

Ripperda, B. et al. (2019). "General-relativistic Resistive Magnetohydrodynamics with Robust Primitive-variable Recovery for Accretion Disk Simulations". In: *ApJS* 244.1, 10, p. 10. DOI: 10.3847/1538-4365/ab3922.

Romero, Gustavo E. and Gabriela S. Vila (2014). *Introduction to Black Hole Astrophysics*. Vol. 876. DOI: 10.1007/978-3-642-39596-3.

Ruediger, G. and L. L. Kichatinov (1993). "Alpha-effect and alpha-quenching". In: *A&A* 269.1-2, pp. 581–588.

Salpeter, E. E. (1964). "Accretion of Interstellar Matter by Massive Objects." In: *ApJ* 140, pp. 796–800. DOI: 10.1086/147973.

Sandage, Allan (1965). "The Existence of a Major New Constituent of the Universe: the Quasistellar Galaxies." In: *ApJ* 141, p. 1560. DOI: 10.1086/148245.

Sądowski, A. et al. (2014). "Numerical simulations of super-critical black hole accretion flows in general relativity". In: *MNRAS* 439, pp. 503–520. DOI: 10.1093/mnras/stt2479.

Schmidt, M. (1963). "3C 273 : A Star-Like Object with Large Red-Shift". In: *Nature* 197.4872, p. 1040. DOI: 10.1038/1971040a0.

Schnittman, Jeremy D. (2014). "Revised Upper Limit to Energy Extraction from a Kerr Black Hole". In: *Phys. Rev. Lett.* 113 (26), p. 261102. DOI: 10.1103/PhysRevLett.113.261102. URL: https://link.aps.org/doi/10.1103/PhysRevLett.113.261102.

Schreier, E. J., P. Gorenstein, and E. D. Feigelson (1982). "High-resolution X-ray observations of M87 - Nucleus, jet and radio halo". In: *ApJ* 261, pp. 42–50. DOI: 10.1086/160316.

Schutz, Bernard F. (1985). *A First Course in General Relativity*.

Schwarzschild, Karl (1916). "Über das Gravitationsfeld eines Massenpunktes nach der Einsteinschen Theorie". In: *Sitzungsberichte der Königlich Preußischen Akademie der Wissenschaften (Berlin*, pp. 189–196.

Seyfert, Carl K. (1943). "Nuclear Emission in Spiral Nebulae." In: *ApJ* 97, p. 28. DOI: 10.1086/144488.

Shafee, Rebecca et al. (2008). "Three-Dimensional Simulations of Magnetized Thin Accretion Disks around Black Holes: Stress in the Plunging Region". In: *ApJ* 687.1, p. L25. DOI: 10.1086/593148.

Shakura, N. I. (1973). "Disk Model of Gas Accretion on a Relativistic Star in a Close Binary System." In: *Sov. Ast.* 16, p. 756.

Shakura, N. I. and R. A. Sunyaev (1973). "Black holes in binary systems. Observational appearance." In: *A&A* 24, pp. 337–355.

Sheikhnezami, S. et al. (2012). "Bipolar Jets Launched from Magnetically Diffusive Accretion Disks. I. Ejection Efficiency versus Field Strength and Diffusivity". In: *ApJ* 757, 65, p. 65. DOI: 10.1088/0004-637X/757/1/65.

Shiokawa, Hotaka et al. (2012). "Global General Relativistic Magnetohydrodynamic Simulations of Black Hole Accretion Flows: A Convergence Study". In: *ApJ* 744.2, 187, p. 187. DOI: 10.1088/0004-637X/744/2/187.

Shiokawa, Hotaka et al. (2015). "General Relativistic Hydrodynamic Simulation of Accretion Flow from a Stellar Tidal Disruption". In: *ApJ* 804.2, 85, p. 85. DOI: 10.1088/0004-637X/804/2/85.

Shklovskii, I. S. (1955). "O Prirode Izlučeniâ Radiogalaktiki NGC 4486O Prirode Izlučeniâ Radiogalaktiki NGC 4486On the Nature of the Emission of Radiogalaxy NGC 4486." In: *Astron.J.USSR* 32, p. 215.

Sikora, Marek, Łukasz Stawarz, and Jean-Pierre Lasota (2007). "Radio Loudness of Active Galactic Nuclei: Observational Facts and Theoretical Implications". In: *ApJ* 658.2, pp. 815–828. DOI: 10.1086/511972.

Sądowski, Aleksander et al. (2015). "Global simulations of axisymmetric radiative black hole accretion discs in general relativity with a mean-field magnetic dynamo". In: *MNRAS* 447.1, pp. 49–71. DOI: 10.1093/mnras/stu2387.

Sądowski, Aleksander et al. (2017). "Radiative, two-temperature simulations of low-luminosity black hole accretion flows in general relativity". In: *MNRAS* 466.1, pp. 705–725. DOI: 10.1093/mnras/stw3116.

Smith, Harlan J. and Dorrit Hoffleit (1963). "Light Variations in the Superluminous Radio Galaxy 3C273". In: *Nature* 198.4881, pp. 650–651. DOI: 10.1038/198650a0.

Steenbeck, M. and F. Krause (1966). "Erklärung stellarer und planetarer Magnetfelder durch einen turbulenzbedingten Dynamomechanismus". In: *Zeitschrift Naturforschung Teil A* 21, p. 1285. DOI: 10.1515/zna-1966-0813.

— (1969a). "On the Dynamo Theory of Stellar and Planetary Magnetic Fields. I. AC Dynamos of Solar Type". In: *Astronomische Nachrichten* 291, pp. 49–84. DOI: 10.1002/asna.19692910201.

— (1969b). "On the Dynamo Theory of Stellar and Planetary Magnetic Fields. II. DC Dynamos of Planetary Type". In: *Astronomische Nachrichten* 291, pp. 271–286.

Stepanovs, D. and C. Fendt (2014). "Modeling MHD Accretion-Ejection from the Launching Area to Propagation Scales". In: *ApJ* 793, 31, p. 31. DOI: 10.1088/0004-637X/793/1/31.

— (2016). "An Extensive Numerical Survey of the Correlation Between Outflow Dynamics and Accretion Disk Magnetization". In: *ApJ* 825, 14, p. 14. DOI: 10.3847/0004-637X/825/1/14.

Stepanovs, D., C. Fendt, and S. Sheikhnezami (2014). "Modeling MHD Accretion-Ejection: Episodic Ejections of Jets Triggered by a Mean-field Disk Dynamo". In: *ApJ* 796, 29, p. 29. DOI: 10.1088/0004-637X/796/1/29.

Stepinski, T. F. and E. H. Levy (1988). "Generation of Dynamo Magnetic Fields in Protoplanetary and Other Astrophysical Accretion Disks". In: *ApJ* 331, p. 416. DOI: 10.1086/166569.

Tchekhovskoy, A. and J. C. McKinney (2012). "Prograde and retrograde black holes: whose jet is more powerful?" In: *MNRAS* 423, pp. L55–L59. DOI: 10.1111/j.1745-3933.2012.01256.x.

Tchekhovskoy, A., J. C. McKinney, and R. Narayan (2009). "Efficiency of Magnetic to Kinetic Energy Conversion in a Monopole Magnetosphere". In: *ApJ* 699, pp. 1789–1808. DOI: 10.1088/0004-637X/699/2/1789.

Tchekhovskoy, A., R. Narayan, and J. C. McKinney (2010). "Black Hole Spin and The Radio Loud/Quiet Dichotomy of Active Galactic Nuclei". In: *ApJ* 711, pp. 50–63. DOI: 10.1088/0004-637X/711/1/50.

— (2011). "Efficient generation of jets from magnetically arrested accretion on a rapidly spinning black hole". In: *MNRAS* 418, pp. L79–L83. DOI: 10.1111/j.1745-3933.2011.01147.x.

Tchekhovskoy, Alexander, Jonathan C. McKinney, and Ramesh Narayan (2007). "WHAM: a WENO-based general relativistic numerical scheme - I. Hydrodynamics". In: *MNRAS* 379.2, pp. 469–497. DOI: 10.1111/j.1365-2966.2007.11876.x.

Thorne, Kip S. (1974). "Disk-Accretion onto a Black Hole. II. Evolution of the Hole". In: *ApJ* 191, pp. 507–520. DOI: 10.1086/152991.

Thorne, Kip S., Richard H. Price, and Douglas A. MacDonald (1986). *Black holes: The membrane paradigm.*

Tremblay, S. E. et al. (2016). "Compact symmetric objects and supermassive binary black holes in the VLBA Imaging and Polarimetry Survey". In: *MNRAS* 459.1, pp. 820–840. DOI: 10.1093/mnras/stw592.

Ustyugova, G. V. et al. (1995). "Magnetohydrodynamic simulations of outflows from accretion disks". In: *ApJ* 439, pp. L39–L42. DOI: 10.1086/187739.

von Rekowski, B. et al. (2003). "Structured outflow from a dynamo active accretion disc". In: *Astronomy and Astrophysics* 398, pp. 825–844. DOI: 10.1051/0004-6361:20021699.

Vourellis, Christos et al. (2019). "GR-MHD Disk Winds and Jets from Black Holes and Resistive Accretion Disks". In: *ApJ* 882.1, 2, p. 2. DOI: 10.3847/1538-4357/ab32e2.

Wald, R. M. (1984). *General relativity.*

Walker, R. Craig et al. (2018). "The Structure and Dynamics of the Subparsec Jet in M87 Based on 50 VLBA Observations over 17 Years at 43 GHz". In: *ApJ* 855.2, 128, p. 128. DOI: 10.3847/1538-4357/aaafcc.

Weinberg, Steven (1972). *Gravitation and Cosmology: Principles and Applications of the General Theory of Relativity.*

White, Christopher J., James M. Stone, and Charles F. Gammie (2016). "An Extension of the Athena++ Code Framework for GRMHD Based on Advanced Riemann Solvers and Staggered-mesh Constrained Transport". In: *ApJS* 225.2, 22, p. 22. DOI: 10.3847/0067-0049/225/2/22.

Wilkinson, P. N. et al. (1977). "Radio structure of 3C 147 determined by multi-element very long baseline interferometry." In: *Nature* 269, pp. 764–768. DOI: 10.1038/269764a0.

Wilkinson, P. N. et al. (1994). "Two-sided Ejection in Powerful Radio Sources: The Compact Symmetric Objects". In: *ApJ* 432, p. L87. DOI: 10.1086/187518.

Wilson, J. R. (1972). "Numerical Study of Fluid Flow in a Kerr Space". In: *ApJ* 173, p. 431. DOI: 10.1086/151434.

Woosley, S. E. and J. S. Bloom (2006). "The Supernova Gamma-Ray Burst Connection". In: *ARA&A* 44, pp. 507–556. DOI: 10.1146/annurev.astro.43.072103.150558.

Xu, Hao et al. (2008). "The Biermann Battery in Cosmological MHD Simulations of Population III Star Formation". In: *The Astrophysical Journal* 688.2, pp. L57–L60. DOI: 10.1086/595617. URL: https://doi.org/10.1086%2F595617.

Zanni, C. et al. (2007). "MHD simulations of jet acceleration from Keplerian accretion disks. The effects of disk resistivity". In: *A&A* 469, pp. 811–828. DOI: 10.1051/0004-6361:20066400.

Zavala, R. T. and G. B. Taylor (2004). "A View through Faraday's Fog. II. Parsec-Scale Rotation Measures in 40 Active Galactic Nuclei". In: *ApJ* 612.2, pp. 749–779. DOI: 10.1086/422741.

Zel'dovich, Ya. B. (1964). "The Fate of a Star and the Evolution of Gravitational Energy Upon Accretion". In: *Soviet Physics Doklady* 9, p. 195.

Acknowledgements

The work presented in this thesis is a result of a journey that started four years ago. In this journey I was never alone, all the time I had people next to me who supported me and helped me during difficult times and celebrated with me all the small and big accomplishments. This is the reason the thesis is written in the first plural person. All the work presented here is done by me and when I started writing I tried to use the singular first person pronoun. The result was sentences that to me seemed full of arrogance, vanity and unnecessary pride. Sentences that gave me the feeling that I was forgetting people, that I was ignoring their (in)direct contribution. It is true that without them, I would not be here, writing this words tonight. So I decided to switch to the "we" pronoun in order to honor everyone for their help, support, friendship and love. In the Acknowledgements section, however, is where I will temporarily distance myself from them–you–in order to give back the credit and the thanks I owe.

First and foremost I want to thank my advisor Christian Fendt for his immense help and support during the last four years. Your office was always open to me and I am glad I can finally buy you the new pair of glasses I own you. I also want to the other members of our jet group Qian Qian and Giancarlo Mattia for their help and useful discussions. I want to thank Scott C. Noble for allowing me to use and modify his code. I want to thank the members of my examination committee, Henrik Beuther, Kurt Roth and especially Cornelis Dullemond who also agreed to act as the referee for this thesis. The Max Planck Institute for Astronomy allowed me to use their computational facilities. All the simulation were run in MPIA's `ISAAC` cluster and MPG's `COBRA` and `DRACO` clusters. I also want to thank IMPRS-HD for funding my PhD project.

As you would have probably already realized by reading this section, my England is not very best. So I would like to thank my native English speaking friends, Jacob Isbel, Melanie Kaasinen, Vincent Carpenter and Steffi Yen who were patient enough to proofread parts of my thesis as well as Jonas Syed for his help with the German version of the abstract.

The Max Planck Institute for Astronomy and the International Max Planck Research School for Astronomy and Cosmic Physics have created the most friendly and supportive environment for young scientists. In the four years I spent in Heidelberg I had the blessing of meeting many people from all over the world who I would never hope to know and who I now can call friends. I know that after some years we will all be in different countries and continents, however the moments we shared will stay in my heart forever.

Office 216B was my second home for four years not only because I was spending the large part of the day there, but also because of the people who were sitting in the other desks. **Asmita Bhandare**, you were the heart and soul of this office. Keep eating and being happy! **Camille Bergez-Casalou**, you brought a French elegance in our office. Keep believing in yourself and you will reach the stars. **Mikhail Kovalëv** your knowledge of physics, astronomy... of everything is astonishing. Please help me cheat during the examination! **Jonas Frings**, you were always so quiet, it was like you were not there. I hope you are happy with your little Jaro. **Jonas Syed**, welcome to the best four years of your life. Make sure you will enjoy them as much as possible.

As I said before, MPIA has a large number of PhD candidates which increases even more with the usual I was (un)lucky enough to serve as a host of the Daily Student's Afternoon Coffee in my office during which I got to know many people from our institute. **Ivana Barisic,**

Arianna Musso-Barcucci, Josha van Houdt, Johanna Coronado, Felipe Goicovic, Sepideh Sadegi, Manuel Riener, Sara Rezaei, Francisco Aros, Christian Lenz, Felix Bosco, Grigorii Smirnov-Pinchukov, Irina Smirnova-Pinchukova, Jacob Isbel, Paula Sarkis, Vincent Carpenter, Theodora Xylaki-Dornbusch, Theodoros Anagnos.

To the people of my generation of students. Thank you for **ector Hiß, Hans Baehr, Christina Eilers, Tobias Buck, Sven Buder, Mayte Alfaro, Gigi Leung, Priscilla Chaucke, Aida Ahmadi, Daniel Rahner, Fabian Klein, Stefan Brems, Johannes Esser, Daniel Haydon, Svenja Jacob, Armelle Jardin-Blicq, Grigoris Katsoulakos, Marcelo Tala Pinto.**

To the heroes of Thor Day's IMPRS dinner, **Alex Hygate, Matthias Samland, Neven Tomicic, Sabina Pürckhauer, Sebastian Bustamante, Steffi Yen, Vikas Joshi, Yulong Zhuang,** who kept the tradition going for more than four years. You became some of my closest friends. I cherish the numerous discussions we had over dinner, the games we played, the trips we had.

Στους γονείς μου, σας ευχαριστω για την βοήθεια και την στήριξη όλα αυτά τα χρόνια στις σπουδές μου στην Ελλάδα και στη Γερμανία. Δεν θα ξεχάσω ποτέ τι κάνατε για μένα. Το **Konstantina**, σε ευχαριστώ για όλες τις στιγμές που περάσαμε μαζί αν και μακρυά ο ένας από τον άλλο. Η υποστήριξή σου με βοήθησε να τα βγάλω πέρα. Σύντομα θα είμαστε και πάλι κόντα!

Finally, to all my friends from all over the world, I will never forget the moments we shared. Thank you for four amazing years.

Ἡ Ἰθάκη σ᾽ ἔδωσε τ᾽ ὡραῖο ταξίδι.	Ithaca gave you the marvelous journey.
Χωρὶς αὐτὴν δὲν θἄβγαινες στὸν δρόμο.	Without her you wouldn't have set out.
Ἄλλα δὲν ἔχει νὰ σὲ δώσει πιά.	She has nothing left to give you now.
Κι ἂν πτωχικὴ τὴν βρῇς, ἡ Ἰθάκη δὲν σὲ γέλασε.	And if you find her poor, Ithaca won't have fooled you.
Ἔτσι σοφὸς ποὺ ἔγινες, μὲ τόση πείρα,	Wise as you will have become, so full of experience,
ἤδη θὰ τὸ κατάλαβες ἡ Ἰθάκες τί σημαίνουν.	you'll have understood by then what these Ithacas mean.

Ithaca, C.P. Cavafy (1863–1933)

Declaration of Authorship

I, Christos Vourellis, declare that this thesis titled, "GRMHD Launching of Outflows from Resistive and Dynamo Active Disks" and the work presented in it are my own. I confirm that:

- This work was done wholly while in candidature for a research degree at this University.
- Where I have consulted the published work of others, this is always clearly attributed.
- Where I have quoted from the work of others, the source is always given. With the exception of such quotations, this thesis is entirely my own work.
- I have acknowledged all main sources of help.

Signed:

Date: